

# Dissertation

submitted to the

Combined Faculties of the Natural Sciences and Mathematics

of the Ruperto-Carola-University of Heidelberg, Germany

for the degree of

Doctor of Natural Sciences

Put forward by

**Xiaoyang Duan**

*born in: Shanxi, P. R. China*

Oral examination: 25.07.2019



# Dynamic Nanoplasmonics

Referees: Prof. Dr. Laura Na Liu

Prof. Dr. Yana Vaynzof



# Abstract

Light can strongly interact with metallic nanostructures, leading collective oscillations of conduction electrons known as particle plasmons. For a long time, gold and silver have been the metals of choice for constructing plasmonic nanodevices, given their excellent optical properties. However, these metals present static optical responses. In the past decade, tremendous interest has been witnessed in dynamically controlling the optical properties of plasmonic nanostructures. To enable dynamic functionality, several approaches have been proposed and implemented. First one is to manipulate the configurations of plasmonic structures. Second one is to tune the dielectric surroundings of plasmonic nanostructures. Third one, which is probably the most intriguing one, is to directly regulate the carrier densities and dielectric functions of the metals themselves.

Magnesium is one of the promising candidates, as it exhibits excellent optical properties at high frequencies and can absorb/desorb hydrogen, undergoing reversible transitions between metal and dielectric hydride states. This offers great opportunities to design and construct dynamic optical nanodevices at visible frequencies. We envision that Magnesium-based dynamic nanoplasmonics will not only provide insights into understanding the catalytic processes of hydrogen diffusion in metals on the nanometer scale by optical means but also it will open an avenue towards functional plasmonic nanodevices with tailored optical properties for real-world applications.

# Zusammenfassung

Interagiert Licht mit metallischen Nanostrukturen, können kollektive Oszillationen von Leitungsband-Elektronen, sogenannte Partikel-Plasmen, angeregt werden. Plasmonische Bauteile bestehend aus solchen Nanostrukturen werden zumeist aus Gold und Silber aufgrund ihrer hervorragenden optischen Eigenschaften angefertigt. Im letzten Jahrzehnt wurden zahlreiche Ansätze erforscht um den ansonsten statischen optischen Eigenschaften der Nanostrukturen eine dynamische Funktionalität zu verleihen: Zum einen kann die Anordnung bzw. das umgebende Medium der plasmonischen Nanostrukturen verändert werden. Zum anderen, und das ist wahrscheinlich der elegantere Ansatz, können die Ladungsträgerdichten und dielektrischen Funktionen der Metalle selbst modifiziert werden.

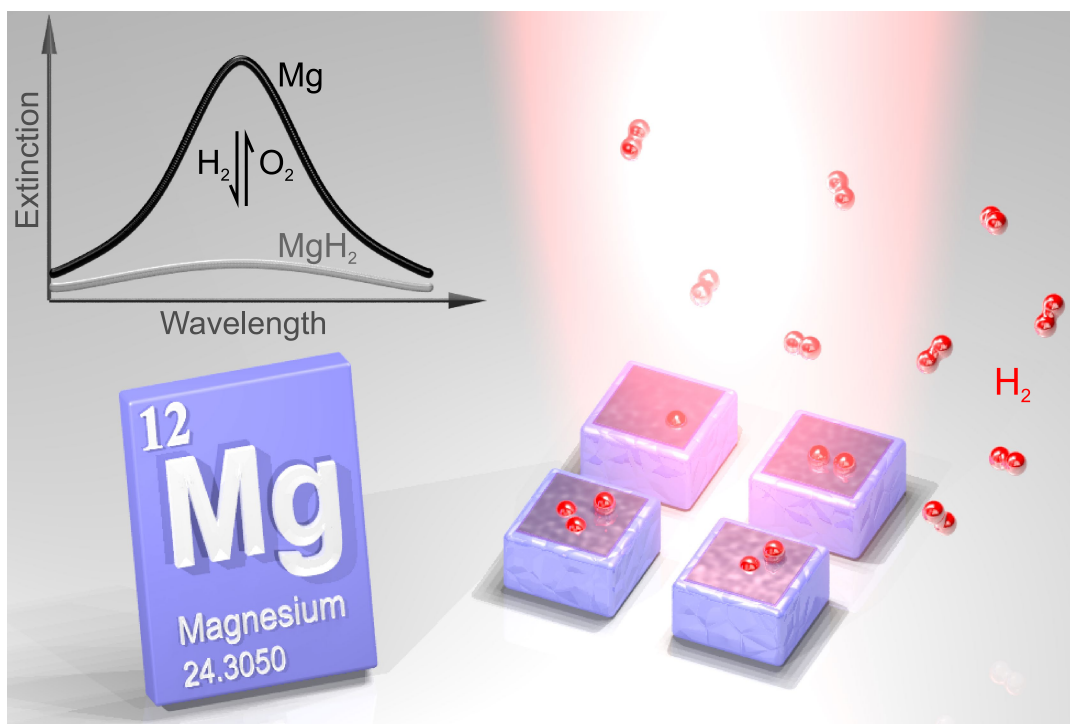
Hierbei ist Magnesium einer der aussichtsreichsten Kandidaten für dynamische optische Bauelemente im sichtbaren Spektralbereich. Magnesium weist neben den exzellenten optischen Eigenschaften einen Metall-Isolator-Phasenübergang auf, der durch die Absorption und Desorption von Wasserstoff gesteuert werden kann. Basierend auf den

Ergebnissen der vorliegenden Arbeit ist davon auszugehen, dass die dynamische Nanoplasmonik mittels Magnesium nicht nur Einblicke in das Verständnis der katalytischen Prozesse der Wasserstoffdiffusion in Metallen im Nanometerbereich bietet, sondern auch die Tür für funktionale plasmonische Nanobauteile mit maßgeschneiderten optischen Eigenschaften zu realen Anwendungen öffnet.

# Foreword

The presented cumulative dissertation summarizes the essential results, which were published on the following peer-reviewed journals.

- ◆ **Hydrogen-regulated chiral nanoplasmonics**  
Duan, X.; Kamin, S.; Sterl, F.; Giessen, H.; Liu, N.  
*Nano Lett.* **2016**, *16*, 1462–1466.
- ◆ **Dynamic plasmonic colour display**  
Duan, X.; Kamin, S.; Liu, N.  
*Nat. Commun.* **2017**, *8*, 14606.
- ◆ **Scanning plasmonic color display**  
Duan, X.; Liu, N.  
*ACS Nano* **2018**, *12*, 8817–8823.
- ◆ **Self-recording and manipulation of fast long-range hydrogen diffusion in quasifree magnesium**  
Duan, X.; Griessen, R.; Wijngaarden, R. J.; Kamin, S.; Liu, N.  
*Phys. Rev. Mater.* **2018**, *2*, 085802.
- ◆ **Dynamic color displays using stepwise cavity resonators**  
Chen, Y.\* Duan, X.\* Matuschek, M.\* Zhou, Y.; Neubrech, F.; Duan, H.; Liu, N.  
*Nano Lett.* **2017**, *17*, 5555–5560.
- ◆ **Magnesium for dynamic nanoplasmonics**  
Duan, X.; Liu, N.  
*Acc. Chem. Res.* **2019**, (invited).





# Contents

Abstract .....	i
Zusammenfassung .....	i
Foreword .....	iii
Contents .....	v
Acronyms .....	ix
1. Introduction .....	1
1.1. Dynamic plasmonics .....	1
1.2. Outline .....	2
2. Theoretical background and methods .....	5
2.1. Plasmonics .....	5
2.1.1. Maxwell's equations .....	5
2.1.2. Optical properties of metals .....	7
2.1.3. Surface plasmon polaritons .....	10
2.1.4. Localized surface plasmons .....	12
2.1.5. Plasmonic color .....	15
2.2. The metal-hydrogen system .....	18
2.2.1. Hydrogen energy .....	18
2.2.2. Hydrogen-storage metals .....	19
2.2.3. Palladium .....	21
2.3. Magnesium .....	22
2.3.1. Plasmonic properties of Mg .....	22
2.3.2. Dynamic properties of Mg .....	24
2.3.3. Dynamic plasmonic nanoparticles .....	27
2.3.4. Stability, reversibility, and durability .....	28
2.4. Methods .....	29
2.4.1. Fabrications .....	29
2.4.2. Simulations .....	30
3. Dynamic plasmonic chirality .....	35
3.1. Introduction to plasmonic chirality .....	36
3.1.1. Chirality .....	36
3.1.2. Plasmonic chirality .....	36
3.2. Mechanism of hydrogen-regulated chiral plasmonics .....	37
3.3. Experiments and simulations .....	39
3.4. Optical response .....	39
3.5. Switching dynamics .....	43
3.6. Durability in ambient air .....	44

3.7.	Conclusion .....	46
4.	Dynamic display based on Mg nanoparticles .....	47
4.1.	Introduction to plasmonic display .....	48
4.2.	Working principle of the dynamic plasmonic colour display.....	49
4.3.	Dynamic display of the Max-Planck-Society's Minerva logo .....	59
4.4.	Plasmonic subwavelength animations .....	62
4.5.	Highly secure information encryption .....	63
4.6.	Dynamic display of arbitrary images.....	64
4.7.	Discussion.....	65
5.	Dynamic display based on Mg cavities .....	67
5.1.	Introduction .....	68
5.2.	Mechanism of colour generation .....	69
5.3.	Optical response of the palette.....	70
5.4.	Ishihara display.....	75
5.5.	Arbitrary dynamic display .....	77
5.6.	Experiments and simulations .....	78
5.6.1.	Sample fabrication .....	78
5.6.2.	Optical measurements.....	79
5.6.3.	Numerical simulations .....	79
5.7.	Conclusions .....	80
6.	Lateral diffusion in Mg .....	81
6.1.	Introduction .....	82
6.2.	Experiment.....	82
6.2.1.	Samples.....	82
6.2.2.	Optical measurements.....	83
6.2.3.	AFM and SEM measurements .....	83
6.2.4.	Focussed-ion beam measurements.....	83
6.3.	Ubiquity and general properties of finger patterns .....	84
6.4.	Manipulation of diffusion streams.....	87
6.5.	Self-recording and simulations of streamlines .....	89
6.6.	Synergetic interaction of finger patterns .....	90
6.7.	Hydrogen diffusion measurements .....	91
6.8.	Detailed sample layout .....	93
6.9.	Reproducibility and general properties of finger patterns .....	93
6.9.1.	Constancy of average height increase .....	93
6.9.2.	Average heights for two loading/unloading cycles .....	94
6.9.3.	Zero in-plane expansion during hydrogenation .....	95
6.9.4.	Absence of buckles .....	96

6.9.5. Mechanism .....	96
6.10. H loading-unloading symmetry.....	98
6.11. Measurements of diffusion front mobility .....	99
6.11.1. Temperature dependence of front mobility.....	99
6.11.2. Dependence of the front mobility on the Mg thickness and H <sub>2</sub> pressure .....	99
6.12. Theoretical model.....	100
6.12.1. Concentration dependent diffusion coefficient .....	100
6.12.2. Diffusion.....	102
6.12.3. Simulation procedure.....	104
6.12.4. Loading-unloading symmetry in diffusion simulations .....	105
6.12.5. Diffusion simulations for samples with inserted objects .....	106
6.12.6. Effective diffusion coefficient of a Pd object in quasi-free Mg.....	106
6.12.7. Model for the pressure dependence of front mobility.....	107
6.12.8. Implications for the pressure-composition isotherms .....	109
6.13. Conclusions.....	110
7. Scanning display using lateral diffusion in Mg.....	111
7.1. Introduction .....	112
7.2. Mechanism of the scanning display .....	112
7.3. Kinetics of the scanning process .....	114
7.4. Palette .....	116
7.5. Sichuan opera facial mask display .....	117
7.6. Flexible Pd entrance .....	118
7.7. Information encryption.....	120
7.8. Experiments.....	122
7.8.1. Structure fabrications.....	122
7.8.2. Optical characterizations .....	123
7.9. Conclusions .....	123
8. Conclusions and outlook .....	125
8.1. Conclusions .....	125
8.2. Outlook.....	127
Bibliography .....	129
Curriculum Vitae .....	139
Acknowledgment .....	141



## Acronyms

1D	One-dimensional
2D	Two-dimensional
3D	Three-dimensional
AFM	Atomic force microscopy
AuNP	Gold nanoparticle
CCD	Charge-coupled device
CD	Circular dichroism
CIE	Commission Internationale de l'Éclairage
CMOS	Complementary metal-oxide-semiconductor
DI	Deionized
EBL	Electron beam lithography
EDX	Energy dispersive X-ray spectroscopy
EELS	Electron energy loss spectroscopy
EOT	Extraordinary optical transmission
FEM	Finite element method
FIB	Focused ion beam
FP	Fabry-Pérot
FTIR	Fourier transform infrared
GDSII	Graphic database system II
HSQ	Hydrogen silsesquioxane
ITO	Indium tin oxide
LCP	Left-handed circular polarized
LSP	Localized surface plasmon
LSPR	Localized surface plasmon resonance
MIBK	Methyl isobutyl ketone
MPG	Max-Planck-Gesellschaft
N.A.	Numerical aperture
NEP	N-Ethyl-2-pyrrolidone
NIR	Near infrared
OR	Optical reflection
PDE	Partial differential equation
PTFE	Polytetra-fluoroethylene

PMMA	Poly (methyl methacrylate)
QR	Quick response code
RA	Rayleigh-Wood anomalies
RCP	Right-handed circular polarized
RF	Radio frequency
RGB	Red, green, and blue
SEM	Scanning electron microscopy
SPP	Surface plasmon polariton
TEM	Transmission electron microscopy
THz	Terahertz
UV	Ultraviolet
VIS	Visible
WRM	Weighted residual method

# 1. Introduction

## 1.1. Dynamic plasmonics

The beautiful colors exhibited by metal nanoparticles have been known since medieval times. Artisans exploited the effect to create colorful glass, long before the underlying mechanisms were understood. This phenomenon results from the absorption of sunlight by the metal particles embedded in glass. At a specific wavelength depending on the size, shape, material of the nanoparticle, the collective oscillations of the conduction electrons, the *so-called* localized surface plasmon resonance (LSPR) are excited.<sup>1,2</sup> LSPRs confine the incident field near the nanoparticle at dimensions much smaller than the operating wavelength. This leads to a strong enhancement of the local fields and allows for manipulation of light below the optical diffraction limit. Such characteristics enable a variety of applications in different disciplines including physics, chemistry, biology, materials science, and others.<sup>2-10</sup>

For a long time, the development of plasmonics has been focused on static systems, whose optical properties are fixed once the structures are fabricated. The concept of active plasmonics or dynamic plasmonics was first proposed in 2004 for controlling signals in a waveguide using nanoscale structural transformations.<sup>11</sup> Since then, the research interest along this direction has flourished. Dynamic plasmonics has taken off as a burgeoning subfield of plasmonics, identifying an inevitable transition of plasmonics from static to dynamic.<sup>12,13</sup> In general, there are two distinct routes to dynamically modulating the optical properties of plasmonic systems. First, tuning the conformations of the plasmonic structures so that the interactions between the constituent metal nanoparticles can be dynamically changed. This is not straightforward for lithographically fabricated samples as the structures are generally restricted on substrates. However, bottom-up approaches such as dynamic DNA nanotechnology provides an elegant solution.<sup>6,14,15</sup> Second, tuning the LSPRs of the individual metal nanoparticles by varying their dielectric surroundings or directly regulating the carrier densities and dielectric functions of the metal particles themselves. For the former, materials that can serve as tunable dielectric surroundings are quite versatile. This includes optically active materials such as photochromic molecules<sup>16</sup>, J-aggregates<sup>17</sup>, quantum dots<sup>5</sup>, and perovskite<sup>18</sup>, thermoresponsive materials such as gallium<sup>11</sup>, vanadium oxide<sup>19</sup>, and germanium antimony telluride<sup>20</sup>, electrically-driven materials such as liquid crystals<sup>21</sup> and graphene<sup>22</sup>, among others. For the latter, metals that can be regulated directly and meanwhile exhibit excellent plasmonic properties are not very choiceful, especially in the visible spectral range.<sup>23-25</sup>

Magnesium is one of the most promising candidates, as it exhibits excellent LSPRs in the ultraviolet (UV) and near infrared (NIR) regimes, and can absorb/desorb hydrogen, undergoing reversible transitions between a perfect metal and a low-loss insulator. This offers great opportunities to design and construct dynamic optical nanodevices at visible frequencies.

## 1.2. Outline

In this thesis, we discuss a relatively new member in nanoplasmonics, magnesium (Mg), and its important role for the development of dynamic plasmonic nanodevices at visible frequencies. We will first elucidate the power of Mg for dynamic nanoplasmonics. Then we introduce a plethora of newly developed Mg-based dynamic optical nanodevices for applications in plasmonic chirality switching, dynamic color displays.

Chapter 2 will present the general theoretical background for understanding light-matter interactions, plasmonics, and hydrogen-metal systems. Furthermore, as a key material in this thesis and a relatively new member in nanoplasmonics, magnesium is introduced comprehensively, including its plasmonics properties, dynamic properties, and previous studies on nanostructures. We also discuss strategies to enhance the stability, reversibility, and durability of the Mg-based nanodevices.

Chapter 3 introduces a new kind of hybrid plasmonic chiral metamolecules, consisting of magnesium and gold nanoparticles. The chiroptical response of such metamolecules can be dynamically controlled by hydrogen in real time without introducing structural reconfiguration. The mechanism, switching dynamics, and durability of the hydrogen-regulated device are investigated in detail. This chapter is adapted from the publication, *Hydrogen-regulated chiral nanoplasmonics*.

Chapter 4 demonstrates a new dynamic plasmonic colour display technique, where hydrogen-regulated magnesium nanoparticles serve as dynamic pixels, allowing for plasmonic color printing, tuning, erasing, and restoring. Then, several novel functionalities of such display technique are introduced in detail, including dynamic multicolour printings, subwavelength animations, and highly secure information encryption. This chapter is adapted from the publication, *Dynamic plasmonic colour display*.

Chapter 5 presents a novel dynamic color printing scheme using magnesium-based pixelated Fabry-Pérot cavities, enabling distinct blank and vivid color states before and after hydrogenation. Afterwards, several novel applications of such display schemes are demonstrated in detail, including information encryption of dynamic Ishihara display and arbitrary dynamic displays. This chapter is adapted from the publication, *Dynamic color displays using stepwise cavity resonators*.

Chapter 6 demonstrates fast lateral hydrogen diffusion in quasi-free magnesium films without the blocking effect. In contrast to the previous Pd-capped Mg scheme where the hydrogen diffused vertically, such lateral diffusion scheme avoids the aggravating blocking effect in a long-range diffusion, and presents a very fast diffusion kinetics. Massive concomitant lattice expansion leads to the formation of remarkable self-organized finger patterns, which self-records the hydrogen diffusion process. By inclusion of fast hydrogen diffusion objects or local gaps, the resulting streamlines exhibit a clear analogy to optical rays in geometric optics. Furthermore, a diffusion model is constructed to reproduce all the salient features of the finger patterns, confirming our conclusions. This chapter is adapted

from the publication, *Self-recording and manipulation of fast long-range hydrogen diffusion in quasifree magnesium*.

Chapter 7 shows a scanning plasmonic color generation scheme, inspired by the lateral fast-long-range hydrogen diffusion in Mg. Such scanning displays consist of aluminum nanoparticles, a thin dielectric spacer, and a scanning Mg screen with a palladium (Pd) strip as a hydrogen entrance. Such a microscopic screen could be laterally erased and restored when the Mg layer was transformed between the metal and dielectric state upon hydrogen loading/unloading. Then, several novel functionalities are introduced in detail, including kinetics of the scanning process, Sichuan opera facial mask displays, firework and peacock animations, information encryption of QR codes. This chapter is adapted from the publication, *Scanning plasmonic color display*.

Chapter 8 summarizes the main results of this thesis and gives an outlook on further research on magnesium. Although Mg has been considered as one of the most promising candidates for dynamic plasmonics, there are still remaining issues which need to be concerned for high-performance dynamic nanodevices of real-world applications.



## 2. Theoretical background and methods

### 2.1. Plasmonics

This part briefly summarizes the main concepts of plasmonics. Starting from Maxwell's equations, the fundamentals of light-matter interactions are introduced. Since the thesis is mainly on nanooptics of metallic nanostructures, the Drude model is derived to describe optical properties of metals. Then, we briefly summarize the main concepts of surface plasmon polaritons and localized surface plasmons. It shows that plasmonic structures exhibit a resonant behavior when they are excited by incident light, and their scattering and absorption are enhanced significantly. The resonant frequency of plasmonic structures can be tuned by varying their geometry, surrounding environment as well as material. It paves the way for plasmonic applications, such as plasmonic color generation, refractive index sensing, and dynamic nanooptical devices.

Famous examples are the Lycurgus cup and church window glasses as shown in **Figure 2.1**. Although people in 4<sup>th</sup> century AD did not understand the physics behind plasmonics, nanosized gold and silver particles were used to generate brilliant colors in glass artefacts. The glass contains gold and silver nanoparticles that show localized surface plasmon resonances.

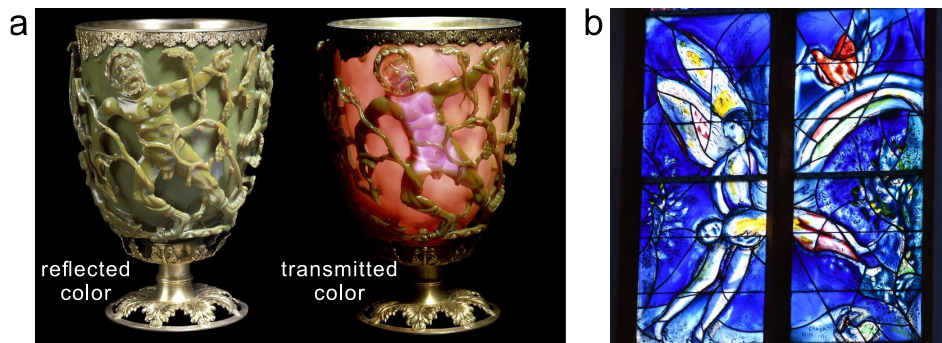


**Figure 2.1** (a) Roman Lycurgus Cup from 4<sup>th</sup> century AD. It shows a green color when illuminating from outside (left: reflected color), but a red color when illumination from inside (right: transmitted color). (b) Color windows made by Marc Chagall, St.

#### 2.1.1. Maxwell's equations

The interaction of electromagnetic waves with metals is completely governed by Maxwell's equations, a set of four partial differential equations, which link the electric field  $\mathbf{E}$ , the magnetic field  $\mathbf{H}$ , the electric displacement  $\mathbf{D}$ , and the magnetic induction  $\mathbf{B}$ , in the following form<sup>26</sup>

$$\nabla \cdot \mathbf{B}(\mathbf{r}, t) = 0$$

$$\nabla \cdot \mathbf{D}(\mathbf{r}, t) = \rho_{\text{ext}}(\mathbf{r}, t)$$

$$\begin{aligned}\nabla \times \mathbf{E}(\mathbf{r}, t) &= -\frac{\partial \mathbf{B}(\mathbf{r}, t)}{\partial t} \\ \nabla \times \mathbf{H}(\mathbf{r}, t) &= \frac{\partial \mathbf{D}(\mathbf{r}, t)}{\partial t} + \mathbf{J}_{\text{ext}}\end{aligned}\tag{2.1}$$

where  $\rho_{\text{ext}}$  and  $\mathbf{J}_{\text{ext}}$  are the external charge density and external current density, respectively. The four macroscopic fields have further relations via the polarization  $\mathbf{P}$  and magnetization  $\mathbf{M}$  by

$$\begin{aligned}\mathbf{D}(\mathbf{r}, t) &= \epsilon_0 \mathbf{E}(\mathbf{r}, t) + \mathbf{P}(\mathbf{r}, t) \\ \mathbf{H}(\mathbf{r}, t) &= \frac{1}{\mu_0} \mathbf{B}(\mathbf{r}, t) - \mathbf{M}(\mathbf{r}, t)\end{aligned}\tag{2.2}$$

where  $\epsilon_0$  and  $\mu_0$  are the electric permittivity and magnetic permeability of vacuum, respectively. In linear and isotropic media, the constitutive relations Eq. (2.2) can be simplified to

$$\begin{aligned}\mathbf{D}(\mathbf{r}, t) &= \epsilon_0 \epsilon \mathbf{E}(\mathbf{r}, t) \\ \mathbf{B}(\mathbf{r}, t) &= \mu_0 \mu \mathbf{H}(\mathbf{r}, t)\end{aligned}\tag{2.3}$$

with a relative permittivity (or dielectric constant)  $\epsilon$  and a relative magnetic permeability  $\mu$ . Usually, the magnetization of materials at optical frequencies is negligible, so  $\mu$  in Eq. (2.3) becomes 1. The frequency dependent  $\epsilon = \epsilon(\omega)$  is in general a complex function

$$\epsilon(\omega) = \epsilon_r + i \cdot \epsilon_i\tag{2.4}$$

where  $\epsilon_r$  and  $\epsilon_i$  are real and imaginary parts of  $\epsilon$ , respectively. It is furthermore connected to the complex refractive index via

$$\tilde{n}(\omega) = n(\omega) + i \cdot k(\omega) = \sqrt{\epsilon(\omega)}\tag{2.5}$$

The real part  $n(\omega)$  can be treated as the refractive index of a material, defining the dispersion of the material. The imaginary part  $k(\omega)$  describes the absorption of electromagnetic waves in a material. Explicitly, one obtains the following relations

$$\begin{aligned}\epsilon_r &= n^2 - k^2 \\ \epsilon_i &= 2nk\end{aligned}\tag{2.6}$$

or

$$n = \sqrt{\frac{\epsilon_r}{2} + \frac{1}{2}\sqrt{\epsilon_r^2 + \epsilon_i^2}} \quad (2.7)$$

$$k = \sqrt{-\frac{\epsilon_r}{2} + \frac{1}{2}\sqrt{\epsilon_r^2 + \epsilon_i^2}}$$

To understand a (linear, isotropic, and non-magnetic) material, the essential step is to find an expression for the dielectric function  $\epsilon(\omega)$ .

### 2.1.2. Optical properties of metals

The dielectric function  $\epsilon(\omega)$  of metals over a large frequency range can be described using the *Drude model*, where a gas of free electrons with number density  $N$  moves against a fixed background of positive ion cores under external field, leading to electric polarization. The electro-ion interaction and the electron-electron interaction are not taken into account. For noble metals, major deviations of this model occur in the UV-visible spectral region due to interband transitions. In NIR and IR, no interband transitions are present and the Drude model describes the dielectric functions very well (One example is shown in **Figure 2.2**).

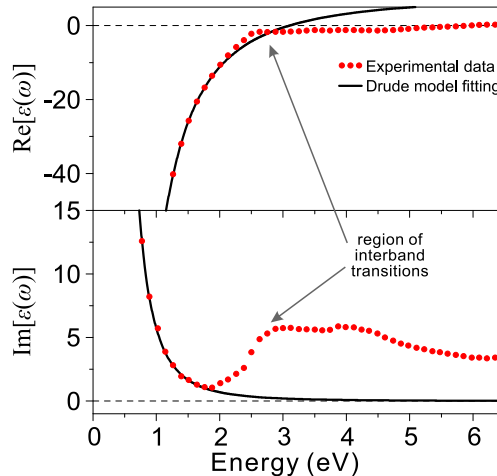


**Figure 2.2** Dielectric function of gold. Experimental data (red dots) are fitted with Drude model (curves).<sup>26</sup> Interband transitions limit the validity of the model at UV-VIS frequencies.

The electrons oscillate in response to the external electromagnetic field [ $\mathbf{E}(t) = \mathbf{E}_0 \cdot \exp(-i\omega t)$ ], which follows the equation of motion

$$m \cdot \frac{d^2\mathbf{r}}{dt^2} + m \cdot \gamma \cdot \frac{d\mathbf{r}}{dt} + e\mathbf{E}(t) = 0 \quad (2.8)$$

where  $m$  is the effective mass of an electron, and  $e$  is the electron charge. The motion of electrons is damped via collisions occurring with a characteristic collision frequency

$\gamma = 1/\tau$ , where  $\tau$  is known as the relaxation time of the free electron gas. Using the ansatz [ $\mathbf{r}(t) = \mathbf{r}_0 \cdot \exp(-i\omega t)$ ] to solve the second order linear differential Eq. (2.8) leads to:

$$\mathbf{r}(t) = \frac{e}{m(\omega^2 + i\gamma\omega)} \mathbf{E}(t) \quad (2.9)$$

The electrons which are displaced relative to the positive ion cores generate a polarization  $\mathbf{P}(t) = -Ner(t)$ . We get

$$\mathbf{P}(t) = \frac{-Ne^2}{m(\omega^2 + i\gamma\omega)} \mathbf{E}(t) \quad (2.10)$$

Combining Eq. (2.10) with Eq. (2.2) and (2.3), we derivate the dielectric function of the free electron gas

$$\varepsilon(\omega) = 1 - \frac{\omega_p^2}{\omega^2 + i\gamma\omega} \quad (2.11)$$

with the plasma frequency

$$\omega_p = \sqrt{\frac{Ne^2}{m\varepsilon_0}} \quad (2.12)$$

Eq. (2.11) can be split into real and imaginary parts:

$$\begin{aligned} \varepsilon_r(\omega) &= 1 - \frac{\omega_p^2 \tau^2}{1 + \omega^2 \tau^2} \\ \varepsilon_i(\omega) &= \frac{\tau \omega_p^2}{\omega(1 + \omega^2 \tau^2)} \end{aligned} \quad (2.13)$$

This simple Drude model describes the dielectric function of free electron gas metals. In the case of low frequencies  $\omega < \omega_p$ , metals retain their metallic character. For large frequencies close to  $\omega_p$ , where  $\omega\tau \gg 1$ , the damping is negligible, and the imaginary part of  $\varepsilon(\omega)$  vanishes

$$\varepsilon(\omega) = \varepsilon_r(\omega) = 1 - \frac{\omega_p^2}{\omega^2} \quad (2.14)$$

It can be considered as the dielectric function of the undamped free electron plasma. The dispersion relation of electromagnetic waves can be determined from  $k^2 = \varepsilon \omega^2/c^2$ ,

$$\omega(k) = \sqrt{\omega_p^2 + k^2 c^2} \quad (2.15)$$

From the dispersion relation in Eq. (2.15), there is no propagation of electromagnetic waves below the plasmon frequency  $\omega < \omega_p$  as shown in **Figure 2.3**.

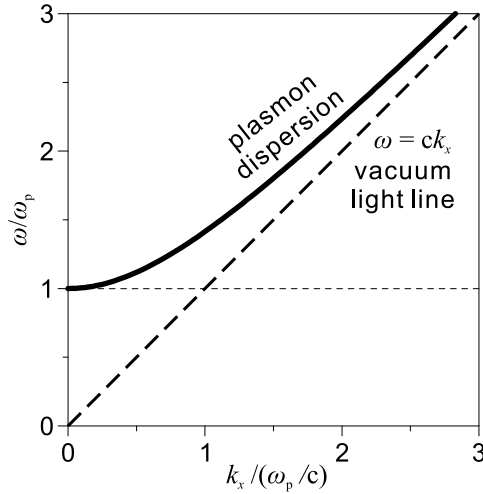


**Figure 2.3** Dispersion relation of the free electron gas from Eq. (2.15).

Substitute Eq. (2.14) into the formula for reflectivity  $R$

$$R(\omega) = \left| \frac{\tilde{n}(\omega) - 1}{\tilde{n}(\omega) + 1} \right|^2 \quad (2.16)$$

We can plot the  $R$  with respect to frequency as shown in **Figure 2.4**. The reflectivity is unity for frequencies  $\omega < \omega_p$  indicating total reflection, which shows good metallic properties. When  $\omega > \omega_p$ ,  $R$  decreases to zero rapidly, and metals become transparent.

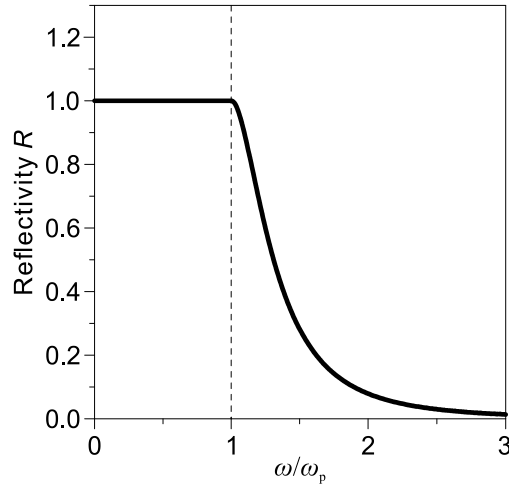


**Figure 2.4** Reflectivity  $R$  of an undamped free electron plasma.

It is notable that for real noble metals such as Au, Ag, and Cu, whose typical plasma frequencies correspond to UV region, this equation is only valid at frequencies  $\omega < \omega_p$ , namely in NIR or IR region. The real permittivity of these metals deviates from Eq. (2.11) significantly at higher frequencies, which is due to interband transitions. The interband transitions can be modeled through a bound electron Lorentz oscillator following the equation of motion

$$m \cdot \frac{d^2\mathbf{r}}{dt^2} + m \cdot \gamma \cdot \frac{d\mathbf{r}}{dt} + m\omega_0\mathbf{r} + e\mathbf{E}(t) = 0 \quad (2.17)$$

where  $\omega_0$  is the resonance frequency of the bound electron. Compared to Eq. (2.11), it leads to an additional Lorentz-oscillator term<sup>27</sup>

$$\varepsilon_{\text{inter}}(\omega) = \frac{A_i}{\omega_p^2 - \omega^2 - i\gamma\omega} \quad (2.18)$$

Equation (2.14) demonstrates that the plasma frequency  $\omega_p$  acts as an important role since the permittivity becomes zeros at  $\omega = \omega_p$ . In this special case, a collective longitudinal excitation mode ( $\mathbf{k} \parallel \mathbf{E}$ ) is formed. The physical interpretation is a collective oscillation of the conduction electron gas with respect to the fixed background of positive ion cores. The quanta of the charge oscillation are called bulk plasmons or volumes plasmons.<sup>26</sup> As these are longitudinal waves, bulk plasmons cannot be excited by transversal electromagnetic waves, but can be excited by charged particles, for example, electrons in electron energy loss spectroscopy (EELS).<sup>28</sup>

### 2.1.3. Surface plasmon polaritons

Surface plasmon polaritons (SPPs) are electromagnetic excitations that propagate along the interface between a metal and a dielectric medium<sup>26</sup> as illustrated in **Figure 2.5 a.**

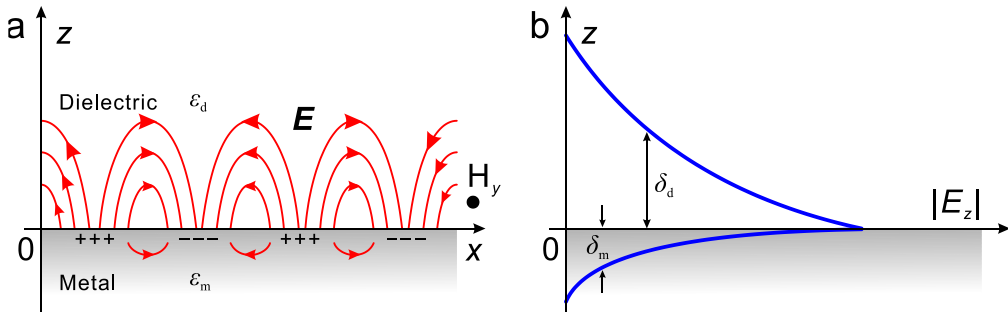


**Figure 2.5** (a) Surface plasmon polaritons at the interface between metal and dielectric.<sup>1</sup> (b) Evanescent fields in the two half spaces. Confinement is achieved since the propagation constant  $k_{\text{SPP}}$  is greater than the wave vector  $k$  in the dielectric, leading to evanescent decay on both sides of the interface.

We assume that the electric field,

$$\mathbf{E} = E_0 \exp[i \cdot (k_{\text{SPP}}x + k_z z - \omega t)] \quad (2.19)$$

where  $k_{\text{SPP}}$  is the wavevector of the excited SPPs, indicating the propagation along  $x$ -direction. To solve the Maxwell's equation at the interface between the metal and dielectric medium with dielectric constant  $\varepsilon_m$  and  $\varepsilon_d$ , respectively, we employ the continuity relations<sup>26</sup>

$$\begin{aligned}
\mathbf{n}_{12} \cdot (\mathbf{B}_2 - \mathbf{B}_1) &= 0 \\
\mathbf{n}_{12} \cdot (\mathbf{D}_2 - \mathbf{D}_1) &= \rho_s \\
\mathbf{n}_{12} \times (\mathbf{E}_2 - \mathbf{E}_1) &= \mathbf{0} \\
\mathbf{n}_{12} \times (\mathbf{H}_2 - \mathbf{H}_1) &= \mathbf{J}_s
\end{aligned} \tag{2.20}$$

where  $\mathbf{n}_{12}$  is the normal vector from medium 1 to 2,  $\rho_s$  is the surface charge,  $\mathbf{J}_s$  is the surface current density. Therefore, the normal component of  $\mathbf{B}$  is continuous across the interface, while the normal component of  $\mathbf{D}$  has a step on the interface surface. The tangential component of  $\mathbf{E}$  is continuous across the interface, while the tangential component of  $\mathbf{H}$  differs by the amount of a surface current.

Combining Eq. (2.19) and Eq. (2.20), yields

$$\begin{aligned}
\frac{k_{z,d}}{\epsilon_d} + \frac{k_{z,m}}{\epsilon_m} &= 0 \\
k_{SPP}^2 - k_{z,d}^2 &= \epsilon_d \left( \frac{\omega}{c} \right)^2 \\
k_{SPP}^2 - k_{z,m}^2 &= \epsilon_m \left( \frac{\omega}{c} \right)^2
\end{aligned} \tag{2.21}$$

First, the  $k_{z,d}$  and  $k_{z,m}$  components have to be imaginary and of opposite sign, namely

$$\begin{aligned}
k_{z,d} &= +i\kappa_d \\
k_{z,m} &= -i\kappa_m
\end{aligned} \tag{2.22}$$

Where  $\kappa_d$  and  $\kappa_m$  are the imaginary part of the wavevectors perpendicular to the interface in two media, respectively. In this way, the field decays exponentially into the respective half spaces, symbolized in **Figure 2.5 b**.

$$\begin{aligned}
E_d|_{z>0} &\propto \exp(+i \cdot k_{z,d} \cdot z) = \exp(-\kappa_d \cdot z) \\
E_m|_{z<0} &\propto \exp(+i \cdot k_{z,m} \cdot z) = \exp(+\kappa_m \cdot z)
\end{aligned} \tag{2.23}$$

Second, Eq. (2.21) also leads to the dispersion relation of SPPs (see **Figure 2.6**)

$$k_{SPP} = k_0 \sqrt{\frac{\epsilon_m \epsilon_d}{\epsilon_m + \epsilon_d}} \tag{2.24}$$

where  $\epsilon_m$  and  $\epsilon_d$  are the frequency-dependent permittivity of the metal and dielectric, respectively.  $k_0 = \omega/c$  is the free-space wavevector.

In order to obtain a propagating SPPs in  $x$ -direction and a bound one in  $z$ -direction as indicated in **Figure 2.5 a**,  $\epsilon_m$  and  $\epsilon_d$  must fulfill the conditions

$$\begin{aligned}
\epsilon_m \epsilon_d &< 0 \\
\epsilon_m + \epsilon_d &< 0
\end{aligned} \tag{2.25}$$

These conditions are fulfilled by most noble metals, leading to the formation of SPPs at the interface between dielectric and metals.

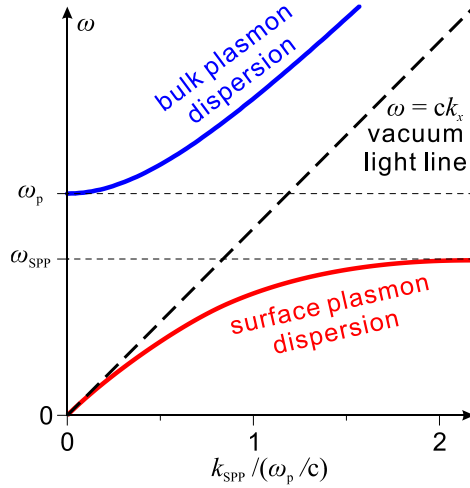


**Figure 2.6** Typical dispersion relation for the bulk plasmon and SPPs.

To investigate the properties of SPPs, we take a closer look to their dispersion relation Eq. (2.24) and **Figure 2.6**. For small wave vectors  $k$  corresponding to long wavelengths, the  $k_{\text{SPP}}$  is close to  $k_0$  at the light line. In this regime, the SPP waves extend over several wavelengths into the dielectric space. For large wave vectors  $k$  corresponding to short wavelengths, where the damping of electron oscillations is negligible ( $\text{Im}[\epsilon_m] \approx 0$ ), the  $k_{\text{SPP}}$  goes to infinity when the frequency approaches  $\omega_{\text{SPP}}$ .

$$\omega_{\text{SPP}} = \frac{\omega_p}{\sqrt{1 + \epsilon_d}} \quad (2.26)$$

Since the SPPs dispersion curve does not cross the light line as shown in **Figure 2.6**, SPPs cannot be excited directly by incident light. Energy and momentum of SPPs have to be matched to the incident light. Thus, special phase-matching techniques are required to excite SPPs,<sup>26</sup> for example:

- A. Excitation upon charged particle impact.
- B. Prism coupling by Kretschmann and Otto configurations.
- C. Grating coupling. Gratings provide an additional momentum  $k_G = 2\pi/\Lambda$ , where  $\Lambda$  is the grating period, to free space light to couple to an SPPs.
- D. Excitation using highly focused optical beams.
- E. Near-field excitation.

#### 2.1.4. Localized surface plasmons

Different from the ideal infinite smooth metal surface, the rough metal surfaces or discrete metal structures support localized surface plasmons (LSPs) as illustrated in **Figure 2.7**. In contrast to SPPs in Chapter 2.1.3, LSPs are localized and associated with bound electron plasmas in nanovoids or nanoparticles with dimensions smaller than the wavelength of incident electromagnetic waves. Especially, noble metal nanoparticles

obtain very distinct localized surface plasmon resonances (LSPRs). The resonance dose not only depend on the metal, but also on the geometry and dielectric environment of the nanoparticles.

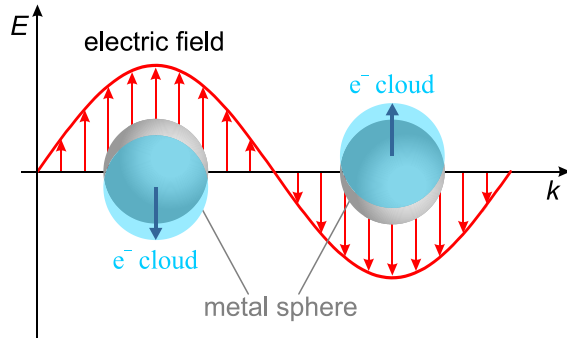


**Figure 2.7** Localized surface plasmon on metal nanoparticles.

The LSPR modes arise from scattering of incident electromagnetic waves with a sub-wavelength metal nanoparticle. An instructive analytical model: a homogeneous, isotropic sphere with a radius  $a$  in a uniform static electric field  $\mathbf{E}_0 = E_0 \hat{\mathbf{z}} = E_0 \cos(\theta)$  (see **Figure 2.8**). The complex dielectric function of the sphere is  $\varepsilon(\omega)$ . The sphere is surrounded by isotropic and non-absorbing dielectric medium  $\varepsilon_d$ . Solving the Laplace equation,

$$\nabla^2 \Phi = 0 \quad (2.27)$$

where  $\Phi$  is the electric potential, and satisfies  $\mathbf{E} = -\nabla\Phi$ . Using the azimuthal symmetry and boundary condition requirements, the solution for the potentials inside ( $\Phi_{\text{in}}$ ) and outside ( $\Phi_{\text{out}}$ ) are

$$\begin{aligned} \Phi_{\text{in}} &= -\frac{3\varepsilon_d}{\varepsilon(\omega) + 2\varepsilon_d} E_0 r \cos(\theta) \\ \Phi_{\text{out}} &= -E_0 r \cos(\theta) + \frac{\varepsilon(\omega) - \varepsilon_d}{\varepsilon(\omega) + 2\varepsilon_d} E_0 a^3 \frac{\cos(\theta)}{r^2} \end{aligned} \quad (2.28)$$

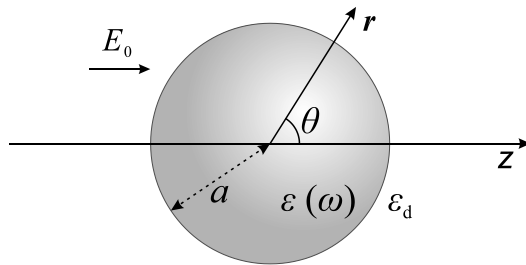


**Figure 2.8** Sketch of a homogeneous sphere located at the origin, with a radius  $a$  and a dielectric function  $\varepsilon(\omega)$ , surrounded by a dielectric medium  $\varepsilon_d$ .

Taking a closer look at  $\Phi_{\text{out}}$  physically, it shows the superposition of the applied field (first part) and a dipole located at the particle center (second part). It can be rewritten as

$$\begin{aligned}\Phi_{\text{out}} &= -E_0 r \cos(\theta) + \frac{\mathbf{p} \cdot \mathbf{r}}{4\pi\epsilon_0\epsilon_d r^3} \\ \mathbf{p} &= 4\pi\epsilon_0\epsilon_d a^3 \frac{\epsilon(\omega) - \epsilon_d}{\epsilon(\omega) + 2\epsilon_d} \mathbf{E}_0\end{aligned}\quad (2.29)$$

It indicates that the applied electric field  $\mathbf{E}_0$  induces a dipole moment inside the sphere. The dipole moment can be rewritten as

$$\mathbf{p} = \epsilon_0\epsilon_d\alpha(\omega)\mathbf{E}_0 \quad (2.30)$$

with the polarizability  $\alpha(\omega)$

$$\alpha(\omega) = 4\pi a^3 \frac{\epsilon(\omega) - \epsilon_d}{\epsilon(\omega) + 2\epsilon_d} \quad (2.31)$$

It is notable that the polarizability  $\alpha$  can be resonantly enhanced when  $|\epsilon(\omega) + 2\epsilon_d|$  is minimum. For the frequency regions with small or constant imaginary part of  $\epsilon(\omega)$  around the resonance, it simplifies as

$$\text{Re}[\epsilon(\omega)] = -2\epsilon_d \quad (2.32)$$

Equation (2.32) is called the Fröhlich condition for a dipole surface plasmon of a metal nanoparticle. In this condition, conductive electrons are resonantly excited by incident electromagnetic waves, presenting strongly absorption and scattering. The resonance is very sensitive to the surrounding dielectric function  $\epsilon_d$  and also the particle size  $a$ , leading to many applications, for example refractive index sensing and structure colors, respectively.

For a Drude model metal sphere in air ( $\epsilon_d = 1$ ), we substitute the  $\epsilon(\omega)$  in Eq. (2.31) with Eq. (2.11),

$$\alpha(\omega) = 4\pi a^3 \frac{\omega_p^2/3}{\omega^2 + i\gamma\omega - \omega_p^2/3} \quad (2.33)$$

The Fröhlich condition is met when

$$\omega = \omega_f = \omega_p/\sqrt{3} \quad (2.34)$$

The real and imaginary parts of the polarizability of the Drude model metal sphere Eq. (2.33) are shown in **Figure 2.9**.

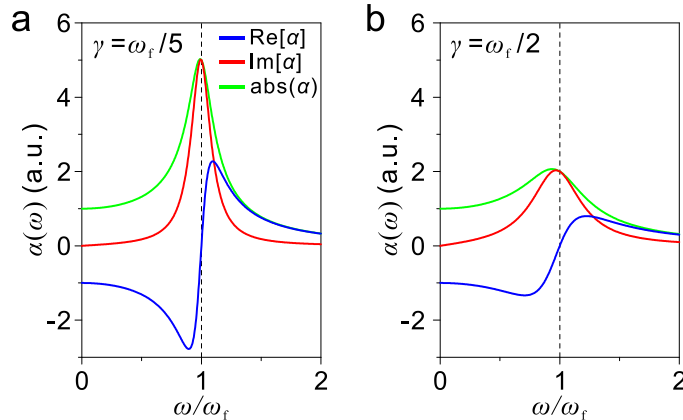


**Figure 2.9** Absolute value, real part, and imaginary part of the polarizability from Eq. (2.33) with (a)  $\gamma = \omega_f/2$  and (b)  $\gamma = \omega_f/5$ .

Then, the electric fields inside and outside of the sphere in **Figure 2.8** can be calculated from Eq.(2.28) and Eq.(2.29) by  $\mathbf{E} = -\nabla\Phi$ ,

$$\begin{aligned}\mathbf{E}_{\text{in}} &= \frac{3\varepsilon_d}{\varepsilon(\omega) + 2\varepsilon_d} \mathbf{E}_0 \\ \mathbf{E}_{\text{out}} &= \mathbf{E}_0 + \frac{1}{4\pi\varepsilon_0\varepsilon_d} \frac{3\hat{\mathbf{n}}(\hat{\mathbf{n}} \cdot \mathbf{p}) - \mathbf{p}}{r^3}\end{aligned}\quad (2.35)$$

where  $\hat{\mathbf{n}} = \mathbf{r}/r$  is the unit vector in direction of  $\mathbf{r}$ . It is clear that both electric fields are enhanced in Fröhlich condition. Using Eq. (2.35), the absorption ( $C_{\text{abs}}$ ) and the scattering ( $C_{\text{scat}}$ ) cross sections are calculated by<sup>26</sup>

$$\begin{aligned}C_{\text{abs}} &= \frac{k}{\varepsilon_0} \text{Im}[\alpha(\omega)] = 4\pi k a^3 \text{Im} \left[ \frac{\varepsilon(\omega) - \varepsilon_d}{\varepsilon(\omega) + 2\varepsilon_d} \right] \\ C_{\text{scat}} &= \frac{k^4}{6\pi\varepsilon_0^2} |\alpha(\omega)|^2 = \frac{8\pi}{3} k^4 a^6 \left| \frac{\varepsilon(\omega) - \varepsilon_d}{\varepsilon(\omega) + 2\varepsilon_d} \right|^2\end{aligned}\quad (2.36)$$

where  $k = 2\pi/\lambda$ ,  $\lambda$  is the wavelength. Specially, the sum of absorption and scattering is called extinction. The scattering scales with  $a^6$ , while the absorption scales with  $a^3$ . For large particles, scattering dominates, whereas for small particles, absorption dominates. For example, small gold particles absorb green and blue light, presenting red, while large gold particles mostly scatter in the green and therefore appear greenish. This effect is used in color glasses as shown in **Figure 2.1**.

### 2.1.5. Plasmonic color

Plasmonics has attracted enormous attention from nano science and technology. When light resonantly interacts with metals, electron oscillations can propagate along a planar interface or be confined on a subwavelength structures. Both forms of surface plasmon resonance can confine the incident light in a deep subwavelength scale, allowing for a remarkable enhancement of the near field and a manipulation of light in nanoscale. With the progress of nanofabrication techniques in the past decades, allowing to precisely

control the geometries and topologies of plasmonic structures, the plasmonics blossomed,<sup>1,9</sup> paving the way for the applications in a wide range of disciplines, including photonics,<sup>9,29</sup> chemistry,<sup>30</sup> energy,<sup>2</sup> biology,<sup>4</sup> and chromatics.<sup>7</sup> The majority of the thesis focused on the development of plasmonic colors, detailed in Chapter 4, 5, and 7.

Plasmonic color (or structural color) emerges from resonant interactions between visible light and plasmonic nanostructures, which has revolutionized color generation science due to its unprecedented subwavelength resolution, high-density optical data storage as well as a significant potential for sustainable production and recycling. Here, we give a brief overview of the most typical mechanisms of structural color generations (see **Figure 2.10**).

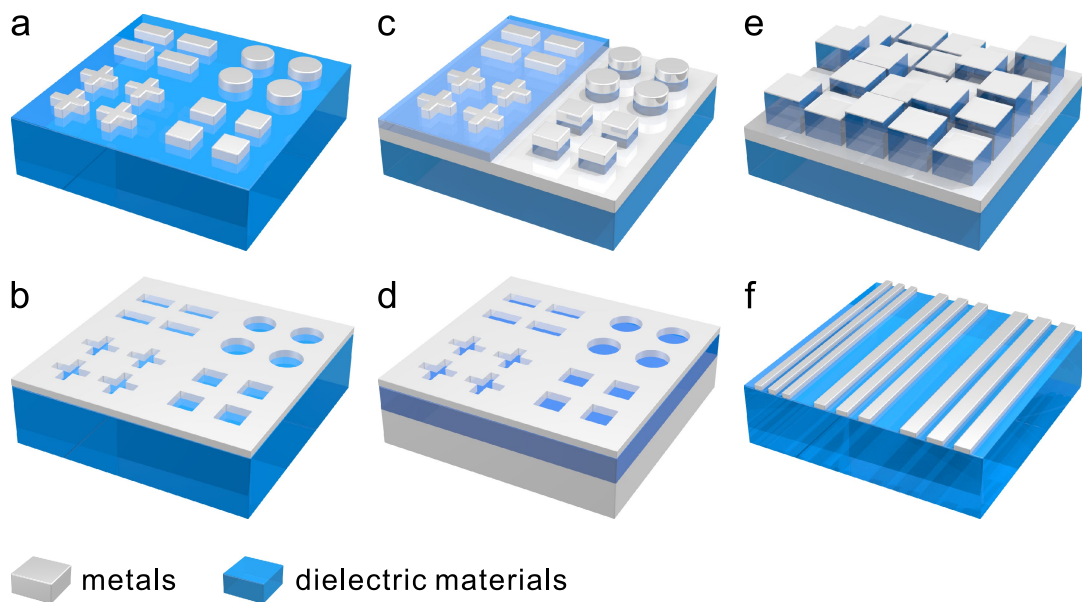


**Figure 2.10** Schematic of several typical types of nanostructures used in color generation. (a) Plasmonic antenna, (b) Plasmonic nanohole, (c) Antenna backreflector, (d) Nanohole backreflector, (e) Fabry-Pérot resonator, (f) Subwavelength gratings.

#### (a) *Plasmonic nanoantenna*

Color generations based on plasmonic nanoantennas are usually a periodic arrangement of metallic nanoparticles (such as disks, rods or crosses) exhibiting LSPRs (see **Figure 2.10 a**). By varying the dimension, nanoantennas render high chromaticity.<sup>31</sup> It can be used in transmission<sup>32,33</sup> (so-called filtering) or in reflection<sup>34,35</sup> (so-called printing). Based on the design of antennas, it can be polarization sensitive or insensitive, which can be applied in polarimeters or displays.<sup>33,36</sup> Furthermore, a random distribution of nanoparticles promotes to realize incident-angle-insensitive properties.<sup>37</sup>

#### (b) *Plasmonic nanohole*

Color generations using plasmonic nanohole are a thin metal film pierced with apertures where light can pass through (see **Figure 2.10 b**).<sup>38,39</sup> The optical properties are referred to extraordinary optical transmission (EOT).<sup>40</sup> This effect is associated with a coupling

between excitation of SPP and incident light in a metallic surface. According to the Babinet's principle, the complements of plasmonic nanoantennas are the plasmonic nanoholes in metal films, presenting dips in the reflection spectra and peaks in the transmission spectra. This makes them highly attractive for COMS applications in camera.<sup>41</sup> The resonance can be tuned by modifying the periodicity, size, and shape of nanoholes.<sup>42</sup>

(c) *Antenna backreflector*

Antenna backreflector structures are the most widely and prominent type for color generation. It consists of metallic nanoantennas as plasmonic pixels, arranged on a backreflector spaced by a dielectric spacer (see **Figure 2.10 c**). The backreflector can be a continuous metal film<sup>43,44</sup> (metallic mirror) or a layer with apertures<sup>45-47</sup> (located below antennas). Apart from its high spatial resolution, beyond  $1 \times 10^6$  dots per inch (dpi),<sup>48</sup> it has a wide range of resonances covering the entire visible range.

(d) *Nanohole backreflector*

Similar to antennas over backreflector structures, nanohole structures can be used instead (see **Figure 2.10 d**).<sup>49</sup> It demonstrates nearly perfect light absorption. Such structures are supposed to show high spatial resolution and angle-insensitive light absorption.<sup>50,51</sup>

(e) *Fabry-Pérot resonator*

Fabry-Pérot (FP) resonances consist of two metallic mirrors separated by an optically transparent dielectric medium (see **Figure 2.10 e**).<sup>52</sup> Constructive interferences take place in a transparent cavity layer at a certain wavelength, leading to a transmission peak for an optical thin bottom metallic layer, or reflection valley for an opaque metallic substrate. The FP resonances can be tuned by varying the thickness of the dielectric spacer, refractive index of the dielectric spacer, and the incident angle.<sup>53,54</sup>

(f) *Subwavelength grating*

Metallic subwavelength gratings are periodic structures with alternating dielectric and metallic regions in 1D or 2D (see **Figure 2.10 f**).<sup>55-58</sup> Generally, metallic subwavelength gratings are dominated by diffractive period (*e.g.* period of 500 nm).<sup>59</sup> However, plasmonic effects or combinations thereof dominate when period is deep subwavelength.<sup>31</sup>

## 2.2. The metal-hydrogen system

So far, we discussed the light-matter interactions, optical properties of metals, and plasmonic resonances. In the following, we will introduce active plasmonic materials, hydrogen-storage metals, which undergo a hydrogen-regulated phase transition accompanied with changes of optical and electric properties. These active metals are promising candidates of building blocks not only for hydrogen storage applications, but also for dynamic plasmonics or dynamic electronics.

### 2.2.1. Hydrogen energy

Energy can be stored in various forms, such as mechanical energy (*e.g.* gravitational or elastic potential energy, rotation energy), electromagnetic energy (*e.g.* capacitors, coils), nuclear energy, and chemical energy (*e.g.* biomass, coal, natural gas, oil, batteries, and hydrogen). However, the overwhelming majority of world energy consumption is from chemical energy. Chemical energy comes from the energy of valence electrons eager to be stable by bonding with other atoms. Here, the hydrogen is most attractive because it is the simplest and smallest element with one proton and one electron in the  $1s$  orbital, which thus has the highest ratio of valence electrons to nucleons (protons and neutrons) in the periodic table.

Hydrogen is the most abundant element on Earth, majorly in a compound of water  $H_2O$ , while less than 1% exhibits as molecular hydrogen gas  $H_2$ .  $H_2$  is colorless, tasteless, and highly flammable. It will burn in air at a very wide range of concentrations between 4 vol.% to 75 vol.%. It is due to an exothermic reaction with oxygen to water:



Hydrogen is considered as one of the most promising synthetic fuel for a future sustainable economy,<sup>60</sup> because it is lightweight, highly abundant, and its exhaust product water is environment friendly. An ideal hydrogen cycle is proposed as shown in **Figure 2.11**, which consists of three procedures<sup>61</sup>: (1) Hydrogen production via water electrolysis, powered by renewable energy, such as hydropower, wind power, geothermal, ocean energy and photovoltaics.<sup>62</sup> (2) Hydrogen storage and transport. (3) Hydrogen combustion in a fuel cell, producing electricity and  $H_2O$  as the only exhaust product.

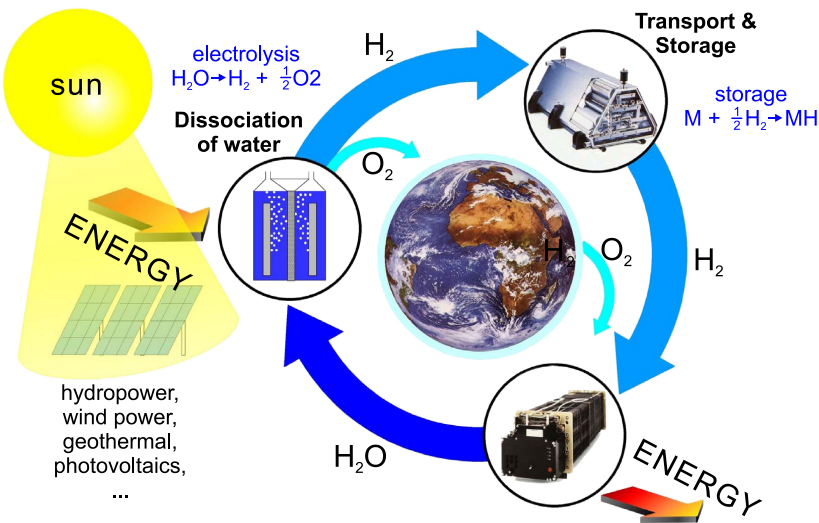


**Figure 2.11** The hydrogen cycle, rearranged from<sup>61</sup>.

Hydrogen as a gas occupies a large volume ( $11 \text{ m}^3 \text{ kg}^{-1}$ ) under ambient conditions. Due to the lightness and volatility of hydrogen, its storage is one of the major technological bottlenecks on the route to *Hydrogen Society*. As an ideal hydrogen storage system, it requires: (1) High gravimetric and volumetric hydrogen densities. (2) An equilibrium hydrogen pressure of atmosphere at room temperature. (3) Fast and reversible kinetics of hydrogen absorption and desorption.

However, all of the existing methods exhibit some drawbacks. Physical storage of hydrogen gas as liquid and pressurized gas, requires ultra-high pressures and ultra-low temperatures, which is connected with significant energy losses, potential security risks and large volumes.<sup>60</sup> Alternatively, it is possible to store atomic hydrogen in metal- or complex-hydrides.<sup>63</sup> Although these compounds usually have lower gravimetric storage densities than hydrogen liquid, they have very high volumetric densities, and more importantly, they are able to absorb and desorb hydrogen near room temperature and atmospheric pressure. Extensive studies have been focusing on improving the thermodynamic and kinetic properties of metal hydrides.

## 2.2.2. Hydrogen-storage metals

Many metals and their alloys are able to reversibly absorb huge amounts of hydrogen, forming metal hydrides. Upon hydrogenation, firstly  $\text{H}_2$  gas molecules are adsorbed on the metal surface, where the  $\text{H}_2$  molecules are split into hydrogen (H) atoms. Then H atoms enter the lattice of host metal (M), and occupy interstitial sites, which expands the volume of the metal lattice (see **Figure 2.12 a**). At low concentrations ( $\text{H}/\text{M} \ll 1$ ), H atoms are exothermically dissolved in host metal (solid-solution, so called  $\alpha$ -phase), expanding metal lattice by  $2\sim 3 \text{ \AA}^3$  per H atom, in which hydrogen atoms are very sparse and move relatively easily.<sup>64</sup> When the amount of hydrogen increases, at larger hydrogen concentrations ( $\text{H}/\text{M} > 0.1$ ), a H-H interaction becomes strong due to lattice expansion, leading to the nucleation

and growth of the hydride phase (so called  $\beta$ -phase)<sup>64</sup>. The appearance of hydrogen-rich  $\beta$ -phase ( $H/M \approx 1$ ) is typically accompanied by large volume expansion and drastic transitions in the chemical and physical properties.

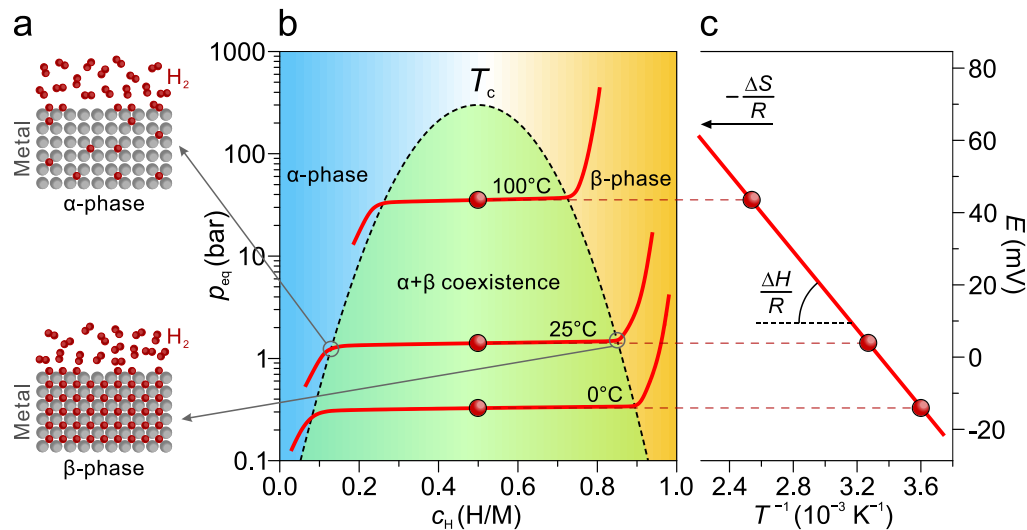


**Figure 2.12** (a) Schematic representation of a metal structure (M) with H atoms in the interstices between the metal atoms. (b) Pressure composition isotherms for hydrogen absorption. The  $\alpha$ -phase, the  $\beta$ -phase, and the region of  $\alpha+\beta$  coexistence are shown. The coexistence region is characterized by a flat plateau and ends at the critical temperature  $T_c$ . (b) The van't Hoff curve, whose slope and the intercept are proportional to the enthalpy  $\Delta H$  and entropy  $\Delta S$  of hydride formation, respectively.  $R$  is the gas constant. This figure is rearranged from<sup>64</sup>.

The thermodynamics of hydride formation from gaseous hydrogen are described by pressure composition isotherms in **Figure 2.12 b**. When solid solution ( $\alpha$ -phase) and hydride phase ( $\beta$ -phase) coexist, there is a pressure plateau in the isotherms. The plateau ends at critical temperature  $T_c$ , and its length indicates the amount of hydrogen storage with small pressure changes.<sup>60</sup> The coexistence region disappears when temperature is higher than  $T_c$ , and then the transition between the two phases is continuous. The equilibrium pressure plateau,  $p_{eq}$  is related to the temperature  $T$  by the Van't Hoff equation (see **Figure 2.12 c**),

$$\ln\left(\frac{p_{eq}}{p^0}\right) = \frac{\Delta H}{R} \cdot \frac{1}{T} - \frac{\Delta S}{R} \quad (2.38)$$

where  $p^0$  is the standard pressure (1.013 bar at 298 K).  $\Delta H$  is the heat of formation of the hydride phase.  $\Delta S$  is the entropy change from molecular hydrogen gas to dissolved hydrogen, and it is approximately  $\Delta S = 130.8 \text{ J K}^{-1}(\text{molH})^{-1}$ .

The thermodynamic properties of metal-hydrogen systems are usually characterized by the strength of the metal-hydrogen (M-H) bond, and thus the enthalpy of the (de)hydriding reaction. Using Eq. (2.38), we calculate that, at standard conditions (1.013 bar at 298 K), an ideal hydrogen storage system will have  $\Delta H = -39 \text{ kJ (molH)}^{-1}$ . The metal-hydrogen bond facilitates very high hydrogen density at ambient pressure and absorption/desorption

of stored hydrogen at the same pressure. Usually, the reversibility of metal-hydrogen system decreases following the type of M-H bonding: metallic > ionic > covalent.<sup>65</sup>

A brief summary of all common hydrides of elements are shown in **Figure 2.13**. Many of them can bind hydrogen reversibly, which are candidates for applications of metal-hydrogen systems, such as hydrogen catalysis, hydrogen detection, hydrogen storage, etc.<sup>66</sup> Notably, combination or alloying of metals to form complex hydrides is possible, sometimes presenting much more promising thermodynamic and reversible properties in practical applications.

	I	II													XIII	XIV	XV	XVI	XVII	XVIII	He
1	H														Covalent Hydrides						
2	LiH 12.7	BeH <sub>2</sub> 18.3	<i>Ionic Hydrides</i>												BH <sub>3</sub> 21.9	CH <sub>4</sub> 25.1	NH <sub>3</sub> 17.8	H <sub>2</sub> O 11.2	HF 5.0	Ne	
3	NaH 4.2	MgH <sub>2</sub> 7.7	<i>Metallic Hydrides</i>												AlH <sub>3</sub> 10.1	SiH <sub>4</sub> 12.6	PH <sub>3</sub> 8.9	H <sub>2</sub> S 5.9	HCl 2.8	Ar	
4	KH 2.5	CaH <sub>2</sub> 4.8	ScH <sub>2</sub> 4.3	TiH <sub>2</sub> 4.0	VH <sub>1/2</sub> 1.9/3.8	CrH <sub>1/2</sub> 1.9/3.7	Mn	Fe	Co	NiH <sub>&lt;1</sub> <1.7	CuH 1.6	ZnH <sub>2</sub> 3.0	GaH <sub>3</sub> 4.2	GeH <sub>4</sub> 5.3	AsH <sub>3</sub> 3.9	H <sub>2</sub> Se 2.5	HBr 1.2	Kr			
5	RbH 1.2	SrH <sub>2</sub> 2.2	YH <sub>2/3</sub> 2.2/3.3	ZrH <sub>2</sub> 2.2	NbH <sub>2</sub> 2.1	Mo	Tc	Ru	Rh	PdH <sub>&lt;1</sub> <0.9	Ag CdH <sub>2</sub> 1.8	InH <sub>3</sub> 2.6	SnH <sub>4</sub> 3.3	SbH <sub>3</sub> 2.4	H <sub>2</sub> Te 1.6	Hl 0.8	Xe				
6	CsH 0.8	BaH <sub>2</sub> 1.4	LaH <sub>2/3</sub> 1.4/2.1	HfH <sub>2</sub> 1.1	TaH 0.6	W	Re	Os	Ir	Pt	AuH <sub>3</sub> 1.5	HgH <sub>2</sub> 1.0	TlH <sub>3</sub> 1.5	PbH <sub>4</sub> 1.9	BiH <sub>3</sub> 1.4	H <sub>2</sub> Po 1.0	HAt 0.5	Rn			
7	Fr	Ra	Ach <sub>2</sub> 0.9																		

**Figure 2.13** Periodic Table with per element the most common hydrides and the corresponding weight fraction in % Hydrogen.<sup>66</sup>

### 2.2.3. Palladium

The metal that is mostly used in hydrogen detection is palladium (Pd). Pd is a rare and lustrous silvery-white transition metal as shown in **Figure 2.14 a**. Its crystal structure is a face-centered cubic (fcc) lattice with a lattice constant of 3.88 Å. Palladium does not react with oxygen in air, and will be oxidized to palladium oxide (PdO) at 800 °C. Thomas Graham firstly described the absorption of hydrogen by Pd in 1866. Pd readily absorbs hydrogen at ambient conditions, forming PdH<sub>x</sub> (0 < x < 1).<sup>67,68</sup> The density of hydrogen atoms stored in Pd can be up to 935 times than that of pure H<sub>2</sub> gas at ambient conditions. This property was a starting point of a long interest for researchers in the investigation of metal-hydrogen systems. The largest use of Pd in industry is in catalysis. Specially, it can speed up heterogeneous catalytic processes, such as hydrogenation and dehydrogenation.

Similar to the typical phase diagram in **Figure 2.12**, Pd undergoes a phase-change (from α to β) when absorbing hydrogen. First, the lattice constant of Pd keeps almost constant when being α-PdH<sub>x</sub> (increasing of 0.1%), while the lattice constant increases 3.4% when being β-phase (10.7% in lattice volume). Second, its dielectric function changes during the

phase transition but only slightly. The dielectric functions of the Pd and PdH are shown in **Figure 2.14 b**. Both Pd and PdH are still metallic.

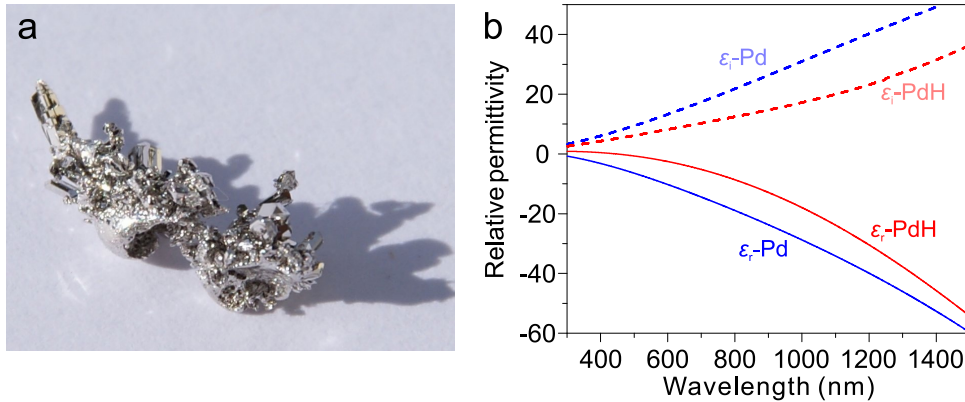


**Figure 2.14** (a) Palladium is a rare and lustrous silvery-white transition metal with atomic number 46. (b) Real  $\epsilon_r$  and imaginary  $\epsilon_i$  part of the Pd (blue) and PdH (red) dielectric function from von Rottkay.<sup>69</sup>

## 2.3. Magnesium

After the fundamental introduction to plasmonics and metal-hydrogen metals, we will elucidate the power of magnesium (Mg) for dynamic nanoplasmatics. Mg is one of the most promising candidates, as it exhibits excellent optical properties at high frequencies and can absorb/desorb hydrogen, undergoing reversible transitions between metal and dielectric hydride ( $MgH_2$ ) states.<sup>23,70</sup> This offers great opportunities to design and construct dynamic optical nanodevices at visible frequencies. We will first evaluate the plasmonic and dynamic properties of Mg. Then, we will then discuss the physical mechanisms of Mg nanoparticles during hydrogenation and dehydrogenation, their stability and protection.

### 2.3.1. Plasmonic properties of Mg

Magnesium is a shiny gray-white lightweight alkaline earth metal with atomic number 12, two-thirds the density of aluminum. It is the fourth most common element in the Earth (after iron, oxygen, and silicon). Mg is very chemically active, and it reacts with oxygen and water at room temperature, slower than alkaline metals. Due to a thin layer of magnesium oxide ( $MgO$ ) shells, oxygen-free condition is unnecessary for Mg storage, but water vapor can hurt the  $MgO$  protection layer (Production of Mg will be discussed in Chapter 2.3.4).

The dielectric function of bulk Mg can be described by the Drude-Lorentz model<sup>71</sup> as discussed in Chapter 2.1.2.

$$\epsilon(\omega) = \epsilon_r(\omega) + i \cdot \epsilon_i(\omega) = \epsilon_\infty - \frac{\omega_p^2}{\omega(\omega + i\gamma)} + \epsilon_{\text{inter}}(\omega) \quad (2.39)$$

where  $\varepsilon_r(\omega)$  and  $\varepsilon_i(\omega)$  are the real and imaginary parts of the dielectric function.  $\varepsilon_\infty$  is the high-frequency limit dielectric constant,  $\varepsilon_{\text{inter}}(\omega)$  represents the contribution from interband transitions,  $\gamma$  is the damping constant, and  $\omega_p$  is the plasma frequency. In the quasi-static regime ( $d \ll \lambda$ ), *i.e.*, the particle size ( $d$ ) is much smaller than the wavelength ( $\lambda$ ) of light in the surrounding medium, the Fröhlich condition is fulfilled at  $\varepsilon_r = -2$ , for a Drude metal sphere located in air as discussed in Chapter 2.1.4.  $\omega_f \approx \omega_p/\sqrt{3}$  from Eq. (2.34) corresponds to the frequency, at which the LSPR can be excited in the metal sphere. The figure of merit, which characterizes the quality of the excited LSPR, can be written as<sup>24</sup>

$$Q_{\text{LSP}} = \frac{\omega}{\Delta\omega} \approx -\frac{\varepsilon_r(\omega)}{\varepsilon_i(\omega)} \quad (2.40)$$

Sanz *et al.*, systematically compared the LSPR positions (Fröhlich energy  $E_f = \hbar\omega_f$ ) and values of  $Q_{\text{LSP}}^{\max}$  for different metals including Mg, Au, Al, Ag, and others as shown in **Figure 2.15**.<sup>23</sup> In general, metals with small  $\varepsilon_i(\omega)$  present strong and narrow resonances. It is apparent that Mg has excellent plasmonic properties, superior to most of the metals (see **Figure 2.15**). More specifically, when compared to conventional plasmonic materials such as Au, Ag, and Al, Mg can produce sharper resonances than Au and Al but is not as good as Ag. Nevertheless, Mg is a more promising material for UV plasmonics than Ag, as interband transitions for Ag already start near 4 eV. In contrary, Mg has no  $d$ -shell electrons and thus no interband transitions involving  $d$ -shell electrons occur.

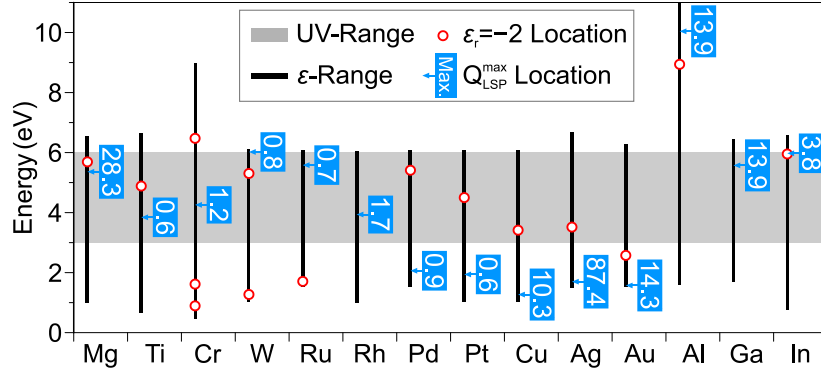


**Figure 2.15** Evaluation of the plasmonic properties of different metals. Fröhlich energy and the maximum plasmonic performance value,  $Q_{\text{LSP}}^{\max}$ , plotted at the spectral position, where it is achieved.<sup>72</sup>

To gain insight into plasmonic properties of Mg, single metallic nanometer-sized hemispheres on flat dielectric substrates were analyzed through the calculations of three representative optical parameters: the absorption efficiency  $Q_{\text{abs}}(\omega)$  of the particle, which is associated with far-field extinction; the maximum enhancement factor of the electric field surrounding the particle  $|E|_{\text{max}}^2(\omega)$  and the electric field enhancement averaged over the surface  $\langle |E|^2 \rangle(\omega)$ , which describe the near-field behavior.<sup>23</sup> Mg nanoparticles with a 20 nm diameter presented a plasmonic resonance (~3.8 eV) in UV-range (shadowed region 3–6 eV in **Figure 2.16 a**), whose frequency was higher than that of Cu (~2.0 eV), Au (~2.1

eV), and Ag ( $\sim 2.7$  eV), but lower than that of Al ( $\sim 4.7$  eV) a little. However, the resonant peak of Mg was sharper and stronger than that of Al, which means that the Mg presents an excellent plasmonic properties in UV-visible range, even better than Al to some extent. The optical properties of Mg could also be understood from its complex dielectric function from the literature<sup>72</sup> (see **Figure 2.16 b**), where the negative real part  $\varepsilon_r$  is essential for the excitation of surface plasmon polaritons on Mg surface, and the smaller imaginary part  $\varepsilon_i$  than that of Al is related to the lower loss of Mg in the whole UV-VIS-NIR range.

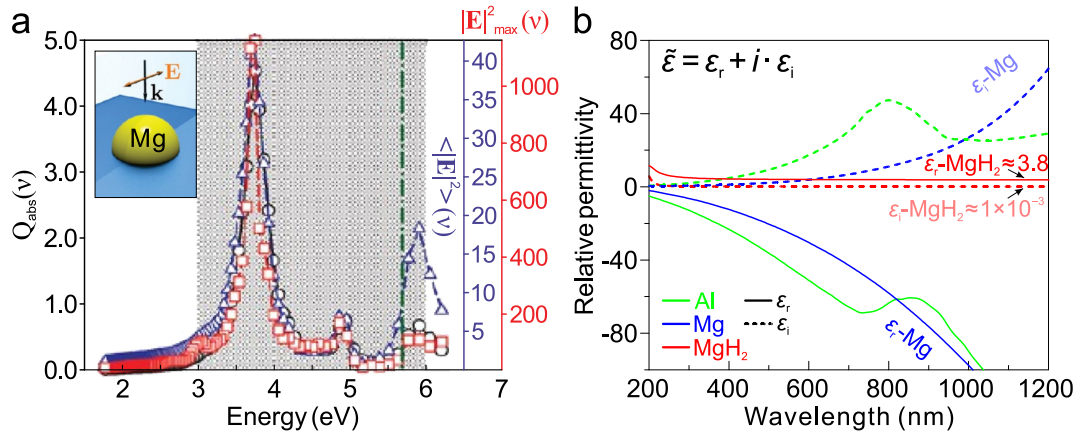


**Figure 2.16** (a) Theoretical calculated spectra of  $Q_{\text{abs}}(\omega)$ ,  $|\mathbf{E}|^2_{\text{max}}(\omega)$ , and  $\langle |\mathbf{E}|^2 \rangle(\omega)$  for hemispherical Mg nanoparticles of 20 nm radius located on a sapphire substrate ( $n = 1.78$ ). (b) Real (solid lines) and imaginary (dashed lines) part of the dielectric functions of Al, Mg, and  $\text{MgH}_2$ , respectively.<sup>72</sup>

### 2.3.2. Dynamic properties of Mg

Another interesting aspect of Mg is its hydrogen storage properties. Mg reacts reversibly with hydrogen to form magnesium hydride ( $\text{MgH}_2$ ),<sup>70,73</sup> which follows the reaction:  $\text{Mg} + \text{H}_2 \leftrightarrow \text{MgH}_2 + 75.2 \text{ kJ mol}^{-1}$ .  $\text{MgH}_2$  is an ionic compound with an appreciable covalent contribution. It exhibits a charge density distribution of  $\text{Mg}^{+1.91}\text{H}^{-0.26}$ , in which Mg is almost fully ionized but H is very weakly ionized, presenting a high thermodynamic stability<sup>74</sup> as discussed in Chapter 2.2.2. The diffusing species in Mg is the H-anion, whose diffusion rate is much slower than the H proton in vanadium, niobium, and palladium.<sup>75</sup>

Optically,  $\text{MgH}_2$  is a transparent and color neutral insulator with a band gap of  $5.6 \pm 0.1$  eV ( $221 \pm 4$  nm),<sup>76</sup> which could also be insight in its dielectric functions in **Figure 2.16 b**.  $\text{MgH}_2$  can be regarded as a nearly non-dispersive and low-loss dielectric material with refractive index  $n+ik = 1.95 + i0.01$  in the visible and near-infrared regimes.<sup>76</sup> Due to the dramatically large switching contrast between Mg and  $\text{MgH}_2$  both in optical and electrical properties, the transition processes can be conveniently investigated by joint optical and electrical measurements (*i.e.*, hydrogenography) in real time,<sup>77</sup> which promotes further the interests and studies on the Mg-H system.

To understand the hydrogen ab- and de-sorption mechanisms in Mg at the atomic level, the dynamics of the crystallographic phase transition of Mg regarding hydrogenation and dehydrogenation have been deeply investigated by transmission electron microscope (TEM), combined with X-ray and neutron scattering techniques, atomic force microscope (AFM), scanning electron microscopy (SEM), etc. With the utilization of TEM, a stronger electron beam was used to desorb the hydrogen from the MgH<sub>2</sub> (so-called electron beam-induced dehydrogenation), and a low-intensity electron beam was used to examine the diffraction patterns and the electron energy loss spectra (EELS), where the electron diffraction reveals the structural change in the transition process, and the EELS defines the state of the constituent compounds owing to the volume plasmon peaks for Mg and MgH<sub>2</sub> are  $10.7 \pm 0.2$  eV and  $14.7 \pm 0.3$  eV, respectively. Advanced environmental TEM, equipped with gas loading component, could implement *in situ* measurements of the hydrogenation process, allowing for a direct understanding of the reaction mechanism.

Mg has a hexagonal-close-packed (hcp) structure with lattice parameters of  $a_1 = a_2 = a_3 = 3.21$  Å,  $c = 5.21$  Å (see **Figure 2.17**).<sup>78,79</sup> Previous studies showed that for Mg films and particles deposited on substrates without lattice matching, for instance, on glass, silicon, aluminum oxide, and titanium (Ti), they attained energetically favorable orientations, determined by interface energies, where the facets corresponded to the closest packed planes.<sup>80-82</sup> In other words, the hexagonal prism is the most preferable shape with the Mg [0001] direction perpendicular to the substrate plane.<sup>80</sup> When a small quantity of hydrogen dissolves into the Mg crystal lattice (up to 10 at.%), the  $\alpha$ -MgH<sub>x</sub> phase (interstitial solid solution of H in Mg) is formed and it has a hexagonal crystal structure.<sup>73,83</sup> With further hydrogenation,  $\beta$ -MgH<sub>2</sub> that has a tetragonal rutile crystal structure occurs with lattice parameters of  $a = b = 4.52$  Å,  $c = 3.02$  Å (see **Figure 2.17**).<sup>78,79</sup> In between these two phases, there exists a mixed region, the  $\alpha+\beta$  phase, in which hydrogen dissolved in Mg is in equilibrium with MgH<sub>2</sub>. The plateau pressure for the transition from the  $\alpha$ -phase to the  $\alpha+\beta$  phase is 0.41 Torr at 353K.<sup>73</sup> Electron diffraction studies revealed that the most intrinsic orientation relationship between Mg and MgH<sub>2</sub> lattices during the phase transition was Mg(0001)[2̄1̄10] || MgH<sub>2</sub>(110)[001] (see insets in **Figure 2.17**).<sup>78,79</sup> Due to the atomic movements resulting from the phase transition, the distance between the Mg atoms is expanded by 23% (from  $c_{\text{Mg}}$  to  $\sqrt{2}a_{\text{MgH}_2}$ ) along the direction perpendicular to the substrate plane. Along the Mg [2̄1̄10] direction, the Mg-Mg distance contracts by 6% (from  $a_{\text{Mg}}$  to  $c_{\text{MgH}_2}$ ), whereas along the Mg [0̄1̄10] direction, the Mg-Mg distance expands by 15% (from  $\sqrt{3}a_{\text{Mg}}$  to  $\sqrt{2}a_{\text{MgH}_2}$ ).<sup>78</sup> The distance between the Mg atoms in the substrate plane is expanded by only 6%. Hence, major lattice distortions occur along the out-of-plane direction, indicating an anisotropic hydrogenation mechanism.<sup>84</sup>

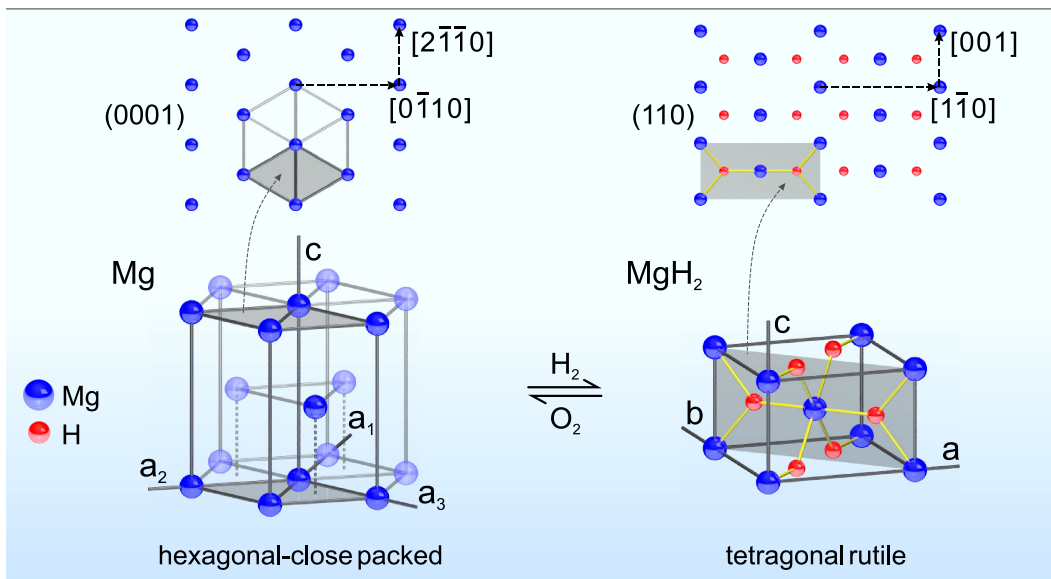


**Figure 2.17** Crystallographic phase transformations between Mg and  $MgH_2$ . Atomic arrangements in the Mg (0001) and  $MgH_2$  (110) planes, respectively, which are parallel to the substrate.

Mg is a potential material for solid-state hydrogen storage owing to its abundance, low cost, reversibility, as well as large hydrogen gravimetric (7.6 wt %) and volumetric (110 g l<sup>-1</sup>) capacities.<sup>70</sup> However, there are two major obstacles for practical applications: high hydrogenation/dehydrogenation temperatures and sluggish hydrogen absorption/desorption kinetics. The surface of pure Mg has a large activation energy for hydrogen dissociation and hydride formation. Hydrogenation of Mg requires high operating temperatures up to ~300 °C at 1 atm pressure and dehydrogenation needs even higher temperatures ~400 °C.<sup>85,86</sup> It was discovered that Pd capping on Mg could reduce the high operating temperatures to ambient conditions by catalyzing the dissociation of  $H_2$  molecules.<sup>86</sup> This has stimulated tremendous studies on Pd-capped Mg films, fibers, and powders for hydrogen storage.<sup>70</sup> In this case (see **Figure 2.18 a**), as the reaction progresses  $MgH_2$  grows at the Mg/Pd interface. The kinetic limiting step is hydrogen diffusion through the growing hydride layer  $MgH_2$ , which acts as a barrier for further hydrogenation of Mg. This is the so-called blocking effects.<sup>87</sup> During dehydrogenation, the growing metallic Mg near the Mg/Pd interface then limits the desorption kinetics (see **Figure 2.18 b**).

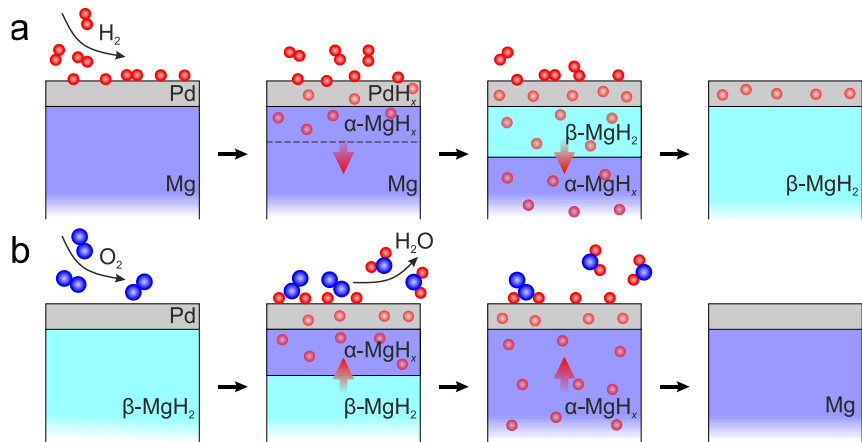


**Figure 2.18** Schematic models of hydrogenation (a) and dehydrogenation (b) processes for the Pd-capped Mg upon hydrogen and oxygen exposure, respectively. Pd is used to promote hydrogen dissociation and recombination, as well as to protect Mg against oxidation.

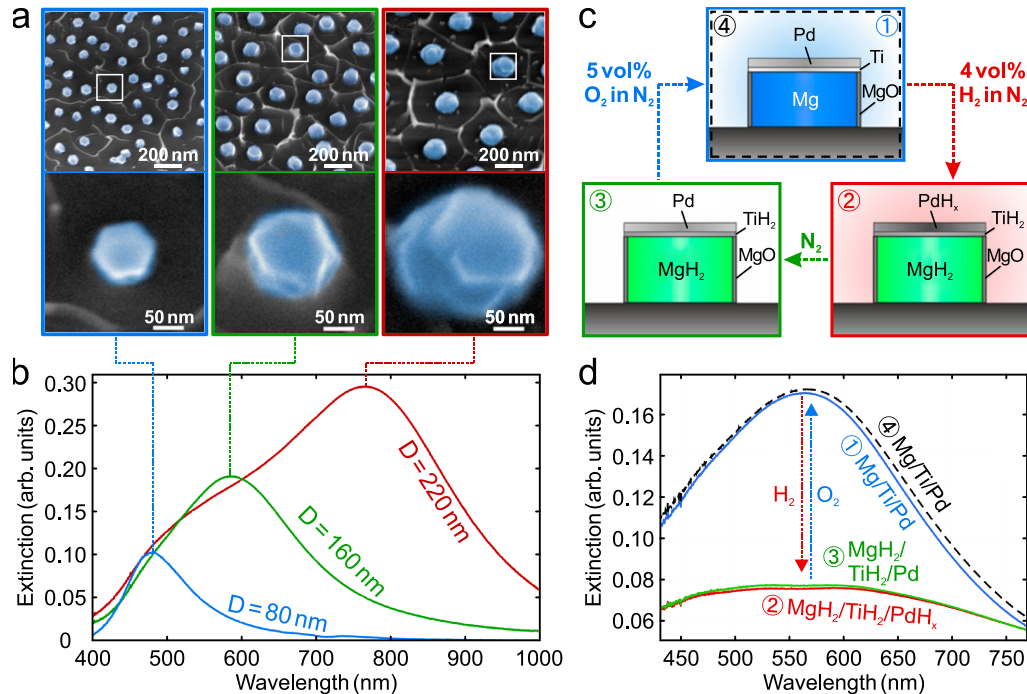
### 2.3.3. Dynamic plasmonic nanoparticles

In 1997, van der Sluis *et al.* demonstrated optical switching of Mg-based films between mirror and transparent states through hydrogenation and dehydrogenation.<sup>88</sup> Since then, ‘switchable mirrors’ have been widely investigated. This has led to a variety of applications including optical hydrogen sensors<sup>89</sup>, switchable solar absorbers<sup>90</sup>, and smart windows.<sup>91</sup> However, the blocking effects as a bottleneck issue remained, hampering the further development for practical applications. Later, Uchida *et al.* showed that Mg films exhibited favorable absorption kinetics only for film thickness below ~100 nm with diffusion coefficient of  $\sim 10^{-16} \text{ m}^2\text{s}^{-1}$ .<sup>83</sup> Subsequently, a MgH<sub>2</sub> layer was formed at the Mg/Pd interface and the diffusion coefficient decreased to  $\sim 10^{-18} \text{ m}^2\text{s}^{-1}$ , preventing hydrogen from further diffusion. Although the kinetics could be improved by increasing temperature and/or decreasing hydrogen concentration,<sup>87</sup> the formation of MgH<sub>2</sub> as diffusion barrier dramatically slowed down the diffusion process, especially when the diffusion length was longer than ~100 nm.

To enhance diffusion kinetics, Mg and MgH<sub>2</sub> particles have been utilized.<sup>92</sup> Small particles possess large surface areas and thus more reaction sites, which can accelerate the kinetics by shortening the diffusion lengths. Decreasing the crystal grain size can also reduce the thermodynamic stabilities of Mg and MgH<sub>2</sub>, resulting in lower hydrogen absorption and desorption temperatures.<sup>93</sup> The most common method to producing Mg particles is mechanical milling. However, the lack of quantitative control over the sizes, morphologies and compositions has encumbered the understanding of hydrogenation/dehydrogenation mechanisms on the nanoscale.

In recent years, advances in nanofabrication techniques have provided great opportunities to pattern Mg nanoparticles with controlled sizes, shapes, compositions, and surface morphologies. This has also enabled a plethora of Mg-based plasmonic nanostructures. For instance, Sterl *et al.*, fabricated Mg nanoparticles of various sizes by

colloidal hole-mask lithography and subsequent electron-beam evaporation (see **Figure 2.19 a**).<sup>94</sup> These Mg particles possessed hexagonal monocrystalline shapes, when their sizes were relatively small ( $\sim 100$  nm). They tended to be polycrystalline with increasing sizes. These Mg nanoparticles also exhibited pronounced LSPRs, which were tunable throughout the visible wavelength range by varying the particle size (see **Figure 2.19 b**). With the help of Pd as catalytic layer, the resonances could be turned off/on upon hydrogen/oxygen exposure at room temperature, when the particles were transformed between the metallic Mg state and the dielectric  $MgH_2$  state (see **Figure 2.19 c** and d). To avoid the Mg-Pd alloy formation<sup>85</sup>, 5 nm Ti was used to separate Mg and Pd. This buffer layer also helped to release the mechanical stress, resulting from the different expansion rates of Mg and Pd upon hydrogen absorption.



### 2.3.4. Stability, reversibility, and durability

Despite these promising advantages, Mg has been argued to be unsuitable for nanoplasmonics for a long time, due to its much higher chemical reactivity than widely used plasmonic metals, such as Au, Ag, Al, and Cu. Concerns about stability, reversibility, and durability as well as approaches to solve these issues are highly relevant. The corrosion of Mg happens rapidly in humid air, resulting deteriorated plasmonic properties. Actually, this argument is oversimplified. The corrosion kinetics of Mg under ambient conditions is mainly governed by two factors: the water content in air and the characteristics of the Mg surface.<sup>95</sup> It was reported that Mg films and particles were very stable when exposed to

dry air owing to the formation of several nanometers thick MgO passivation shells. In humid environment, the MgO could physically and chemically absorb moisture to form Mg(OH)<sub>2</sub>, which no longer serves as a protective barrier layer analogous to the passive oxide layer formed on Al. While, this hydration process of MgO is strongly influenced both by the crystallographic orientation and by the presence of defects at the oxide surface, and furthermore the structure and quality of the MgO shells are determined by the characteristics of the Mg surface.<sup>80</sup> Several studies showed that the hydration process was limited to the surface for a denser Mg film surface with less defects.

Kooi *et al.*, demonstrated that crystallized Mg nanoparticles exhibited a dense and crystalline MgO shell (~3 nm), which has an orientation relation to Mg, preventing further oxidation under ambient conditions at room temperature for one month.<sup>80</sup> In contrast, poorly crystallized Mg with low-density surface possessed a porous and amorphous MgO shell, which could hydride easily to form a porous Mg(OH)<sub>2</sub> layer. This open structure will lead to continuing corrosion rapidly. Therefore, improving the crystallinity of Mg surfaces during fabrications and operating the Mg-based nanodevices in dry environment are critical actions to consider. To operate Mg-based nanodevices in humid air, a thin polytetrafluoroethylene (PTFE) layer can be deposited on the Mg surface to isolate water but still allow for hydrogen diffusion.<sup>96,97</sup> In addition, for all the aforementioned Mg-based nanodevices, the utilization of Pd and Ti capping layers was proved to be very effective for Mg protection, showing good device performance in terms of reversibility and durability. A coating procedure with gallium (Ga) on Mg particles has also been proposed.<sup>98</sup>

## 2.4. Methods

### 2.4.1. Fabrications

All nanostructures presented in this thesis were prepared by electron-beam lithography (EBL). EBL is the practice of scanning a focused beam of electrons to define nearly arbitrarily shaped structures in two dimensions (2D). By using layer-by-layer stacking techniques, it can be used to build quasi three dimensional (3D) nanostructures. Nanostructures with resolutions down to sub-10 nm are achievable with EBL either using positive or negative electron beam resists.

EBL can draw custom patterns with sub-10 nm resolution, which is the most advantage, but the throughput is very low. It is hard to get large area structures. Generally, EBL processes can be categorized in two types, depending on the resists that are used (positive or negative electron beam resists).

Gold and Mg nanostructures discussed in Chapters 3, 4, 6, and 7 were fabricated with a positive resist using standard EBL. **Figure 2.20** depicts the schematic of each processing step. The positive resist we used is poly-methyl-methacrylate (PMMA), which is a kind of polymers with different chain lengths dissolved in chlorobenzene. The chain length

determines the sensitivity of the resist upon electron exposure. The electron beam changes the solubility of resists, which can selectively remove the exposed regions of the resist by immersing it in a solvent. Then, the proposed nanostructure can be created with resist. In order to transfer the resist pattern into a metal structure, lift-off process is used after evaporation of metal films.

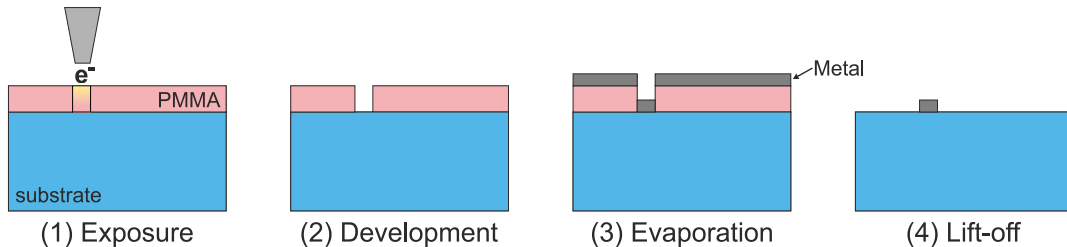


**Figure 2.20** Schematic of EBL procedure using positive resist (PMMA).

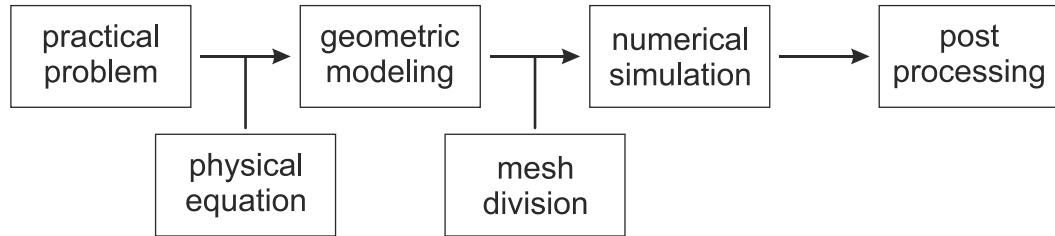
Firstly, a thin layer of PMMA is spin coated on top of a substrate. The thickness of the polymer layer is determined by the concentration of the PMMA and the spinning speed. Then, the sample need to be baked at 160 °C for 3 min to remove all solvent and stiffen the polymer layer. Usually, we spin two layers of PMMA (250K, 2.5% and 950K, 1.5%, Allresist) separately. In order to ensure the conductivity and avoid charging effects of the sample during e-beam exposure, a layer of the conductive polymer (Spacer, Showa Denko, 60s at 5000 rpm, no baking) is spin coated afterwards on the sample. Secondly, the sample is loaded in the Raith eLine. Usually, we choose 20 kV acceleration voltage, 20  $\mu\text{m}$  aperture ( $\sim$ 130 pA current), elements step size 6.4 nm, elements dose 325  $\mu\text{C}/\text{cm}^2$ , write-field size  $100\times 100 \mu\text{m}^2$ . Then, the designed structures are exposed in the resist. After removal of the Spacer by DI-water, the sample is developed for 90 s in a MIBK solution (Methyl isobutyl ketone, diluted 1:3 in isopropanol), and the development is stopped by soaking the sample in isopropanol for 60 s. Thirdly, different metals were successively deposited on the substrate through electron beam evaporation (PFEIFFER Vacuum, PLS-500). Finally, the metal film and the remaining resist were removed by lift-off process (soaking the sample in N-Ethyl-2-pyrrolidone, NEP, Allresist, 2 hours at 65 °C).

The second type of EBL process uses the negative resist, for example, hydrogen silsesquioxane (HSQ). In contrast to the positive resist, during EBL writing, the non-exposed regions of the resist can be selectively removed by immersing it in a solvent. It can also be used in grey-scale lithography. Details can be found in Chapter 5.6.1.

#### 2.4.2. Simulations

Although the interaction of light with simple plasmonic structures such as spheres and ellipsoids can be analytically solved, more complex structures and conditions require numerical techniques to solve Maxwell's equations. In this thesis, the commercial software COMSOL Multiphysics was used to gain deep insight into the nature of the experimental results.<sup>99</sup> It is a general-purpose software platform, based on the finite element method

(FEM), for modeling and simulating physical problems. The general circuit of FEM modeling can be show as follow:



The FEM is a powerful numerical technique for numerically finding solutions to boundary value problems for partial differential equations (PDE).<sup>100</sup> The basic idea is the subdivision of a whole computational domain into simpler and smaller parts, called finite elements. By using variational methods from the calculus of variations to solve the problem by minimizing an associated error function, FEM connects many simple element equations over many small subdomains to approximate a more complex equation over a larger domain.

Here, we use the Radio Frequency (RF) Module of the COMSOL Multiphysics, which can simulate electromagnetic wave propagation and resonant behavior. The simulation offers the electromagnetic field and charge distributions, transmission, reflection, impedance, Q-factors, S-parameters, and any other physical quantities.

The general time-varying electromagnetic fields in linear and isotropic medium can be described by Maxwell's equations of Eq. (2.1) and the constitutive relations of Eq. (2.3). In applications one needs to include Ohm's law in the form

$$\mathbf{J}_{\text{ext}}(\mathbf{r}, t) = \sigma \mathbf{E}(\mathbf{r}, t) \quad (2.41)$$

where,  $\sigma$  is the electric conductivity. Thus, Eqs. (2.1), (2.3), and (2.41) can completely describe the relationship between electromagnetic field and source in materials, namely

$$\begin{aligned} \nabla \times \mathbf{E}(\mathbf{r}, t) &= -\mu_0 \frac{\partial \mu \mathbf{H}(\mathbf{r}, t)}{\partial t} \\ \nabla \times \mathbf{H}(\mathbf{r}, t) &= \epsilon_0 \frac{\partial \epsilon \mathbf{D}(\mathbf{r}, t)}{\partial t} + \sigma \mathbf{E}(\mathbf{r}, t). \end{aligned} \quad (2.42)$$

Due to the fact that magnetic induction  $\mathbf{B}$  is divergence-free (namely,  $\nabla \cdot \mathbf{B} = 0$ ), we can introduce a magnetic potential  $\mathbf{A}$ , so that

$$\begin{aligned} \mathbf{B}(\mathbf{r}, t) &= \nabla \times \mathbf{A}(\mathbf{r}, t) \\ \mathbf{E}(\mathbf{r}, t) &= -\frac{\partial \mathbf{A}(\mathbf{r}, t)}{\partial t} \end{aligned} \quad (2.43)$$

Substituting Eq. (2.43) in Eq. (2.42),

$$\mu_0\sigma \frac{\partial \mathbf{A}(\mathbf{r}, t)}{\partial t} + \mu_0\epsilon_0 \frac{\partial}{\partial t} \epsilon \frac{\partial \mathbf{A}(\mathbf{r}, t)}{\partial t} + \nabla \times [\mu^{-1}\nabla \times \mathbf{A}(\mathbf{r}, t)] = 0 \quad (2.44)$$

Equation (2.44) is used to solve a time-domain wave equation for the magnetic vector potential. It is primarily used to model electromagnetic wave propagation in different media and structures when a time-domain solution is required. For example, for non-sinusoidal waveforms or for nonlinear media. Typical applications involve the propagation of electromagnetic pulses.

In a linear and isotropic medium, the ansatz of a harmonic plane wave is

$$\begin{aligned} \mathbf{E}(\mathbf{r}, t) &= \mathbf{E}(\mathbf{r})e^{i\omega t} \\ \mathbf{H}(\mathbf{r}, t) &= \mathbf{H}(\mathbf{r})e^{i\omega t} \end{aligned} \quad (2.45)$$

Then, substituting Eq. (2.45) in Eq. (2.42), we get the Maxwell's equation in time-harmonic form, namely Helmholtz equation,

$$\nabla \times [\mu^{-1}\nabla \times \mathbf{E}(\mathbf{r})] - k_0^2 \left( \epsilon - \frac{i\sigma}{\omega\epsilon_0} \right) \mathbf{E}(\mathbf{r}) = 0 \quad (2.46)$$

$$\nabla \times \left[ \left( \epsilon - \frac{i\sigma}{\omega\epsilon_0} \right)^{-1} \nabla \times \mathbf{H}(\mathbf{r}) \right] - k_0^2 \mu \mathbf{H}(\mathbf{r}) = 0 \quad (2.47)$$

In this thesis, we mainly focus on the time-harmonic electromagnetic field distributions. Thus, the key point is to get the solution to Eq. (2.46) or Eq.(2.47). By using Weighted Residual Method or Calculus of Variations, the partial differential Eq. (2.46) can be converted into a set of linear algebraic equations,<sup>100</sup> which can be solved by computer afterwards.

FEM divides a complex problem into small elements. It connects many simple element equations over many small subdomains, to approximate a more complex equation over a large domain, which is a good choice for analyzing problems over complicated domains. FEM uses a complex system of points called nodes which set up a grid called a mesh as shown in **Figure 2.21**. Tetrahedral meshes are used in 3D modeling, which enables higher accuracies for curved geometries. This mesh is programmed to contain the material properties that define how the structure react to the local conditions. The nodes are assigned throughout the material at a proper density.

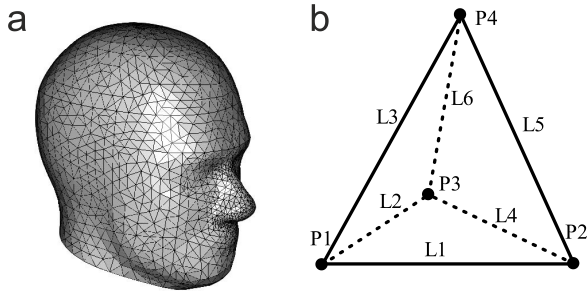


**Figure 2.21** (a) FEM modelling for head. (b) Tetrahedral mesh and nodes of FEM modelling elements.

Here, we take the tetrahedral mesh in **Figure 2.21 b** as an example to describe the process.

After the mesh generation, we can build the FEM algebraic equations by choosing interpolation functions. Mostly, we treat Whitney base function as interpolation,

$$\mathbf{w}_i = (\zeta_{i1} \nabla \zeta_{i2} - \zeta_{i2} \nabla \zeta_{i1}) l_i \quad (2.48)$$

where  $i$  indicates the edge  $L_i$ ,  $i_1 i_2$  indicates the two nodes numbering of the edge  $L_i$ , and  $\zeta$  is the volume coordinate. The definition of volume coordinate is as follows: We select a point  $P$  in tetrahedron  $e$ , the coordinate of  $P$  is  $(x, y, z)$ .  $V_i$  is the volume of tetrahedron defined by point  $P$  and the other three points of  $e$  excluding point  $i$ .  $V^e$  is the volume of tetrahedron  $e$ . Then, the volume coordinate is

$$\zeta_i(x, y, z) = \frac{V_i}{V^e} = \frac{a_i + b_i x + c_i y + d_i z}{6V^e} \quad (2.49)$$

Where  $a$ ,  $b$ ,  $c$ , and  $d$  are the related constants of the tetrahedron. It can be shown that  $\mathbf{w}_i$  has the constant tangential component on the edge  $L_i$ , while the tangential component on the other edge is zero. Thus, the coefficient of  $\mathbf{w}_i$  base function is corresponding to the electric field on related edge.

After substituting the Eq. (2.48) into the FEM algebraic equations divided by WRM or Calculus of Variations, we get a discrete linear FEM algebraic equation. After getting its solution, we obtain all electromagnetic parameters in the model.



### 3. Dynamic plasmonic chirality

Chirality is a highly important topic in modern chemistry, given the dramatically different pharmacological effects that enantiomers can have on the body. Chirality of natural molecules can be controlled by reconfiguration of molecular structures through external stimuli. Despite the rapid progress in plasmonics, active regulation of plasmonic chirality, particularly in the visible spectral range, still faces significant challenges. In this Chapter, we demonstrate a new class of hybrid plasmonic metamolecules composed of magnesium and gold nanoparticles. The plasmonic chirality from such plasmonic metamolecules can be dynamically controlled by hydrogen in real time without introducing macroscopic structural reconfiguration. We experimentally investigate the switching dynamics of the hydrogen-regulated chiroptical response in the visible spectral range using circular dichroism spectroscopy. In addition, energy dispersive X-ray spectroscopy is used to examine the morphology changes of the magnesium particles through hydrogenation and dehydrogenation processes. Our study can enable plasmonic chiral platforms for a variety of gas detection schemes by exploiting the high sensitivity of circular dichroism spectroscopy.

This chapter is adapted with permission from “Duan, X.; Kamin, S.; Sterl, F.; Giessen, H.; Liu, N. Hydrogen-regulated chiral nanoplasmonics. *Nano Lett.* **2016**, *16*, 1462–1466.”

### 3.1. Introduction to plasmonic chirality

#### 3.1.1. Chirality

Chirality is a geometrical property of an object. An object is chiral if it is distinguishable from its mirror image, and namely, it cannot be superposed with its mirror image. The original structure and the mirror image are called the two enantiomers of a chiral compound. A non-chiral object is called achiral if it can be superposed with its mirror image. Human hands are the most intuitive example of chirality as shown in **Figure 3.1**.

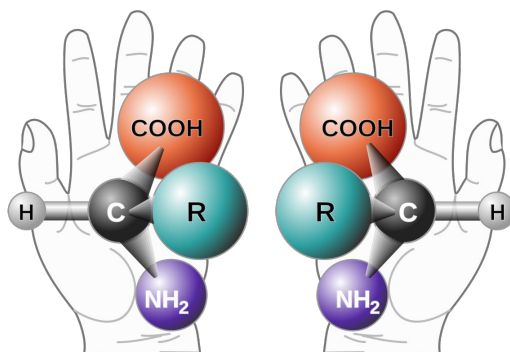


**Figure 3.1** Two enantiomers of a generic amino acid.

Starting from the amino acids and nucleic acids, the building block of life, to the proteins and DNA molecules, all biological molecules are chiral. In short, life itself is about chirality. Chirality is fundamentally linked to structure and biological function, which has been the subject of intense research on the route to understand the basic foundation of life.<sup>101-103</sup>

Apart from geometrical properties, chirality can also manifest itself optically via a different response to left- and right-handed circularly polarized (LCP and RCP) light. The resulting absorption difference is called circular dichroism (CD).<sup>104</sup> CD spectroscopy is a powerful tool in biology, chemistry, medicine, and physics for discrimination of enantiomers as well as for studying the conformation changes of macromolecules.

Controlling molecular chirality is of great importance in stereochemistry, as enantiomers of a given compound may give rise to strikingly different biological activities.<sup>105-111</sup> Chirality of natural molecules can be manipulated by reconfiguring molecular structures through light<sup>105-108</sup>, electric field<sup>109</sup>, and thermal stimuli<sup>110,111</sup>. However, such chirality regulation is not prominent. In general, CD of natural chiral molecules such as amino acids, proteins, carbohydrates, *etc.*, is very weak and located only in the UV spectral region.

#### 3.1.2. Plasmonic chirality

In contrast, chiral plasmonic structures can exhibit spectrally tunable and pronounced CD. Recent advances in plasmonics renders the realization of artificial chiral

metamolecules possible.<sup>112-116</sup> These plasmonic metamolecules composed of metallic structures arranged in chiral configurations can exhibit pronounced CD that is several orders of magnitude stronger than that of natural molecules.<sup>117-128</sup> Nevertheless, reconfiguring plasmonic metamolecules, which are restrained on substrates, faces significant challenges. In 2012, S. Zhang *et al.* have proposed a seminal concept of chirality switching without structural reconfiguration in the terahertz range.<sup>129,130</sup> The underlying idea is to break the mirror symmetry of the structure through the integrated silicon component upon photoexcitation. Later, a thermally-controlled plasmonic chiral system in the mid-infrared range has been demonstrated through integration of Ge<sub>3</sub>Sb<sub>2</sub>Te<sub>6</sub>.<sup>131,132</sup> As a result, utilization of active materials, in particular phase-transition materials, brings about an elegant solution to regulating plasmonic chirality without structural reconfiguration.<sup>133</sup> This is in stark contrast to the case of natural molecules.

Among a variety of phase-transition materials, Mg possesses a unique role due to its multifunctional character.<sup>23,82,94,134-136</sup> First, Mg can undergo phase-transition from metal to dielectric to form MgH<sub>2</sub> upon hydrogen loading. MgH<sub>2</sub> can contain up to 7.6 wt % of hydrogen, featuring a remarkable capacity that exceeds all known reversible metal hydrides. Together with its abundance and low-cost aspects, Mg bears great potential for hydrogen-related applications. Second, different from other phase-transition metals for hydrogen storage, such as yttrium<sup>137,138</sup> and palladium<sup>139-142</sup>, which yield poor plasmonic properties, Mg constitutes a promising candidate for high-frequency plasmonics due to its excellent extinction efficiencies in the UV and blue visible wavelength range.<sup>23,24</sup>

We demonstrate hydrogen-regulated chiroptical response in hybrid plasmonic metamolecules in the visible spectral range. Here, Mg works not only as active material for hydrogen uptake but also as plasmonic material for resonant coupling with the satellite gold (Au) particles. Each metamolecule consists of coupled hybrid components that are arranged in a prescribed chiral geometry to generate chiroptical response. Au particles are particularly employed here to assist Mg particles for achieving sharp and pronounced CD spectra. Such chiroptical response can be switched on/off by dynamically unloading/loading hydrogen in real time. In addition, energy dispersive X-ray spectroscopy (EDX) reveals the morphology changes of the Mg particles that result from hydrogenation and dehydrogenation processes. With integration of appropriate active materials, our design scheme can be generalized to create sensitive chiral platforms for a variety of gas detection, given the high sensitivity of CD spectroscopy. This could provide a powerful addition to the conventional sensing paradigm.

### 3.2. Mechanism of hydrogen-regulated chiral plasmonics

**Figure 3.2 a** shows the schematic of the hybrid plasmonic metamolecules. Four Mg particles are surrounded by four satellite Au particles. These closely-spaced particles reside on a glass substrate and form a gammadiion-like hybrid superstructure.<sup>119,131</sup> To facilitate hydrogen loading/unloading in Mg at room temperature, titanium (Ti, 5 nm) and Pd (10

nm) are capped on top of the Mg particles. Pd serves as catalyst to dissociate molecular hydrogen into atomic hydrogen.<sup>135,136</sup> Ti is used as spacer to prevent Mg and Pd from alloying as well as to release the mechanical stress resulting from different expansions of Mg (32%) and Pd (11%) upon hydrogen uptake.<sup>82,94</sup> The structural parameters of the Mg and Au particles are designed such that they can be resonantly coupled and consequently the chiral plasmonic metamolecule can yield different absorbance in response to left- and right-handed circularly polarized light, this is, CD. The different refractive indices of the substrate and air as superstrate are the symmetry-breaking factors that lead to the required CD response.

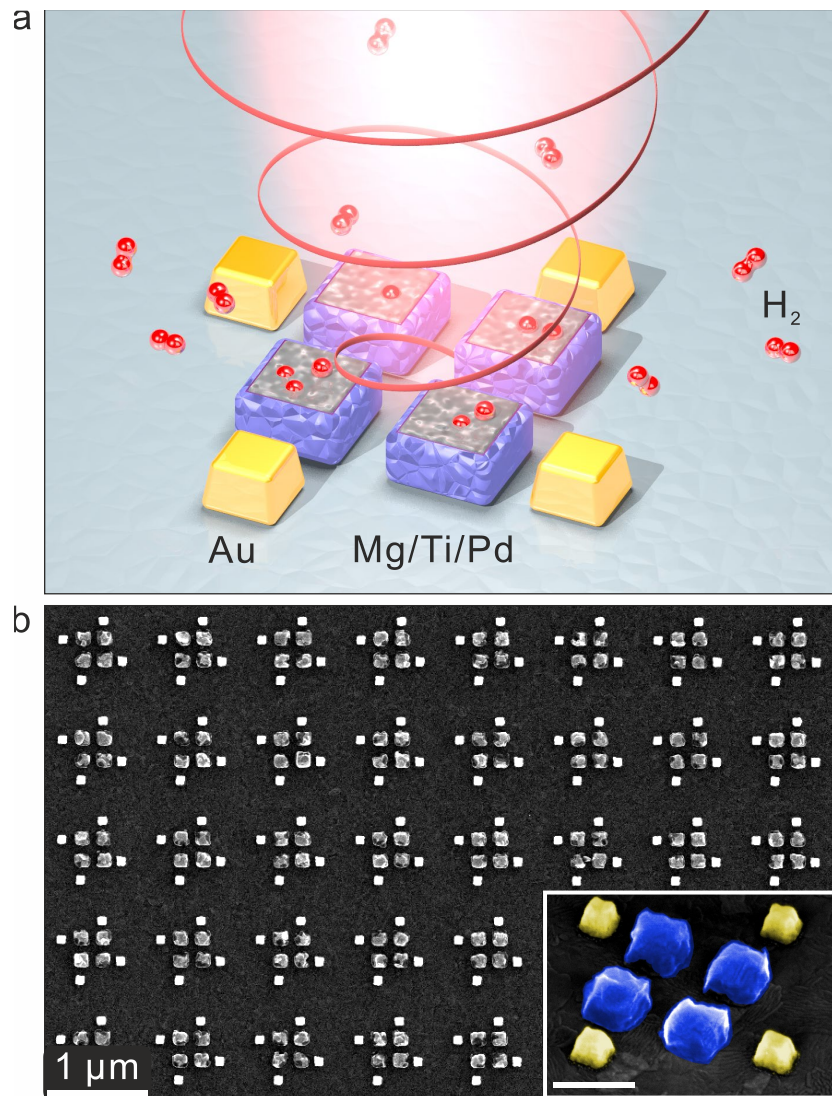


**Figure 3.2** (a) Schematic of a hybrid plasmonic metamolecule on a glass substrate. Four Mg particles ( $160\text{ nm} \times 160\text{ nm} \times 75\text{ nm}$ ) are surrounded by four Au satellite particles ( $100\text{ nm} \times 100\text{ nm} \times 80\text{ nm}$ ). The Mg particles are capped with a 5 nm Ti spacer and a 10 nm catalytic Pd layer. The gaps between the Mg particles are 80 nm. The gaps between the Mg and Au particles are 60 nm. Circularly polarized light is incident perpendicularly onto the structure. Hydrogen is represented by the red spheres. (b) Over-view SEM image of the hybrid plasmonic structures in left-handedness. The period along both directions is 1  $\mu\text{m}$ . The scale bar in the tilted SEM image is 200 nm.

The samples were fabricated with a double electron-beam lithography process. An exemplary scanning electron microscopy (SEM) image of a left-handed sample is presented in **Figure 3.2(b)**, where the Mg and Au particles can be clearly distinguished due to the high contrast between these two materials. The Mg particles show more grainy features, when compared to the Au particles. A tilted-view of one enlarged structure is presented in the inset.

### 3.3. Experiments and simulations

The samples were manufactured using double electron-beam lithography (EBL). First, a structural layer composed of four satellite Au particles and alignment markers were defined in a double layer PMMA resist (Allresist) using EBL (Raith e\_line) on an ITO coated glass substrate (Delta Technologies, Limited). A 2 nm chromium adhesion layer and an 80 nm Au film were deposited on the substrate using thermal evaporation followed by a lift-off procedure. Next, the substrate was coated with a double layer PMMA again. Computer-controlled alignment using the Au markers was carried out to define a second structural layer. Subsequently, 75 nm Mg, 5 nm Ti, and 10 nm Pd multilayers were deposited on the substrate using electron-beam evaporation followed by the same lift-off procedure. All samples have a total area of 1.6 mm × 1.6 mm.

The CD spectra were measured using a Jasco-1500 CD spectrometer with a custom gas cell holder. All measurements were carried out at room temperature (~25 °C). The flow rate of the gas was 1.0 l/min. The measured spectra were normalized with respect to that of the bare substrate. For the *in situ* CD measurements, the CD signal at 705 nm was monitored using a time-scan acquisition mode with a data pitch of 2 s.

Numerical simulations were carried out using commercial software COMSOL Multiphysics based on a finite element method (FEM). Periodic boundary conditions and waveguide port boundary conditions were used in the simulations. The refractive index of the glass substrate was taken as 1.5, and a 20 nm ITO layer with  $n = 1.775$ , and  $k = 0.012$  (Delta Technologies, Limited) was considered in the simulations. The dielectric constants of Au, Mg, and MgH<sub>2</sub> were taken from Johnson and Christy<sup>143</sup>, Palik<sup>72</sup>, and Griessen<sup>76</sup>. The dielectric constants of Pd and PdH were taken from von Rottkay<sup>69</sup>.

### 3.4. Optical response

The working principle of hydrogen regulation to the chiroptical response is illustrated in **Figure 3.3 a and b**. Initially, the left-handed plasmonic metamolecules exhibit a characteristic peak-to-dip line shape in the CD spectrum, which is simulated using commercial software COMSOL (see the red line in **Figure 3.3 b**). This stems from the resonant coupling between the collective plasmons excited in the eight plasmonic particles within one hybrid metamolecule. As shown by the simulated field distribution in **Figure**

**3.3** a, the electromagnetic near-fields are strongly localized between the Mg and Au particles.

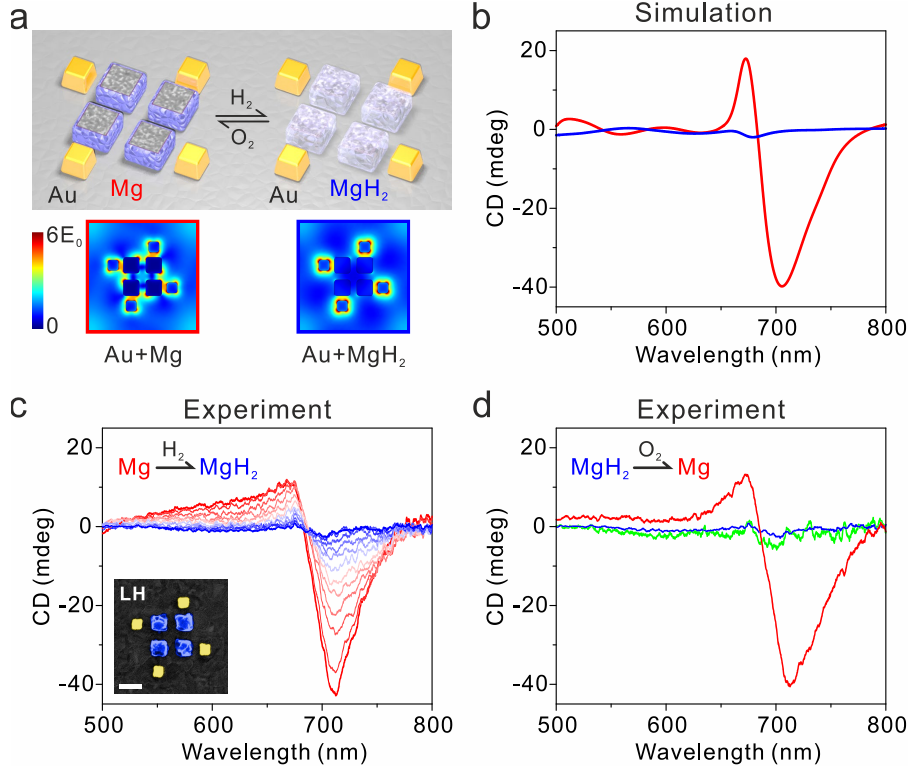


**Figure 3.3** (a) Working principle of hydrogen-regulation to the chiroptical response. Simulated field distributions of the hybrid structure before and after hydrogen loading. The snapshots are obtained at 700 nm, where is the resonance position of the plasmonic metamolecule. (b) Simulated CD spectra of the hybrid structure before (red) and after (blue) hydrogen loading. (c) Evolution of the measured CD spectra of the left-handed sample upon hydrogen loading over time. The CD spectra are continuously recorded with an interval of 10 min. The distinct CD response (thick red) is switched off (see the thick blue line) by 0.25 vol. % hydrogen after 100 min. The scale bar in the SEM image is 200 nm. (d) Dehydrogenation of the left-handed sample in ambient air. The featureless CD spectrum (blue) can be recovered after 27 hours (see the red line). The CD spectrum in green is measured after the sample has been cycled through hydrogen loading/unloading three times, followed by being exposed to ambient air for one week.

Upon hydrogen loading, Pd catalyzes the dissociation of hydrogen molecules into hydrogen atoms, which then diffuse through the Ti spacer into the Mg particle.<sup>135,136</sup> Subsequently, the center four Mg particles are hydrogenated into MgH<sub>2</sub>, undergoing a phase-transition from metal to dielectric.<sup>94</sup> As a result, the plasmonic metamolecule becomes achiral, giving rise to a featureless CD spectrum (see the blue line in **Figure 3.3 b**). The corresponding field distribution reveals that only the four far-spaced Au particles are excited in this case.

The dynamics of hydrogen-regulation to the chiroptical response is investigated by placing the respective samples in a custom gas cell and measuring the CD spectra with a Jasco-1500 CD spectrometer in real time at room temperature. As shown in **Figure 3.3 c**, before hydrogen loading, the left-handed sample exhibits a distinct bisignated spectral profile (see the thick red line), which agrees well with the simulated spectrum in **Figure 3.3 b**. Then, the sample is exposed to 0.25 vol. % hydrogen (in nitrogen carrier gas). The

CD spectra are continuously recorded with an interval of 10 min. It is observed that the CD strength shows successive decrease over time until the bisignated spectral profile vanishes eventually (see the thick blue line in **Figure 3.3 c**). The whole hydrogenation process takes approximately 100 min to complete at a hydrogen concentration of 0.25 vol. %. In this regard, the chiroptical response of the plasmonic metamolecules can be dynamically switched off by hydrogen.

Previously, it has been demonstrated that hydrogen can be unloaded from Mg-based films in the presence of oxygen<sup>134-136</sup>. Such oxidative dehydrogenation has also recently been observed in Mg nanoparticles that were exposed to oxygen in nitrogen carrier gas<sup>29</sup>. To provide deeper insight into dehydrogenation of Mg nanoparticles under realistic environment conditions, the hydrogenated left-handed sample is exposed to ambient air at room temperature. For a direct comparison, the CD spectrum presented by the thick-blue line in **Figure 3.3 c** is replotted in **Figure 3.3 d**, as it is the starting curve for the dehydrogenation process. It is observed that hydrogen unloading from the Mg particles proceeds quite slowly. The measured intermediate CD spectra can be found in **Figure 3.4**. The chiroptical response of the plasmonic metamolecules can be recovered after 27 hours in ambient air. The recovered CD spectrum (see the red line in **Figure 3.3 d**) exhibits slight alterations, when compared to that in **Figure 3.3 c** (see the thick red line). This is due to morphology changes of the Mg particles through hydrogenation and dehydrogenation processes, which will be discussed in detail later.

Subsequently, the left-handed sample is exposed to hydrogen for the second cycle. It turns out that 0.25 vol. % hydrogen cannot introduce rapid CD changes any longer. A higher hydrogen concentration of 0.5 vol. % is then utilized. The chiroptical response is gradually switched off after 120 min (see **Figure 3.4**), longer than the operation time in the first cycle, where even hydrogen at a half concentration is applied. This reflects a substantial influence of the morphology changes of the Mg particles on the hydrogen loading efficiency. The sample is then placed in ambient air for dehydrogenation again. The recovered chiroptical response shows degradation compared to that in the first cycle. In the third cycle, a higher hydrogen concentration of 2.0 vol. % is needed to switch off the chiroptical response after approximately 60 min (see **Figure 3.4**). The experimental results from these three cycles unambiguously indicate a close relationship between the hydrogen concentration and the switching dynamics of the plasmonic metamolecules, which warrants further investigation.

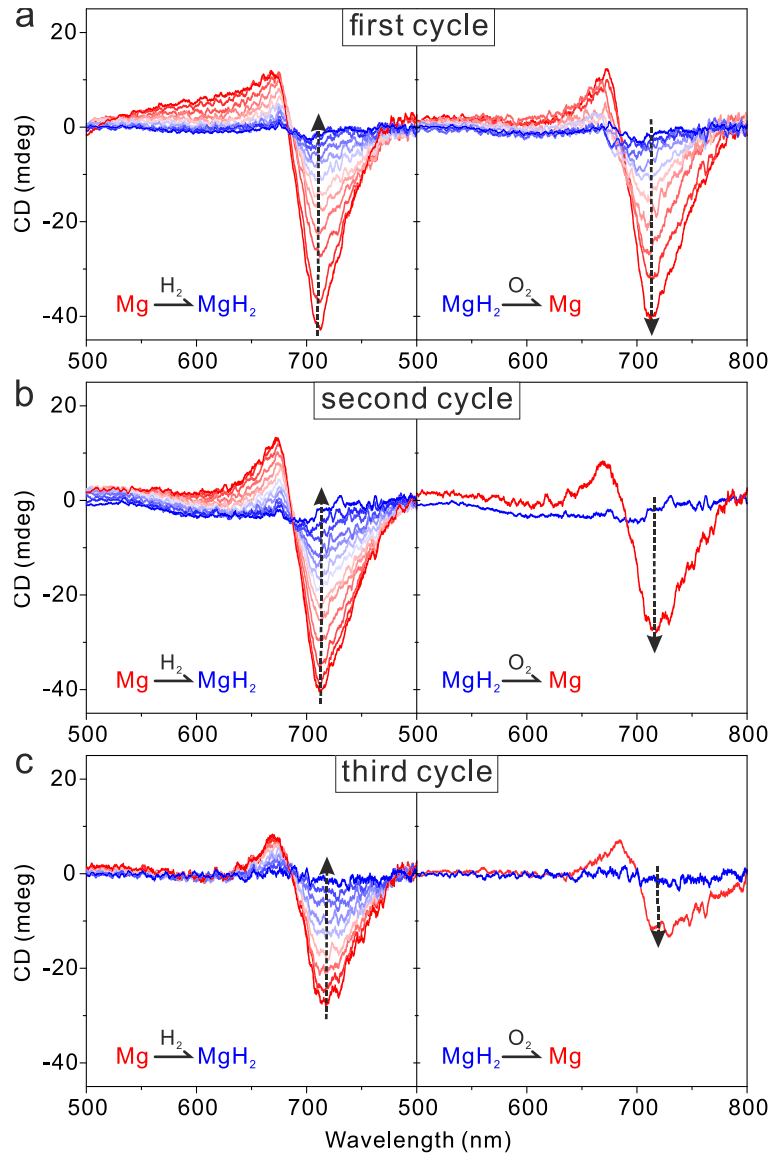


**Figure 3.4** Hydrogen loading/unloading in a left-handed sample in three cycles. The hydrogen concentrations used in the three cycles are 0.25%, 0.5%, and 2.0 %.

To corroborate our results, several control experiments have been performed. The CD response of an achiral sample, where the four Au particles are positioned along the center gaps between the four Mg particles is first examined. As shown in **Figure 3.5 a**, hydrogen loading does not introduce significant influence on the achiral sample. The negligible CD features come from the alignment imperfection between the Au and Mg particles during sample fabrication. Furthermore, as shown in **Figure 3.5 b**, the four satellite Au particles and the four Mg particles alone exhibit unstructured and noisy CD spectra. They do not respond to hydrogen loading.

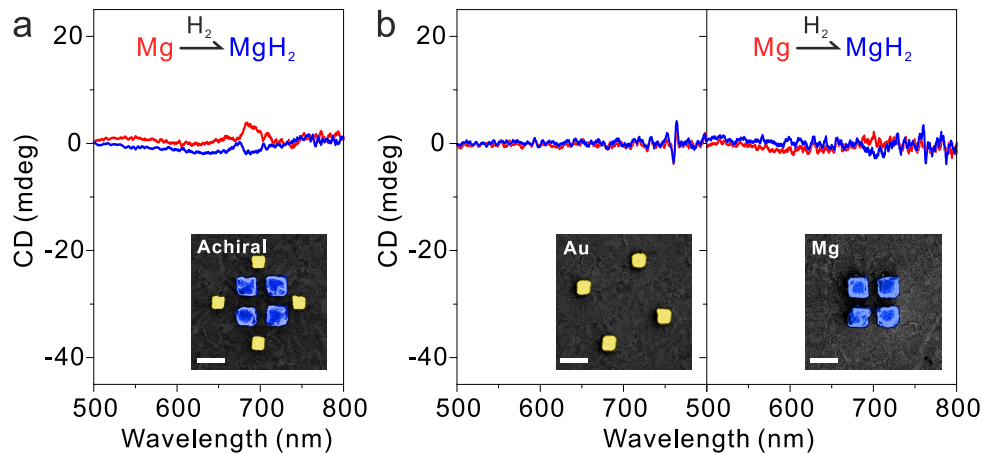


**Figure 3.5** Samples in control experiments before (red) and after (blue) hydrogen loading. The applied hydrogen concentration is 3%. (a) Achiral sample. (b) Satellite Au particles. (c) Centered Mg particles. All these samples do not show substantial response to hydrogen loading. The scale bars in the SEM images are 200 nm.

Finally, a chiral sample composed of pure Mg particles is investigated and the results can be found in **Figure 3.6**. In principle, it can also serve for generating hydrogen-regulated chiroptical response, however, associated with a much weaker CD magnitude and therefore lower sensitivity, when compared to the Au particle assisted scheme (see **Figure 3.3**).

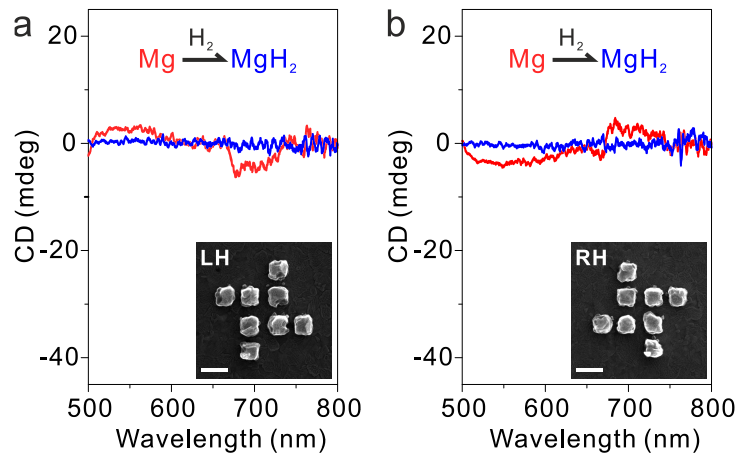


**Figure 3.6** (a) Left-handed and (b) right-handed samples with eight Mg particles ( $160\text{ nm} \times 160\text{ nm} \times 75\text{ nm}$ ) before (red) and after (blue) hydrogen loading. The applied hydrogen concentration is 3.0 %. 5 nm Ti, and 10 nm Pd are capped on the Mg particles. The scale bars in the SEM images are 200 nm.

### 3.5. Switching dynamics

To further investigate the relationship between the hydrogen concentration and the switching dynamics of the plasmonic metamolecules, CD spectra of two identical samples

in right-handedness are measured using a time-scan function of the CD spectrometer in real time. A representative CD spectrum is shown by the red line in the inset of **Figure 3.7**.

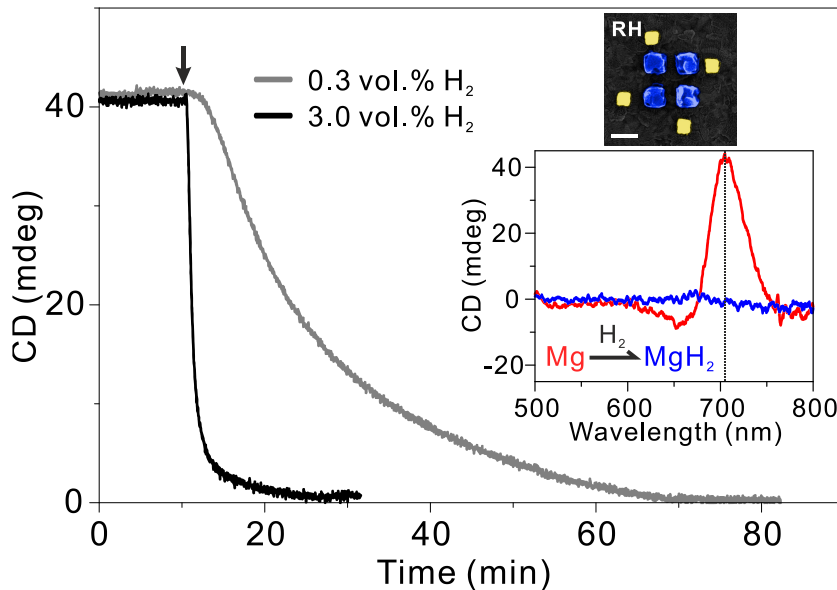


**Figure 3.7** Switching dynamics of the hybrid plasmonic metamolecules at different hydrogen concentrations. The CD spectra of two identical samples in right-handedness are recorded using a time-scan function of the CD spectrometer at a fixed wavelength of 705 nm in real time. The measured CD spectra before and after hydrogen loading are shown by the red and blue lines in the inset, respectively. A representative SEM image of the right-handed structure is also shown in the inset. The scale bar in the SEM image is 200 nm.

It displays a dip-to-peak line shape, which is mirrored to the CD spectrum of the left-handed sample in **Figure 3.3 b**. The two right-handed samples are exposed to 0.3 vol. % and 3.0 vol. % hydrogen, and the corresponding CD spectra are recorded at a fixed wavelength of 705 nm, respectively. The results are shown in **Figure 3.7**, where several interesting features are observed. First, at a low concentration of 0.3 vol. %, a short accumulation time ( $\sim 2$  min) is lapsed, before the system starts to respond to hydrogen, whereas at a high concentration of 3.0 vol. %, the response to hydrogen loading is almost instant, giving rise to an abrupt CD change. Second, in stark contrast to Pd hydrogenation, which is totally concentration dependent, Mg hydrogenation at different concentrations, can reach the same ending hydride state, as long as the hydrogen loading time is sufficient. The chiroptical response is switched off after 25 min and 70 min at hydrogen concentrations of 3.0 vol. % and 0.3 vol. %, respectively. The featureless CD spectrum after hydrogenation is presented by the blue line in the inset of **Figure 3.7**.

### 3.6. Durability in ambient air

To provide deeper insight into the hydrogen loading efficiency change, the left-handed sample exposed to ambient air for one week after three cycles of hydrogen loading/unloading has been examined by EDX. A fresh left-handed sample has also been analyzed together for a direct comparison. EDX mapping offers a detailed illustration of

the present elements and their localization in the samples. The EDX results for the fresh and used samples are shown in **Figure 3.8** a and b, respectively.

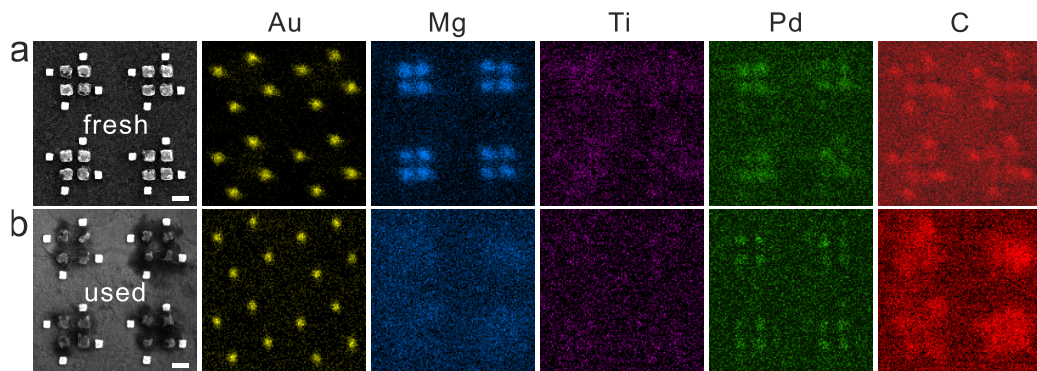


**Figure 3.8** EDX mapping of the (a) fresh and (b) used left-handed samples. The left-handed sample has been cycled through hydrogen loading/unloading three times, followed by exposure to ambient air for one week. The scale bars in the SEM images are 200 nm.

It is evident that Au, Ti, and Pd do not really show dissimilarity between the two samples, whereas Mg exhibits remarkable transformations. More specifically, in the fresh sample, the EDX signal of Mg from the centered four particles is very distinct and localized. On the contrary, in the used sample, the EDX signal of Mg becomes largely spread out. This is likely due to cracking of the Mg particles, resulting from significant hydrogen-induced expansion and contraction (32%).<sup>94</sup> Consequently, the Mg particles become brittle and prone to be fragmented over the surroundings. Meanwhile, chemical compounds containing considerable carbon are found to accumulate around the central areas, where the four Mg particles are located originally. It is known that Mg, as a chemically active material, can be involved in several gaseous reactions. In ambient air, Mg can form magnesium oxides with oxygen, magnesium hydroxycarbonate with carbon dioxide, and possibly becomes hydroxylated due to formation of brucite in a humid environment.<sup>95,144</sup> These Mg-based chemical compounds may first form on the particle surfaces in ambient air. Along with the cracking, the inner part of the particles is also gradually decomposed into Mg-based chemical compounds.

As a result, the chiroptical response of the plasmonic metamolecules is eventually switched off as shown by the green line in **Figure 3.3** c. This CD spectrum is measured after the left-handed sample has been cycled through hydrogen loading/unloading three times, followed by being exposed to ambient air for one week. It is noteworthy that if the hydrogenated Mg particles were exposed to oxygen in nitrogen carrier gas, due to the formation of magnesium oxide, certain morphological changes would still exist, resulting from repetitive structural expansions and contractions during hydrogenation and dehydrogenation processes.

### 3.7. Conclusion

In conclusion, we have demonstrated hybrid plasmonic metamolecules, which allow for hydrogen-regulated chiroptical response in the visible range. The switching dynamics has been investigated using CD spectroscopy in real time. The chiroptical response of the plasmonic metamolecules can be switched on/off through hydrogen unloading/loading in cycles. In addition, EDX mapping has been carried out to investigate the morphology changes of the Mg particles placed in ambient air after hydrogen loading/unloading in cycles. Our results suggest that due to its active chemical reactivity, Mg could be used as plasmonic sensors for humidity, carbon dioxide, and hydrogen detection, given specific surface protection is taken into consideration. Also, different from Pd and Y, which release the stored hydrogen as soon as hydrogen in the environment drops, Mg can preserve its stored hydrogen, as long as oxygen is absent at room temperature. Therefore, Mg can be retained at any hydrogenated state between fully metallic and fully dielectric. In this regard, our chiral plasmonic platform could enable the realization of dynamically tunable circular polarizers and polarization modulators regulated by hydrogen.

## 4. Dynamic display based on Mg nanoparticles

Plasmonic colour printing based on engineered metasurfaces has revolutionized colour display science due to its unprecedented subwavelength resolution and high-density optical data storage. However, advanced plasmonic displays with novel functionalities including dynamic multicolour printing, animations, and highly secure encryption have remained in their infancy. Here we demonstrate a dynamic plasmonic colour display technique which enables all the aforementioned functionalities using catalytic magnesium metasurfaces. Controlled hydrogenation and dehydrogenation of the constituent magnesium nanoparticles, which serve as dynamic pixels, allow for plasmonic colour printing, tuning, erasing, and restoration of colour. Different dynamic pixels feature distinct colour transformation kinetics, enabling plasmonic animations. Through smart material processing, information encoded on selected pixels, which are indiscernible to both optical and scanning electron microscopies, can only be read out using hydrogen as a decoding key, suggesting a new generation of information encryption and anti-counterfeiting applications.

This chapter is adapted with permission from “Duan, X.; Kamin, S.; Liu, N. Dynamic plasmonic colour display. *Nat. Commun.* **2017**, *8*, 14606.”

## 4.1. Introduction to plasmonic display

Plasmonic colour printing based on engineered metasurfaces has revolutionized colour display science due to its unprecedented subwavelength resolution and high-density optical data storage.<sup>7,48</sup> However, advanced plasmonic displays with novel functionalities including dynamic multicolour printing, animations, and highly secure encryption have remained in their infancy. Here we demonstrate a dynamic plasmonic colour display technique which enables all the aforementioned functionalities using catalytic magnesium metasurfaces. Controlled hydrogenation and dehydrogenation of the constituent magnesium nanoparticles, which serve as dynamic pixels, allow for plasmonic colour printing, tuning, erasing, and restoration of colour. Different dynamic pixels feature distinct colour transformation kinetics, enabling plasmonic animations. Through smart material processing, information encoded on selected pixels, which are indiscernible to both optical and scanning electron microscopies, can only be read out using hydrogen as a decoding key, suggesting a new generation of information encryption and anti-counterfeiting applications.

Plasmonic colour generation based on metallic metasurfaces has suggested an exciting new route towards producing colour images with resolution far beyond the limit of current display technologies.<sup>33,39,45,47-49,145,146</sup> Although in its infancy, significant advances in plasmonic colour generation have been accomplished including the realization of colour displays at the optical diffraction limit<sup>45,47,48</sup>, scalable full-colour chromotropic printing<sup>39,49,145,146</sup>, actively tunable plasmonic surfaces<sup>33,147-149</sup>, plasmonic colour laser printing<sup>46</sup>. Apart from these primary applications, plasmonic colour display technology also features great potentials in stereoscopic imaging<sup>150</sup>, high-density data storage<sup>150,151</sup>, and anticounterfeiting applications<sup>49,57</sup>. Nevertheless, the fast development of this field inevitably calls for plasmonic displays with advanced functionalities, for example, dynamic multicolour printing, animations, and highly secure encryption.

In this Chapter, we demonstrate a dynamic plasmonic display technique based on catalytic Mg metasurfaces. Different from other hydrogen-storage metals such as palladium (Pd)<sup>68</sup> and yttrium<sup>138</sup>, which are associated with poor optical response, Mg exhibits excellent plasmonic properties at high frequencies<sup>23,94,116,152</sup>. For example, Mg nanostructures have been used for chiral sensing in the UV spectral range and for hydrogen sensing in the visible spectral range<sup>116,152</sup>. Most importantly, the unique hydrogenation/dehydrogenation kinetics of Mg nanoparticles is ideally suited for creating dynamic plasmonic systems. Here, we demonstrate successively plasmonic microprint displays with high reversibility, plasmonic animations with subwavelength resolution, and highly secure plasmonic encryption. Our work will stimulate fascinating colour display applications utilizing plasmonic dynamic pixels with nanoscale controllability.

## 4.2. Working principle of the dynamic plasmonic colour display

The concept of our dynamic plasmonic colour display technique is illustrated in **Figure 4.1**. The dynamic plasmonic pixels comprise Mg nanoparticles, which are sandwiched between titanium (Ti)/Pd capping layers and a Ti adhesion layer. These particles reside on a silicon dioxide film (100 nm) supported by a silicon substrate. In order to render a palette of colours with a broad range, stepwise tuning of the lateral particle size  $s$  and the interparticle distance  $d$  is employed. Each square (10  $\mu\text{m}$ ), which presents a characteristic colour, contains Mg particles that are arranged in a lattice with periodicity of  $s$  and  $d$ .

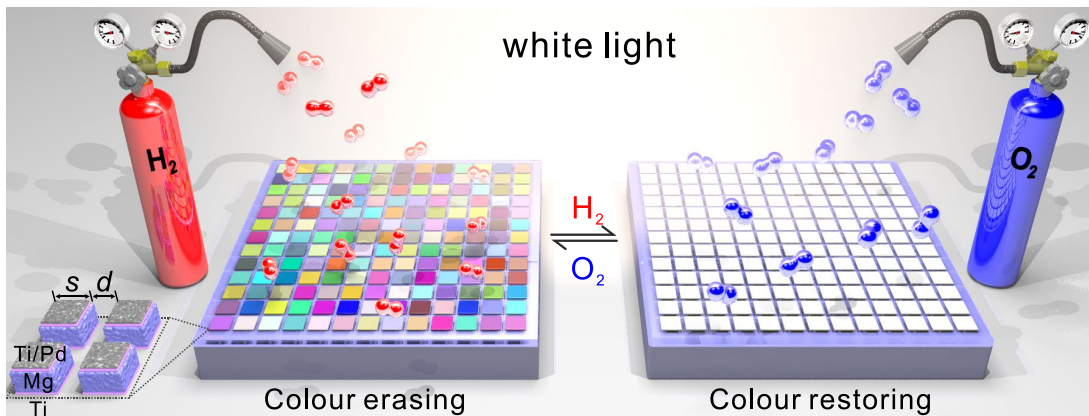


**Figure 4.1** Schematic of the plasmonic metasurface composed of hydrogen-responsive Mg nanoparticles interacting with incident unpolarized white light. These Mg nanoparticles are sandwiched between Ti/Pd capping layers and a Ti adhesion layer. In each colour square (10  $\mu\text{m}$ ), they are arranged in a lattice with a period of  $s+d$  along both directions.  $s$  and  $d$  are the size of the square-shaped particles and the interparticle distance, respectively. The colours of the plasmonic metasurface can be erased upon hydrogen exposure through phase-transition from Mg to MgH<sub>2</sub>. The colours can be restored upon oxygen exposure through transformation of MgH<sub>2</sub> back to Mg.

The brilliant colours from the palette can be revealed using reflection bright-field microscopy as shown in **Figure 4.2**. The charge-coupled device (CCD) image of the palette is captured using a 20  $\times$  objective with a numerical aperture (N.A.) of 0.4. The spectral analysis of the representative colour squares (indicated by the individual horizontal and vertical boxes in **Figure 4.2**) is carried out and presented in **Figure 4.3**. The scanning electron microscopy (SEM) images of the corresponding structures are also included in the same figure. Enlarged SEM images of the representative structures can be found in **Figure 4.4**. When  $d$  increases successively ( $s = 150$  nm), a wide range of colours are observed (see **Figure 4.3 a**). The reflectance peak exhibits evident red-shifts (see the red-dashed line) with increasing  $d$  and thus the periodicity,  $s + d$ . The corresponding simulated reflectance spectra presented by the blue-dotted lines show an overall good agreement with respect to the experimental spectra. The simulated colours using the simulated reflectance spectra and the Commission Internationale de l'Éclairage (CIE) 1931 colour matching functions agree well with the observed colours. On the other hand, when  $s$  increases successively ( $d = 300$  nm), colour tuning is less dramatic (see **Figure 4.3 b**). The reflectance peak experiences red-shifts (see the red-dashed line) with increasing  $s$ . Meanwhile, a new reflectance peak is observed at shorter wavelengths. The corresponding simulated spectra

presented by the blue-dotted lines and the simulated colours both agree well with the experimental results.

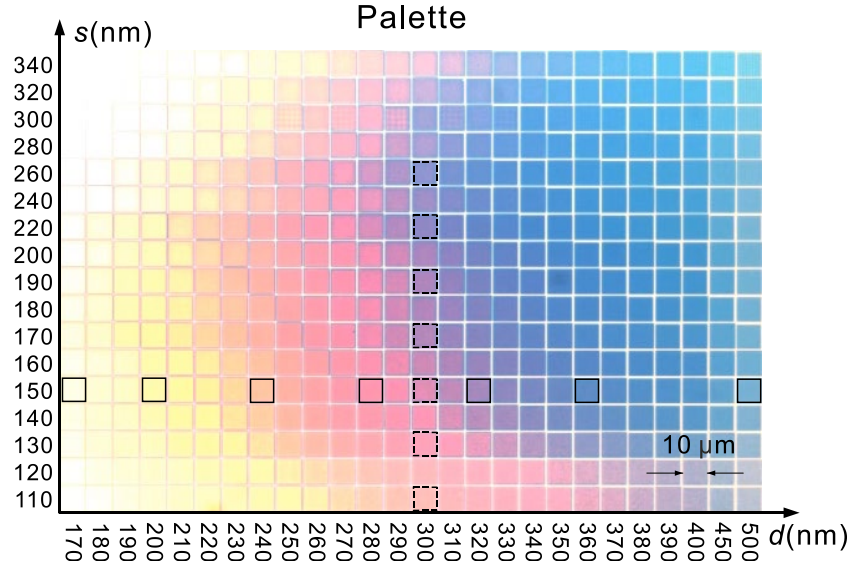


**Figure 4.2** Colour palette obtained by stepwise tuning of  $s$  and  $d$ .

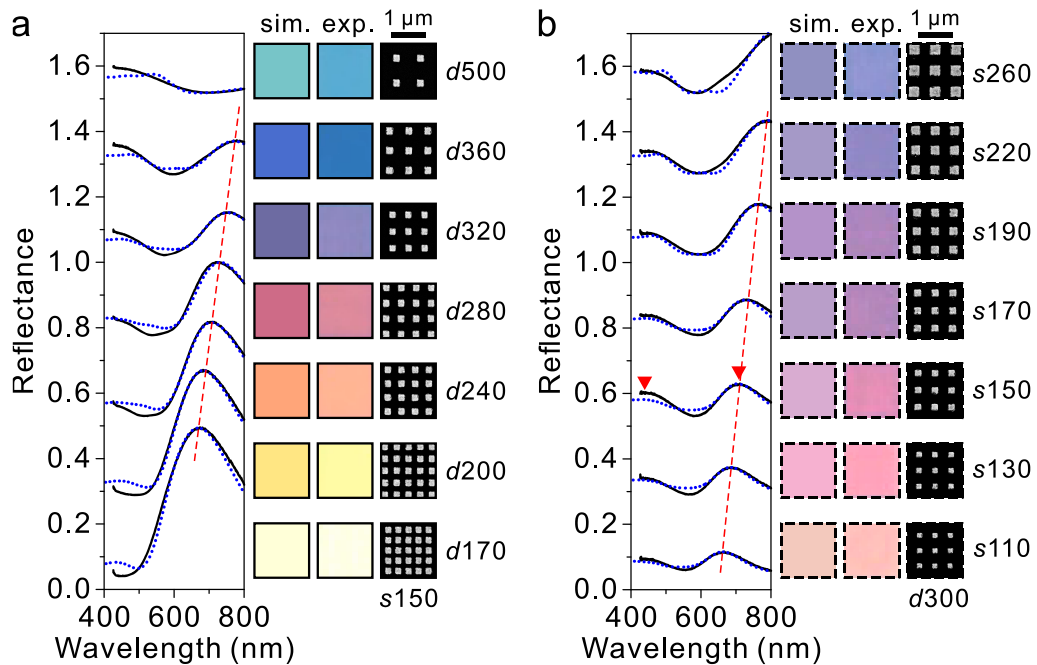


**Figure 4.3** Experimental (black) and simulated (blue-dotted) reflectance spectra of the colour squares selected from **Figure 4.2**. The spectral curves are shifted upwards for clarity. In (a)/(b), the selected colours correspond to those indicated using solid/dashed squares along the horizontal/vertical direction in **Figure 4.2**. Experimental and simulated colours as well as the corresponding SEM images of the structures. The red dashed line indicates the shift of the reflectance peak.

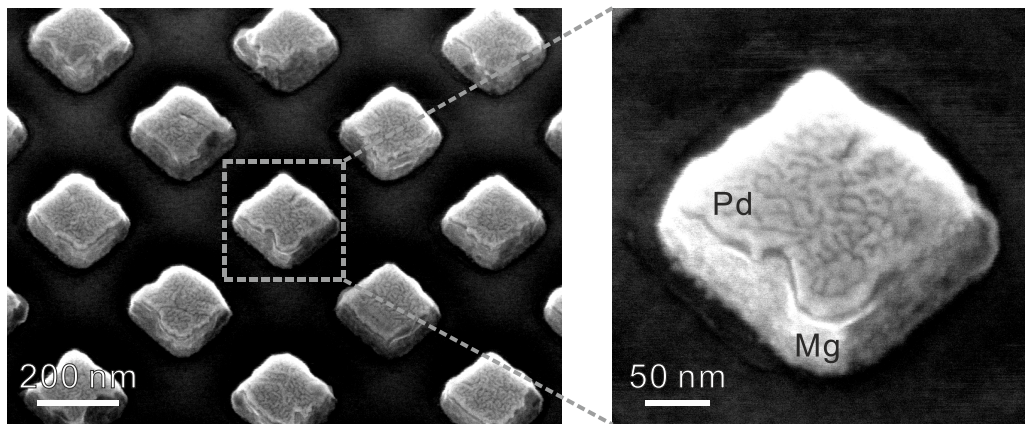


**Figure 4.4** Enlarged SEM images of the representative Mg nanostructures.

To elucidate the underlying physics of the observed spectral characteristics, contour maps of the resonance positions in dependence on  $d$  (see **Figure 4.5 a**) and  $s$  (see **Figure 4.5 b**) were calculated, respectively. The contributions from the localized surface plasmon resonances (LSPRs)<sup>3,29</sup> of the individual Mg nanoparticles and the Rayleigh-Wood anomalies (RAs) of the particle arrays are indicated using black and white lines, respectively. The analytical dispersion curves of the RAs are given by

$$\lambda_{\text{RA}} = \frac{(s + d)}{m} \sqrt{\varepsilon_d} \quad (4.1)$$

where  $\varepsilon_d$  is the permittivity of the corresponding dielectric layer,  $m$  is an integer, signifying the order of the resonance, and  $s+d$  is the periodicity of the array. The LSPR positions were calculated using FEM simulations based on single particles.

As shown in **Figure 4.5 a** and **b**, the longer-wavelength reflectance peak located in between the black and white-solid lines is associated with a hybrid plasmonic mode<sup>31</sup>, which stems from the excitations of the LSPR and the RA for the Mg/SiO<sub>2</sub> interface. The RA for the air/Mg interface is presented by the white-dotted line.

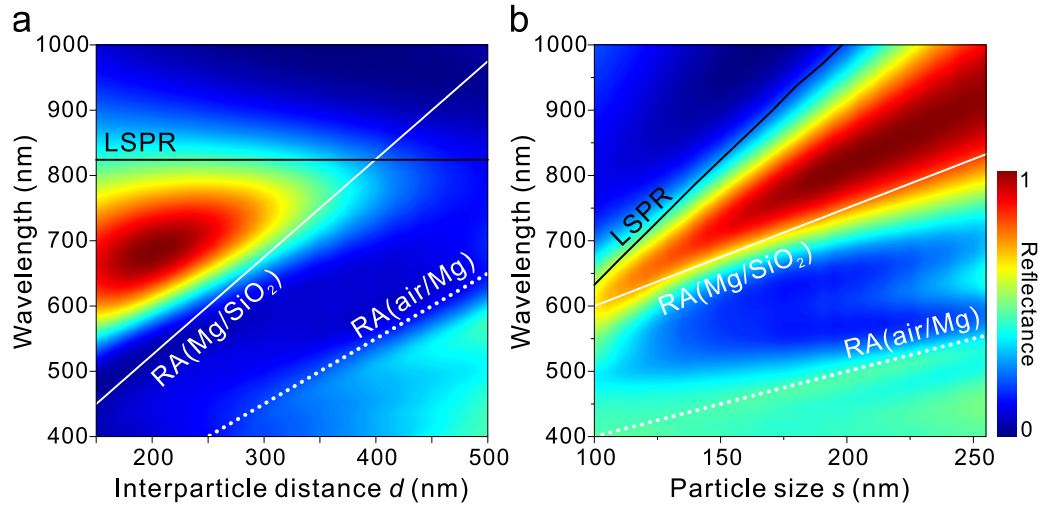


**Figure 4.5** (a) Simulated contour map of the reflectance peak positions in dependence on  $d$  ( $s = 150$  nm). (b) Simulated contour map of the reflectance peak positions in dependence on  $s$  ( $d = 300$  nm). The black line indicates the LSPR modes. The white-solid and white-dotted lines indicate the RAs for the Mg/SiO<sub>2</sub> and air/Mg interfaces, respectively.

To provide deeper insights into the mechanisms of the plasmonic modes, as a representative example, electric field and charge distributions at the respective resonance positions (indicated by the red arrows in the right plot in **Figure 4.3**) for the colour square ( $s150, d300$ ) were calculated. At the resonance of 710 nm, the charge distribution reveals the excitation of a dipolar LSPR mode in the Mg nanoparticle (see **Figure 4.6 a**). The corresponding electric field distribution demonstrates that the electric fields are confined at the corners of the particle near the Mg/SiO<sub>2</sub> interface. At the resonance of 430 nm, the charge distribution reveals the excitation of a quadrupolar LSPR mode (see **Figure 4.6 b**). The associated electric fields are localized at the corners of the particle near the air/Mg interface.

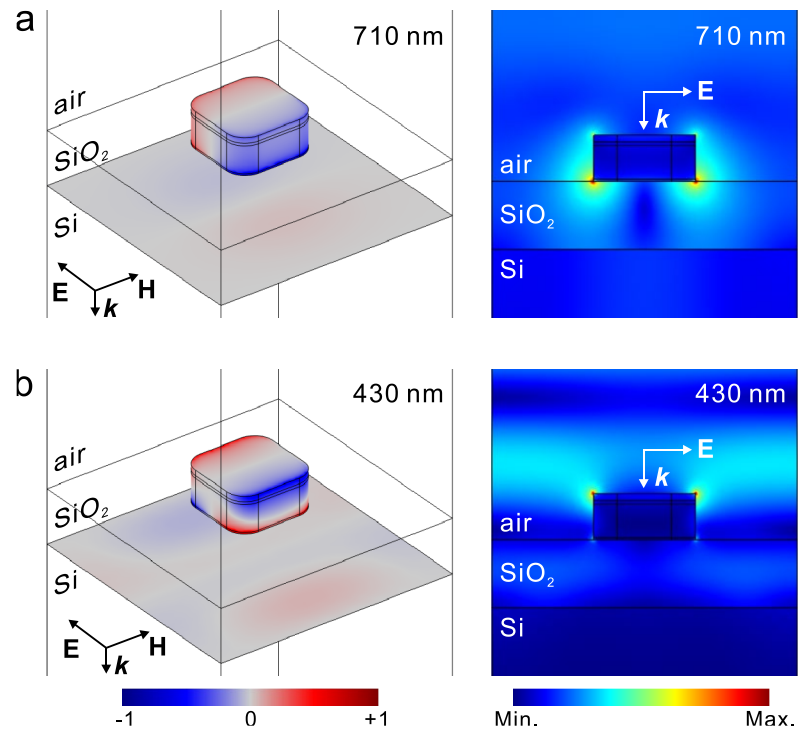


**Figure 4.6** Simulated charge and electric field distributions at 710 nm (a) and 430 nm (b).  $s = 150$  nm and  $d = 300$  nm.

The dynamic behaviour of the plasmonic pixels is enabled by the unique phase-transition of Mg in response to hydrogen<sup>85,89,134,135,153,154</sup>. Mg can absorb up to 7.6 wt % of hydrogen and subsequently undergoes a metal-to-dielectric transition to form magnesium hydride ( $MgH_2$ ).<sup>85</sup> This remarkable capacity surpasses all known reversible metal hydrides in hydrogen uptake capability. Upon hydrogen exposure, the Pd capping layer catalyzes the dissociation of hydrogen molecules into hydrogen atoms, which then diffuse through the Ti capping layer into the Mg particle<sup>94,135,152</sup>. The Ti adhesion and capping layers help to release the mechanical stress from volume expansions of Mg (32%) and Pd (11%). The Ti capping layer also plays an important role as spacer to prevent Mg and Pd from alloying<sup>94,152</sup>. Different colour squares undergo a series of vivid colour changes until all colours vanish. The hydrogenation process is rather complicated and essentially associated with a gradual decrease of the metallic fraction of the particles, formation of  $MgH_2$  as dielectric surrounding, and simultaneous hybrid particle volume expansion. Such a catalytic process renders dynamic alterations to the reflectance spectra possible as shown in **Figure 4.7**, thus leading to dynamic colour changes. After hydrogenation, the reflectance spectra become nearly featureless as observed from both the experimental and simulated reflectance spectra in **Figure 4.7 a** and **Figure 4.8**. When all the Mg particles are transformed into  $MgH_2$  particles, the colours of the palette are erased. The optical images of the palette under different illumination intensities can be found in **Figure 4.9**. It is worth mentioning that the colour changing speed during the hydrogenation process can be manipulated by several key parameters including the thickness of the Pd catalytic layer, the hydrogen concentration, and the substrate temperature. In this work, 10 nm Pd, 10%

hydrogen, and room temperature are employed in the different display demonstrations, if not particularly specified.

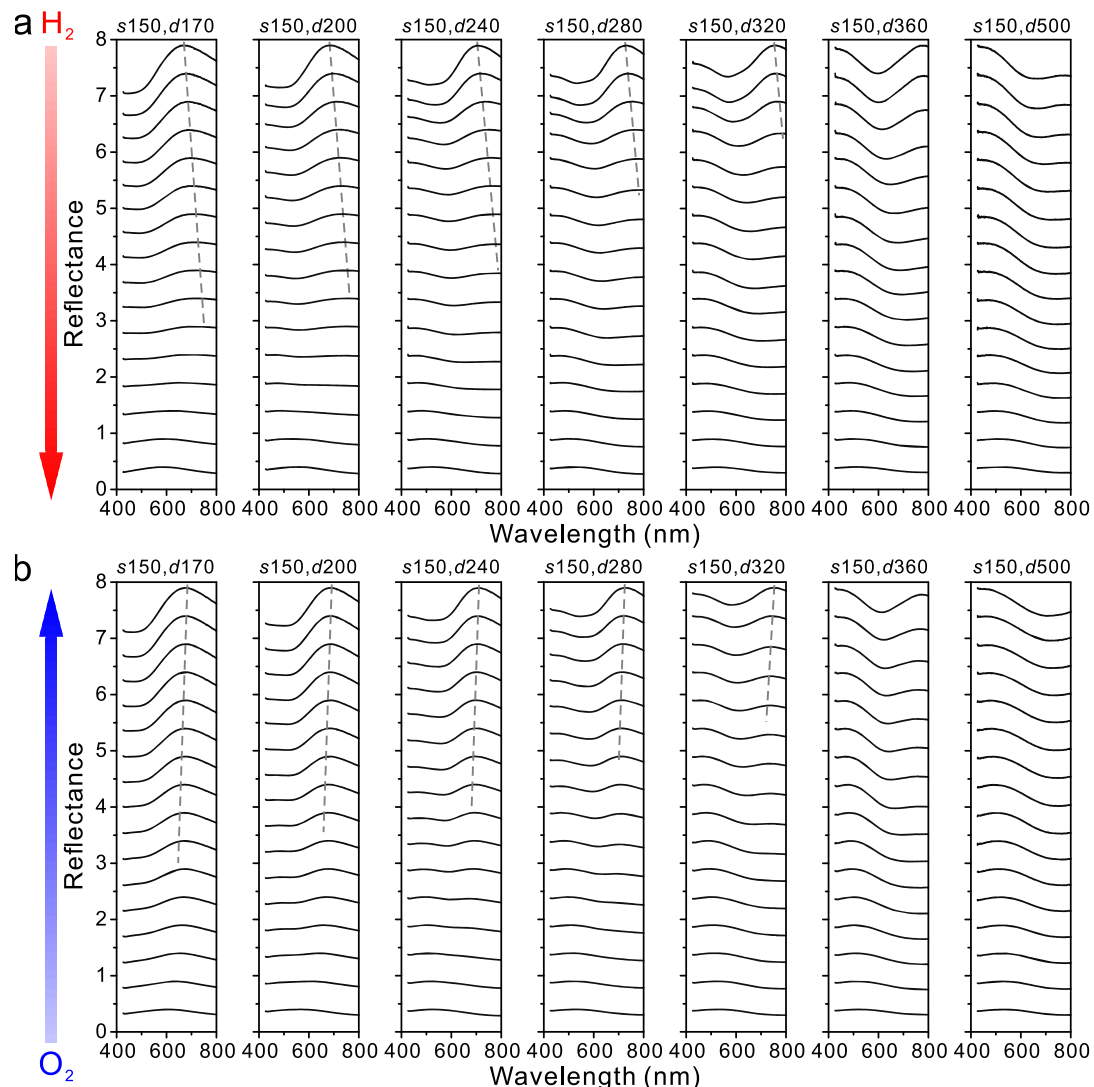


**Figure 4.7** Representative dynamic reflectance spectra recorded during hydrogen (a) and oxygen exposure (b). The dotted lines indicate the positions of the reflectance peaks.

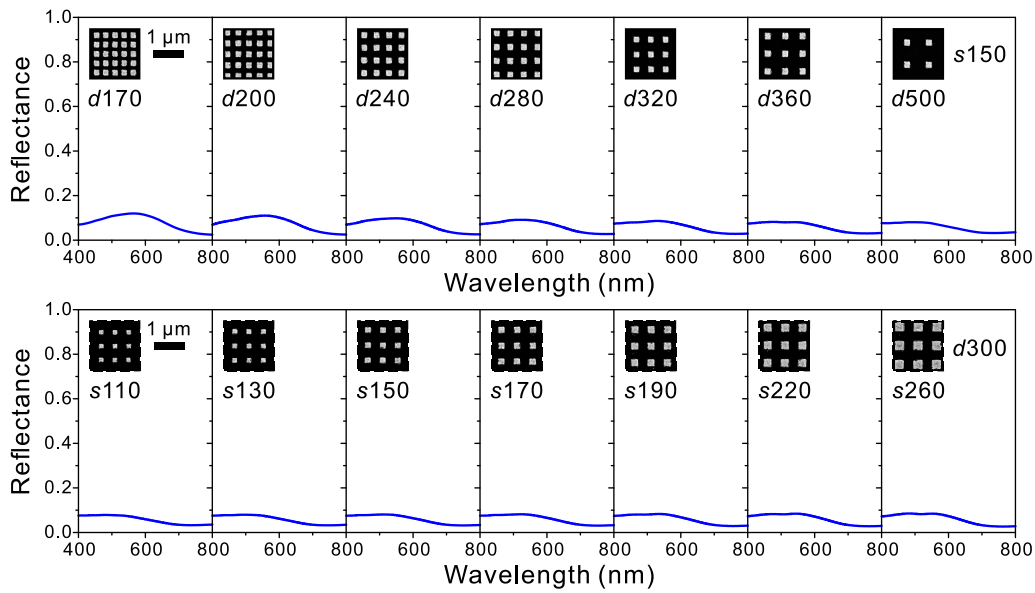


**Figure 4.8** Simulated reflectance spectra of the colour squares in **Figure 4.3** after hydrogenation.

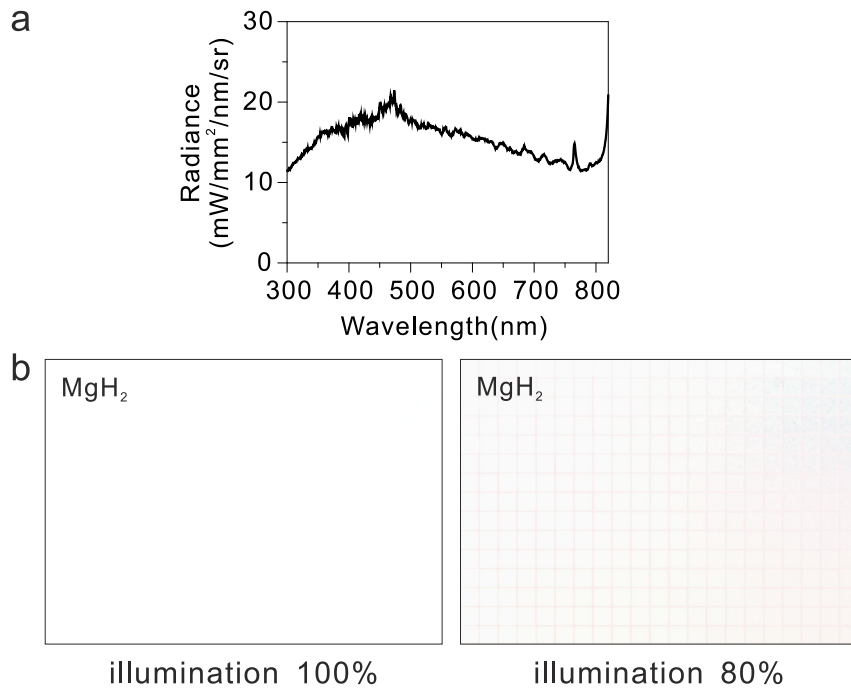


**Figure 4.9** (a) Spectral radiance of the EQ-99 white light source. (b) Optical images of the colour palette after hydrogenation under different illumination intensities. When the illumination intensity is reduced from the full power (100%) to a lower value (80%), colours are observed at areas with large pitches. This issue can be solved by creating individual colour elements with pitches all no larger than 250 nm.

To explore the colour transformation kinetics during hydrogenation, evolutions of the exemplary colour squares are investigated as shown in **Figure 4.10**. The snapshot images were extracted from the movie of **Figure 4.2** and are arranged as a function of  $\ln(t)$ . The top figure in **Figure 4.10** corresponds to the evolution of the colour squares, in which the constituent Mg particles have the same size but different interparticle distances. It

illustrates that smaller interparticle distances are associated with richer colour changes over time, exhibiting a dynamic transition from yellow, red, blue, colour fading to complete colour erasing. In contrast, larger interparticle distances are essentially correlated with a blue colour diminishing process. Interestingly, the erasing times for different colour squares are nearly identical (see the vertical grey-dashed line). The bottom figure in **Figure 4.10** presents the evolution of the colour squares, in which the Mg particles have the same interparticle distance but different sizes. The erasing times differ significantly for different colour squares as indicated by the slanted grey-dashed line. Evidently, colour squares that contain smaller Mg particles vanish faster than those composed of larger particles. This elucidates clear size-dependent hydrogenation kinetics of the Mg nanoparticles.

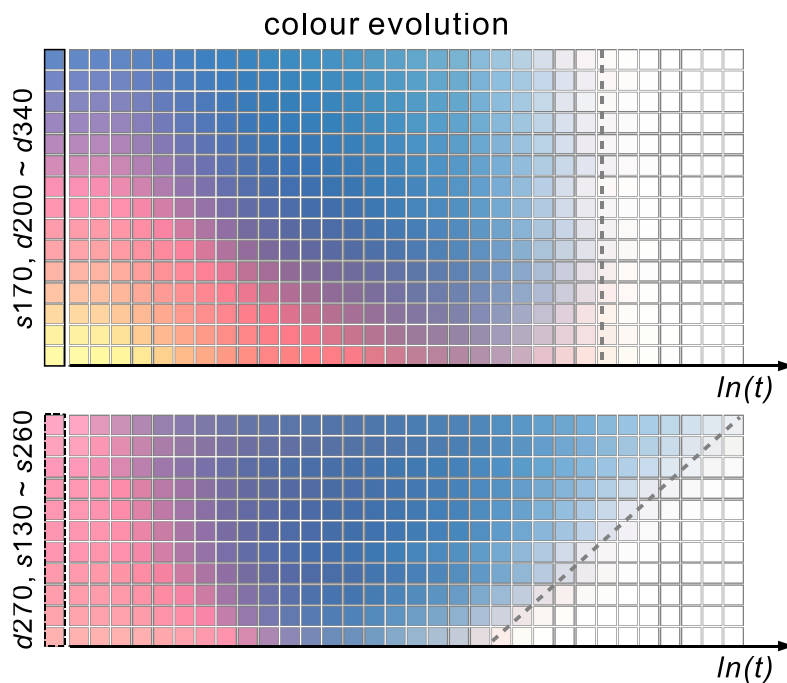


**Figure 4.10** Colour evolutions of the selected colour squares upon hydrogen exposure over time  $\ln(t)$ . The grey-dashed lines indicate the colour vanishing times in the two cases.

Importantly, the erased colours can be restored through dehydrogenation of the Mg particles in the presence of oxygen<sup>94,152</sup>. Such reversible colour transformations are of great importance for dynamic display applications. The dynamic reflectance spectra of the representative colour squares during dehydrogenation can be found in **Figure 4.7 b**. The oxidative dehydrogenation process involves binding of oxygen with the desorbed hydrogen atoms from  $\text{MgH}_2$  to form  $\text{H}_2\text{O}$ .<sup>89,154</sup> This avoids a build-up of hydrogen at the Pd surface, thus facilitating hydrogen desorption. The colours of the palette can be nicely restored. This indicates that the  $\text{MgH}_2$  particles are converted back to Mg particles, therefore displaying brilliant colours again. The dynamic CIE maps for the palette and the selected colour squares in **Figure 4.3** during hydrogenation/ dehydrogenation can be found in **Figure 4.11** and **Figure 4.12**, respectively.

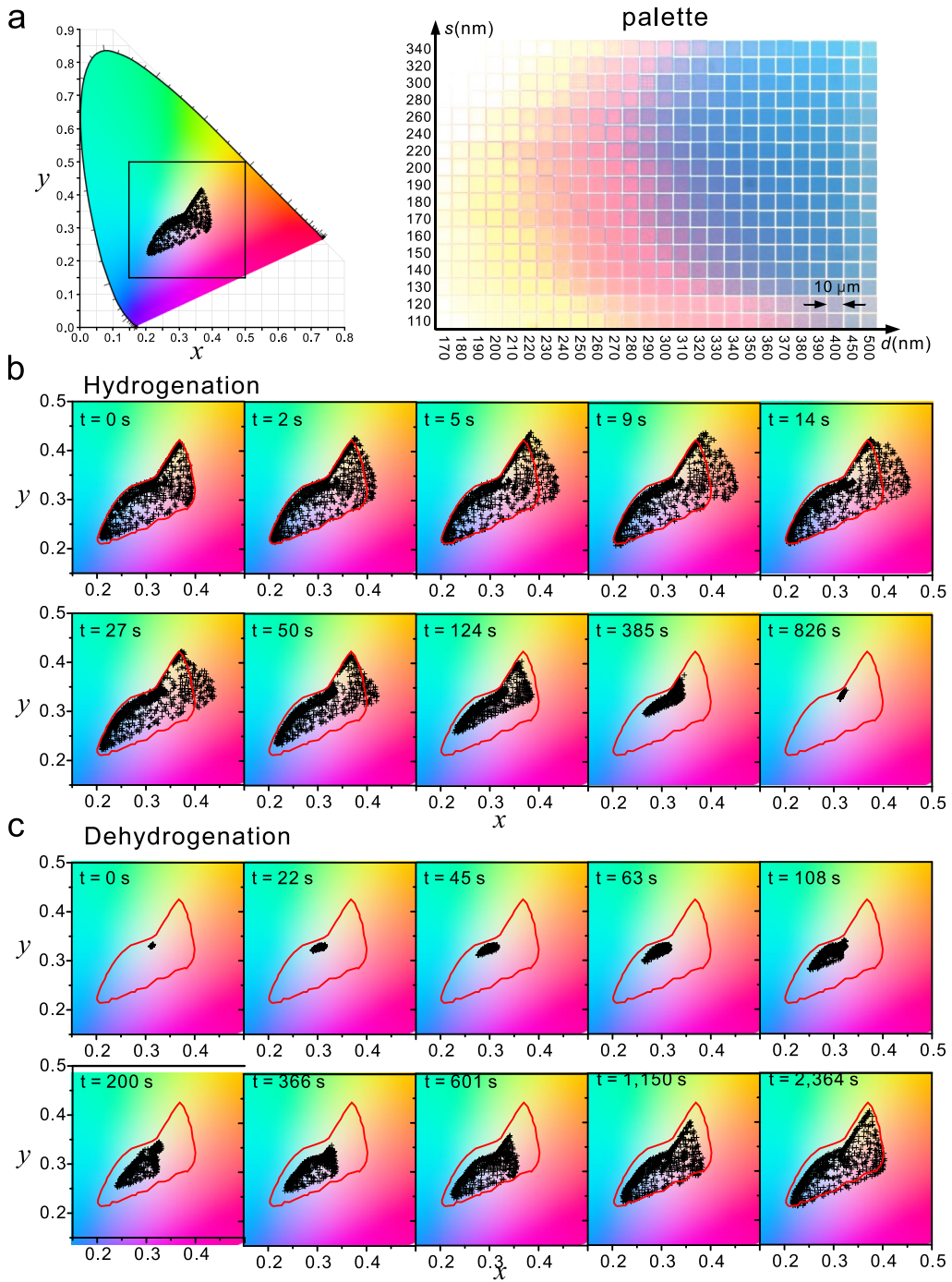


**Figure 4.11** (a) CIE 1931 chromaticity diagram overlaid with all the colours from the palette. The CIE illuminant D65 is used for the conversion to the chromaticity coordinate. Each black cross in the CIE map indicates a colour square from the palette. (b) Evolution of all the palette colours during hydrogenation. Red lines indicate the original colour range. New colours are generated during hydrogenation between  $t = 0$  s and  $t = 50$  s. (c) Evolution of all the palette colours during dehydrogenation.

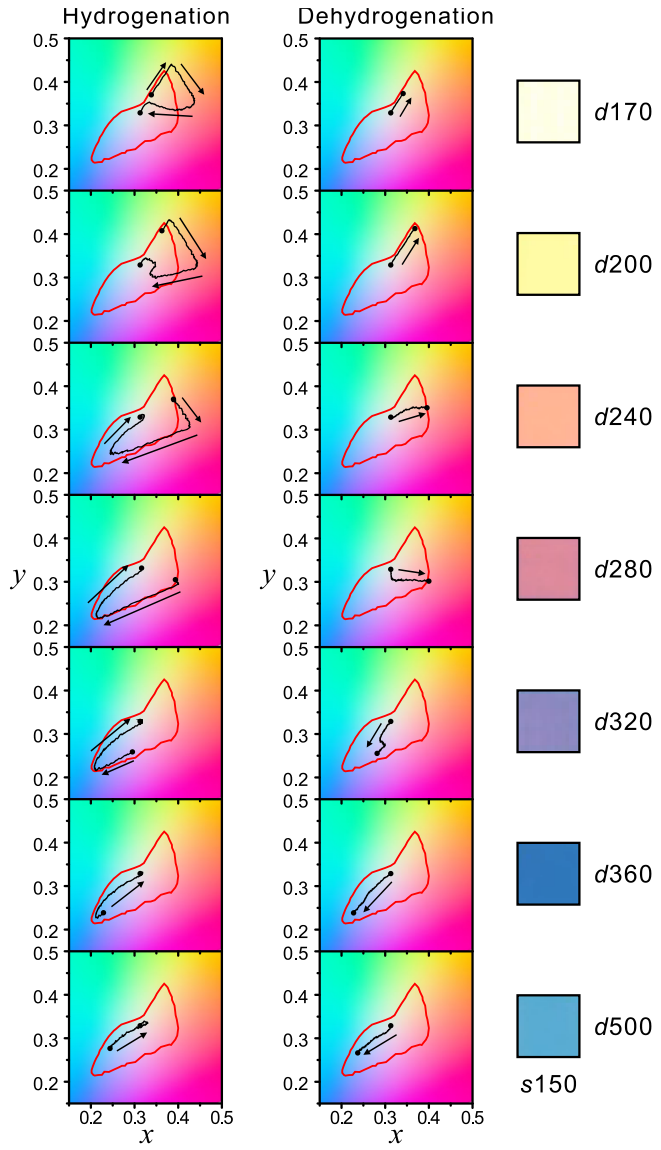


**Figure 4.12** CIE 1931 chromaticity coordinate for the selected seven colours in **Figure 4.3 a.** Black lines represent the pathways of the colour changes during hydrogenation /dehydrogenation.

Hysteresis is observed, when the colours of the palette evolve along the hydrogenation and dehydrogenation pathways, respectively. This is also seen from the recorded dynamic spectra of the selected colour squares as shown in **Figure 4.7**. The hysteresis behaviour can be attributed to the different changes of the particle geometries, the local hydrogen concentrations in the Mg particles, and the propagation directions of the Mg/MgH<sub>2</sub> interfaces during hydrogenation and dehydrogenation, respectively. A simple model has been proposed that after hydrogenation a layer of MgH<sub>2</sub> is formed directly beneath the hydrogenated Ti layer and it proceeds towards the substrate<sup>94</sup>. This results in successive spectral red-shifts due to effective thickness decreases of the Mg particles (see **Figure 4.7 a**). Subsequently, during dehydrogenation the optical spectra exhibit spectral shifts with hysteresis (see **Figure 4.7 b**). A systemic study on the complex hydrogenation and dehydrogenation processes in the Mg particles, for example, using environmental transmission electron microscopy and atomic force microscopy will be highly desirable

for providing an insightful understanding of the local catalytic kinetics in the Mg particles and their correlated dynamic optical spectra.

### 4.3. Dynamic display of the Max-Planck-Society's Minerva logo

Such plasmonic colour tuning, erasing, and restoring based on catalytic metasurfaces open an avenue for a variety of dynamic colour display applications. A direct application is to produce high-quality colour-tunable plasmonic microprints. As a demonstration, the Minerva logo of the Max-Planck Society has been prepared using selected colours and their corresponding matrix numbers from the palette are indicated in **Figure 4.13 a**. A description about the layout generation approach can be found in **Figure 4.14**. A discussion about the N.A. dependence and the angle dependence of the colours can be found in **Figure 4.15**. The representative snapshot images of the selected colour squares during hydrogenation and dehydrogenation are shown in **Figure 4.13 a**. The SEM images illustrating the details of the Minerva logo are presented in **Figure 4.13 b**. **Figure 4.16** shows the performance of the dynamic plasmonic display. Upon hydrogen loading, the Minerva logo undergoes dynamic colour changes with the individual colour blocks following the changing routes of the respective colour squares (see **Figure 4.13 a**). A series of abrupt colour alterations take place within 23 s. Subsequently, the logo starts to fade and completely vanishes after 566 s. Owing to the identical sizing of the constitute Mg nanoparticles, different colours in the logo are erased nearly simultaneously, as discussed in **Figure 4.10**. Upon oxygen exposure, the logo is gradually restored to its starting state without experiencing drastic colour changes. The restoring process takes approximately 2,224 s to complete. To enhance the durability of our samples, exhaustive optimization of the fabrication procedures has been carried out.

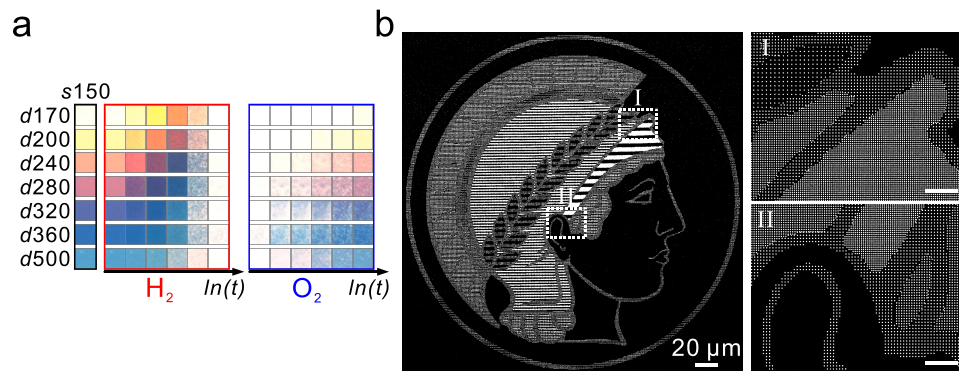


**Figure 4.13** Colour evolutions of the selected colours used to construct the Minerva logo during hydrogenation and dehydrogenation, respectively. **b**, Overview and enlarged SEM images of the Minerva logo. The scale bars in I and II are 5 mm.

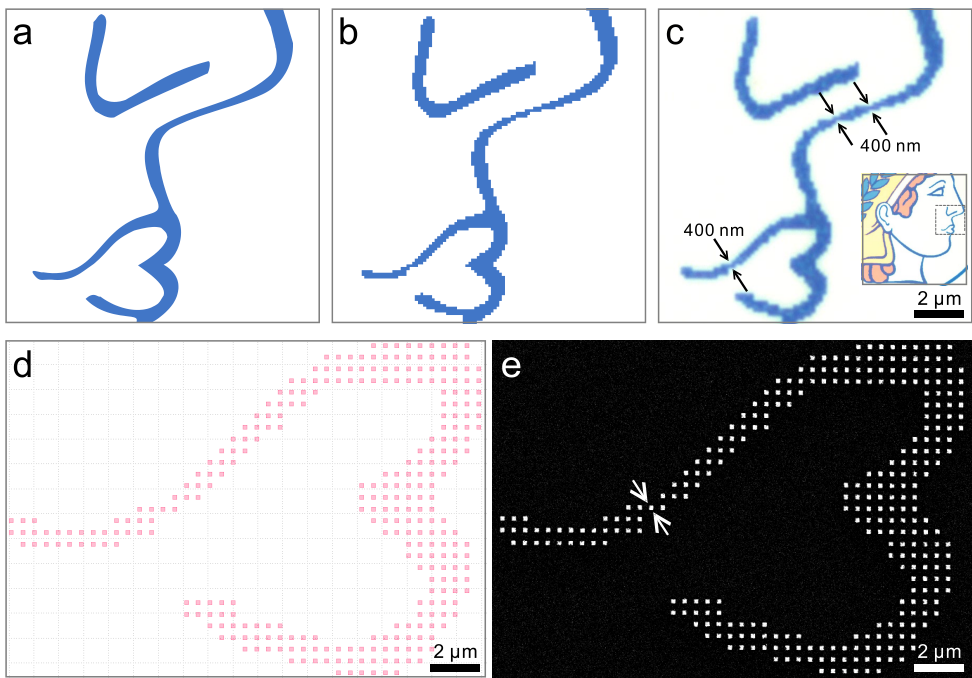


**Figure 4.14** Red, green, and blue (RGB) values for each colour square were extracted from the optical micrograph of the palette in **Figure 4.2**, and this serves as a colour database. Any arbitrary image can be pixelated using a code written in MATLAB. The code extracts the RGB values for each pixel and finds a closest match to a certain  $(s, d)$  from the palette using a CIE L\*a\*b\* space least distance method based on the colour database. (a) Finest part of the MPG's Minerva logo in **Figure 4.13**. (b) Corresponding pixelated image. (c) Optical micrograph of the logo. A  $50 \times$  objective (N.A. = 0.55) was used in this case. The overview image is shown as the inset. (d) Corresponding layout. (e) SEM image of the logo. The narrowest part consists of only one Mg nanoparticle.

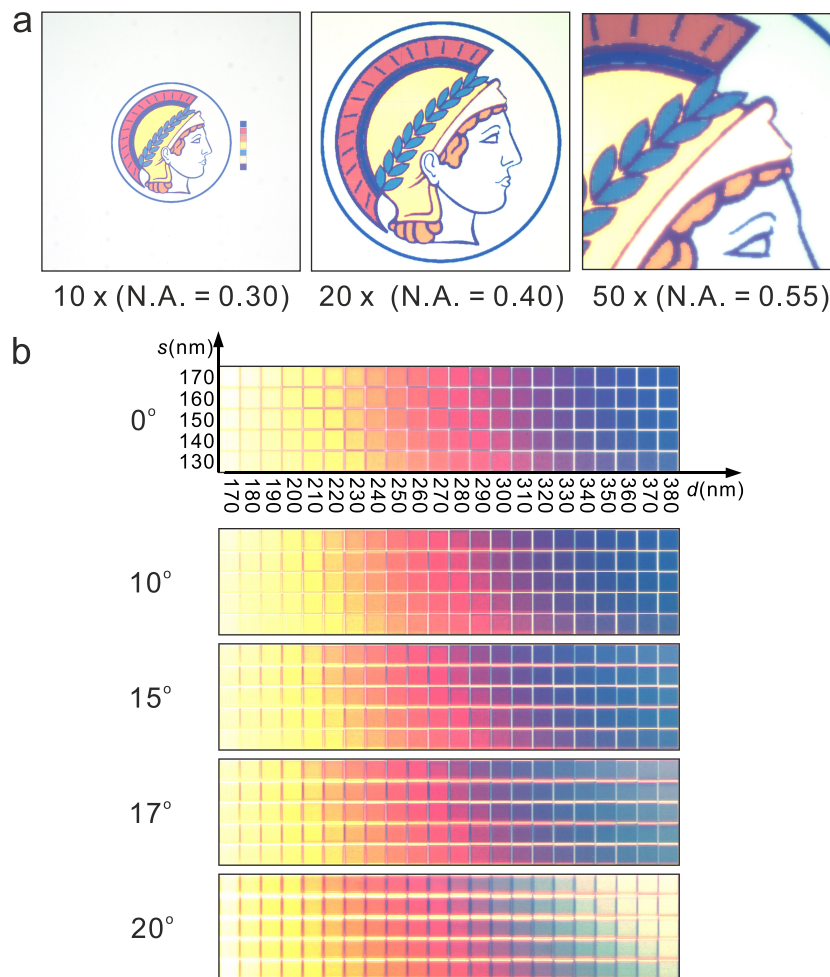


**Figure 4.15** (a) Optical images of the Minerva logo under objectives with different N.A. values. (b) Optical images of one representative part of the colour palette illuminated under unpolarised light with the sample tilted at 0°, 10°, 15°, 17°, and 20°. Each of the rows in the tilted palette was imaged individually and arranged together to achieve a sharp, focused image. No significant colour changes are observed for tilting angles smaller than 17°. The colour changes are gradually observed from the colour squares with large pitches, when the tilting angle increases to 20°.

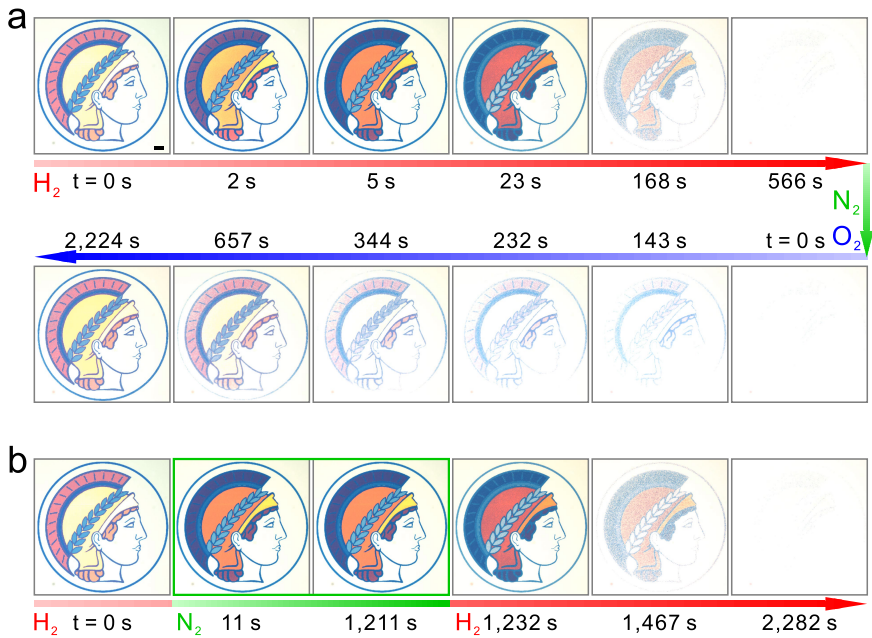


**Figure 4.16** (a) Optical micrographs of the Minerva logo during hydrogenation and dehydrogenation for colour erasing and restoring, respectively. Scale bar: 20  $\mu m$ . (b) Colour state ‘freezing’ by switching off hydrogen.

An interesting functionality of our display technique is image ‘freezing’ at any designated display state, owing to the unique hydrogenation process of Mg, which can be paused in between a fully metallic state (Mg) and a fully dielectric state ( $MgH_2$ ). To demonstrate this aspect, in a new cycle of hydrogenation as shown in **Figure 4.16 b**, the logo display is held at an arbitrary state by switching off hydrogen. For example, at 11 s, hydrogen is switched off and only pure nitrogen is present. As a result, the dynamic process halts immediately and the logo display is ‘frozen’ at the specific colour state (see the green box in **Figure 4.16 b**). When hydrogen is switched on again, the dynamic process proceeds subsequently.

#### 4.4. Plasmonic subwavelength animations

Remarkably, the distinct colour transformation kinetics of the Mg particles allows for the realization of the first plasmonic animations with subwavelength resolution. To demonstrate this functionality, a variety of fireworks have been designed as shown in **Figure 4.17**. The matrix numbers of the selected colours from the palette are labeled next to the individual firework schemes. One of the underlying design mechanisms lies in the fact that Mg particles of different sizes but identical interparticle distance are subject to dramatically distinct colour erasing times during hydrogenation. To this end, fireworks I and IV are designed to display radially explosive effects. Firework V is a spirally propagating animation. Firework II combines both the radial and spiral effects. On the contrary, the inner part of firework III essentially employs Mg particles of identical size but different interparticle distances, which allow for a propagating animation with rich

colour variations. The outermost part of firework III utilizes the same design principle as firework I.

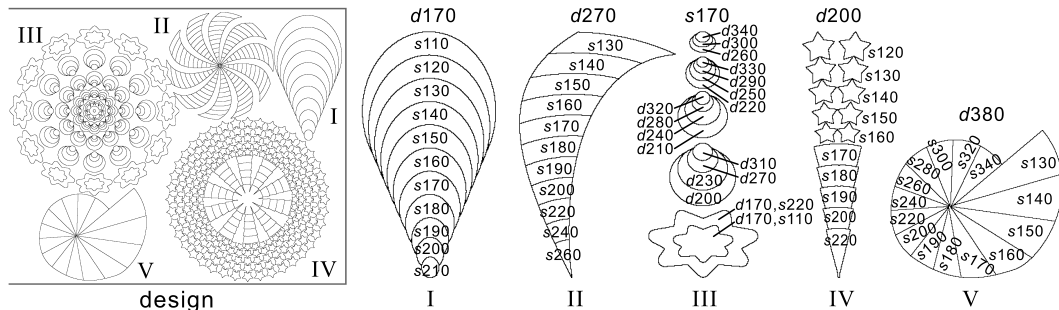


**Figure 4.17** Schematics of the firework animations characterized with different dynamic effects.

**Figure 4.18 a** presents the optical microscopy image of the fabricated plasmonic firework display. The representative snapshot images of the fireworks during hydrogenation are presented in **Figure 4.18 b**. All the fireworks demonstrate dynamic animation effects, which agree well with our design. For example, the balloon firework I displays a clear radially explosive effect, dispatching wave-like colour changes from yellow to orange along the radial axis. Afterwards, the orange colour diminishes along the backward direction until the firework completely disappears. The spiral firework V exhibits a vivid propagating effect following a spiral route with the blue colour gradually disappearing from the exterior.

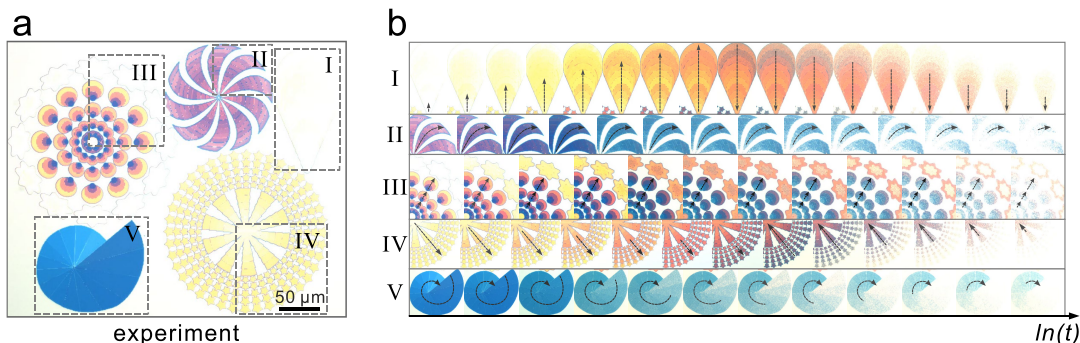


**Figure 4.18** (a) Optical micrograph of the fireworks. (b) Selected snapshots of the firework animations over time  $\ln(t)$ , illustrating the individual dynamic effects.

## 4.5. Highly secure information encryption

Importantly, our dynamic plasmonic display technique is ideally suited for highly secure information encryption and anti-counterfeiting applications<sup>49,57</sup>. To achieve a superior security level, a fabrication protocol with smart material processing has been developed. The fabrication procedures are illustrated in **Figure 4.19 a**. The first information pattern (for example, a letter ‘N’) is defined in a PMMA resist using electron-beam lithography (EBL), followed by Ti/Mg/Ti (3 nm/50 nm/5 nm) evaporation using an electron-gun evaporator. Subsequently, the sample is placed in ambient air for 10 min and then loaded

back to the evaporator for Pd (10 nm) evaporation. After lift-off, the second information pattern (for example, a letter ‘A’) is created using EBL with alignment markers, followed by Ti/Mg/Ti/Pd (3 nm/50 nm/5 nm/10 nm) evaporation and lift-off. Due to the formation of thin oxide layers between Pd and Mg, the letter ‘N’ is inactive to hydrogen. On the contrary, the letter ‘A’ is active to hydrogen.

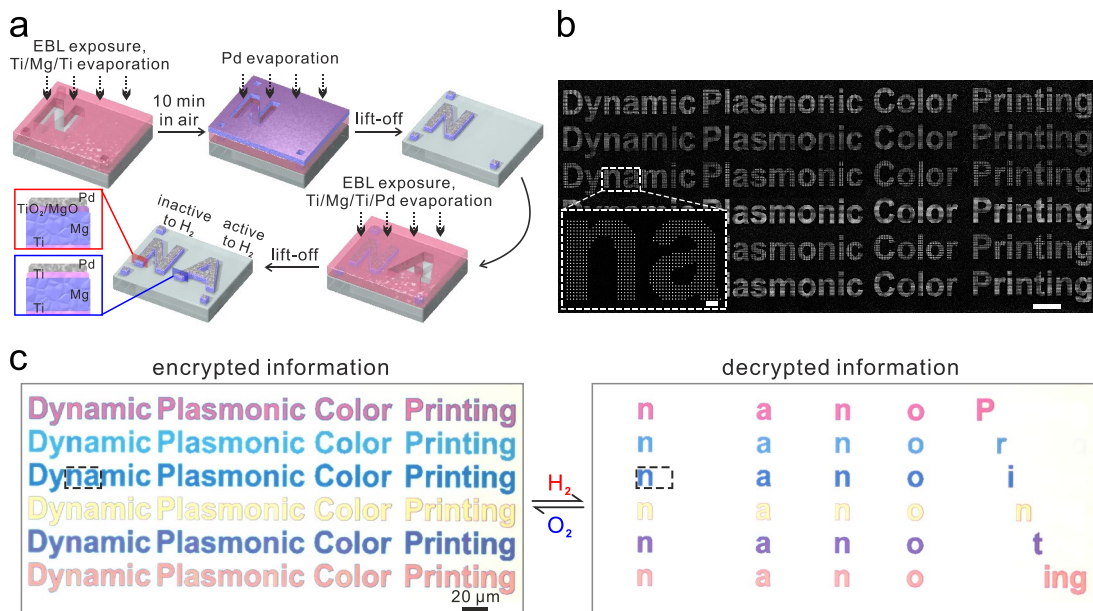


**Figure 4.19** (a) Schematic of the fabrication process. (b) Overview (scale bar: 20  $\mu\text{m}$ ) and enlarged (scale bar: 2  $\mu\text{m}$ ) SEM images of the encrypted microprint. (c) Optical micrographs of the encrypted plasmonic display and the decrypted plasmonic display.

As shown by the SEM images in **Figure 4.19 b**, the letters in each line do not exhibit any discernable differences, neither can the encrypted information be differentiated using optical microscopy (see **Figure 4.19 c**). Only upon hydrogen exposure, the hidden code ‘nano Printing’ is decrypted as shown in **Figure 4.19 d**. The information decryption takes approximately 10 min to complete. In this regard, information encoded on selected pixels, which are indiscernible to both optical and scanning electron microscopies, can only be read out using hydrogen as decoding key, demonstrating the superior security level of our display technique. Importantly, the information can be reversibly encrypted using oxygen within 40 min.

## 4.6. Dynamic display of arbitrary images

Crucial for practical applications, our technique can also be used to create arbitrary dynamic microprints with excellent colour and tonal control. To demonstrate this ability, Vincent van Gogh’s *Flowers in a Blue Vase* has been utilized as design blueprint (see **Figure 4.20 a**). To particularly highlight the colour dynamics of the flowers, the background of the original artwork was removed. The modified design and the optical microscopy image of the fabricated artwork display are presented in **Figure 4.20 b** and c,

respectively. The corresponding SEM images are shown in **Figure 4.20 d**. **Figure 4.20 e** presents the colour erasing and restoring of the dynamic artwork display.

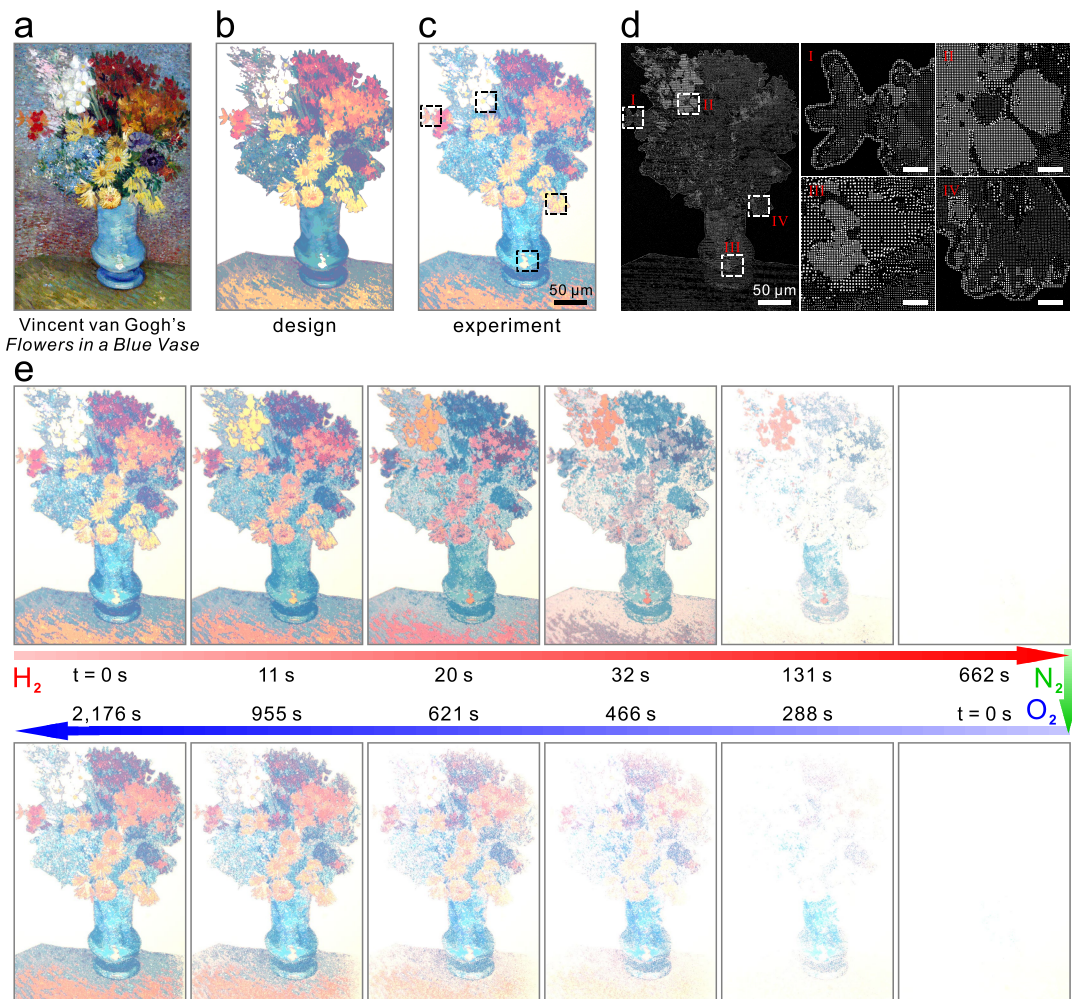


**Figure 4.20** (a) Digital copy of a Vincent van Gogh painting (*Flowers in a Blue Vase*). (b) Modified design of the original artwork in order to highlight the dynamic changes of the flowers. (c) Optical micrograph of the modified artwork. (d) Overview and enlarged SEM images of the microprint. Scale bars are 5  $\mu\text{m}$  in the enlarged images. (e) Dynamic processes of the plasmonic artwork display during hydrogenation and dehydrogenation for colour erasing and restoring, respectively.

## 4.7. Discussion

In summary, we have presented a dynamic plasmonic display technique based on catalytic Mg metasurfaces. The excellent plasmonic properties and unique hydrogenation/dehydrogenation kinetics afforded by Mg nanoparticles enable dynamic plasmonic displays with unprecedented functionalities and subwavelength resolution. Careful material engineering and optimization using Mg alloys<sup>85,134,153</sup> can be carried out to further improve the display durability for real world applications. In addition, polytetrafluoroethylene protective coating can be applied to avoid water staining on the display surface<sup>96,97</sup>. Our technique suggests promising avenues for applications in actively

tunable displays<sup>33,147-149</sup> and filters<sup>33,39,58,148</sup>, plasmonic holograms<sup>155,156</sup>, plasmonic colourimetric sensing<sup>157</sup>, advanced optical data storage<sup>151</sup>, security tagging and cryptography<sup>57</sup>, as well as realization of plasmonic movies with subwavelength resolution in the future.

## 5. Dynamic display based on Mg cavities

High-resolution multicolor printing based on pixelated optical nanostructures is of great importance for promoting advances in color display science. So far, most of the work in this field has been focused on achieving static colors, limiting many potential applications. This inevitably calls for the development of dynamic color displays with advanced and innovative functionalities. In this Chapter, we demonstrate a novel dynamic color printing scheme using magnesium-based pixelated Fabry-Pérot cavities. With controlled hydrogenation and dehydrogenation, magnesium undergoes unique metal and dielectric transitions, enabling distinct blank and color states from the pixelated Fabry-Pérot resonators. Following such a scheme, we first demonstrate dynamic Ishihara plates, in which the encrypted images can only be read out using hydrogen as information decoding key. We also demonstrate a new type of dynamic color generation, which enables fascinating transformations between black/white printing and color printing with fine tonal tuning. Our work will find wide-ranging applications in full-color printing and displays, colorimetric sensing, information encryption and anti-counterfeiting.

This chapter is adapted with permission from “Chen, Y.;\* Duan, X.;\* Matuschek, M.;\* Zhou, Y.; Neubrech, F.; Duan, H.; Liu, N. Dynamic color displays using stepwise cavity resonators. *Nano Lett.* **2017**, *17*, 5555–5560.”

## 5.1. Introduction

Color printing based on engineered optical nanostructures represents an important step forward in optical science, as it fosters a variety of applications for high-resolution color displays,<sup>7,45-48,145,146,158-161</sup> color filters,<sup>31,39,41,58,162-165</sup> high-density optical data storage,<sup>36,166</sup> commercial anti-counterfeiting and data encryption.<sup>33,39,149</sup> Compared to conventional pigment-based color generation, structural colors hold the advantages of higher pixel resolution, higher data density, higher compactness, and enhanced stability without color fading. Using modern nanofabrication techniques, pixelated nanostructures with controlled size, geometry, and arrangement can be well defined, enabling precise tuning of the structural colors pixel by pixel via selective reflection, transmission, or scattering of light. Since the first demonstration of full-color printing using plasmonic nanoparticles by Kumar *et al.*,<sup>48</sup> this research field has flourished with significant advances, particularly on the pursuit of advanced functionalities with lower cost and better color tunability, taking the advantage of plasmonic resonances or optical interference effects.

So far, most of the research efforts in this field have been exerted on static color printing. A transition towards dynamic color printing is inevitable and imperative, as dynamic colors carry much richer information and can enable a wealth of advanced functionalities. In general, there are two schemes to create dynamic color displays using optical nanostructures. One is to introduce dynamic materials in the surroundings of optical structure pixels.<sup>148,149,157,167,168</sup> As a result, the spectral profiles of the optical nanostructures can be influenced and indirectly controlled by external stimuli including electric field, heat, light, *etc.*, thus leading to dynamic color changes. The other is to utilize optical nanostructures made of dynamic materials as pixels.<sup>169</sup> Such dynamic pixels can directly respond to external stimuli for achieving color changes. Nevertheless, optical materials that possess both reversible dynamic responses and distinct optical behavior in the visible spectral range are not choiceful. Magnesium (Mg) is one of the promising candidates, as it exhibits excellent optical properties at high frequencies and also can absorb/desorb hydrogen, undergoing reversible transitions between metal and dielectric hydride ( $MgH_2$ ) states.<sup>76,85</sup> Very recently, dynamic color tuning has been accomplished through controlled hydrogenation/dehydrogenation of Mg nanoparticles, which served as dynamic pixels in color microprints.<sup>169</sup>

In this Chapter, we introduce a third scheme to create dynamic color displays. Here, Mg is not only a surrounding material, but also takes part in constituting dynamic pixels. More specifically, we utilize grey-scale nanolithography to generate stepwise hydrogen silsesquioxane (HSQ) pillars, which are sandwiched between a thick aluminum (Al) film as back mirror and a metallic capping layer composed of Mg/titanium (Ti)/Palladium (Pd). This results in stepwise pixelated Fabry-Pérot (FP) cavities with different cavity heights. Upon hydrogen absorption and desorption, the Mg layer can be reversibly switched between a reflective metal state and a dielectric hydride state, enabling vivid color changes from individual FP resonators. Due to the well-modulated and sharp FP resonances, the

generated colors are much more brilliant and richer than those from dynamic displays composed of Mg nanoparticles. In addition, this scheme utilizes the Mg layer directly from thin film deposition to achieve dynamic color changes without any post-nanofabrication steps. This avoids exhaustive optimization and special care for catalytic nanoparticle manufacturing, which can significantly influence the catalytic efficiency and performance. Following such a scheme, we first demonstrate dynamic Ishihara plates, in which the encrypted images can only be read out using hydrogen as information decoding key. Taking a further step, we demonstrate a novel dynamic color display, which exhibits fascinating transformations between black/white printing and color printing.

## 5.2. Mechanism of colour generation

The working scheme of our dynamic color printing is illustrated in **Figure 5.1**. HSQ pillars of different heights are patterned on a thick Al film (100 nm) using grey-scale nanolithography as shown in **Figure 5.1 a**. The fabrication details can be found in Chapter 5.6.1. The capping layer consists of Mg/Ti/Pd materials (50 nm/2 nm/3 nm). This metallic capping layer, HSQ pillars, and the Al mirror form a series of FP cavities. Before hydrogenation, the 55 nm Mg/Ti/Pd capping layer efficiently reflects the visible light, resulting in no color generation. This defines a blank state (see **Figure 5.1 b**). Upon hydrogen exposure, Pd catalyzes the dissociation of hydrogen molecules into hydrogen atoms, which then diffuse through Ti into the Mg layer. Ti is adopted here to prevent Mg and Pd from easy alloying.<sup>94,152</sup> As Mg is gradually transformed to MgH<sub>2</sub>, the effective thickness of the metallic capping layer decreases and light starts to transmit through it. When Mg is fully hydrogenated into MgH<sub>2</sub>, a variety of FP interference resonators are formed and colors are selectively reflected (see **Figure 5.1 b**). In this case, each FP resonator consists of a TiH<sub>2</sub>/PdH capping layer, a double dielectric spacer (MgH<sub>2</sub> + HSQ), and an Al back mirror. Such asymmetrical FP resonators with ultrathin lossy capping can generate vivid and high-contrast colors with a wide gamut,<sup>53,54</sup> representing a color state. The resonance properties such as the reflectance peak positions and the number of allowed modes in the FP resonators are largely governed by the individual cavity heights (see **Figure 5.1 b**).

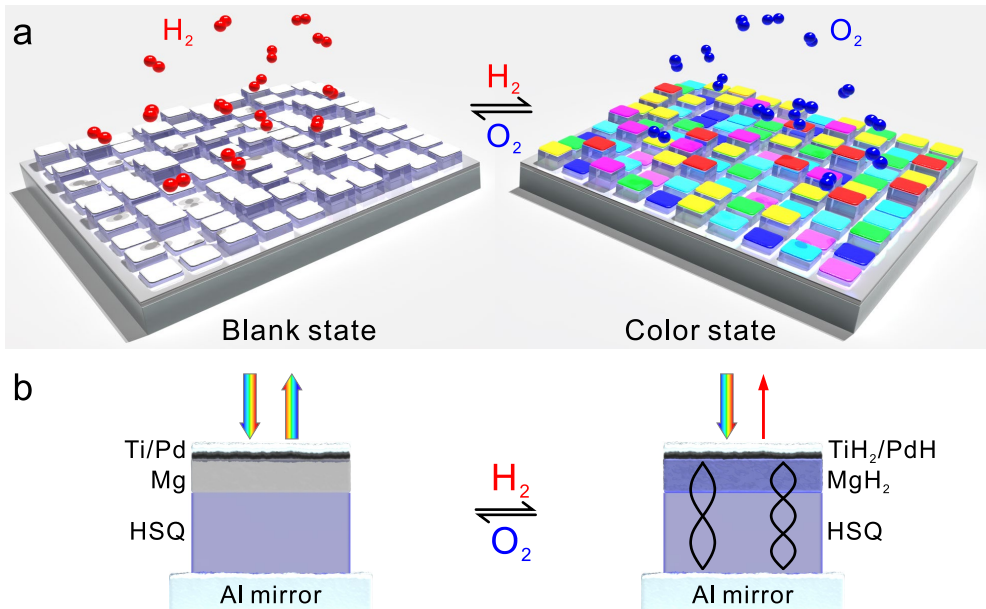


**Figure 5.1** (a) Schematic of the dynamic color display using stepwise FP resonators. Pixelated HSQ pillars generated by grey-scale nanolithography are sandwiched between a Mg/Ti/Pd (50 nm/2 nm/3 nm) capping layer and an Al mirror. Before hydrogenation, the palette is in the blank state. After hydrogenation, the palette reaches the color state through the transition of Mg to MgH<sub>2</sub>, which allows for the formation of a series of FP resonators with different cavity heights. The colors can be erased using oxygen through transition of MgH<sub>2</sub> back to Mg. (b) Before hydrogenation, due to the Mg/Ti/Pd capping layer, the visible light is efficiently reflected. After hydrogenation, the ultrathin capping layer TiH<sub>2</sub>/PdH allows light to pass through the double dielectric spacer (MgH<sub>2</sub>+HSQ) and reaches the Al mirror. FP modes of different orders can be formed in the cavity, selectively reflecting light with specific colors.

Crucially for applications, the color state can be switched back to the blank state using oxygen as shown in **Figure 5.1 a**. The oxidative dehydrogenation process involves binding of oxygen with the desorbed hydrogen atoms from MgH<sub>2</sub> to form H<sub>2</sub>O.<sup>89,154</sup> This avoids a buildup of hydrogen at the Pd surface, thus facilitating hydrogen desorption. When MgH<sub>2</sub> is fully dehydrogenated into Mg, the visible light is efficiently reflected by the thick metallic capping layer (Mg/Ti/Pd) and the palette reaches the blank state again. It is noteworthy that the presented scheme here is in evident difference from our previous work using Mg nanoparticles as dynamic pixels.<sup>169</sup> In the latter case, the color state was always the initial state and hydrogen was used majorly to erase images or information, whereas in our new scheme the blank state is the initial state and hydrogen is employed to uncover images or information. In this regard, the new scheme offers a much higher level of information encryption.

### 5.3. Optical response of the palette

In order to render a palette of colors with a broad range, successive resonance tuning of the FP cavities is carried out by varying the electron exposure dose ( $D$ ) and filling factor ( $F$ ). Each square-shaped tile in the palette has a side length of 20  $\mu\text{m}$  and contains 40  $\times$  40 HSQ pillars arranged in a lattice with a fixed periodicity ( $P$ ) of 500 nm along both

directions.  $F$  is defined as the ratio between the electron exposure area and the lattice area ( $P^2$ ). **Figure 5.2 a** shows an optical microscopy image of the palette in the blank state captured using a  $10\times$  objective with a numerical aperture (N.A.) of 0.3 in a reflection bright-field mode. Along the horizontal axis, the electron exposure dose increases from 29 to  $118\ \mu\text{C}/\text{cm}^2$ , while along the vertical axis the filling factor decreases from 94% to 38%. Altogether, this gives rise to stepwise pillar height tuning from 250 nm to 460 nm in the palette.

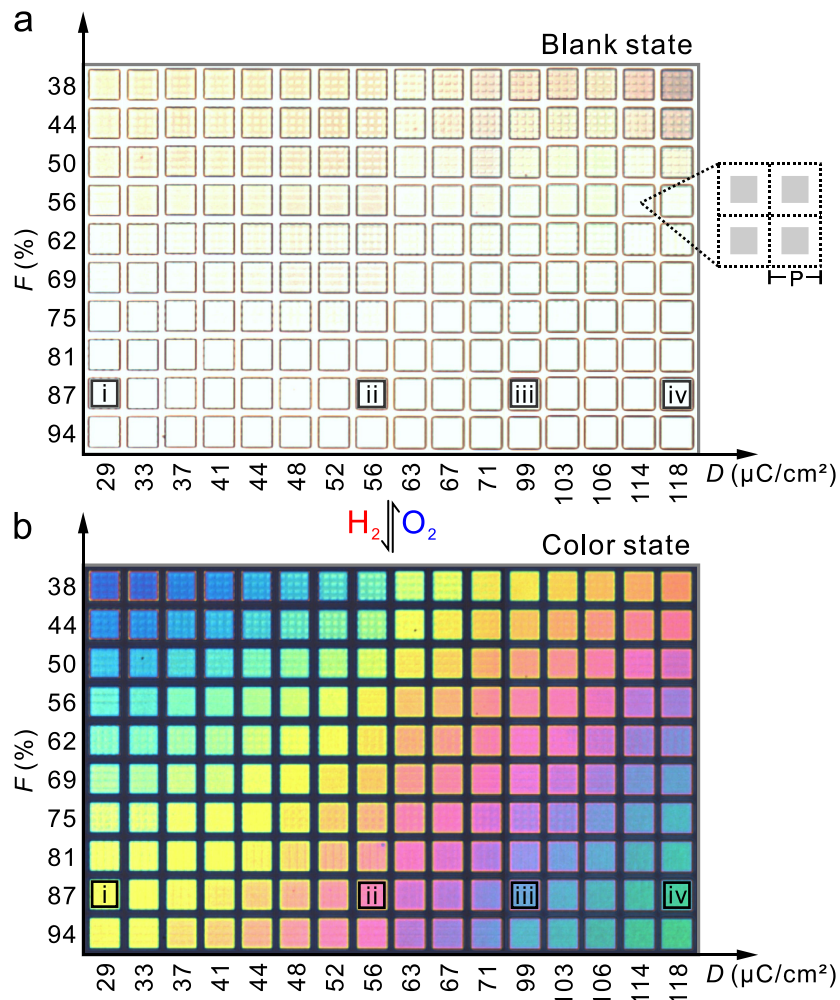


**Figure 5.2** (a) Optical microscopy image of the palette in the blank state. Successive resonance tuning of the FP cavities is carried out by varying the electron exposure dose ( $D$ ) along the horizontal axis and filling factor ( $F$ ) along the vertical axis. Each tile in the palette has a side size of  $20\ \mu\text{m}$ . It contains  $40 \times 40$  HSQ pillars arranged in a lattice with a fixed periodicity ( $P$ ) of  $500\ \text{nm}$  along both directions.  $F$  is defined as the ratio between the electron exposure area and the lattice area ( $P^2$ ). (b) Optical microscopy image of the palette in the color state. Selective tiles are highlighted using black frames for spectral analysis in **Figure 5.6**.

As shown in **Figure 5.2 a**, overall the palette does not exhibit colors in the blank state. The slightly dull colors in the upper regions of the palette can be attributed to the suppressed reflectance from the tiles with small filling factors due to strong scattering from the HSQ pillars capped with rough metals. The dull colors occur in the tiles with small filling factors in the palette. To understand this phenomenon, the reflectance spectra of two

representative tiles with small ( $F = 38\%$ ) and large ( $F = 94\%$ ) filling factors but with the same electron exposure dose ( $D = 103 \mu\text{C}/\text{cm}^2$ ) were measured and are shown in **Figure 5.3**. The reflectance profile of the tile with small filling factor (grey line) is lower than that of the tile with large filling factor (black line), therefore resulting in a dull color. This can be attributed to the suppressed reflectance from the tile with small filling factor due to stronger scattering. In general, the Mg/Ti/Pd films without an underlying Ti adhesion layer are rough. This actually helps for facilitating hydrogenation/ dehydrogenation processes. For the small filling factor case, the Mg/Ti/Pd films deposited on the small HSQ pillars are even rougher due to the extruding HSQ objects as shown in the SEM image (grey-line framed). On the other side, the large HSQ pillars provide more flat platforms for the Mg/Ti/Pd films and there is not a significant difference in roughness between the films on the pillars and in the background as shown in the SEM image (black-line framed).

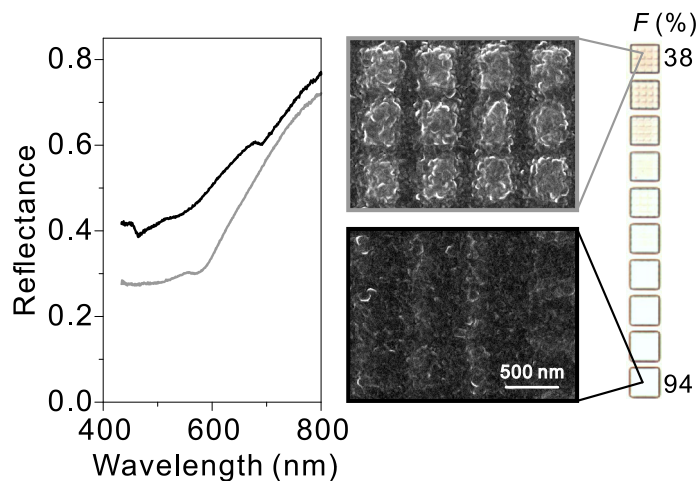


**Figure 5.3** Measured reflectance spectra and SEM images of two tiles with small (grey line) and large (black line) filling factors, respectively.

The dull colors can be elegantly utilized for advanced display applications, which will be discussed in Chapter 5.5. The optical microscopy image of the palette after hydrogenation in the color state is presented in **Figure 5.2 b**, in which brilliant colors covering a wide gamut are observed. The blank and color states can be reversibly switched through controlled hydrogenation and dehydrogenation. In this work, 0.2% hydrogen and 20% oxygen at 80°C were employed for facilitating complete hydrogenation and dehydrogenation of the Mg films, respectively. A control experiment to validate the crucial role of Mg for dynamic color displays was also carried out in **Figure 5.4**. In the absence of Mg, a palette composed of a Ti/Pd (2 nm/3 nm) capping layer, stepwise HSQ pillars, and an Al mirror does not show dynamic color switching through hydrogenation/ dehydrogenation.

A discussion about the angle dependence of the colours can be found in **Figure 5.5**. Such a control sample is used for characterizing the viewing angle dependence, as it can exhibit a color state before hydrogenation, *i.e.*, the sample does not need to be hosted in

the H<sub>2</sub> chamber to generate colors. No significant color changes are observed for tilting angles smaller than 10°.

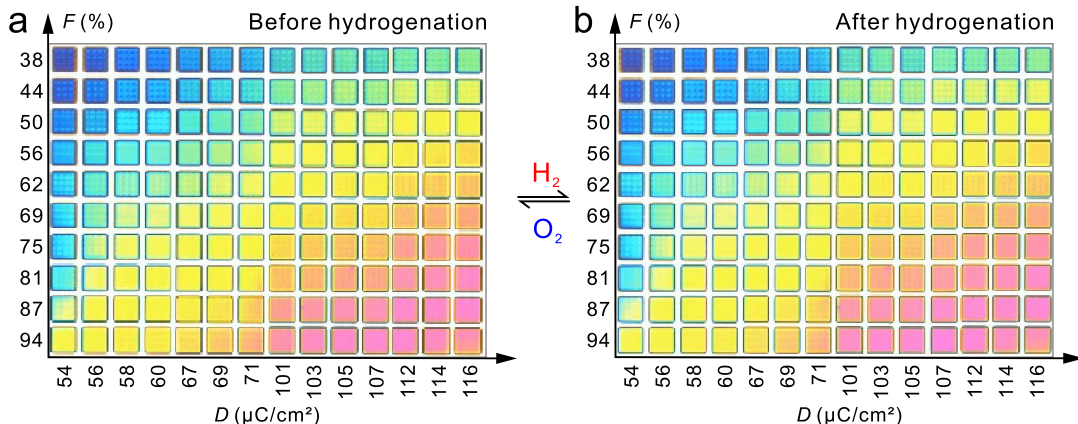


**Figure 5.4** Palette of the control experiment before hydrogenation and after hydrogenation. The HSQ pillars that reside on an Al mirror are only capped by Ti/Pd (2 nm/3 nm) without Mg. Upon hydrogen or oxygen exposure, the colors exhibit nearly no changes, indicating the critical role of Mg for dynamic color displays.

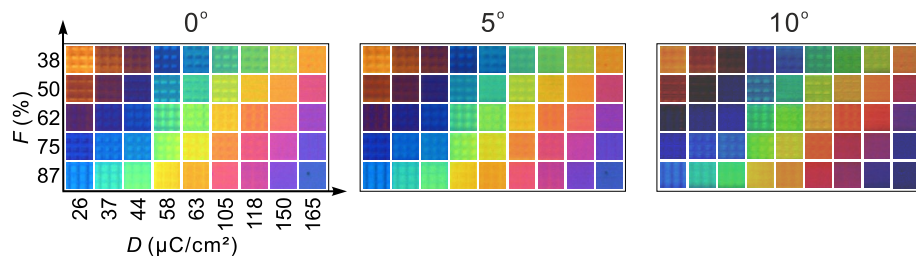


**Figure 5.5** Optical images of the color palette (one representative part) of a control sample with only Ti/Pd (2 nm/3 nm) capping illuminated under unpolarized light with the sample tilted at 0°, 5°, and 10°.

To further understand the dynamic color generation, the spectral evolutions of the representative tiles during hydrogenation are presented in **Figure 5.6 a**. These tiles (i-iv) with increasing cavity heights are highlighted in **Figure 5.2 a** and **b** in the blank and color states, respectively. Before hydrogenation, these tiles appear ‘white’. This is also confirmed by their overall broad spectral profiles of the measured reflectance spectra in the visible range.

We first examine the case in **Figure 5.6 a** (i). Within the broad reflectance spectrum, there is a tiny kink observable near 505 nm. This corresponds to the FP resonance arising from the cavity formed between the Mg/Ti/Pd capping layer and the Al mirror. Upon hydrogen exposure, this FP resonance becomes more and more prominent over time, eventually manifesting itself as a distinct reflectance peak. It is also accompanied with successive intensity decreases of the two resonance shoulders as highlighted by the grey dashed lines in **Figure 5.6 a** (i). Simultaneously, the reflectance peak exhibits successive red-shifts, until it halts at approximately 584 nm. Such red-shifts are due to the gradual transition of Mg into MgH<sub>2</sub> through hydrogenation, which successively leads to a final

cavity with double spacer, HSQ+MgH<sub>2</sub>. This results in a pronounced FP resonance, giving rise to a yellowish color.

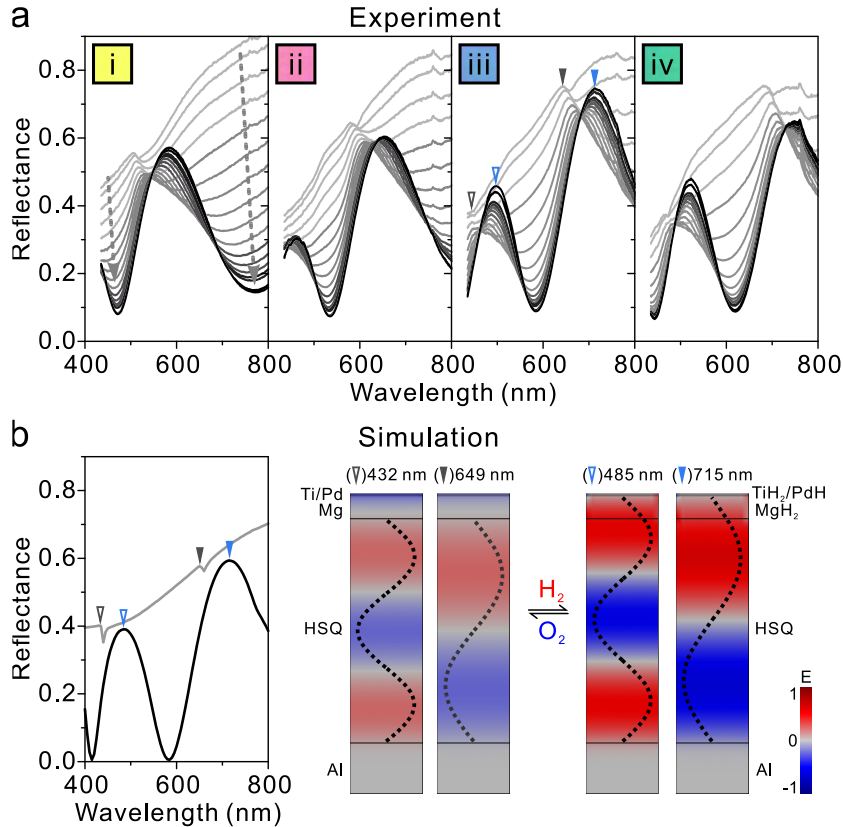


**Figure 5.6** (a) Experimental spectral evolution of the representative tiles highlighted in **Figure 5.2** during hydrogenation. The reflectance spectra are developed from overall broad profiles to sharp FP resonances. (b) Simulated reflectance spectra of tile iii in (a) in the blank (grey line) and color (black line) states, respectively. The field distributions of the different FP resonances (highlighted using arrows) before and after hydrogenation.

Such drastic modifications of the resonance behavior through hydrogenation render sharp transformations between the blank and color states possible. As the HSQ pillar height increases (see from **Figure 5.6** a (i) to (iv)), the reflectance peak shifts to longer wavelengths and meanwhile a new reflectance peak emerges at shorter wavelengths. This corresponds to a higher order FP resonance, which further helps to alter the spectral profile, enabling color generation with a wide gamut. Notably, the colors generated from this Mg-based FP resonator scheme are more vivid and show higher contrast than those from our previous Mg particle scheme,<sup>169</sup> in that the new scheme offers much sharper and pronounced resonances. In addition, the possibility to largely tune the resonance positions and greatly modify the spectral profiles by dynamically changing the effective cavity heights through hydrogenation of a simple Mg layer suggests a straightforward solution to achieving dynamic color displays for practical applications.

To provide a deeper insight into the resonance behavior, numerical simulations were carried out for the configuration in **Figure 5.6** a (iii), as it nicely involves two FP resonances in the color state. In the simulation, the height of the HSQ pillar was taken as 440 nm. As shown in **Figure 5.6** b, the simulated reflectance spectra in the blank state

(grey line) and color state (black line) overall agree well with the measured data. The relatively low reflectance at shorter wavelengths is due to strong scattering at rough metal surfaces (see Chapter 5.6.3). The electric field distributions at 649 nm (grey solid arrow) and 432 nm (grey hollow arrow) in the blank state reveal the formation of the 2<sup>nd</sup> and 3<sup>rd</sup> order FP resonances formed between the Mg/Ti/Pd capping layer and the Al mirror, respectively. In the color state, the electric field distributions at 715 nm (blue solid arrow) and 485 nm (blue hollow arrow) suggest the formation of the 2<sup>nd</sup> and 3<sup>rd</sup> orders of the FP cavity modes formed between the TiH<sub>2</sub>/PdH layer and Al mirror, respectively. The FP resonances in the color state are much more pronounced than those in the blank state due to the ultrathin capping layer after hydrogenation, which allows for more light to pass through and therefore enables much stronger interference effects.

#### 5.4. Ishihara display

The drastic color transformations between the blank and color states constitute an ideal platform for information encryption in microprints. As a demonstration, we have designed and fabricated two dynamic Ishihara color plates, in which different information is encoded. Ishihara plates are often used in clinics for color vision tests. Generally, a symbol is made with colored dots placed in a background comprising dots of a different color. **Figure 5.7** a (i) and b (i) present the optical microscopy images of the two Ishihara plates fabricated following the same procedures for the palette. We deliberately constructed the two Ishihara plates using only the ‘white’ pixels selected from the palette so that the plates display no information before hydrogenation. The enlarged scanning electron microscopy (SEM) images of the two plates are also shown in **Figure 5.7** a and b, respectively. Each plate contains many dotted areas. In each dotted area, HSQ pillars with lattice spacing of 500 nm are sandwiched between a 55 nm Mg/Ti/Pd capping layer and an Al mirror. In different dotted areas, the HSQ pillar heights can be readily tuned by grey-scale nanolithography to generate designated colors. For the unpatterned regions in between the dotted areas, the Mg/Ti/Pd layer directly resides on the Al mirror.

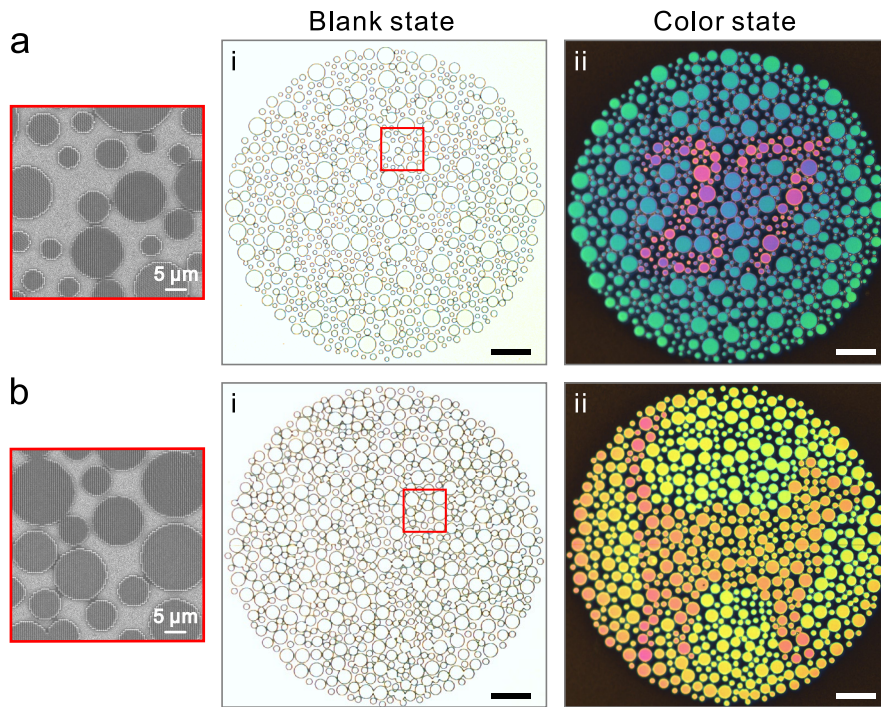


**Figure 5.7** (a) Optical microscopy images of the Ishihara display ‘27’ in the blank and color states. Enlarged SEM image of the highlighted area. (b) Optical microscopy images of the Ishihara display ‘dog’ in the blank and color states. Enlarged SEM image of the highlighted area. Scale bar: 50  $\mu\text{m}$ .

The information encrypted in the two Ishihara plates can be decoded after hydrogenation as shown in **Figure 5.7** a (ii) and b (ii), respectively. In **Figure 5.7** a (ii), ‘27’ in magenta is revealed against a gradually changing bluish-greenish color background with high contrast. Alternatively, in **Figure 5.7** b (ii), a ‘dog’ symbol in orange is displayed against a yellowish background. Although the two hues have a small discrepancy in the color space, the plate presents a high-contrast image, demonstrating precise generation of the designated colors. The unpatterned areas in both plates exhibit a uniform black background color, further enhancing the contrast of the Ishihara color plates. The spectral evolution of the background during hydrogenation can be found in **Figure 5.8**, in which broadband low reflectance, *i.e.*, high absorbance is gradually formed. These experimental results elucidate that our scheme is ideally suited for highly secure information encryption and anti-counterfeiting applications.

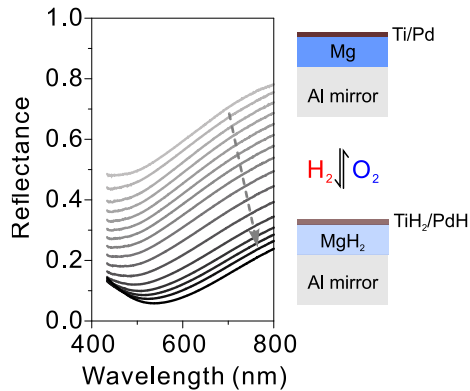


**Figure 5.8** Spectral evolution of the unpatterned area with the Mg/Ti/Pd films directly on the Al mirror during hydrogenation. The background black color in the Ishihara microplates results from the nearly perfect absorbance from the Al/MgH<sub>2</sub>/TiH<sub>2</sub>/PdH configuration in the broad visible spectral range.

## 5.5. Arbitrary dynamic display

To demonstrate the possibility of creating arbitrary dynamic microprints with excellent color and tonal control, we have fabricated a color display using ‘*The Starry Night*’ from Vincent van Gogh as design blueprint. A database was first created using the palette colors in **Figure 5.2 b**. This database includes a library of Red-Green-Blue (RGB) values as well as their corresponding electron exposure doses and filling factors. The computer-generated layout as shown in **Figure 5.9 a (i)** was obtained using a MATLAB script through color matching. The SEM image of the fabricated display is included in **Figure 5.9 a (ii)**. The performance of the dynamic color display presented using snapshot images is shown in **Figure 5.9 b**. We particularly utilized the dull colors in the palette to create a black/white display for the initial state (see **Figure 5.9 b**, at  $t = 0$  s), in which only the tree, mountains, and houses are clearly visible. Upon hydrogen exposure, abrupt color alterations take place. The sky and the mountains are dynamically tinted with brilliant bluish and yellowish colors. At  $t = 78$  s, the display reaches the final color state, beautifully reproducing the details of the blueprint. Upon oxygen exposure, the display can be gradually restored to the initial black/white state within 35 s.

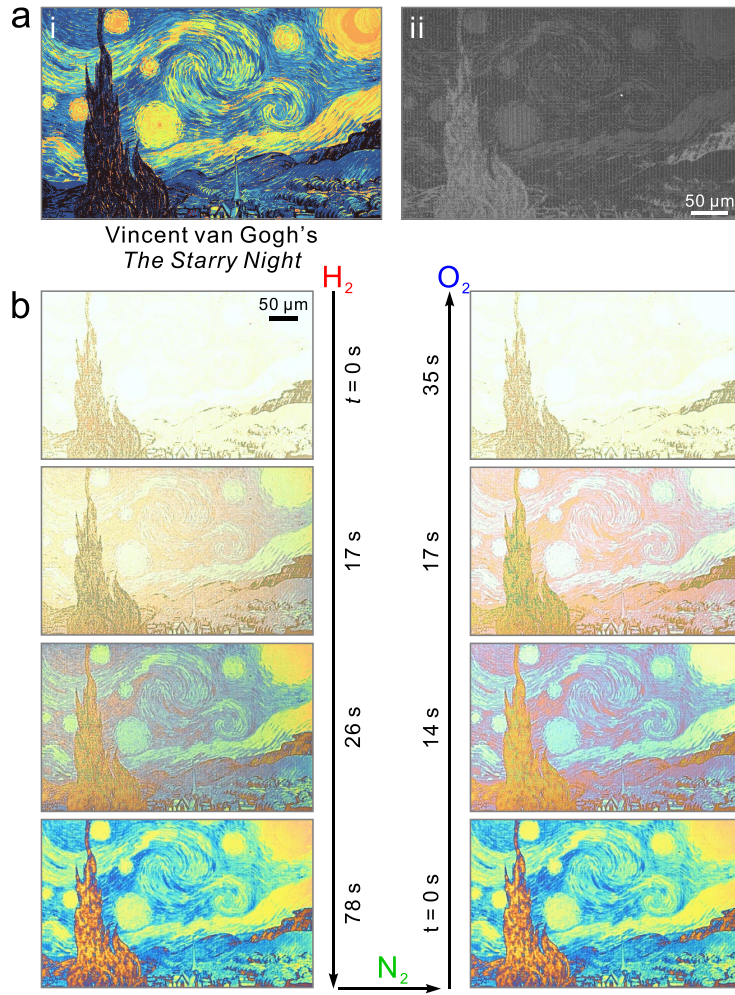


**Figure 5.9** (a) Computer-generated layout of Vincent van Gogh's *The Starry Night* using the color database obtained from the palette and the overview SEM image of the fabricated display. (b) Dynamic display of the artwork during hydrogenation and dehydrogenation.

## 5.6. Experiments and simulations

### 5.6.1. Sample fabrication

As shown in **Figure 5.10**, first, the HSQ resist (FOx-16, Dow Corning) was spin-coated on a 100 nm Al film supported by a silicon substrate at 3000 rpm for 60 s. To minimize thermal-induced cross-linking, the as-coated sample was loaded into the electron-beam lithography system (Raith-150 TWO) without prebake. The grey-scale patterning was achieved by varying the electron exposure doses ( $D$ ) and filling factors ( $F$ ) at different exposure areas following the generated GDSII layout file.  $F$  is defined as the ratio between the electron exposure area and the lattice area.  $F$  was found to also influence the brightness of the tiles after deposition of the metal films. The patterning process was carried out at 15 kV using a 60 μm aperture (beam current of 860 pA). An accelerating voltage of 15 kV was chosen for the grey-scale lithography process, as it allowed for low backscattering of the incident electrons as well as a narrow dose distribution. The small interaction volume

of the incident electrons with the resist enabled fine tuning of the HSQ pillar height. Subsequently, the sample was developed in a 1 wt.% NaOH aqueous solution for 60 s at 20 °C and rinsed in DI water for 60 s. The sample was dried using nitrogen gas. Finally, Mg 50 nm, Ti 2 nm, and Pd 3 nm were successively deposited onto the substrate using an electron-beam evaporator (PFEIFFER Vacuum, PLS-500).

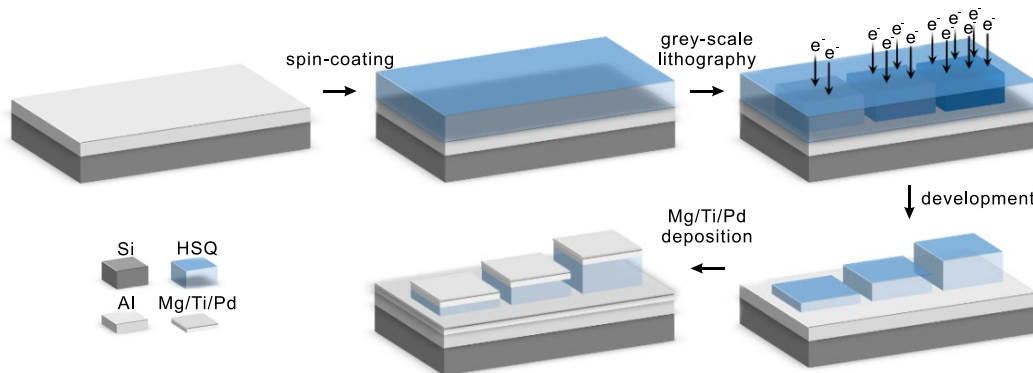


**Figure 5.10** Schematic of the fabrication process.

### 5.6.2. Optical measurements

The color images were revealed using a NT&C bright-field reflection microscopy set-up (using a Nikon ECLIPSE LV100ND microscope) illuminated by a white light source (Energetiq Laser-Driven Light Source, EQ-99). A digital CCD Camera (Allied-Vision Prosilica GT2450C) was used to capture the color micrographs with a  $10\times$  (N.A. = 0.3) objective. The optical spectra were measured in reflection mode using a microspectrometer (Princeton Instruments, Acton SP-2356 Spectrograph with Pixis:256E silicon CCD camera) with the electric field of the unpolarized light in plane with the substrate surface. The reflectance spectra were measured from samples in a stainless-steel cell during hydrogenation and dehydrogenation. The flow rate of the hydrogen and oxygen gases was 2.0 L/min. The measured reflectance spectra were normalized with respect to that of an Al mirror.

### 5.6.3. Numerical simulations

Numerical simulations were carried out using commercial software COMSOL Multiphysics based on a finite element method. Periodic boundary conditions and waveguide port conditions were used for calculations. The refractive index of HSQ was taken as 1.4. The dielectric constants of Ti,  $TiH_2$ , Mg, and  $MgH_2$  were taken from Green<sup>1</sup>, Palik<sup>2</sup>, and Griessen<sup>3</sup>. The dielectric constants of Pd and  $PdH$  were taken from Ref. 4.

The simulated (dash line) and measured (solid line) reflectance spectra of the metallic background are shown in **Figure 5.11 a**. The measured spectrum is lower in reflectance due to the rough Al mirror after the development process in NaOH and the rough Mg/Ti/Pd

films without adhesion layer, which can largely influence the optical properties. The simulated reflectance spectrum of **Figure 5.6** a (iii) using a perfect and uniform 100 nm Al film as back reflector is presented **Figure 5.11** b (black line), in which the two FP resonances show similar intensities. Nevertheless, the experimental reflectance spectrum of **Figure 5.6** a (iii) in the color state shows relatively low reflectance at shorter wavelengths. To qualitatively validate this, the simulated spectrum (black line in **Figure 5.11** b) is normalized using the experimental rough metallic background as back reflector and the result is shown using the back line in **Figure 5.11** c. This confirms the influence from the rough metallic films to the optical properties.

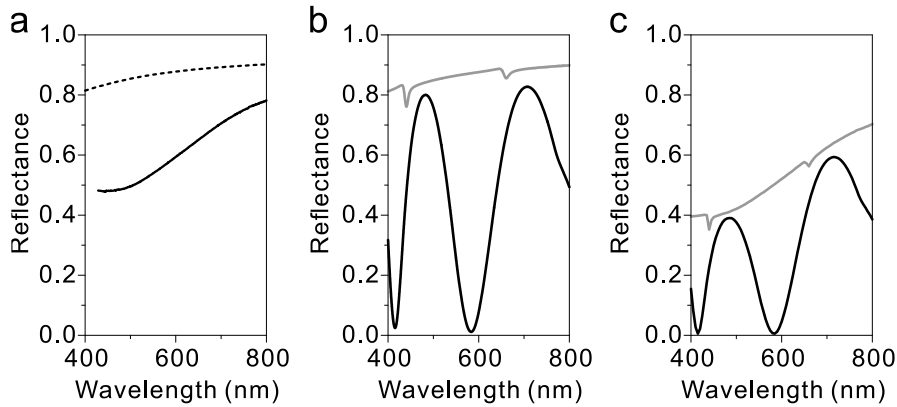


**Figure 5.11** (a) Simulated (dash line) and measured (solid line) reflectance spectra of the Al/Mg/Ti/Pd background. (b) Simulated reflectance spectra in the blank state (grey line) and in the color state (black line) using a perfect and uniform Al film as back reflector, respectively. (c) Simulated reflectance spectra in the blank state (grey line) and in the color state (black line) using the experimental rough metallic background as back reflector, respectively.

## 5.7. Conclusions

In conclusion, we have demonstrated a novel scheme for generating dynamic color displays using Mg-based pixelated FP cavities. The unique hydrogenation/dehydrogenation kinetics of Mg enables dynamic alterations to the FP resonances, resulting in drastic color changes. This scheme provides a promising solution to achieving dynamic color displays with high contrast, wide gamut, and advanced properties including high-level information encryption and fascinating transformations between black/white and color microprints. Our work will shed light on creation of anti-counterfeiting and high-resolution chromatic devices with unprecedented functionalities.

## 6. Lateral diffusion in Mg

Understanding diffusion of large solutes such as hydrogen and lithium in solids is of paramount importance for energy storage in metal hydrides and advanced batteries. Due to its high gravimetric and volumetric densities, magnesium (Mg) is a material of great potential for solid-state hydrogen storage. However, the slow hydrogen diffusion kinetics and the deleterious blocking effect in magnesium have hampered its practical applications. In this Chapter, we demonstrate fast lateral hydrogen diffusion in quasi-free magnesium films without the blocking effect. Massive concomitant lattice expansion leads to the formation of remarkable self-organized finger patterns extending over tens of micrometres. Detailed visualization of diffusion fronts reveals that the fingers in these patterns follow locally the direction of hydrogen diffusion. Thus, the streamlines of the diffusion process are self-recorded by means of the finger pattern. By inclusion of fast hydrogen diffusion objects or local gaps, the resulting streamlines exhibit a clear analogy to optical rays in geometric optics. The possibility to spatially manipulate hydrogen diffusion opens a new avenue to build advanced hydrogen storage systems, cloaking and active plasmonic devices, as well as prototype systems for computational models.

This chapter is adapted with permission from “Duan, X.; Griessen, R.; Wijngaarden, R. J.; Kamin, S.; Liu, N. Self-recording and manipulation of fast long-range hydrogen diffusion in quasifree magnesium. *Phys. Rev. Mater.* **2018**, *2*, 085802.”

## 6.1. Introduction

The magnesium-hydrogen (Mg-H) system has constantly fascinated researchers due to its interesting hydrogen storage properties. With relatively high gravimetric and volumetric densities (7.6 wt% and 110 g l<sup>-1</sup>, respectively), inexpensive and abundant Mg is one of the most attractive metals for solid-state hydrogen storage<sup>60,170</sup>. The relentless interest in Mg-H is, however, also due to a large extent to the high thermodynamic stability of MgH<sub>2</sub> as well as its slow and complex H absorption/desorption kinetics. Despite an impressive body of information<sup>75,86,170</sup>, the published values for H diffusion in Mg exhibit a large spread varying from 10<sup>-20</sup> up to 10<sup>-15</sup> m<sup>2</sup>s<sup>-1</sup> near room temperature.<sup>83,171</sup> Detailed studies of H absorption and desorption in Mg thin films<sup>73,83,87,171-173</sup> have shown that the sluggish kinetics and the resulting notorious ‘blocking effect’ are mainly due to the formation of a superficial layer of the extremely stable hydride<sup>170</sup>, MgH<sub>2</sub>. This has led to the belief that fast H diffusion in concentrated Mg-H systems is inherently impossible.

Here we demonstrate that the blocking effect is absent, when H enters a Mg film laterally, *i.e.*, parallel to the film plane as indicated in **Figure 6.1**. We further show that in such a lateral diffusion geometry a quasi-free Mg film has the possibility to minimize the very large H-induced lattice dilation by a massive modification of its morphology. This generates self-organized finger patterns that extend over tens of micrometres along the diffusion direction. These finger patterns are optically monitored in real time and can be used for simultaneous measurements of H diffusion coefficients in a large number of samples. The corresponding finger landscapes shown in atomic force microscopy (AFM) images reveal the H streamlines during diffusion, which can be manipulated by spatial modulations using objects with different H diffusion coefficients. The existence of H diffusion finger patterns and the possibility to manipulate them have never been reported thus far. Especially interesting is that the diffusion process is self-recording its progress in Mg by means of the finger pattern.

## 6.2. Experiment

### 6.2.1. Samples

Each sample consists of a Pd entrance gate or multiple Pd gates (typically 20 nm thick) and a layer of Mg with thickness varied between 22 and 372 nm. In all samples, a 3 nm Ti buffer layer is deposited on a SiO<sub>2</sub> (100 nm)/Si substrate to minimize the clamping of the Mg layer to the substrate<sup>85,94,135,174-176</sup>. An oxidized TiO<sub>x</sub> capping layer covers the Mg layer so that H absorption or desorption can only occur via the Pd gate(s). The Ti buffer layer, the Mg layer, and the Ti capping layer are successively deposited on the substrate through electron-beam evaporation (PFEIFFER Vacuum, PLS-500). The deposition rates of Mg and Ti are 1.0 and 0.2 nm/s, respectively. The vacuum and temperature during depositions are 1×10<sup>-5</sup> Pa and ~20 °C, respectively.

The samples are manufactured using multiple electron-beam lithography (EBL). First, alignment markers are defined in a double layer PMMA resist (200k-3.5% and 950k-1.5%, Allresist) using EBL (Raith e\_line) on the substrate. A 2 nm chromium adhesion layer and a 40 nm Au film are deposited on the substrate using thermal evaporation followed by a standard lift-off procedure. Next, the substrate is coated with a double layer PMMA. Computer-controlled alignment using Au markers of the first layer are carried out to define a structural layer. Subsequently, 20 nm Pd for the hydrogen entrance gates and fast H-diffusion objects (*e.g.*, Pd prisms and lenses) is deposited on the substrate using thermal evaporation followed by the same lift-off procedure. Then, the substrate is coated with a double layer PMMA again, and the alignment Au markers are used to define another structural layer. After development (90 s in MIBK and 60 s in isopropanol), 3 nm Ti, 22–372 nm Mg, and 5 nm Ti are successively deposited on the substrate through electron-beam evaporation (PFEIFFER Vacuum, PLS-500).

### 6.2.2. Optical measurements

During hydrogen absorption or desorption optical images and videos of the samples are taken using a bright-field reflection microscope (Nikon, ECLIPSE LV100ND) illuminated by a white light source (Energetiq Laser-Driven Light Source, EQ-99). A digital CCD Camera (Allied-Vision Prosilica GT2450C) is used to capture images with a  $\times 100$  (N.A. = 0.6) objective. The hydrogenation and dehydrogenation experiments are carried out in a homemade optical gas chamber. The flow rate of the gas (hydrogen or oxygen) is  $2.0 \text{ l min}^{-1}$ . The temperature of the cell can be varied between room temperature and 100 °C.

### 6.2.3. AFM and SEM measurements

The topographies of all samples are measured with an AFM instrument (MultiMode 8) equipped with NanoScope V controller, vertical J-scanner, and NanoScope version 8 software (Bruker AXS, Santa Barbara, CA). AFM measurements are performed using Si cantilevers (NANOSENSORS, PointProbe-Plus) with scan size of 40  $\mu\text{m}$ , scan rate of 0.5 Hz, and resolution of  $1024 \times 1024$ . The SEM images are taken using an ULTRA 55 system (Carl Zeiss AG) at 15 kV.

### 6.2.4. Focussed-ion beam measurements

Cross-sections of the samples are generated by Focused Ion Beam (FIB) system (Raith FEI Multibeam equipped with a gallium ion beam etching function) to check that the topographic finger patterns observed in AFM are not due to delamination or buckling. To observe a fresh surface, the sample is tilted 52° to perform ion milling with a gallium ion beam current of 10 pA operating at 30 kV, in a series of steps across the surface, at increasing depths, until the sample milled into the substrate.

### 6.3. Ubiquity and general properties of finger patterns

We have observed finger patterns in all our samples. Three representative examples are shown in **Figure 6.1** (see Chapter 6.8 for details). Regardless of whether H is introduced via a narrow underlying Pd strip (see **Figure 6.1 a**), a Pd ring at the periphery of a Mg disk (see **Figure 6.1 b**), or a Pd ‘star’ consisting of 6 radial strips (see **Figure 6.1 c**), in all cases finger patterns are observed both in AFM and optical reflection (OR) images.

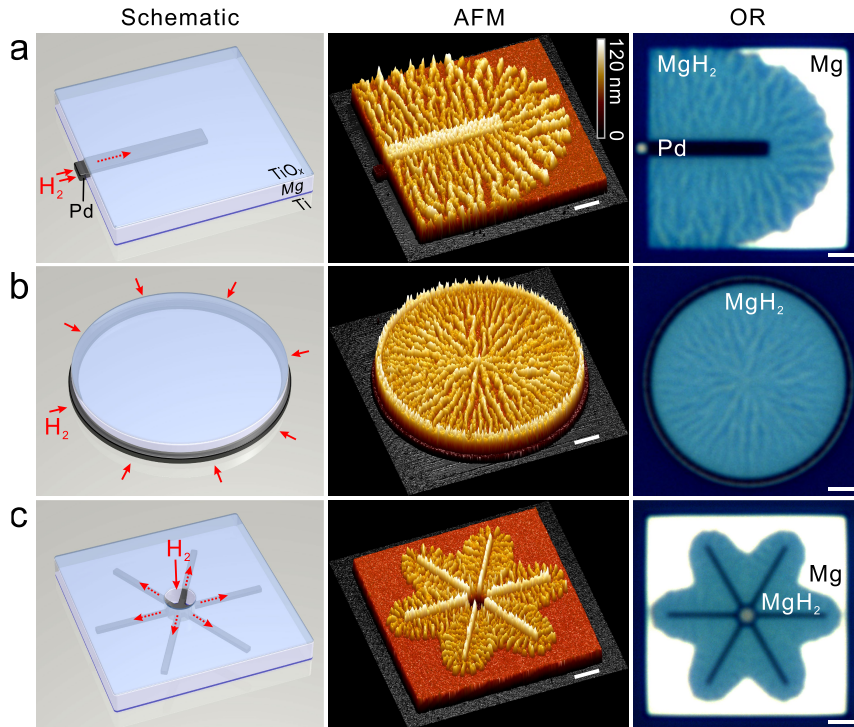


**Figure 6.1** H enters quasi-free Mg through (a) a 1  $\mu\text{m}$  wide Pd strip under a 3 nm Ti/45 nm Mg/5 nm TiO<sub>x</sub> patch, (b) a 0.6  $\mu\text{m}$  wide Pd ring at the periphery of a Mg disk, and (c) a 1.5  $\mu\text{m}$  opening in a Mg patch with 6 radial Pd strips of 0.2  $\mu\text{m}$  width underneath. Schematics of the samples are shown in the left column. The red arrows indicate how H enters the samples and then diffuses parallel to the Mg film plane. The AFM landscapes and the corresponding OR images taken after H loading of (a) 28,350 s, (b) 11,580 s, and (c) 1,390 s at 353 K at a hydrogen pressure of 20 kPa. The light blue regions in the OR images of (a), (b), and (c) correspond to MgH<sub>2</sub>, while the bright regions in the OR images of (a) and (c) are due to metallic Mg. (Scale bar: 2  $\mu\text{m}$ ).

There is a remarkable one-to-one correspondence between the AFM and OR finger patterns. While a radial finger pattern is expected due to the symmetric configuration in **Figure 6.1 b**, the patterns in **Figure 6.1 a** and **c** show that the fingers tend to nucleate in a direction perpendicular to the radial Pd strips. For different samples, the finger patterns exhibit universal characteristics, although the details vary in individual samples. With increasing distance from the Pd entrance gate, i) the average separation between two adjacent fingers increases; ii) the width of the individual fingers increases; iii) the sample height averaged along lines perpendicular to the H streamlines remains constant; iv) the out-of-plane expansion averaged over the entire finger pattern region is essentially equal to the total volume expansion (see Chapter 0 for more details).

To unravel the nature of the finger patterns and unambiguously identify the involved hydride phases, we consider the simple geometry shown in **Figure 6.2 a**. The  $15 \times 15 \mu\text{m}^2$  sample consists of a 45 nm thick Mg film sandwiched between a 3 nm Ti buffer layer and a 5 nm  $\text{TiO}_x$  capping layer. H enters the sample via a 20 nm thick and 15  $\mu\text{m}$  long Pd strip spanning the entire left-hand side of the Mg patch. The AFM, OR, and scanning electron microscopy (SEM) images are recorded after H loading at pressure of 20 kPa at 353 K. It reveals that the AFM, OR, and SEM finger patterns are strikingly similar.

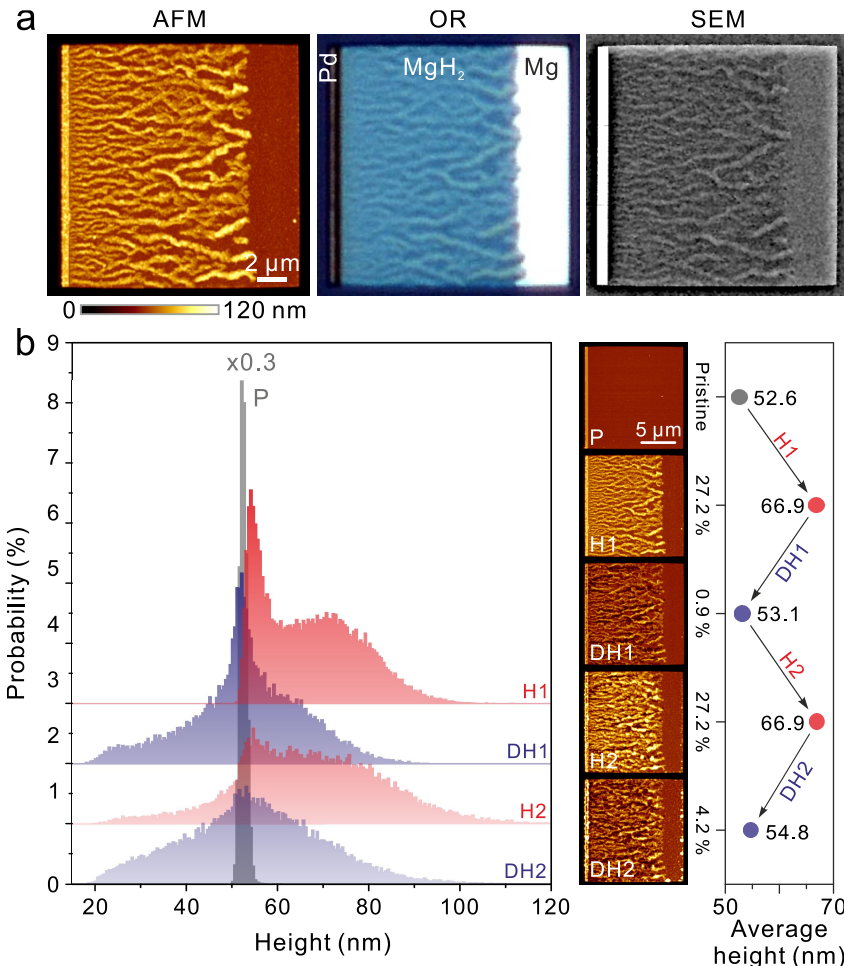


**Figure 6.2** (a) AFM, OR, and SEM images of the finger patterns after the first hydrogenation (41,390 s) at 20 kPa at 353 K in a 3 nm Ti/45 nm Mg/5 nm  $\text{TiO}_x$  sample with a 20 nm thick Pd entrance strip. The light yellowish and bluish colours in the OR image correspond to the hills and plains in the AFM image, respectively. The hills and plains are all in the  $\text{MgH}_2$  phase. The metallic Mg phase appears very bright in the OR image to the right side of the finger pattern. (b) Histograms of the finger patterns for the pristine (P), first hydrogenation (H1), first dehydrogenation (DH1), second hydrogenation (H2), and second dehydrogenation (DH2) states sequentially. The histograms are all calculated within the same region of the AFM images, which is determined by the extent of the finger pattern in the hydrogenated zone (approximately  $15 \times 11 \mu\text{m}^2$ ). The histogram P is scaled by a factor 0.3 for clarity. For each state, the average height derived from the corresponding histogram is indicated in the right panel. These average heights are in excellent agreement with the predicted values from a model assuming that the total volume expansion is entirely accommodated out-of-plane.

At first sight one might naively associate the formed hills with MgH<sub>2</sub> and the plains with Mg, respectively. Reality is, however, quite different. As shown by the OR image in **Figure 6.2 a**, the hills and plains are optically yellowish and bluish, respectively. Both are much darker than the region ahead of the finger pattern. This indicates that the entire finger pattern, *i.e.*, both hills and plains, occurs within the insulating MgH<sub>2</sub> phase and the region ahead of the pattern is essentially metallic Mg. The various shades in blue colour are due to interference effects in the transparent dihydride<sup>76,177</sup>, whose thickness is strongly position dependent. As evidenced by the AFM image, the sample landscape comprises plains and hills (*i.e.*, the fingers). The hills can be approximately 200% higher than the plains. An essential clue for the interpretation of such high hills is provided by the SEM measurements in **Figure 6.2 a**, which show within 0.5% accuracy there is no in-plane dilation upon hydrogenation. A direct consequence of this observation is that the out-of-plane dilation averaged over the entire finger pattern measured with AFM is expected to be approximately 30%, as the molar volumes of Mg and MgH<sub>2</sub> are 13.98 and 18.15 cm<sup>3</sup>mol<sup>-1</sup>, respectively. This expectation is confirmed by the measured average heights derived from the height histogram of the sample in **Figure 6.2 b**.

For an unambiguous identification of the phases involved in the finger patterns, we have characterized this sample using AFM for two H loading/unloading cycles in **Figure 6.2 b**. The sharply peaked histogram of the pristine state (P) in **Figure 6.2 b** indicates that the surface of the as-fabricated sample is flat with an average height of 52.6 nm. After H loading for 41,390 s at 20 kPa, the histogram of the first hydrogenation (H1) exhibits two peaks. The peak centred at ~54.2 nm arises from the plains of the landscape, while the broad peak at ~70.8 nm is due to the hills, whose maximum height can be larger than 100 nm. Most interesting is that the average height derived from histogram H1 is 66.9 nm. After the first unloading, the average height derived from histogram of the first dehydrogenation (DH1) is 53.1 nm. The two measured average heights are in excellent agreement with the values 67.17 nm and 53.75 nm predicted by assuming that the volume changes from Mg to MgH<sub>2</sub> (29.83%) and from Ti to TiH<sub>2</sub> (24.95%) are entirely accommodated out-of-plane (see Chapter 6.9.2). The average height 53.1 nm measured after the first unloading is also in excellent agreement with 53.75 nm since the much larger stability<sup>178</sup> of TiH<sub>2</sub> compared to MgH<sub>2</sub> prevents it from unloading. In the DH1 state, the sample therefore consists of a TiH<sub>2</sub> buffer layer and a metallic Mg film. Further justification of this interpretation is that upon the second H loading the average height reaches again 66.9 nm. After the second H unloading, the slightly higher average height 54.8 nm is probably due to an incomplete dehydrogenation. An additional proof of the vanishing in-plane expansion upon H loading follows directly from the SEM analysis of the samples containing various amounts of hydrogen as indicated in Chapter 6.9.3.

That the entire finger pattern consists of MgH<sub>2</sub> is further substantiated by two essential observations: i) after the first unloading, histogram DH1 is almost symmetric and broad, ranging from 20 to 80 nm. This implies, as shown in the AFM images of **Figure 6.2 b**, that hills have been lowered. More important is that deep crevasses have developed between

the hills. This is only possible if, after the first H loading, the plains are also fully hydrogenated; ii) the dark and light blue colours in the OR image of **Figure 6.2 a** are fully consistent with interference colours through a transparent layer of MgH<sub>2</sub>.

For all samples investigated in this work, we have observed well-developed finger patterns exhibiting the same characteristic features. The finger patterns are generated in order to minimize the internal stresses in the Mg-H system that must expand by approximately 30% in volume, while keeping its in-plane dimensions constant. Very important is to realize that the constancy of in-plane dimensions cannot be due to a strong sticking of the Mg film to the substrate, as Mg does not alloy with the Ti buffer layer. It is thus an intrinsic property of the quasi-free thin Mg films<sup>85,94,135,174-176</sup>, which are in resemblance to wrinkling of skins<sup>179</sup>.

#### 6.4. Manipulation of diffusion streams

The three representative examples shown in **Figure 6.1** demonstrate clearly that the finger patterns depend on the geometries of the samples and the Pd entrance gates. This immediately suggests that H diffusion in composite samples with spatially modulated diffusion coefficients should lead to specific distortions of the finger pattern presented in **Figure 6.2 a**. Typical examples of such composite samples are shown in Fig. 3. The leading idea of the sample architecture is to include an object with H diffusion properties that are markedly different from those of the surrounding Mg film. For example, in the schematic of **Figure 6.3 a**, a Pd prism is embedded in the Mg film. At the temperatures of interest in this work, *i.e.*, between 20 °C and 100 °C, H diffuses through Pd several orders of magnitude faster than through Mg. Both the AFM and OR images in **Figure 6.3 b-i** confirm that the finger pattern is drastically modified due to the presence of the Pd prism. The same also evidently happens for the convex and concave lenses shown in **Figure 6.3 b-ii,iii**. On the other hand, a control experiment with a gold prism embedded in Mg (see **Figure 6.3 c**) confirms that the finger pattern is unaffected by an object that does not absorb H.

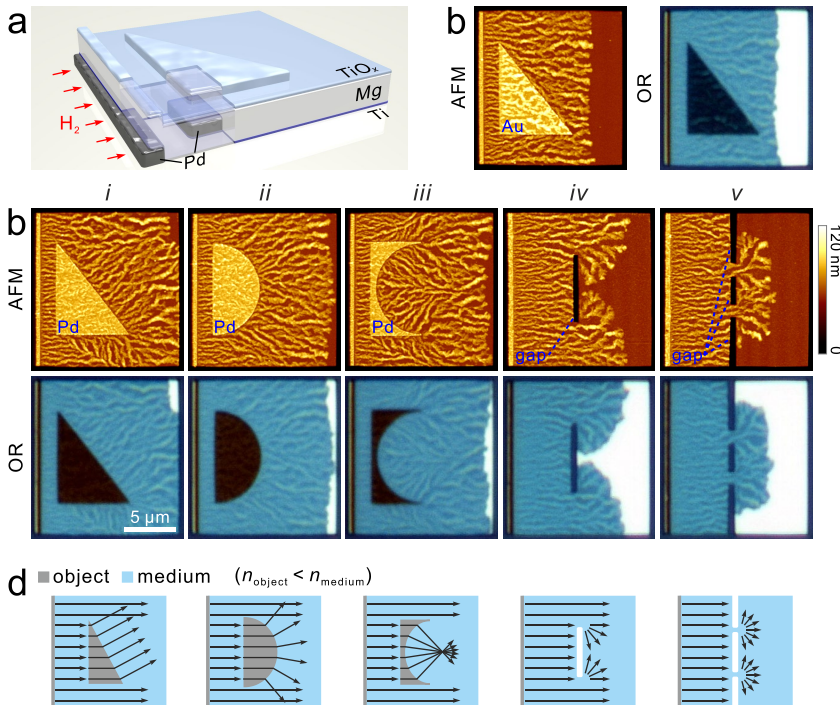


**Figure 6.3** (a) Schematic of a composite sample with a Pd prism under a 3 nm Ti/45 nm Mg/5 nm TiO<sub>x</sub> patch. A corner of the structure is made transparent for better visibility of the embedded 20 nm thick Pd prism. The red arrows indicate that H enters the sample via the Pd strip and diffuses parallel to the Mg film plane. (b) AFM and OR images of the Mg patches with various embedded Pd objects (characterized by a fast H diffusion) in *i*, *ii*, and *iii*, or with local air gaps (corresponding to impenetrable H diffusion obstacles) in *iv* and *v* (c) AFM and OR images of a control sample, in which an Au prism is embedded in a Mg patch. In this case, the finger pattern is not affected by the Au object, since Au does not absorb H. For all the samples, H loading is carried out under the same experimental conditions as in Fig. 1. (d) Analogy between lateral H diffusion in Mg and optical wave behaviour. Prism (*i*), convex (*ii*), and concave (*iii*) lens-like behaviour is obtained using geometric optics analogues with  $n_{\text{object}} < n_{\text{medium}}$ . H circumvents the single gap in *iv* and diffuses through the two slits defined by three gaps in *v*.

The observed finger patterns in **Figure 6.3 b-i** to *iii* seem to be counterintuitive, as it is well known in geometric optics that light is focused by convex lenses and defocused by concave lenses. One should however realize that conventional optical lenses are made of materials with refractive indices larger than 1, *i.e.*,  $n_{\text{object}} > n_{\text{medium}}$ . In our case, however, the Pd objects locally enhance the H diffusion. Here the geometric optics analogue is  $n_{\text{object}} < n_{\text{medium}}$ . Schematic representations of the geometric optical properties of such objects are indicated in **Figure 6.3 d**. Another type of objects is small gaps in Mg films, generated by locally removing materials throughout the entire sample thickness. The finger patterns for the single gap and double slits in **Figure 6.3 b-iv,v** resemble the patterns encountered in wave optics. The clear analogy between H diffusion streams and optical rays is a direct consequence of the observation that Snell's law is approximately obeyed in diffusive processes<sup>180,181</sup>.

## 6.5. Self-recording and simulations of streamlines

So far, we have only presented the results obtained *after* H loading/unloading by means of AFM, OR and SEM characterizations. As a matter of fact, we have also recorded the OR videos of the diffusion processes *in real time* (see Chapter 6.10). As the MgH<sub>2</sub> phase is much darker than the metallic Mg phase in OR, the recorded videos contain detailed information about the time dependence of the H diffusion front through a sample. This has led to the striking discovery that the diffusion fronts extracted from snapshots of the OR video at different times are locally orthogonal to the fingers. It is explicitly demonstrated in **Figure 6.4** a for the five cases in **Figure 6.3** b. The fact that the sample unveils its H streamlines by itself in the form of a finger pattern due to a self-organized corrugation of its surface amounts to a self-recording of the entire diffusion process. In other words, the fingers are always generated along a direction locally perpendicular to the momentary diffusion front.

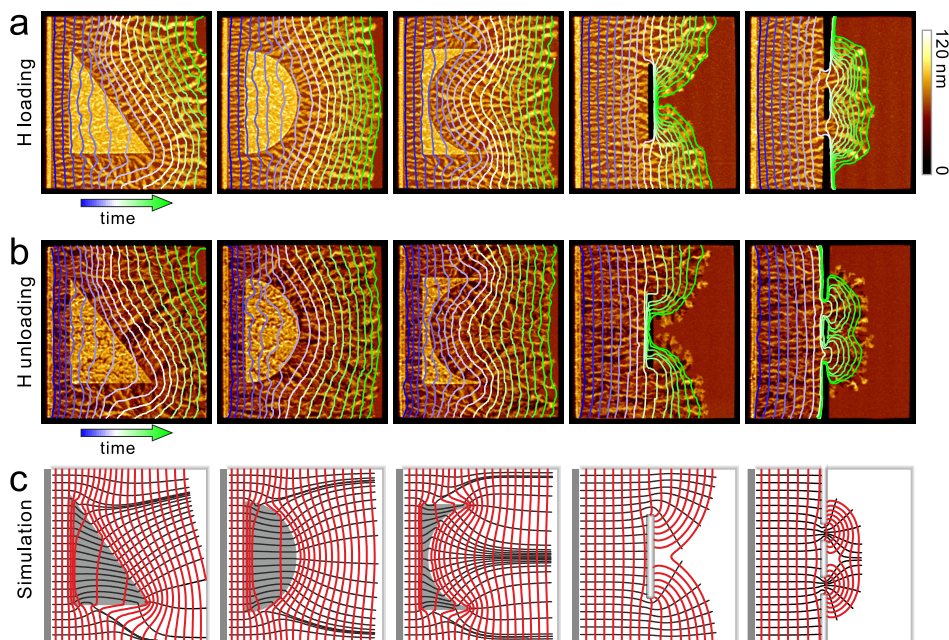


**Figure 6.4** (a) Diffusion fronts (blue to green lines) extracted from OR videos at times  $t_n$  so that  $\sqrt{t_n}$  are equally spaced. The diffusion front lines are superimposed on the AFM images of the samples in **Figure 6.3** b, taken after H loading. It demonstrates that the fingers are locally orthogonal to the diffusion fronts. (b) Diffusion fronts (blue to green lines) extracted from OR videos during H unloading are superimposed on the AFM images of samples in **Figure 6.3** b, taken after H unloading. The similarity between the recorded diffusion fronts during H loading (a) and unloading (b) demonstrates the reversibility of the diffusion processes and implies the symmetric form of the function in Eq. (6.2). (c) Diffusion fronts (red lines) and streamlines (black lines) obtained from the simulations described in Chapter 6.12 are in excellent agreement with the experimental data in (a) and (b).

All the salient features of the finger patterns in **Figure 6.3** b can be nicely reproduced by the diffusion model described in detail in Chapter 6.12. They are based on numerical solutions to the diffusion equation

$$\frac{\partial c}{\partial t} = D_i \nabla f(c) \cdot \nabla c + D_i f(c) \nabla^2 c \quad (6.1)$$

where  $t$  is the time and  $D_i$  is the amplitude of the H concentration dependent diffusion coefficient. The index  $i$  stands for medium (Mg) or object (Pd underneath Mg). The H concentration  $c$  dependent function  $f(c)$  is chosen for all simulations as

$$f(c) = e^{-\alpha c} + e^{-\alpha(1-c)} \quad (6.2)$$

with  $\alpha = 20$  derived using a lattice-gas model for H in a metal. The symmetry of  $f(c)$  is a direct consequence of the observed H loading/unloading symmetry (see Chapter 6.10), which proves unambiguously that all the effects observed in this work result from genuine H diffusion and not from uncontrolled spurious effects. Important is to stress that the simulations involve only one adjustable parameter,  $D_{\text{object}}/D_{\text{medium}}$ , which is the same for all simulations shown in **Figure 6.4 c**. An excellent agreement between the finger patterns in the AFM images and the simulated streamlines (black lines in **Figure 6.4 c**) is obtained with  $D_{\text{object}}/D_{\text{medium}} = 100$ . At time  $t_0$ , the H concentration in Mg is set equal to  $c_0$  at the Pd entrance gate, while it is zero everywhere else. From this initial situation, Eq. (6.1) is numerically solved. At times  $t_n \propto n^2$ , where  $n$  is an integer, the diffusion front lines (red lines) are plotted in **Figure 6.4 c**. Meanwhile, the streamlines that are locally orthogonal to the front lines are constructed. The good agreement between experimental finger patterns and simulated streamlines confirm that the fingers are in fact a self-recording of the entire diffusion history.

## 6.6. Synergetic interaction of finger patterns

An interesting feature of the time dependence of the measured diffusion front positions (see Chapter 6.11.1 for details) is that the square root of time behaviour occurs only after a time delay of approximately 140 s at 353 K. This is the characteristic signature of a diffusive process<sup>182</sup> following a nucleation step. A close inspection of the AFM images in the immediate vicinity of the Pd entrance strip reveals a full row of regularly spaced hills, somewhat reminiscent of the patterns observed in compressed thin films on compliant substrates<sup>183</sup>. The observed time delay is due to the nucleation of these primordial hills. Once formed, they serve as seeds for the finger pattern generated by the continuous H absorption. While the H diffusion front moves through the sample, there is a competition between fingers. This leads to a slow increase of the width of the dominant fingers, while other fingers are terminated. The evolution of the finger pattern has been observed in all samples investigated in this work. It is obviously energetically more favourable to extend existing hills rather than generating new ones. Hydrogen is a dilation center in metals (see Chapter 0). Therefore, at the tip of a finger, where the lattice is dilated out-of-plane, it is more favourable for H to nucleate and form a new dihydride in this region. This is at the origin of the self-organisation of the finger patterns. A vivid demonstration of the favoured hill nucleation at the tip of fingers is shown in **Figure 6.5**. By using several Pd entrance

gates for H diffusion, finger patterns can collide with each other. For example in **Figure 6.5 a-iii**, finger patterns generated from two opposite directions collide at the median line. The head-on collision of two fingers leads to the synergetic generation of a huge central ridge. This synergetic effect, although weakened when two fingers meet under a sizeable angle (for example 90°), leads to the formation of meeting-lines that depend on the sample geometry and the geometric arrangement of the Pd entrance gates. This is clearly seen in the AFM images from **Figure 6.5 a-ii** to **v**. Although the finger patterns are largely influenced by the positions and the number of the Pd entrance gates, the height increase (averaged over the entire patch) generated by lateral H absorption is remarkably constant and close to 27.2%, which is the value measured in **Figure 6.2**. The ridges highlighted in the dashed boxes in **Figure 6.5 a** can reach relative height changes as high as 300%, which slightly increases the average height values from *i* to *v* stepwisely. The experimental finger patterns agree very well with the simulated streamlines (black lines) as shown in **Figure 6.5 b**.

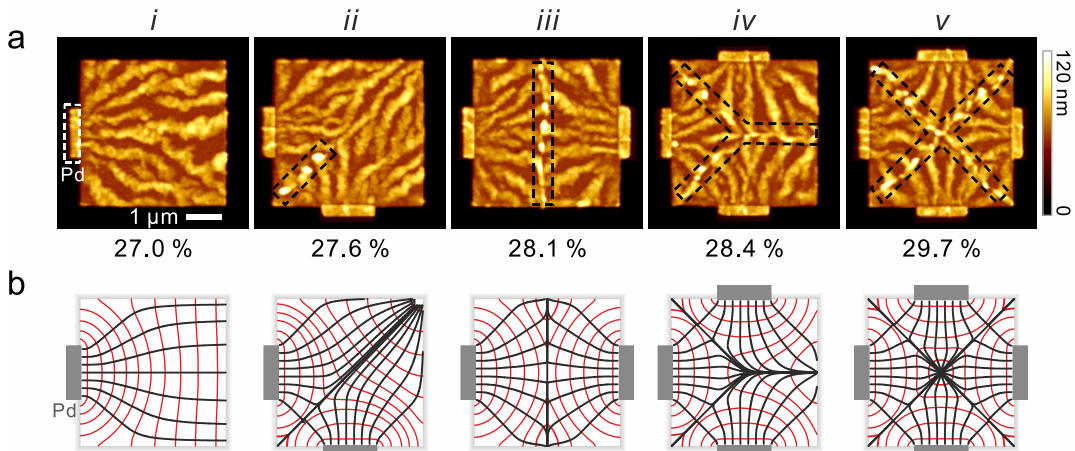


**Figure 6.5** (a) AFM images of the finger patterns for different arrangements of the Pd entrance gates. The samples are all  $4 \times 4 \mu\text{m}^2$  in size. The thicknesses of the individual Mg and Ti layers are the same as those in the previous figures. The black-dashed boxes highlight the high ridges resulting from the synergetically enhanced local piling up of Mg. The relative height changes averaged over the entire individual samples are (*i*) for one Pd gate, 27.0%; (*ii*) for two perpendicular Pd gates, 27.6%; (*iii*) for two parallel Pd gates, 28.1%; (*iv*) for three Pd gates, 28.4%; and (*v*) for four Pd gates, 29.7%. The ridges highlighted in the dashed boxes can reach relative height changes as high as 300%, which increases the average height values from *ii* to *v* stepwisely. (b) Simulation results for the sample configurations in (a). The diffusion fronts (red lines) are obtained from the simulations described in Appendix E. They are obtained for a chosen set of times  $t_n$  so that  $\sqrt{t_n}$  are equally spaced. The streamlines (black lines) are locally orthogonal to the diffusion fronts (red lines).

## 6.7. Hydrogen diffusion measurements

The recorded OR videos used to demonstrate the H loading/unloading symmetry in **Figure 6.4** are also directly relevant to measurements of the front mobility itself. The sharp colour change at the front of the finger patterns makes it possible to monitor accurately the time dependence of the diffusion front position. The results in Chapter 6.11.1 show that

the square of the front position  $x_{\text{front}}^2$  is proportional to time  $t$ , after the original finger seeds have been nucleated at  $t_{\text{nucleation}}$ . The front mobility  $K$  is defined as

$$K = \frac{x_{\text{front}}^2}{t - t_{\text{nucleation}}} \quad (6.3)$$

and has the same dimension ( $\text{m}^2\text{s}^{-1}$ ) as a diffusion coefficient<sup>182</sup>.

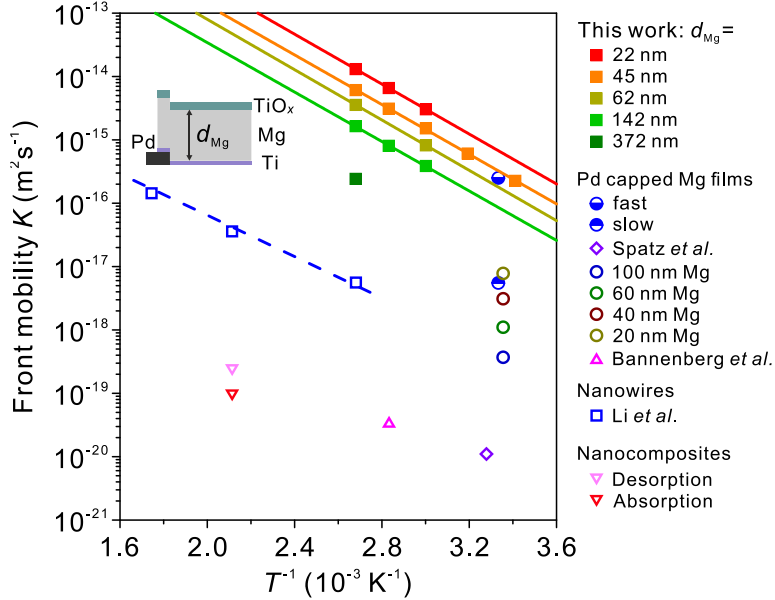


**Figure 6.6** Lateral front mobilities measured optically on 18 equivalent 3 nm Ti/ $d_{\text{Mg}}$  Mg/5 nm  $\text{TiO}_x$  samples with  $d_{\text{Mg}}$  varying from 22 to 372 nm (filled squares). For all the samples, the Pd entrance gate is 20 nm thick (see the inset schematic). The activation energy determined from the slope of the Arrhenius plot for the sample with  $d_{\text{Mg}} = 45$  nm is  $0.389 \pm 0.005$  eV. Considering the fact that the front mobility depends only on the ratio of the Mg and Pd entrance strip thicknesses (see **Figure 6.14 a**), the slopes of all Arrhenius plots should be the same. From the four Arrhenius plots in Fig.6, one finds an activation energy of  $0.390 \text{ eV} \pm 0.003 \text{ eV}$ . Estimated values of the front mobilities for Pd capped Mg films<sup>83,171,175,184</sup>, nanowires<sup>185</sup>, and nanocomposites<sup>186</sup> are also included. The values for H diffusion in a very thin Mg layer sandwiched between relatively thick Ti and Pd layers<sup>175</sup>, in 20–100 nm Mg films capped with a 5 nm Pd layer<sup>184</sup>, in nanowires<sup>185</sup>, and in nanocomposites<sup>186</sup> are estimated from the published absorption or desorption curves using  $K \propto L^2/t_{1/2}$ , where  $L$  is the characteristic size of the samples and  $t_{1/2}$  is the time necessary to half-fill the samples. Interestingly, the slope of the Arrhenius plot for the nanowire data<sup>185</sup> is comparable to the slopes of our plots.

The great advantage of the optical hydrogenography is that it allows to monitor simultaneously a large number of samples<sup>187</sup>, therefore reducing statistical errors to an unprecedented minimum. The results of the samples with various Mg thicknesses in **Figure 6.6** exhibit a series of absolutely remarkable features. First, in-plane H diffusion is fast. It is almost five orders of magnitude faster at 300 K than the value of out-of-plane diffusion from Spatz *et al.*<sup>171</sup>. It remains fast over macroscopic distances in sharp contrast to the results of Uchida *et al.*<sup>83</sup>, who observed fast diffusion only during a relatively short period of time ( $\sim 1,400$  s) over a short distance ( $\sim 200$  nm) before the blocking layer was formed. In their case, the formation of a 200 nm thick blocking layer reduced further H absorption by approximately two orders of magnitude and the corresponding apparent

diffusion coefficient dropped to typically  $10^{-18} \text{ m}^2\text{s}^{-1}$ . Second, the temperature  $T$  dependence of the front mobility follows accurately the Arrhenius relation

$$K = K_0 \exp\left(-\frac{E_a}{k_B T}\right) \quad (6.4)$$

with the prefactor  $K_0 = 1.11 \times 10^{-9} \text{ m}^2\text{s}^{-1}$ , and the activation energy  $E_a = 0.389 \text{ eV}$  independent of the Mg thickness.  $k_B$  is the Boltzmann constant. The value of  $E_a$  is close to that of H in Mg alloyed<sup>188</sup> with 2 at% cerium, where  $E_a = 0.41 \text{ eV}$ . It is also comparable to that for H diffusion in the fcc metals Cu (0.40 eV), Ni (0.40 eV), Pd (0.23 eV)<sup>189</sup> and the hcp Y (0.37-0.38 eV)<sup>190</sup>. Comparison with hcp and fcc metals is meaningful as these two structures differ only by the stacking of closed packed hexagonal planes.

Third, in contrast to perpendicular diffusion experiments where relatively low  $\text{H}_2$  pressures must be used in order to minimize the deleterious effects of the  $\text{MgH}_2$  blocking layer<sup>83,87</sup>, we find for lateral H diffusion that the front mobility increases with increasing hydrogen pressure as indicated in Chapter 6.11.2.

## 6.8. Detailed sample layout

Here, we illustrate all the relevant dimensions of the samples in **Figure 6.1**.

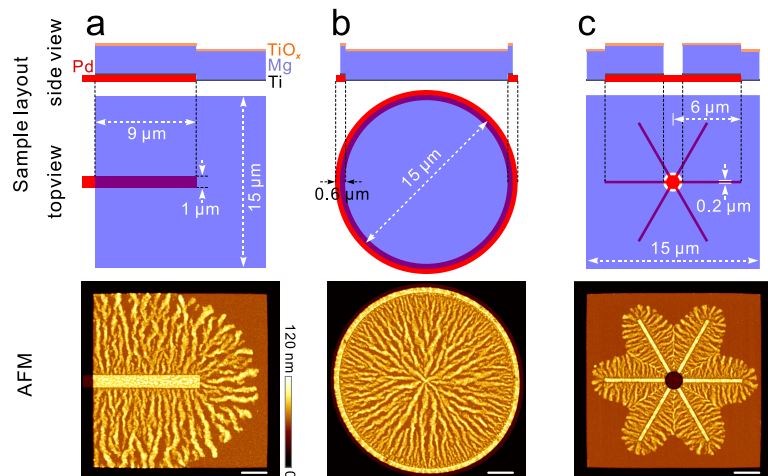


**Figure 6.7** Details of the layout of the three samples in **Figure 6.1**. The AFM images are the same as in **Figure 6.1** but now in top view for a direct correlation with the sample layout. The 45 nm thick Mg layer is sandwiched between a 3 nm Ti buffer layer and a 5 nm  $\text{TiO}_x$  capping layer. (Scale bar: 2  $\mu\text{m}$ ).

## 6.9. Reproducibility and general properties of finger patterns

### 6.9.1. Constancy of average height increase

Here, we indicate how the average heights  $\bar{z}(x)$  calculated along the  $y$ -direction of the four samples in **Figure 6.8** a depends on position  $x$  with respect to the Pd-entrance gate. It

is remarkable that  $\bar{z}(x)$  is essentially independent of  $x$  and the total average height increase  $\overline{z(x)}$  is nearly the same for all four samples within 0.7%.

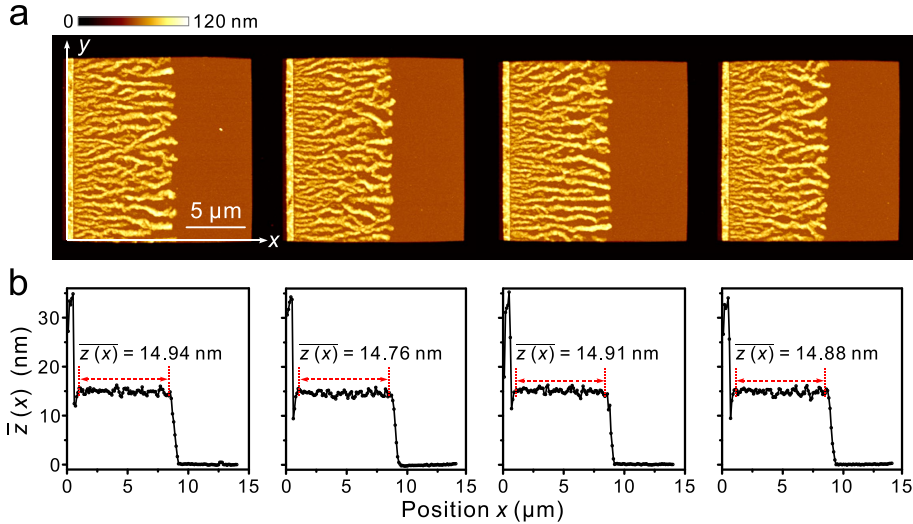


**Figure 6.8** (a) Finger patterns measured at 353 K after H loading at 20 kPa of H<sub>2</sub> in four identical  $15 \times 15 \mu\text{m}^2$  3 nm Ti/45 nm Mg/5 nm TiO<sub>x</sub> patches. The thickness of the Pd entrance gates are 20 nm. (b) Average heights calculated along the  $y$ -direction as a function of the  $x$ -position for the corresponding samples in (a). The total average height increase  $\overline{z(x)}$  is the mean value of all line-averages  $\bar{z}(x)$  evaluated within the finger pattern region in each sample.

### 6.9.2. Average heights for two loading/unloading cycles

The variations of the average sample height during the two loading/unloading cycles in **Figure 6.2** can fully be rationalized if one assumes that the bulk volume expansion of Mg and Ti upon H absorption is entirely accommodated out-of-plane. The molar volumes  $V$  of Mg and MgH<sub>2</sub> are 13.98 and 18.15 cm<sup>3</sup>mol<sup>-1</sup>, respectively. The relative volume expansion of Mg is

$$\left(\frac{\delta V}{V}\right)_{\text{Mg}} = \frac{V_{\text{MgH}_2} - V_{\text{Mg}}}{V_{\text{Mg}}} = 29.83\% \quad (6.5)$$

For titanium,  $V_{\text{Ti}} = 10.62 \text{ cm}^3\text{mol}^{-1}$ ,  $V_{\text{TiH}_2} = 13.27 \text{ cm}^3\text{mol}^{-1}$  and

$$\left(\frac{\delta V}{V}\right)_{\text{Ti}} = \frac{V_{\text{TiH}_2} - V_{\text{Ti}}}{V_{\text{Ti}}} = 24.95\% \quad (6.6)$$

For the sample in **Figure 6.2**, the pristine total thickness of design is 53 nm. After first H loading, the 3 nm Ti buffer layer and 45 nm Mg layer have formed dihydrides, while the 5 nm TiO<sub>x</sub> capping layer does not react with H. The resulting thickness predicted by Eqs. (6.5) and (6.6) is  $[3 \text{ nm} \times (1+24.95\%) + 45 \text{ nm} \times (1+29.83\%) + 5 \text{ nm}] = 67.17 \text{ nm}$ . This agrees nicely with the measured value 66.9 nm indicated for the first H loading in the right panel of **Figure 6.2 b**. After the first H unloading, the large negative enthalpy of hydride formation of TiH<sub>2</sub> prevents the buffer layer from unloading and the predicted height is  $[3 \text{ nm} \times (1+24.95\%) + 45 \text{ nm} + 5 \text{ nm}] = 53.75 \text{ nm}$ , again in good agreement with the measured

value of 53.1 nm. According to this model, the average heights of fully loaded samples should remain the same, *i.e.*, 66.9 nm, after the second loading and in fact for all subsequent loadings. This is nicely confirmed by the measured average height of 66.9 nm. Similar behaviour is expected for the unloaded samples. Fully unloaded samples should all have an average height of 53.75 nm. After the second unloading, the measured average height is however 54.8 nm, which is ~1 nm higher than after the first unloading. This could be due to the formation of voids. Cross-sections of the samples by means of the FIB did, however, not reveal blisters or buckling (see Chapter 6.9.4). More likely is that the sample was not fully unloaded after the second unloading. Nonetheless, it is absolutely remarkable that the assumption of a complete out-of-plane expansion during hydrogenation leads to average height estimates that are in very good agreement with the experiments.

### 6.9.3. Zero in-plane expansion during hydrogenation

The excellent agreement between the measured and predicted average heights in Chapter 6.9.2 is *a posteriori* confirmation of the validity of the assumption that the volume change upon hydrogenation is entirely accommodated out-of-plane for the Ti/Mg/TiO<sub>x</sub> samples considered in this work.

Another proof of the vanishing in-plane expansion, can be obtained by looking simultaneously at patches with various overall hydrogen contents. The 9 patches in **Figure 6.9** have all the same dimensions. The only difference is the lengths of the Pd entrance gates that vary from 0.3 μm up to 5 μm. The SEM images are recorded at a time when the patch with the full length Pd gate (top right patch) is almost completely loaded with hydrogen, while only little hydrogen has entered the patch with the smallest Pd entrance gate (bottom left patch). The identical sample sizes (yellow and blue arrows) demonstrate that the lateral dimensions do not depend on the total amount of hydrogen. The total hydrogen content of a patch thus has obviously very little influence on the in-plane patch dimensions. Within experimental errors we conclude that for all the samples investigated in this work the lateral relative expansion is smaller than 0.5%.

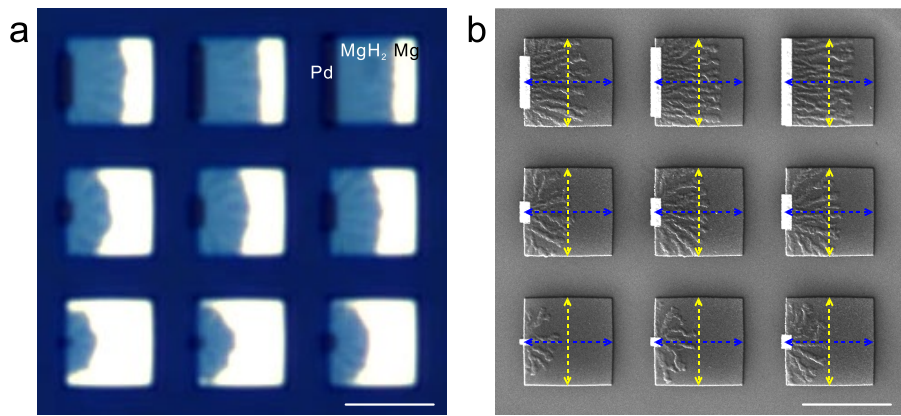


**Figure 6.9** (a) OR and (b) SEM images of 9 identical 3 nm Ti/45 nm Mg/5 nm TiO<sub>x</sub> samples with various lengths of the Pd entrance gates. The 5 × 5 μm<sup>2</sup> samples are simultaneously loaded with H for 1,390 s at 353 K at 20 kPa. The yellow and blue arrows in (b) are a guide to the eye to check that the lateral dimensions do not depend on the total amount of H. (Scale bar: 5 μm).

#### 6.9.4. Absence of buckles

Cross-sections of the samples generated by Focused Ion Beam (FIB) show that the topographic finger patterns observed in AFM are not due to delamination or buckling. A representative example is given in **Figure 6.10**.

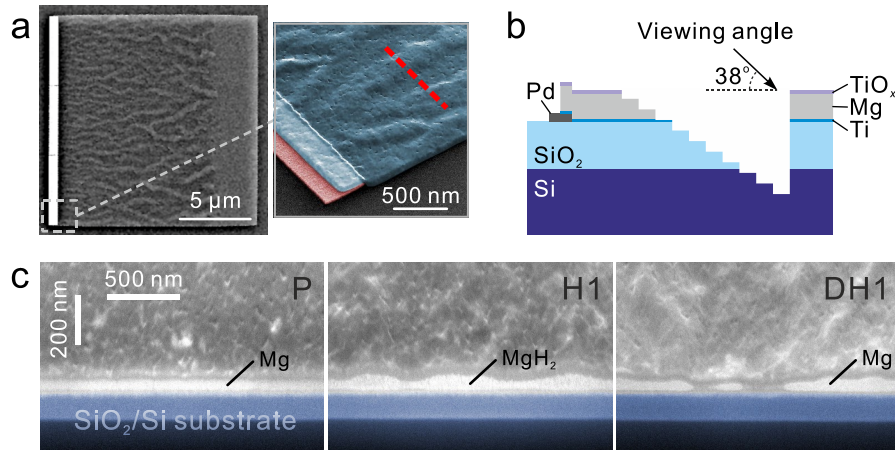


**Figure 6.10** (a) SEM images (top and detail of tilted view) of a representative sample. The red dash line indicates the position of the FIB milling. (b) Schematic of the FIB milling. (c) SEM cross-sectional images of the samples for the pristine (P), first hydrogenation (H1), and dehydrogenation (DH1) states, respectively, after stepped ion-milling to expose the surface. The images are taken with a 38° tilt from horizontal to provide perspective on the vertically etched film surface.

#### 6.9.5. Mechanism

The large lattice expansion induced by H absorption in metals can lead to delamination and buckling of metallic films evaporated on low adhesion substrates. This is for example the case for Niobium films evaporated on mica<sup>191</sup> or Pd films deposited on quartz<sup>192</sup>. The

typical size of buckles is typically tens of micrometers. In our samples cross-sections obtained by means of FIB do not reveal any delamination or buckle. Furthermore, the width of individual fingers is always submicron.

The mechanism responsible for the accommodation of the large volume expansion (approx. 32%) accompanying H absorption in Mg is therefore of a different nature. It is related to the texture of our samples. Our Mg films have predominantly their hexagonal *c*-axis in a direction perpendicular to the substrate. During hydrogenation, rutile MgH<sub>2-d</sub> grows predominantly with a (110) direction perpendicular to the substrate. This is schematically indicated in **Figure 6.11**. The resulting structure can be visualized as a structure made of quasi-hexagonal planes separated by  $d(\text{MgH}_2) = 3.197 \text{ \AA}$  with H occupying in-plane and inter-plane positions. The separation between hexagonal planes in the hcp structure of Mg being  $2.065 \text{ \AA}$  we see that the out-of-plane expansion [ $d(\text{MgH}_2) - d(\text{Mg})]/d(\text{Mg})$ ] upon H absorption in Mg is  $\sim 22.7\%$ . The relative in-plane increase of the (quasi)hexagon area is only 8.3%. As a consequence stresses are efficiently minimized by nucleating the dihydride phase with a (110) direction perpendicular to the substrate. Delamination would destroy the Mg/Ti interface and cost additional surface energy<sup>174</sup>. In a lateral diffusion experiment the Mg layer has further the possibility to continuously minimize strains near the front. The overall result is that in our samples the lateral relative expansion is at most 0.5%. This is reminiscent of the morphological changes induced by H in another hexagonal host metal, yttrium<sup>193-195</sup>.

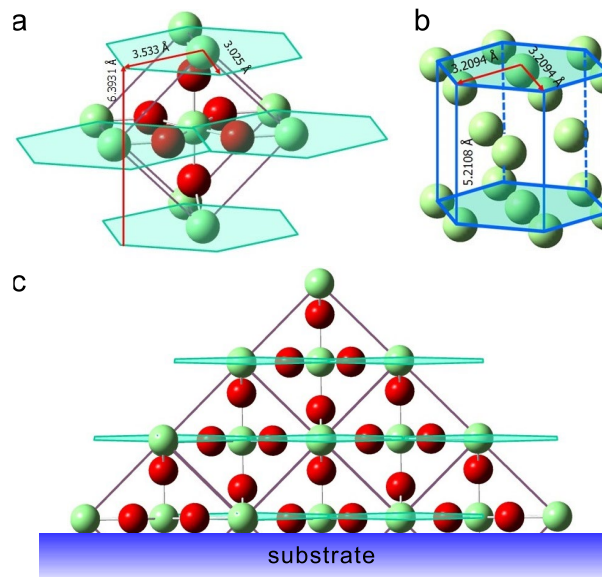


**Figure 6.11** (a) MgH<sub>2</sub> rutile unit cell with [110] direction perpendicular to the substrate. The quasi-hexagons are indicated in semi-transparent green. (b) HCP structure of Mg. (c) Part of the MgH<sub>2</sub> lattice viewed along the [001] direction of the rutile cell showing that H occupies both in-plane and inter-plane position of the Mg sublattice. The red and green balls represent H and Mg atoms, respectively.

## 6.10. H loading-unloading symmetry

Snapshots taken from the videos of the H loading and unloading of the five samples in **Figure 6.3 b** are shown in **Figure 6.12**. They illustrate nicely that the diffusion fronts during H absorption have the same shape as during H desorption at similar times after starting the absorption and starting the desorption, respectively. The times are not identical because different processes take place at the Pd entrance gate. During absorption, H<sub>2</sub> is catalytically split into two H atoms at the Pd surface, while during desorption two separate H atoms have to recombine to leave the Pd surface. The snapshots demonstrate also unambiguously that all the exchange of hydrogen with the Mg patches occurs via the Pd gates. During desorption, this is the reason why a bright reflection due to metallic Mg formation moves from left to right starting at the Pd gate.

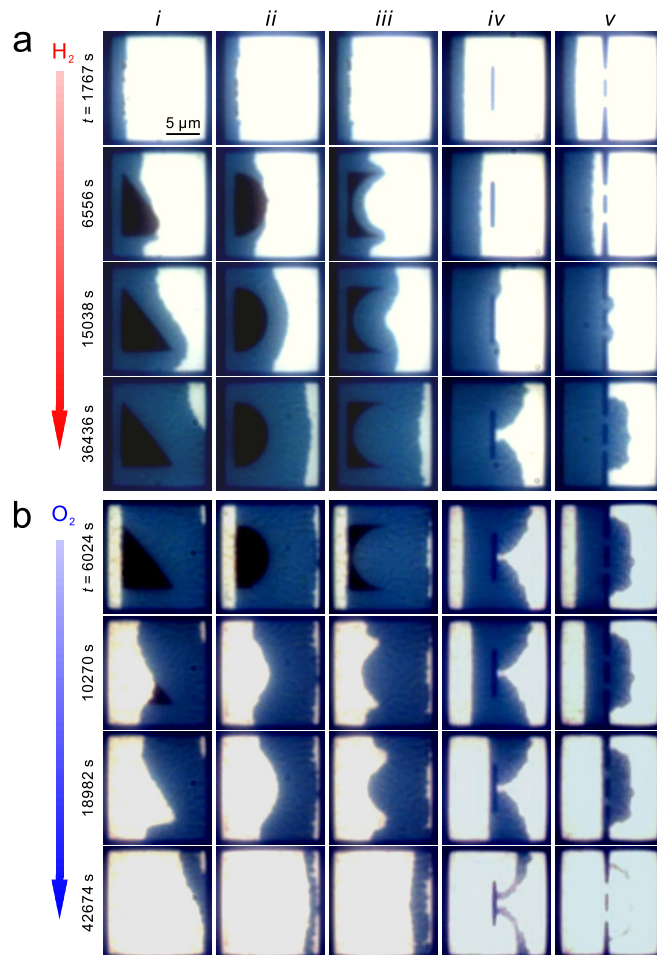


**Figure 6.12** (a) Snapshots of the OR video recorded at 353 K during H loading at 20 kPa of H<sub>2</sub> at times 1,767 s, 6,556 s, 15,038 s, and 36,436 s for the five samples in **Figure 6.3 b**. (b) Snapshots of the OR video during H unloading at 353 K at 20 kPa of O<sub>2</sub> for the same samples taken at times 6,024 s, 10,270 s, 18,982 s, and 42,674 s, respectively. In all snapshot images, the dark bluish regions correspond to MgH<sub>2</sub>, while the bright reflection areas are due to metallic Mg.

## 6.11. Measurements of diffusion front mobility

### 6.11.1. Temperature dependence of front mobility

Here, we indicate a typical example of parallel measurements. The sharp colour change at the front of the finger patterns makes it possible to monitor accurately the time dependence of the diffusion front position as shown in **Figure 6.13**. The diffusion front positions separating the dark bluish  $\text{MgH}_2$  finger regions from the bright metallic Mg are recorded with a camera and plotted as a function of time. The linear dependence of the squared front position as a function of time indicates the diffusive origin of the H motion. The slope of each line in the bottom panel is equal to the H diffusion front mobility  $K$ . The corresponding standard deviations are 3.51%, 3.51%, 5.25%, 4.93%, and 6.27%, respectively. Such an accuracy has never been demonstrated for H diffusion experiments between room temperature and 373 K. As a result the errors in the data points in Fig. 6 are much smaller than the size of the square symbols.

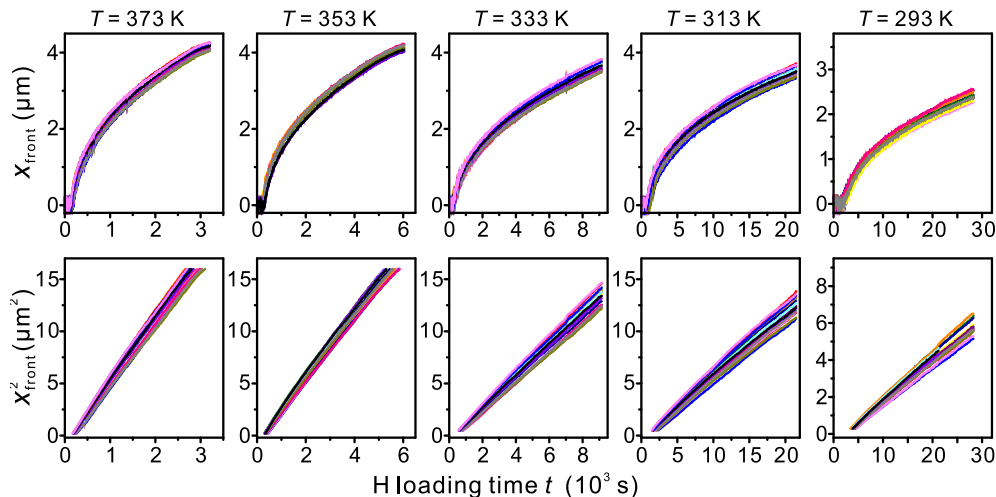


**Figure 6.13** Time dependence of the front position during H diffusion in 18 identical  $5 \times 5 \mu\text{m}^2$  3 nm Ti/45 nm Mg/5 nm  $\text{TiO}_x$  patches loaded at 20 kPa of  $\text{H}_2$  at different temperatures.

### 6.11.2. Dependence of the front mobility on the Mg thickness and $\text{H}_2$ pressure

Here we find that the front mobility depends on the thickness of the sample as shown in **Figure 6.14 a**. For the sample architecture indicated in the inset of **Figure 6.14 a**, one expects that the amount of hydrogen entering the 3 nm Ti/ $d_{\text{Mg}}$  Mg/5 nm  $\text{TiO}_x$  patch depends on the ratio of the thickness of the Pd entrance gate  $d_{\text{Pd}}$  and that of the Mg  $d_{\text{Mg}}$ . To lowest order we expect that

$$K(d_{\text{Pd}}, d_{\text{Mg}}) \propto \frac{d_{\text{Pd}}}{d_{\text{Mg}}} \quad (6.7)$$

This expectation is confirmed by measurements of the front mobility for a series of samples with  $d_{\text{Pd}} = 20 \text{ nm}$  and  $22 \text{ nm} \leq d_{\text{Mg}} \leq 372 \text{ nm}$ . The front mobility varies linearly as a function of the inverse Mg thickness. Extrapolation of the data to  $d_{\text{Mg}}^{-1} = 0.05$  leads to

$$K(d_{\text{Pd}} = d_{\text{Mg}} = 20 \text{ nm}) = 1.41 \times 10^{-14} \text{ m}^2 \text{s}^{-1} \quad (6.8)$$

This is the front mobility of a sample with the same thickness of the Pd entrance gate and the Mg layer.

We also find that in contrast to perpendicular diffusion experiments where relatively low H<sub>2</sub> pressures must be used in order to minimize the deleterious effects of the MgH<sub>2</sub> blocking layer, for lateral H diffusion the front mobility increases with increasing hydrogen pressure as indicated in **Figure 6.14 b**.

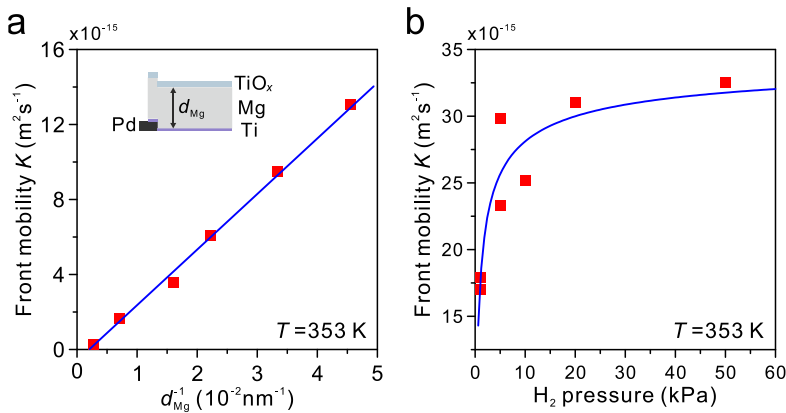


**Figure 6.14** (a) H diffusion front mobility measured on 3 nm Ti/ $d_{\text{Mg}}$  Mg/5 nm TiO<sub>x</sub> samples at 353 K at 20 kPa. The thickness of the Pd entrance gate is always 20 nm while the thickness  $d_{\text{Mg}}$  of the Mg layer varies from 22 to 372 nm. The observed linear dependence (blue line) confirms Eq. (6.7). (b) H diffusion front mobility measured on 3 nm Ti/45 nm Mg/5 nm TiO<sub>x</sub> samples at 353 K at H<sub>2</sub> pressure varying from 1 to 50 kPa. The blue curve is obtained from a model based on the simulations described in Chapter 6.12.

## 6.12. Theoretical model

The purpose of the simulations is to reproduce all the characteristic features of the finger patterns investigated in this work. To keep the simulations simple, the 3 nm Ti/ $d_{\text{Mg}}$  Mg / 5 nm TiO<sub>x</sub> samples are treated as one vertically homogeneous medium characterized with a hydrogen concentration dependent diffusion coefficient  $D(c)$ . We do not take into account the different crystal structures of Mg (hexagonal) and MgH<sub>2</sub> (rutile) and treat the Mg-H system as a lattice-gas MH<sub>c</sub> with  $0 \leq c \leq 1$  and a critical temperature much higher than room temperature since the pressure-composition isotherms of Mg-H exhibit clear plateaus at all temperatures investigated here. Within this model the inclusion of objects with fast H diffusion (made for example of Pd) in the Mg layer is taken into account as a local modification of  $D(c)$  that depends on the geometry of the inserted object. Excellent agreement with the observed finger patterns is obtained with a local enhancement factor of 100 at the object location for  $D_i$  in Eq. (6.1).

### 6.12.1. Concentration dependent diffusion coefficient

The symmetry between H loading and unloading illustrated in Chapter 6.10 implies that the diffusion coefficient assumes similar values in the limit of small and high hydrogen concentrations. The concentration dependence chosen for all simulations is

$$D(c) = D_0 [e^{-\alpha c} + e^{-\alpha(1-c)}] \quad (6.9)$$

with  $\alpha = 20$ , where  $D_0$  is a prefactor. Below we show that this relation, which is inspired by a simple lattice-gas model, leads to diffusion concentration profiles with a sharp front that mimics the coexistence of the dilute  $\alpha\text{-MH}_c$  (with typically  $0 < c < 0.1$ ) and concentrated  $\beta\text{-MH}_c$  (with typically  $0.9 < c < 1$ ).

In the simplest mean-field description of a lattice gas the chemical potential of H in a metal M is

$$\mu_{\text{H}} = RT \ln \left( \frac{c}{1-c} \right) + H_{\text{H}}^{\infty} - Ac - TS_{\text{H}} \quad (6.10)$$

where  $R$  is the gas constant;  $T$  is the absolute temperature;  $c$  is the H concentration,  $c = \text{H/M}$ ;  $H_{\text{H}}^{\infty}$  is the enthalpy of H solution in M;  $A$  is the magnitude of the long-range effective H-H interaction; and  $S_{\text{H}}$  is the entropy of H in M. The minus sign in front of  $A$ , which is assumed to be a positive quantity (*i.e.*,  $A > 0$ ), corresponds to an attractive H-H interaction. At thermodynamic equilibrium with surrounding  $\text{H}_2$  gas we have

$$\mu_{\text{H}} = \frac{1}{2} \mu_{\text{H}_2} \quad (6.11)$$

The chemical potential of  $\text{H}_2$  gas is

$$\mu_{\text{H}_2} = H_{\text{H}_2} - TS_{\text{H}_2} = H_{\text{H}_2} - TS_{\text{H}_2}^0 + RT \ln p \quad (6.12)$$

where  $p$  is the  $\text{H}_2$  pressure expressed in unit of bar. Equations (6.10) and (6.12) together with Eq. (6.11) lead to the pressure-composition isotherms<sup>68</sup>

$$\ln p = 2 \ln \left( \frac{c}{1-c} \right) + 2 \frac{\Delta H_{\infty} - Ac - T \Delta S}{RT} \quad (6.13)$$

where

$$\Delta H_{\infty} = H_{\text{H}}^{\infty} - \frac{1}{2} H_{\text{H}_2} \quad (6.14)$$

and

$$\Delta S = S_{\text{H}} - \frac{1}{2} S_{\text{H}_2}^0 \quad (6.15)$$

are the enthalpy and entropy of H solution in M, respectively.

The isotherm for the critical temperature  $T_c$ , has an inflection point with zero slope, *i.e.*, the first and second derivatives of  $\ln p$  as a function of  $c$  are both zero at the critical concentration  $c = c_c$ . From these conditions, we find

$$c_c = \frac{1}{2} \quad (6.16)$$

and

$$T_c = \frac{A}{4R} \quad (6.17)$$

The spinodal is by definition the curve,  $T_s = T_s(c_s)$  for which

$$\frac{d}{dc}(\ln p) = 0 \quad (6.18)$$

From Eq. (6.13) with Eq. (6.17) follows that

$$T_s = 4T_c c_s (1 - c_s) \quad (6.19)$$

This simple relation shows that the spinodal curve is a parabola with its top at  $c_s = 1/2$ . Thus the spinodal is symmetric under the transformation  $c = \delta \rightarrow c = 1 - \delta$  and at each temperature  $T < T_c$  there are two spinodal concentrations  $c_s^{\text{low}}$  and  $c_s^{\text{high}}$ : at temperatures below  $T_c$  the dilute  $\alpha\text{-MH}_c$  and concentrated  $\beta\text{-MH}_c$  coexist. The concentration  $c_i$  of the coexisting  $\alpha$ - and  $\beta$ -phases are given by the condition

$$\ln\left(\frac{c_i}{1 - c_i}\right) - 4\frac{T_c}{T}\left(\frac{1}{2} - c_i\right) = 0 \quad (6.20)$$

with  $i = \alpha$ -phase or  $\beta$ -phase. The coexistence curve  $T_{\alpha-\beta} = T_{\alpha-\beta}(c)$  is then

$$T_{\alpha-\beta} = 4T_c \frac{\left(\frac{1}{2} - c_i\right)}{\ln\left(\frac{c_i}{1 - c_i}\right)} \quad (6.21)$$

### 6.12.2. Diffusion

From irreversible thermodynamics follows that a gradient in chemical potential  $\mu_H$  induces a current  $\mathbf{J}$  of hydrogen such that

$$\mathbf{J} = -L\nabla\mu_H \quad (6.22)$$

At a given temperature, the chemical potential  $\mu_H$  is only a function of the hydrogen concentration  $c$  as shown in Eq. (6.10). Thus the Eq. (6.22) reduces to

$$\mathbf{J} = -D(c)\nabla c \quad (6.23)$$

with

$$D(c) = L \frac{d\mu_H}{dc} \quad (6.24)$$

We do not know *a priori* the function  $L = L(c)$ , however the lattice gas expression

$$\frac{d\mu_H}{dc} = \frac{RT}{c(1 - c)} - A \quad (6.25)$$

from Eq. (6.13) can be used to determine the behaviour of  $L = L(c)$  in two limiting cases. From Fick's law<sup>182</sup>, we know that the diffusion coefficient  $D(c)$  in Eq. (6.9) tends towards a constant for  $c \rightarrow 0$  or  $c \rightarrow 1$ . In the limit  $c \rightarrow 0$ ,

$$D_0 = D(c)|_{c \rightarrow 0} = L \frac{d\mu_H}{dc} \Big|_{c \rightarrow 0} \cong L \frac{RT}{c} \quad (6.26)$$

hence

$$L_{c \rightarrow 0} = \frac{D(c)|_{c \rightarrow 0}}{RT} c = \frac{D_0}{RT} c \quad (6.27)$$

Similarly, in the limit  $c \rightarrow 1$ , we have

$$L_{c \rightarrow 1} = \frac{D(c)|_{c \rightarrow 1}}{RT} (1 - c) = \frac{D_1}{RT} (1 - c) \quad (6.28)$$

Assuming for simplicity that

$$D_0 = D_1 \quad (6.29)$$

we obtain from Eqs. (6.22), (6.27)–(6.29)

$$\mathbf{J} = -D_0 \left[ 1 - \frac{A}{RT} c(1 - c) \right] \nabla c \quad (6.30)$$

This equation implies that the diffusion coefficient

$$D(c) = D_0 f(c) = D_0 \left[ 1 - \frac{A}{RT} c(1 - c) \right] \quad (6.31)$$

is strongly dependent on the H concentration  $c$ . This is fully in agreement with the detailed measurements on Nb-H discussed extensively by Alefeld *et al.*<sup>196</sup> The function  $f(c)$  in Eq. (6.31) can also be expressed in terms of the critical temperature in Eq. (6.17). Then

$$f(c) = \left[ 1 - 4 \frac{T_c}{T} c(1 - c) \right] \quad (6.32)$$

At the critical concentration  $c_c = 1/2$ , the diffusion coefficient tends towards zero when the temperature is decreased to the critical temperature  $T_c$ . At the critical temperature Eq. (6.32) reduces to

$$f_c(c) = 1 - 4c(1 - c) \quad (6.33)$$

The concentration dependence predicted by Eq. (6.32) for various values of the parameter  $T/T_c$  are shown in **Figure 6.15**.

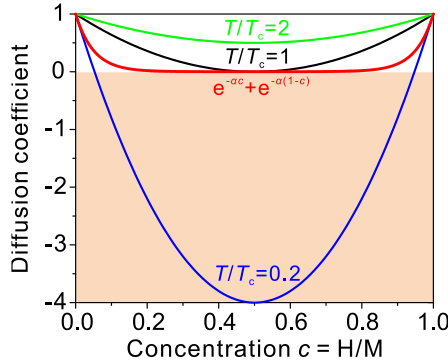


**Figure 6.15** Concentration dependence of the diffusion coefficient predicted by the lattice-gas expression in Eq. (6.32) for three temperatures  $T$  normalized to the critical temperature  $T_c$ . The red curve represents the concentration dependent diffusion coefficient function  $[e^{-\alpha c} + e^{-\alpha(1-c)}]$  actually used for the simulations. At low  $c$  and  $c \approx 1$ , the red curve has the same slope as the parabola (blue) with  $T/T_c = 0.2$ .

Although Eq. (6.33) has been used to model Li diffusion in Li-ion batteries<sup>197</sup>, it is not applicable to the simulation of the finger patterns in this work. This is easily understood since our experiments are carried out at temperatures where the dilute  $\alpha\text{-MH}_c$  and concentrated  $\beta\text{-MH}_c$  coexist. This corresponds to a situation in our model with  $T \ll T_c$  and thus Eq. (6.31) implies negative diffusion coefficients for concentrations  $c_s^{\text{low}} < c < c_s^{\text{high}}$ , where  $c_s^{\text{low}}$  and  $c_s^{\text{high}}$  are the two solutions of Eq. (6.19). We found that an efficient way to simulate diffusion fronts is to use the following concentration dependent diffusion coefficient

$$D(c) = D_0 f(c) = D_0 [e^{-\alpha c} + e^{-\alpha(1-c)}] \quad (6.34)$$

Good agreement with experiment is obtained with  $\alpha = 20$ . The very small value of  $D(c)$  for concentrations  $\frac{1}{\alpha} < c < 1 - \frac{1}{\alpha}$  leads to a drastic slowing down of the diffusion process, and thus to a very steep front, in agreement with the experimental data in **Figure 6.3** to **Figure 6.5**. The good agreement obtained with the observed finger patterns is obviously an indication of the usefulness of Eq. (6.34). It is furthermore important to point out that the same concentration dependent diffusion coefficient explains also the observed  $\text{H}_2$  pressure dependence of the front mobility described in Chapter 6.11.

### 6.12.3. Simulation procedure

Our simulations are based on a diffusion equation. Particle conservation

$$\frac{\partial c}{\partial t} + \nabla \cdot \mathbf{J} = 0 \quad (6.35)$$

together with Eqs. (6.23), (6.34), and (6.35), lead to the non-linear diffusion partial differential equation

$$\frac{\partial c}{\partial t} = D_0 \nabla \cdot [f(c) \nabla c] \quad (6.36)$$

In our numerical procedure, this equation is solved using Euler integration with for hydrogen loading a  $c = 1$  boundary condition at the Pd entrance gate and zero flux boundary conditions elsewhere at the borders of the sample. For unloading, a  $c = 0$  boundary condition is used. For the numerical algorithm, Eq. (6.36) is rewritten as

$$\frac{\partial c}{\partial t} = D_0 \nabla f(c) \cdot \nabla c + D_0 f(c) \nabla^2 c \quad (6.37)$$

The first order numerical derivatives yield values in between the cells that tile the sample and hence are averaged between adjacent inter cell values, thus yielding values at the cells. This (together with a not too large time step) prevents the well-known unphysical generation of checkerboard patterns. The second order numerical derivative automatically gives values at the cells and is adjusted to prevent the generation of rectangular patterns that reflect the cells by a method analogous to that of Oono *et al.*<sup>192</sup>

#### 6.12.4. Loading-unloading symmetry in diffusion simulations

For a deeper understanding of the H loading/unloading symmetry, we indicate in **Figure 6.16** a how the concentration profiles evolve during H loading with a fixed concentration  $c = 1$  applied at the left-hand side of the sample until the sample is half filled with hydrogen. Then the concentration on the left-hand side is abruptly decreased to 0 and the concentration profiles evolve as indicated in **Figure 6.16** b. Two features are remarkable: i) the front moves in both cases in the same way, *i.e.*, from left to right, although the concentration gradient at the H loading/unloading diffusion front is reversed; ii) the diffusion front at the end of H loading time (indicated by the dash line in **Figure 6.16**) remains essentially unchanged until it is hit by the unloading front (from left-hand side). This is exactly what is observed experimentally in **Figure 6.12**.

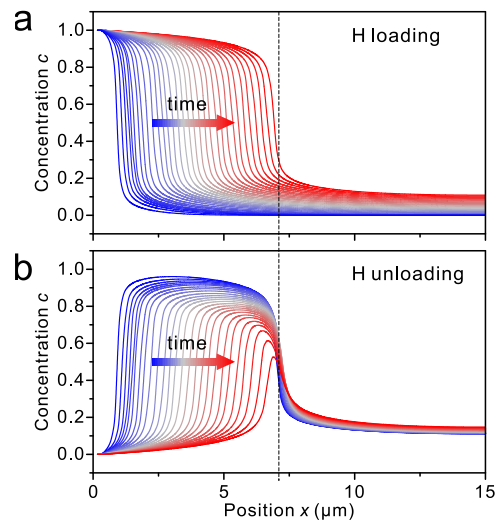


**Figure 6.16** Time evolution of calculated concentration profiles (a) during H loading with an imposed boundary concentration equal to 1 on the left-hand side, and (b) after a sudden decrease of the boundary concentration to 0. In both cases, there is no particle current at the right-hand side of the sample. The arrows indicate that the front movements are the same in both cases. The dash line indicates the diffusion front position at the end of H loading time.

### 6.12.5. Diffusion simulations for samples with inserted objects

We describe here in detail the procedure followed to generate the simulated fronts in **Figure 6.4 c** and **Figure 6.5 b**. For example, we consider the situation where a prism (*i.e.*, Pd) is inserted in a medium (*i.e.*, Mg) as shown in **Figure 6.3 a**. For the medium, we set  $D_0$  in Eq. (6.34) equal to unity, *i.e.*,  $D_{\text{medium}} = 1$ , while for the object we choose  $D_{\text{object}} = 100$ , so that  $D_{\text{object}}/D_{\text{medium}} = 100$ . In **Figure 6.17 a**, a simulated concentration profile for this situation is shown at a time when the prism is partially filled with H. The line of constant concentration  $c = 0.5$  (thick blue lines in **Figure 6.17**) is taken as the diffusion front at that time. Front lines for a set of selected times are shown as red lines in **Figure 6.17 b**.

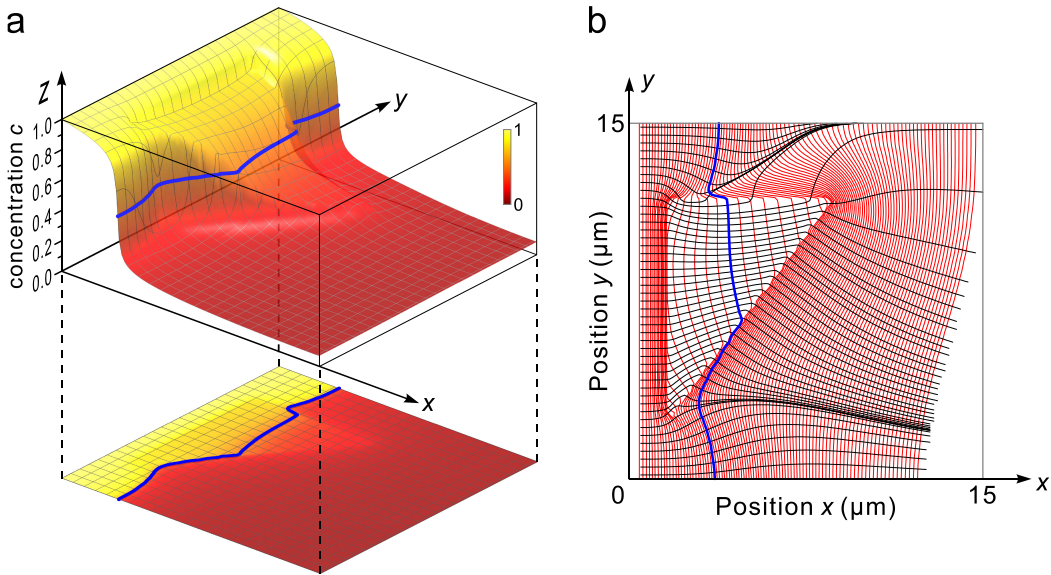


**Figure 6.17** (a) Concentration profile obtained from Eqs. (6.34) and (6.36) with  $D_{\text{object}}/D_{\text{medium}} = 100$  at a time where the inserted prism with fast H diffusion is approximately half-filled with H. The blue line of constant concentration  $c = 0.5$  is taken as the diffusion front line. (b) Front lines (red) for a large set of times  $t_n$  that are equidistant in  $\sqrt{t_n}$ . The corresponding streamlines (black) are locally perpendicular to the front lines.

### 6.12.6. Effective diffusion coefficient of a Pd object in quasi-free Mg

The simulations lead to streamlines that are consistent with the observed finger patterns measured at 353 K if the ratio

$$\frac{D_{\text{object}}}{D_{\text{medium}}} = 100 \quad (6.38)$$

Our object is made of Pd, while our medium is Mg. At 353 K the diffusion coefficient of H in Pd is<sup>196</sup>

$$D_{\text{Pd}}(353 \text{ K}) = 1.5 \times 10^{-10} \text{ m}^2 \text{s}^{-1} \quad (6.39)$$

and from the measured value of  $D_{\text{Mg}}(353 \text{ K})$ , we expect naively

$$\frac{D_{\text{Pd}}}{D_{\text{Mg}}} = \frac{1.5 \times 10^{-10} \text{ m}^2 \text{s}^{-1}}{3.1 \times 10^{-15} \text{ m}^2 \text{s}^{-1}} \approx 4.8 \times 10^4 \quad (6.40)$$

That the actual ratio in Eq. (6.38) is much lower is due to the fact that as soon as the  $\text{MgH}_2/\text{Mg}$  front hits the Pd object (*i.e.*, prism, concave or convex lenses), H atoms do not only diffuse in the Pd, but also leak constantly towards the medium above it. We have then a bi-layer situation as considered by de Man *et al.*<sup>198</sup> Using the same model for a Pd/Mg bilayer we obtain

$$K_{\text{object}} = 2D_{\text{object}} \frac{c'_{\text{Pd}}}{c'_{\text{Mg}}} \frac{d_{\text{Pd}}}{d_{\text{Mg}}} \quad (6.41)$$

where  $c'_{\text{Pd}}$  is the concentration of H (unit:  $\text{mol cm}^{-3}$ ) when the front is reaching the left side of the object. For the samples in **Figure 6.1** to **Figure 6.5**,  $d_{\text{Pd}} = 20 \text{ nm}$  and  $d_{\text{Mg}} = 45 \text{ nm}$ . The concentration in the Mg is taken as

$$c'_{\text{Mg}} = \frac{2}{13.98} \text{ mol cm}^{-3} \quad (6.42)$$

The front mobility at the object is thus a function of the concentration  $c'_{\text{Pd}}$

$$K_{\text{object}} = \frac{2D_{\text{Pd}}c'_{\text{Pd}}}{c'_{\text{Mg}}} \frac{20 \text{ nm}}{45 \text{ nm}} = \frac{9.3 \times 10^{-10} \text{ m}^2 \text{s}^{-1}}{\text{mol cm}^{-3}} c'_{\text{Pd}} \quad (6.43)$$

From the observation that the experimental fronts are well reproduced with  $D_{\text{object}}/D_{\text{medium}} = 100$ , we conclude that

$$K_{\text{object}} = 100K_{\text{medium}} = 100 \times 3.1 \times 10^{-15} \text{ m}^2 \text{s}^{-1} \quad (6.44)$$

and consequently that

$$c'_{\text{Pd}} = 3.3 \times 10^{-4} \text{ mol cm}^{-3} \quad (6.45)$$

which corresponds to (considering the molar volume of Pd,  $V_{\text{Pd}} = 8.85 \text{ mol}^3 \text{cm}^{-1}$ )

$$c_{\text{Pd}} = \frac{H}{V_{\text{Pd}}} = c'_{\text{Pd}} V_{\text{Pd}} = 2.9 \times 10^{-3} \quad (6.46)$$

This is the H concentration at the entrance of the Pd object when the  $\text{MgH}_2/\text{Mg}$  front in the medium hits the Pd object. It is thus the H/Pd at a pressure equal to the plateau pressure of Mg at 353 K which is approximately 0.1 kPa. The low value for the concentration H/Pd in Eq. (6.46) is fully consistent with the hydrogenography data of Pivak *et al.*<sup>199</sup> on free standing Pd films.

### 6.12.7. Model for the pressure dependence of front mobility

The purpose of this part is to demonstrate that the remarkable increase of the front mobility with increasing  $\text{H}_2$  pressure shown in **Figure 6.14 b** can fully be understood by means of this model without introducing any new fitting parameter. It turns out to be a direct consequence of the concentration dependence of the diffusion coefficient in Eq.

(6.34). As the applied hydrogen pressure  $p$  determines the H concentration  $c_{\text{boundary}}$  at the entrance gate of the sample, one expects that the front mobility  $K$  depends on  $p$  via the concentration dependence of the diffusion coefficient.

In the first step we use a 1-dimensional simulation to determine the connection between  $c_{\text{boundary}}$  and  $K_{\text{simulation}}$ . The simulations done with

$$D(c) = e^{-20c} + e^{-20(1-c)} \quad (6.47)$$

lead to the results in **Figure 6.18** a. There is indeed a strong variation of the simulated mobility  $K_{\text{simulation}}$  with the boundary concentration, which is accurately described by

$$K_{\text{simulation}} = \exp(23.35 c_{\text{boundary}} - 25.72) \quad (6.48)$$

In the second step, we use Eq. (6.13) to relate the applied  $\text{H}_2$  pressure  $p$  to  $c_{\text{boundary}}$

$$\ln p = 2 \ln \left( \frac{c_{\text{boundary}}}{1 - c_{\text{boundary}}} \right) + 2 \frac{\Delta H_{\infty} - A c_{\text{boundary}} - T \Delta S}{RT} \quad (6.49)$$

As shown in **Figure 6.15**, the red curve that corresponds to Eq. (6.47) has the same slopes at low and high  $c$  as the parabola with  $T/T_c = 0.2$ . From Eqs. (6.17) and (6.49) follows then that

$$\ln p = 2 \ln \left( \frac{c_{\text{boundary}}}{1 - c_{\text{boundary}}} \right) + 2 \frac{\Delta H_{\infty}}{RT} - 40 c_{\text{boundary}} - 2 \frac{\Delta S}{R} \quad (6.50)$$

For high concentrations, when  $c_{\text{boundary}}$  is close to 1,

$$\begin{aligned} \ln p &\approx -2 \ln(1 - c_{\text{boundary}}) + 2 \frac{\Delta H_{\infty}}{RT} - 40 - 2 \frac{\Delta S}{R} \\ &= -2 \ln(1 - c_{\text{boundary}}) + X \end{aligned} \quad (6.51)$$

where

$$X = 2 \frac{\Delta H_{\infty}}{RT} - 40 - 2 \frac{\Delta S}{R} \quad (6.52)$$

is constant as all experiments are carried out at a constant temperature of 353 K. Solving Eq. (6.51) for  $c_{\text{boundary}}$  and introducing it into Eq. (6.48) gives

$$K_{\text{simulation}} = \exp \left[ 23.35 \left( 1 - \frac{1}{\sqrt{p}} e^{\frac{1}{2}X} \right) - 25.72 \right] \quad (6.53)$$

As the measured front mobility  $K$  is equal to  $K_{\text{simulation}}$  up to a multiplicative factor  $K_0$ , we expect for our experimental data

$$K = K_0 \exp \left[ 23.35 \left( 1 - \frac{1}{\sqrt{p}} e^{\frac{1}{2}X} \right) - 25.72 \right] \quad (6.54)$$

and thus that a plot of  $\ln K$  versus  $1/\sqrt{p}$  should be a straight line

$$\ln K = \frac{a}{\sqrt{p}} + b \quad (6.55)$$

with

$$a = -23.35 \exp\left(\frac{1}{2}X\right) \quad (6.56)$$

and

$$b = -2.37 + \ln K_0 \quad (6.57)$$

The experimental data points in **Figure 6.14 b** obey nicely the linear relation predicted by Eq. (6.55). The slope  $a = -0.07$  and the intercept  $b = -33.3$  lead to

$$K = \exp\left(\frac{-0.07}{\sqrt{p}} - 33.3\right) \quad (6.58)$$

which corresponds to the blue curve in **Figure 6.18 b**.

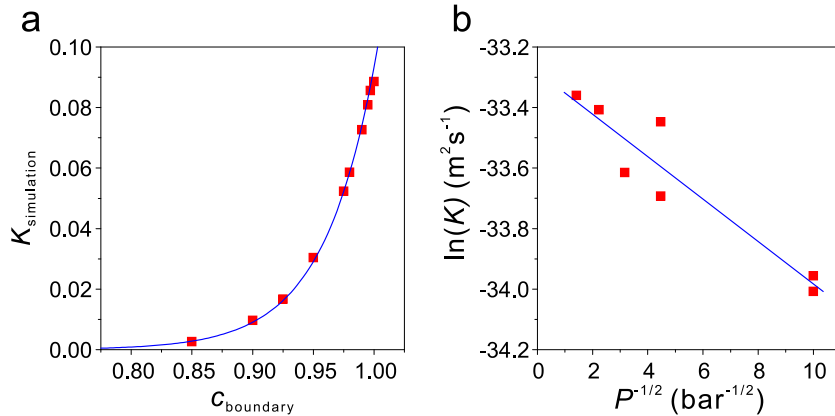


**Figure 6.18** (a) Influence of the boundary concentration on the front mobility. The blue curve is the fit to the calculated points given in Eq. (6.48). (b) The same experimental data in **Figure 6.14 b** for the pressure dependence of the front mobility plotted according to Eq. (6.55), which confirms the predicted linear dependence between  $\ln K$  and  $P^{-1/2}$ .

### 6.12.8. Implications for the pressure-composition isotherms

From Eq. (6.56) and the value for the parameter  $a = -0.07$  we find

$$X = -11.63 \quad (6.59)$$

From the definition of  $X$  in Eq. (6.52) and the values  $\Delta H_\infty = 21 \text{ kJ (moleH)}^{-1}$  and  $\Delta S = -67.5 \text{ JK}^{-1}(\text{moleH})^{-1}$  from Ref.<sup>178</sup>, we obtain

$$X = 2 \frac{\Delta H_\infty}{RT} - 40 - 2 \frac{\Delta S}{R} = -9.45 \quad (6.60)$$

This is in remarkably good agreement with the experimental value in Eq. (6.59) considering the simplicity of the model and the uncertainties in the thermodynamic values for the Mg-H system in the dilute regime.

## 6.13. Conclusions

Using a sample architecture where H diffuses laterally in a Mg film via Pd entrance gates, we have discovered that self-organized finger patterns made of MgH<sub>2</sub> can be generated over tens of micrometres. Their front mobility is large at all times and not hampered by the well-known ‘blocking effect’ generally observed in the published work<sup>73,83,87,171-173</sup>, where H diffuses perpendicularly to Mg films. We have also demonstrated that the finger patterns are effectively a self-recording of the entire H diffusion history. The fast lateral H diffusion and the possibility to manipulate H streamlines by inclusion of different diffusion objects or local gaps enable entirely new possibilities for applications in hydrogen storage systems<sup>60,170</sup>, active plasmonics<sup>52,94,152,169,200</sup> and cloaking<sup>201,202</sup>. Furthermore, as lithium is also a large dilation solute in electrodes, our work is relevant to electrical energy storage in batteries<sup>203-207</sup>. In particular, the very detailed information gathered in this work about the massive influence of H diffusion on the structure and morphology of Mg films can be advantageously used to evaluate the applicability of (chemo)mechanical multiscale computational models for describing lithiation processes in high-volume-change electrode materials<sup>208</sup>. Finally, it is noteworthy that there is a remarkable similarity between the H-induced finger patterns in Mg and the vortex avalanches in superconductors<sup>209</sup>.

## 7. Scanning display using lateral diffusion in Mg

Control over plasmonic colors on the nanoscale is of great interest for high-resolution display, imaging, and information encryption applications. However, so far very limited schemes have been attempted for dynamic plasmonic color generation. In this Chapter, we demonstrate a scanning plasmonic color generation scheme, in which subwavelength plasmonic pixels can be laterally switched on/off through directional hydrogenation/dehydrogenation of a magnesium screen. We show several dynamic plasmonic color displays with different scanning functions by varying the number and geometries of the palladium gates, where hydrogen enters the scanning screens. In particular, we employ the scanning effects to create a dynamic plasmonic quick response code. The information cannot be decrypted by varying the polarization states of light or by accessing the physical features. Rather, it can only be read out using hydrogen as decoding key. Our work advances the established design concepts for plasmonic color printing as well as provides insights into the development of optical information storage and anticounterfeiting features.

This chapter is adapted with permission from “Duan, X.; Liu, N. Scanning plasmonic color display. *ACS Nano* **2018**, *12*, 8817–8823.”

Chapter 7 shows a scanning plasmonic color generation,

## 7.1. Introduction

Color generation has been a perpetual pursuit through art exploration and scientific advancement along the history of humankind. Compared to conventional coloration methods based on pigmentary, structural colors possess many advantages, such as high spatial resolution, material simplicity, environmental friendliness, and long-term durability.<sup>7,45-48,58,145,146,150,151,160</sup> In particular, structural color generation using plasmonic nanoparticles as subwavelength pixels has recently gained tremendous momentum. Plasmonic colors emerge from resonant interactions between light and metal nanostructures, resulting in collective oscillations of the conduction electrons, *i.e.*, the so-called localized surface plasmons.<sup>3</sup> With the drive towards practical applications, a variety of potential prototype devices have been implemented for color printing,<sup>46-48,145,150</sup> colorimetric sensing,<sup>41,157</sup> color filtering<sup>33,39,147,210</sup> as well as anticounterfeiting and authentication.<sup>49,57,169</sup> However, the bottleneck of plasmonic color generation lies in its static nature. To this end, several approaches have been suggested and successfully employed for plasmonic color tuning, including polarization control,<sup>33,39,57,147,210</sup> alignment of liquid crystals,<sup>38,148,211</sup> mechanical strain,<sup>59,212</sup> integration of phase-transition materials<sup>52,94,152,187,213,214</sup> and so forth.<sup>50,149,215,216</sup> Nevertheless, dynamic plasmonic color control so far has been limited to very primitive schemes. Only simultaneous tuning or switching on/off plasmonic colors has been shown.<sup>52,94,152</sup> Endowing plasmonic pixels with versatile and rigorous dynamics is essential to enrich the plasmonic color generation toolbox as well as to further promote a broader range of applications.

In this Chapter, we demonstrate scanning plasmonic color displays, taking inspiration from macroscopic scanning devices. Scanning control over subwavelength plasmonic pixels, *i.e.*, aluminum (Al) nanoparticles is enabled by introducing an underlying magnesium (Mg) layer as scanning screen. Such a microscopic screen can be refreshed by laterally erasing or restoring plasmonic colors, when the Mg layer is transformed between the metal and dielectric (magnesium hydride, MgH<sub>2</sub>) states through directional hydrogenation/dehydrogenation. We show several dynamic plasmonic color displays with versatile scanning effects. The potential of this scheme for information encryption is also demonstrated using a scanning plasmonic quick response (QR) code, which contains highly secure information.

## 7.2. Mechanism of the scanning display

**Figure 7.1** illustrates the working principle of the scanning plasmonic color display. The microscopic scanning screen is a titanium (Ti, 3 nm)/Mg (30 nm) layer with dimensions of  $15 \times 15 \mu\text{m}^2$ , which resides on a silicon dioxide substrate. To impart the scanning characteristics, the left side of the screen is in contact with a palladium (Pd) strip, which works as a gate for hydrogen loading or unloading. The Ti layer helps to release the mechanical stress from volume expansions of Mg and Pd. It also plays an important role as spacer to prevent Mg and Pd from alloying.<sup>169</sup> Al nanoparticles, *i.e.*, the plasmonic

pixels, are arranged on top of the scanning screen spaced by an aluminum oxide ( $\text{Al}_2\text{O}_3$ , 20 nm) layer. The Al particle diameter and interparticle gap are defined as  $D$  and  $g$ , respectively. Upon hydrogen loading, hydrogenation of Mg starts from the Pd gate such that the plasmonic pixels are laterally scanned, following the hydrogen diffusion direction. During the process, the scanning screen transits from a mirror (Mg) to a transparent spacer ( $\text{MgH}_2$ ). This process is reversible through dehydrogenation using oxygen.<sup>52,94,150,152</sup> **Figure 7.2** presents a scanning electron microscopy (SEM) image of the palette (left-bottom corner), in which the different functional layers are clearly visible.

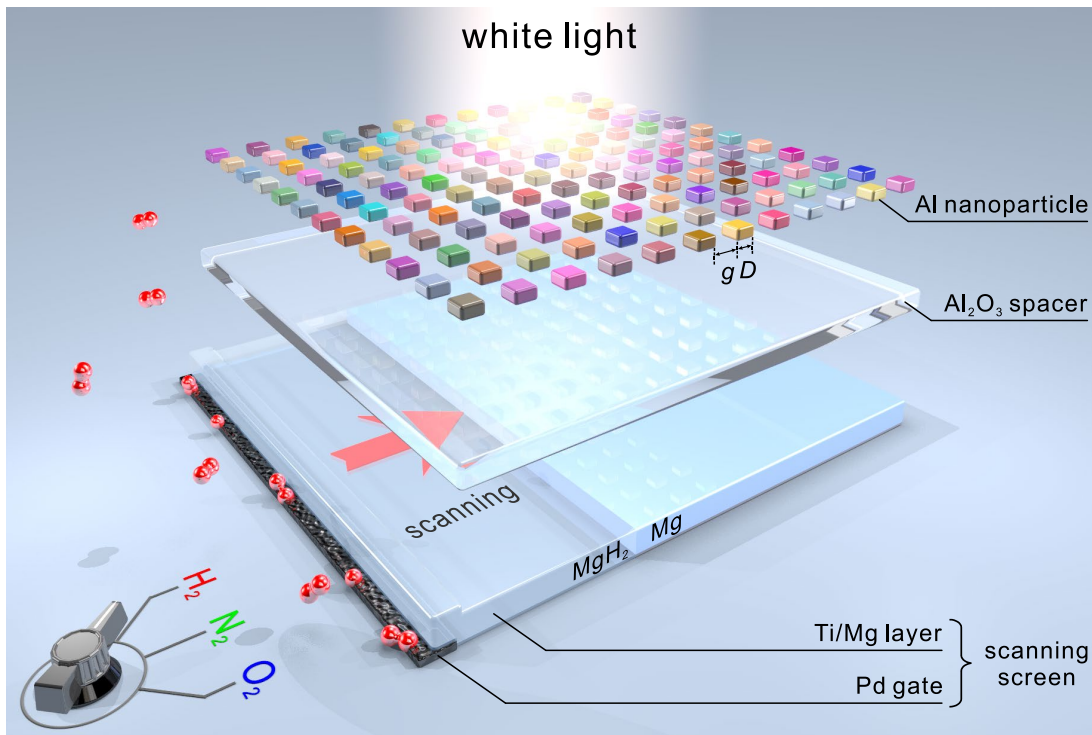


**Figure 7.1** Schematic of the scanning plasmonic color display, which consists of Al nanoparticles (diameter  $D$ ; interparticle gap  $g$ ; thickness 25 nm) as plasmonic pixels, a dielectric  $\text{Al}_2\text{O}_3$  (20 nm) spacer, and a scanning Mg screen ( $15 \mu\text{m} \times 15 \mu\text{m} \times 30 \text{ nm}$ ) with a 3 nm Ti buffer layer. The different functional layers are vertically shifted for clarity. The display is illuminated by unpolarized white light. A Pd strip ( $15 \mu\text{m} \times 400 \text{ nm} \times 15 \text{ nm}$ ) on the left is placed under the edge of the Mg screen. The Pd strip serves as a gate for gas loading or unloading. Upon hydrogen (or oxygen) loading, the Mg to  $\text{MgH}_2$  (or  $\text{MgH}_2$  to Mg) transition starts from the Pd gate, giving rise to lateral scanning effects.

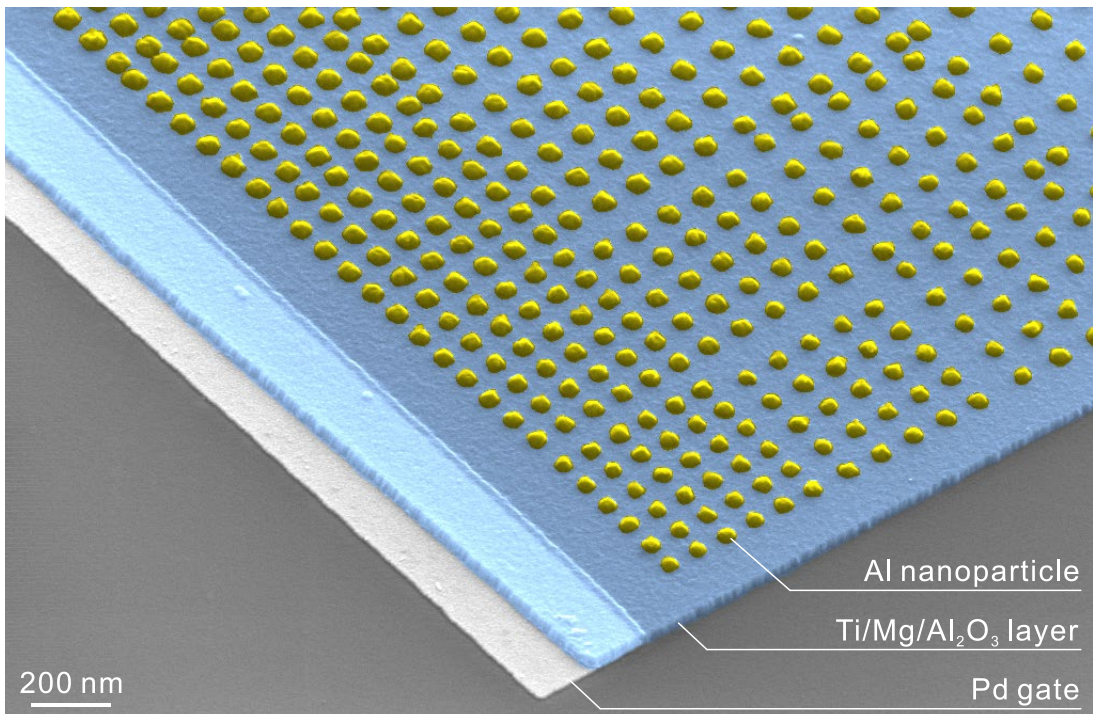


**Figure 7.2** Tilted SEM image of the left-bottom corner of the scanning plasmonic color display.

### 7.3. Kinetics of the scanning process

We first investigate the lateral diffusion process of hydrogen in Mg (see **Figure 7.3**), which governs the scanning function of the dynamic plasmonic color display. As the top and side surfaces of the Mg layer are protected by its native oxide (MgO), hydrogen can only enter Mg *via* the Pd gate, which catalyzes the dissociation of hydrogen molecules into atoms.<sup>76,154</sup> In order to characterize the diffusion front mobility, optical hydrogenography is utilized to *in situ* record the optical reflection (OR) images of the diffusion process at hydrogen concentration of 20% and 80 °C (see **Figure 7.3 a**). The sharp color change at the diffusion front arising from the Mg to MgH<sub>2</sub> transition makes it possible to accurately monitor the time-dependent diffusion characteristics. The experimental data (red curve in **Figure 7.3 c**) reveal a typical diffusive process following a nucleation step. More specifically, the square of the front position  $x^2$  (see **Figure 7.3 b**), is proportional to time  $t$ , after a short nucleation time,  $t_0$ . The front mobility  $K$  is defined as

$$K = \frac{x^2}{t - t_0} \quad (7.1)$$

which has the same dimension ( $\text{m}^2 \text{ s}^{-1}$ ) as a diffusion coefficient. Fitting of the experimental curve gives rise to  $K = 0.949 \times 10^{-8} \text{ m}^2 \text{ s}^{-1}$  and  $t_0 = 326 \text{ s}$  (see the black-dashed curve in **Figure 7.3 c**). This indicates the absence of blocking effects for lateral hydrogen diffusion, which is in sharp contrast to the out-of-plane diffusion.<sup>83,171</sup>

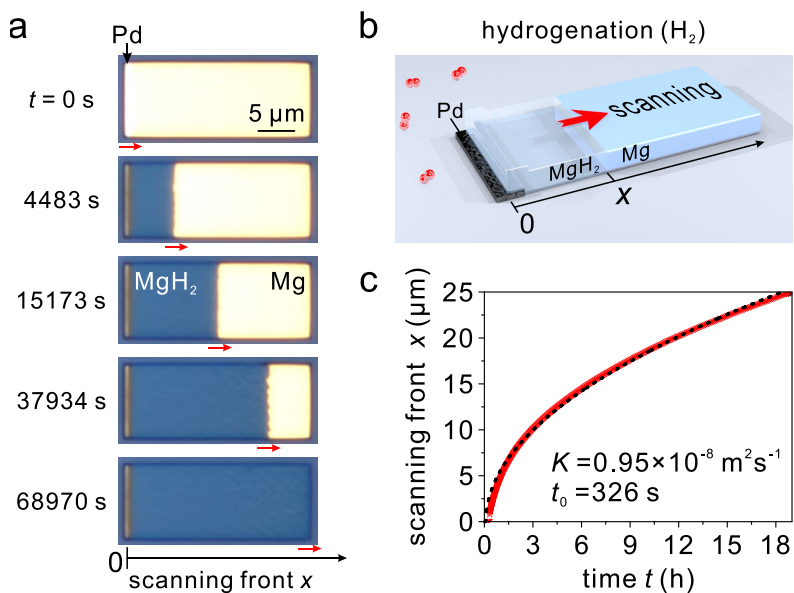


**Figure 7.3** Scanning front  $x$  of the screen during hydrogenation at different diffusion times obtained by *in situ* optical hydrogenography. (a) The red arrows indicate the movements of the diffusion fronts during hydrogenation. The dark and bright regions correspond to  $\text{MgH}_2$  and  $\text{Mg}$ , respectively. The sharp color change at the diffusion front is tracked as scanning front  $x$ . Schematics of the scanning screen during (b) hydrogenation. Scanning starts from the Pd gate. Experimental (red) and fitting (black-dashed) results of the time-dependent scanning front during (c) hydrogenation. The fitting parameters  $K$  and  $t_0$  from Eq. (7.1).

The process is reversible through dehydrogenation of  $\text{MgH}_2$  using oxygen (20% at 80 °C) as shown in **Figure 7.4 a**. The oxidative dehydrogenation involves binding of oxygen with the desorbed hydrogen atoms from  $\text{MgH}_2$ . This avoids a buildup of hydrogen at the Pd surface, thus facilitating hydrogen desorption.<sup>154</sup> It is noteworthy that the dehydrogenation process (the  $\text{MgH}_2$  to  $\text{Mg}$  transition) also starts from the Pd gate, therefore giving rise to the same scanning direction (see **Figure 7.4 b**) as that in the hydrogenation process. The top and side surfaces of the Mg screen are covered by the  $\text{Al}_2\text{O}_3$  spacer and  $\text{MgO}$ , respectively, while its bottom surface resides on the substrate. Therefore, during dehydrogenation the desorbed hydrogen atoms from  $\text{MgH}_2$  can only bind oxygen at the Pd gate. In addition, the high hydrogen concentration gradient across the gate region facilitates hydrogen desorption at the Pd gate, where  $\text{MgH}_2$  is transformed into  $\text{Mg}$ . The measured time-dependent diffusion characteristics are presented by a blue curve in **Figure 7.4 c**. Fitting of the experimental curve gives rise to  $K = 1.037 \times 10^{-8}\text{ m}^2\text{s}^{-1}$  and  $t_0 = 2398\text{ s}$  (see the black-dashed curve in **Figure 7.4 c**).

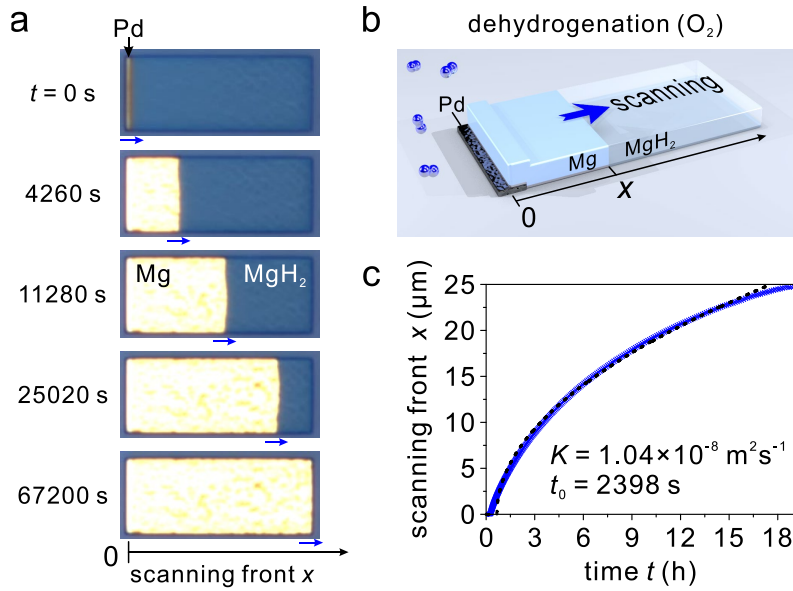


**Figure 7.4** Scanning front  $x$  of the screen during dehydrogenation at different diffusion times obtained by *in situ* optical hydrogenography. (a) The blue arrows indicate the movements of the diffusion fronts during dehydrogenation. The sharp color change at the diffusion front is tracked as scanning front  $x$ . (b) Schematics of the scanning screen during dehydrogenation. Scanning starts from the Pd gate. Experimental (blue) and fitting (black-dashed) results of the time-dependent scanning front during dehydrogenation. The fitting parameters  $K$  and  $t_0$  from Eq. (7.1).

## 7.4. Palette

Next, color generation from the Al nanoparticles on such a scanning screen is examined. **Figure 7.5 a** and **b** present the reflection bright-field microscopy images of the palette, when the screen is in the Mg and  $\text{MgH}_2$  states, respectively. When it is in the Mg state (color state, see **Figure 7.5 a**), the palette exhibits a wealth of brilliant colors. In this case, the screening screen serves as a back reflector. The Al nanoparticle, the  $\text{Al}_2\text{O}_3$  spacer, and the Mg layer construct a particle-on-mirror geometry<sup>217</sup>. The optical spectra of five representative color squares (i–v) from the palette are shown in **Figure 7.5 c**. When the interparticle gap ( $g$ ) is fixed, the particle diameter ( $D$ ) increase leads to the red-shift of the resonance dip. The experimental and simulated reflectance spectra agree well. The simulated electric-field distribution at the resonance position (565 nm) of color square iv confirms the strong interactions between the Al particle plasmons and the Mg mirror, generating electromagnetic fields localized in the  $\text{Al}_2\text{O}_3$  spacer. After hydrogenation, the scanning screen is in the  $\text{MgH}_2$  state (plain state, see **Figure 7.5 b**). The brilliant colors in the palette diminish. The experimental spectra of the selected color squares (i–v) exhibit nearly featureless profiles in the wavelength range of interest as shown in **Figure 7.5 d**. In the absence of the mirror, the dipolar plasmon excitation of the Al nanoparticle results in a resonance peak, shifting to the red when the particle diameter ( $D$ ) increases. The switching between the color and plain states of the palette is reversible through hydrogenation and dehydrogenation.

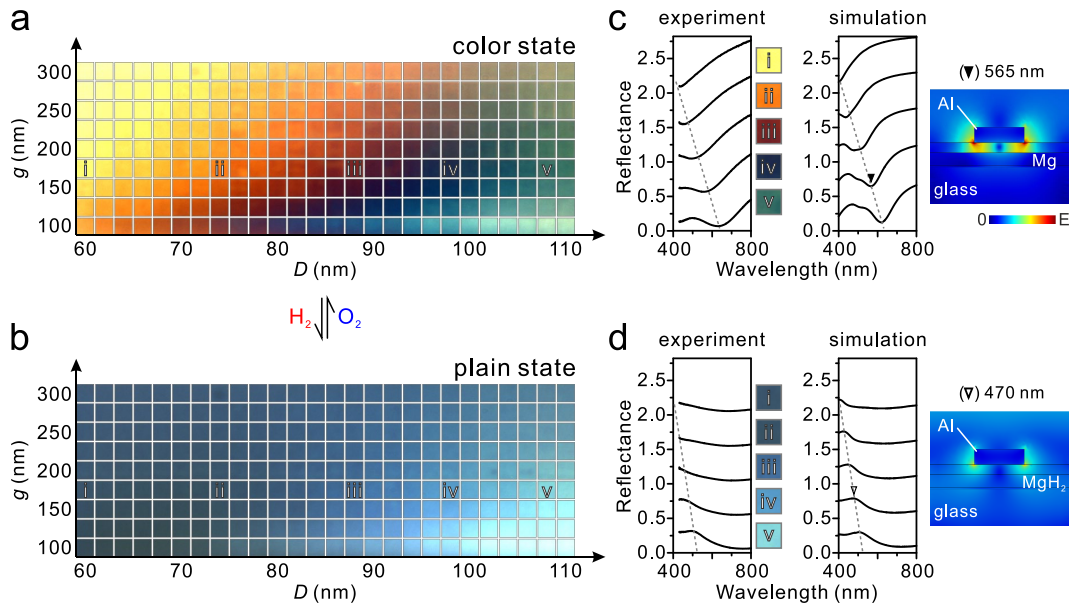


**Figure 7.5** Optical micrographs of the palette with stepwise tuning of  $D$  and  $g$  at color state (a) and plain state (b). Representative color squares i–v for spectral characterizations are highlighted. The total dimension of each color square is 3  $\mu\text{m}$ . Experimental and simulated reflectance spectra of the selected squares at color state (c) and plain state (d). The spectral curves are shifted upwards stepwise for clarity. The grey-dashed line indicates the shift of the reflectance dip (c) or peak (d). The simulated electric-field distributions of color square v at resonance positions of 565 nm and 470 nm (indicated by arrows) before and after hydrogenation, respectively.

## 7.5. Sichuan opera facial mask display

The interesting ability to laterally erase and restore plasmonic colors enables the realization of scanning plasmonic color displays. As a demonstration, a Sichuan opera facial mask has been employed as blueprint to design a dynamic plasmonic color display. Face-changing is an important subgenre of Chinese Sichuan opera. The SEM images in **Figure 7.6** illustrate the details of the microprint.

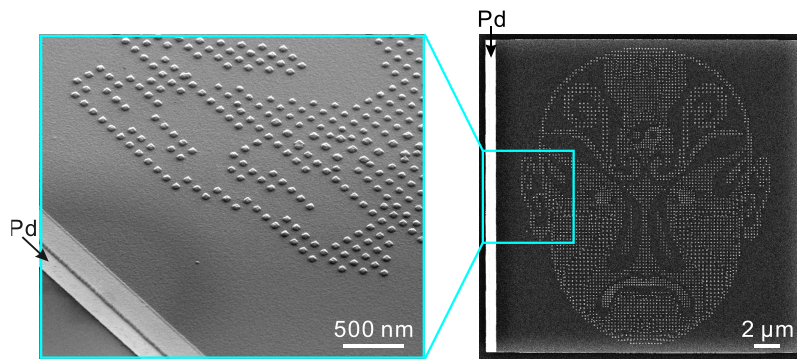


**Figure 7.6** Overview and enlarged tilted SEM images of the Sichuan opera facial mask display.

**Figure 7.7** shows the performance of the scanning plasmonic display. Upon hydrogen loading, hydrogenation starts from the Pd gate on the left. Absorption of hydrogen in Mg leads to a uniform diffusion front, scanning the microprint from the left to the right (see

the red arrows). Along the diffusion route, the plasmonic colors are switched off laterally. Upon oxygen loading, dehydrogenation also starts from the Pd gate. Desorption of hydrogen in MgH<sub>2</sub> leads to the formation of Mg, therefore laterally switching on the plasmonic colors and restoring the color microprint from the left to the right (see the blue arrows).

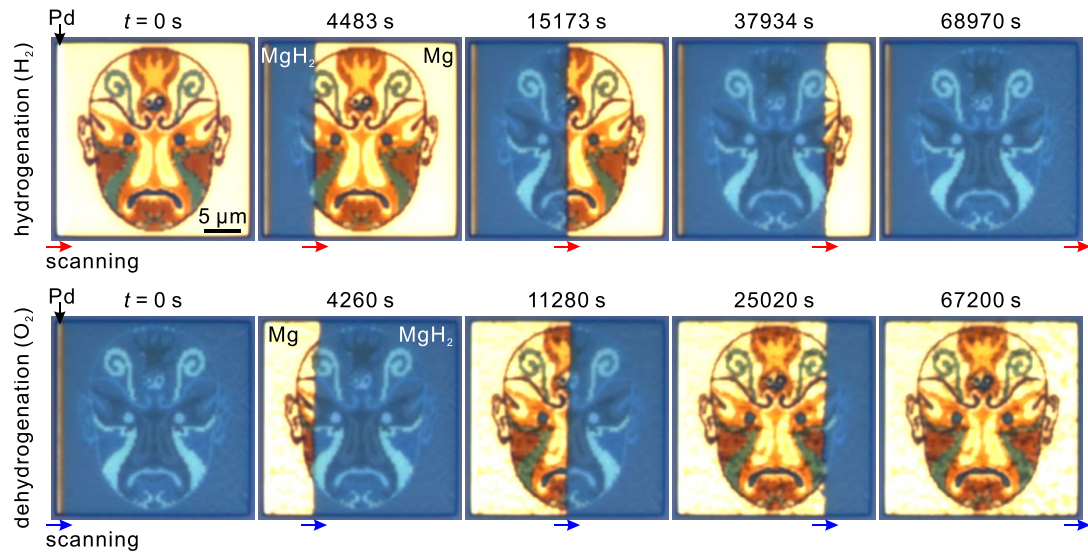


**Figure 7.7** Optical micrographs of the display during hydrogenation and dehydrogenation, respectively. The red and blue arrows indicate the scanning directions during hydrogenation and dehydrogenation, respectively.

## 7.6. Flexible Pd entrance

Our scheme can be extended to generate a variety of scanning effects by tailoring the Pd gates, where hydrogen enters Mg. For instance, when a Pd disk is placed in the center of a firework display, the isotropic diffusion of hydrogen in Mg leads to a radially propagating effect as shown in **Figure 7.8 a**. The detailed schematic of the firework display can be found in **Figure 7.9**. Inclusion of several Pd gates and variation of their positions add extra degrees of freedom to manipulate the scanning effects. Other firework display examples can be found in **Figure 7.10**. **Figure 7.8 b** shows a peacock display, in which the Pd stripe is curved along the tail of the peacock (see **Figure 7.11** for the detailed schematic). Color scanning along the tail feathers is nicely visualized.

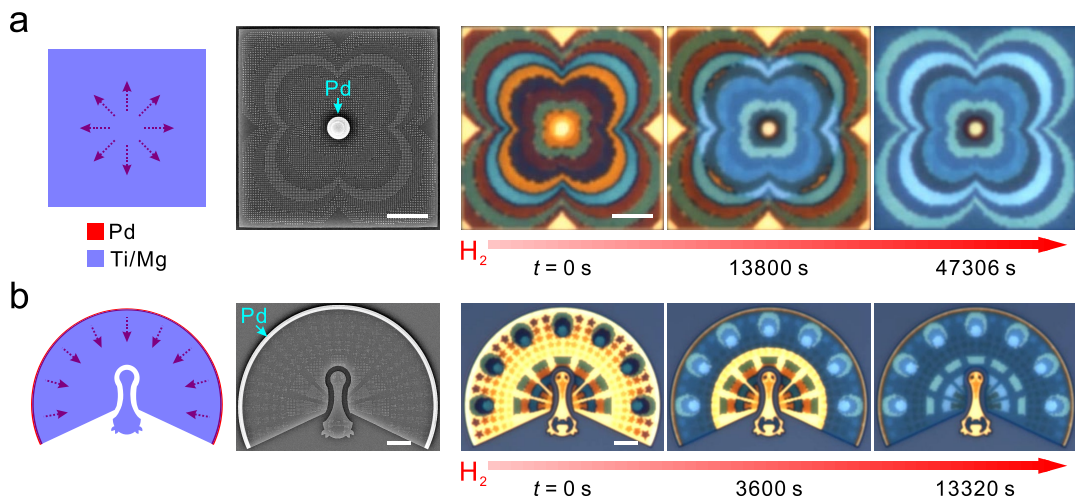


**Figure 7.8** Schematics of the firework (a) and the peacock (b) displays, with the dashed arrows indicating the scanning directions. SEM images of the firework (a) and the peacock (b) displays. Scale bars:  $5\text{ }\mu\text{m}$ . Selected snapshots of the firework (a) and the peacock (b) displays during hydrogenation, demonstrating different scanning effects. Scale bars:  $5\text{ }\mu\text{m}$ .

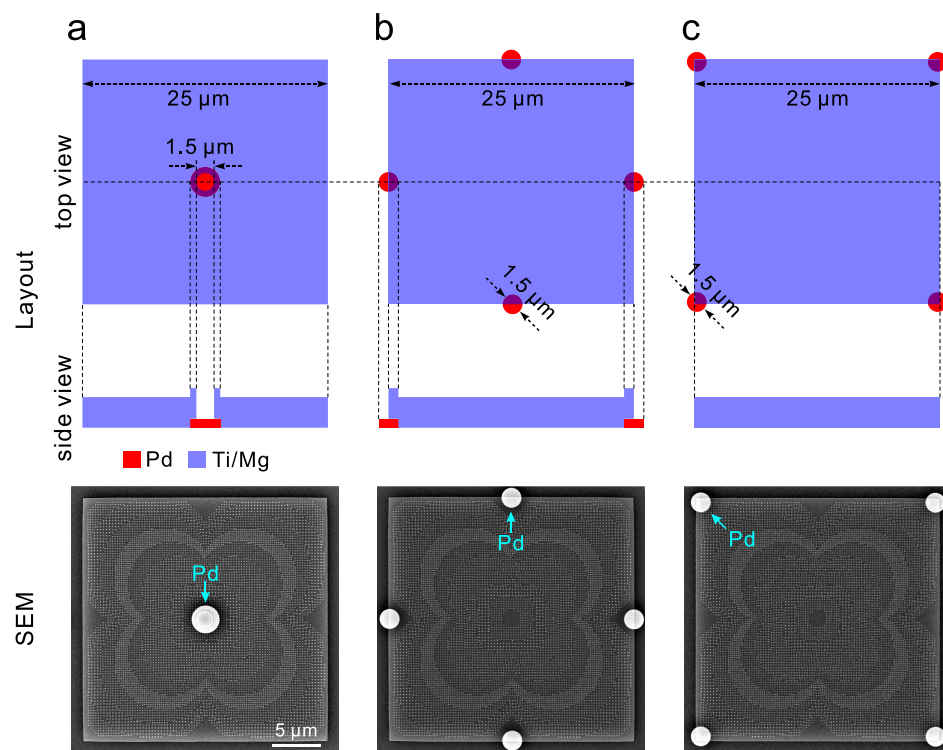


**Figure 7.9** Detailed layouts and SEM images of three different firework displays with a Pd gate in the center (a), four Pd gates at the borders (b), and four Pd gates at the corners (c) of the Mg screens.

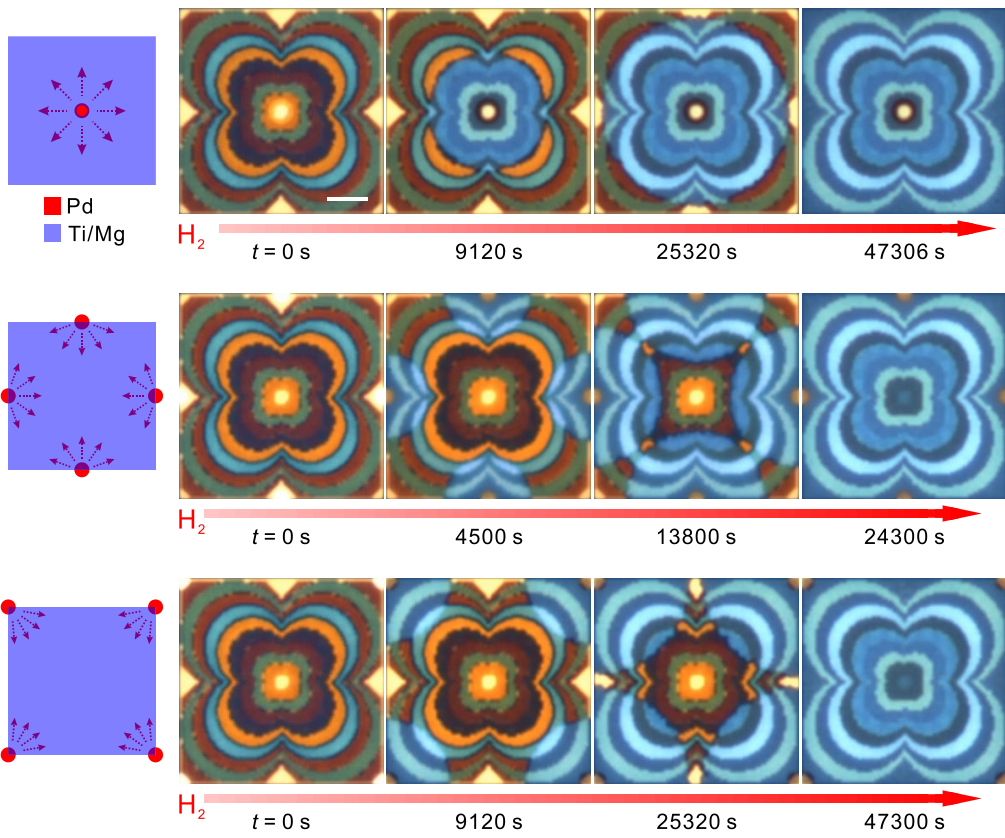


**Figure 7.10** Layouts and selected snapshots of three different fireworks displays. Scale bar: 5  $\mu\text{m}$ .

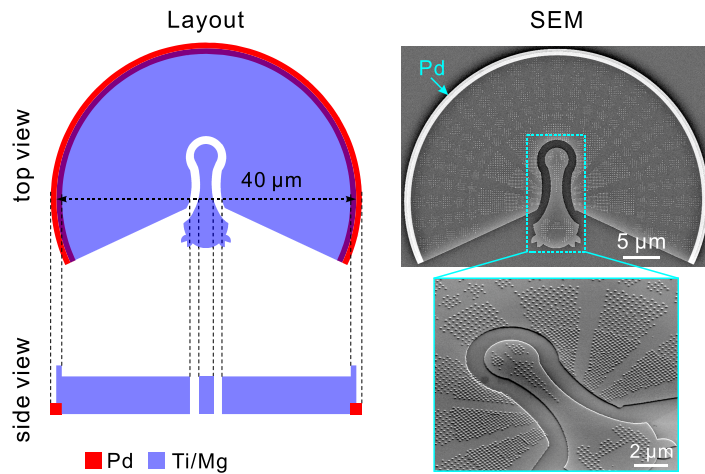


**Figure 7.11** Detailed layout and SEM images of the peacock display in **Figure 7.8 b.**

## 7.7. Information encryption

The scanning functions enable information encryption and cryptography concepts using plasmonic colors. Traditional anticounterfeiting features with plasmonic nanostructures often utilize polarization control to switch between two pre-defined images.<sup>57,210</sup> However, this is insufficient to securely protect information against piracy, because the information

can be straightforwardly decrypted by simply varying the polarization states. To deter forgery, the protected information should not be easily accessible through physical features. **Figure 7.12** presents our design and working principle of information encryption as a proof-of-concept experiment.

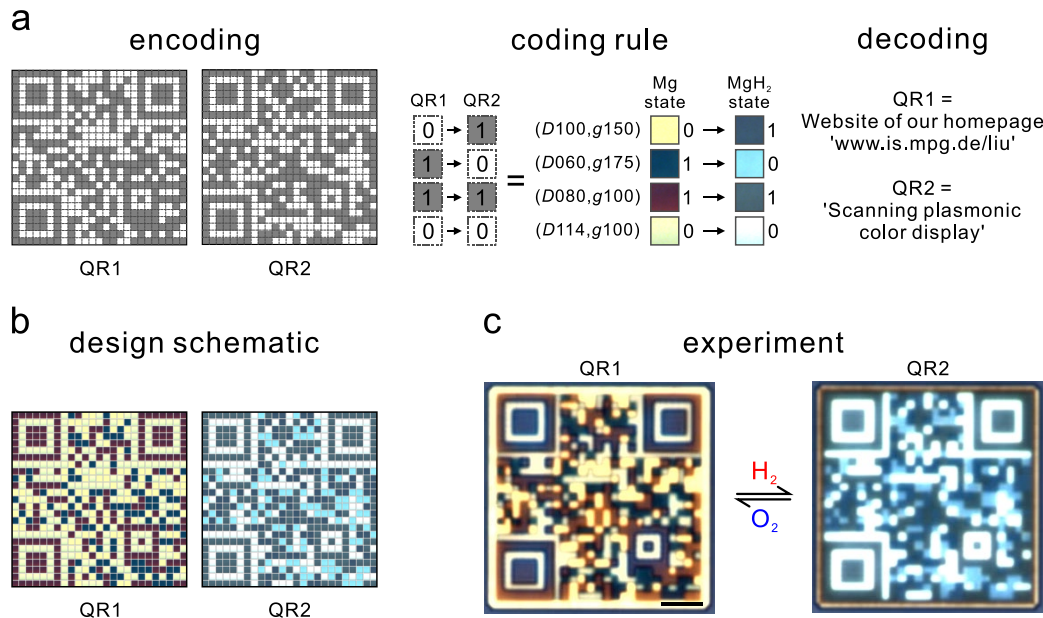


**Figure 7.12** (a) Principle of information encoding, coding rule, and decoding. Four different structures are selected from the palette to achieve binary information transitions, namely, ‘0’→‘1’, ‘1’→‘0’, ‘1’→‘1’, and ‘0’→‘0’, during hydrogenation. (b) Design schematic of QR1 and QR2 by filling the adopted colors in the corresponding positions. (c) Optical micrographs of the encrypted plasmonic QR code before and after hydrogenation, switching between QR1 and QR2. Scale bar: 5 μm.

We have created two QR codes, QR1 and QR2, respectively. ‘0’ in QR1 is represented using two bright colors, (D100, g150) and (D114, g100), which are selected from the palette in **Figure 7.5**. The distinction between the two bright colors is that after hydrogenation (D100, g150) is transformed to dark color (therefore ‘1’), whereas (D114, g100) remains bright (therefore ‘0’) as shown in **Figure 7.12 a** (also see **Figure 7.5**). ‘1’ in QR1 is represented using two dark colors, (D060, g175) and (D080, g100) from the palette. The difference between (D060, g175) and (D080, g100) is that after hydrogenation the former is transformed to bright color (therefore ‘0’), whereas the latter remains dark (therefore ‘1’). In this context, four different state transitions, namely, ‘0’→‘1’, ‘1’→‘0’, ‘1’→‘1’, ‘0’→‘0’ can be achieved through hydrogenation. The four transitions can be reversed through dehydrogenation. The design schematic of QR1 and QR2 is shown in **Figure 7.12 b** by filling the adopted colors according to the palette in **Figure 7.5** in the corresponding positions before and after hydrogenation, respectively. The detailed sample descriptions can be found in **Figure 7.13**.

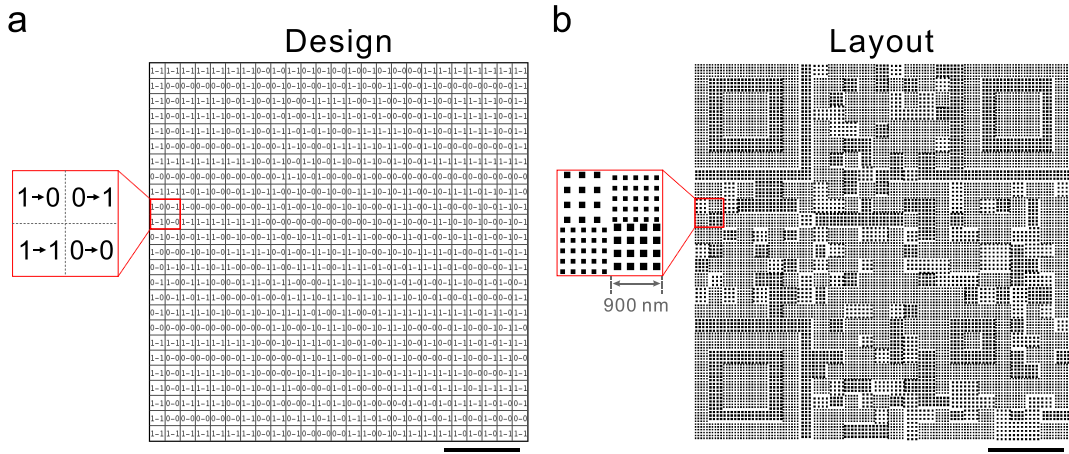


**Figure 7.13** (a) Different state transitions at corresponding positions. (b) Layout of the QR code. Scale bar: 5  $\mu\text{m}$ .

The experimental results are shown in **Figure 7.12 c**, which agrees very well with the design schematic in **Figure 7.12 b**. Before hydrogenation, the microprint shows QR1, presenting information of our website ‘[www.is.mpg.de/liu](http://www.is.mpg.de/liu)’. Upon hydrogen loading, the four aforementioned transitions take place. QR1 is scanned by the hydrogen diffusion fronts and transformed to QR2, presenting information of ‘scanning plasmonic color display’. Upon oxygen loading, QR2 is switched back to QR1. As a result, dual information can be dynamically encoded within the same plasmonic color microprint. Hydrogen is the only decoding key to read out the protected information, which in the case is QR2. QR2 cannot be decrypted using optical microscopy or even SEM, as QR1 and QR2 are obtained from one single microprint with identical physical features.

## 7.8. Experiments

### 7.8.1. Structure fabrications

The samples were manufactured using multiple electron-beam lithography (EBL). First, alignment markers were defined in a double-layer PMMA resist (200k-3.5% and 950k-1.5%, Allresist) using EBL (Raith e\_line) on an ITO coated glass substrate (Delta Technologies, Limited). A 2 nm chromium adhesion layer and a 40 nm Au film were deposited on the substrate through electron-beam evaporation (PFEIFFER Vacuum, PLS-500) followed by a standard lift-off procedure. Next, the substrate was again coated with a double-layer PMMA. Computer-controlled alignment using Au markers of the first layer were carried out to define the structural layer of the Pd gates. Subsequently, 15 nm Pd was deposited on the substrate using electron-beam evaporation followed by the same lift-off procedure. Then, the substrate was coated with a double-layer PMMA, and the alignment Au markers were used to define the structural layer of the scanning screens. After development (90 s in MIBK and 60 s in isopropanol), 3 nm Ti, 30 nm Mg, and 20 nm Al<sub>2</sub>O<sub>3</sub> were successively deposited on the substrate through electron-beam evaporation followed by the same lift-off procedure. Finally, the substrate was coated with a double

layer PMMA again, and the alignment Au markers were used to define the structural layer of the plasmonic pixels. After development, 25 nm Al was deposited on the substrate through electron-beam evaporation followed by the same lift-off procedure.

### 7.8.2. Optical characterizations

The optical images and videos of the samples were taken using a bright-field reflection microscope (Nikon, ECLIPSE LV100ND) illuminated by a white light source (Energetiq Laser-Driven Light Source, EQ-99). A digital CCD Camera (Allied-Vision Prosilica GT2450C) was used to capture images with a  $\times 100$  (N.A. = 0.6) objective. The hydrogenation and dehydrogenation experiments were carried out in a homemade gas chamber. The flow rate of the gas (hydrogen or oxygen in nitrogen) was 1.0 l/min.

## 7.9. Conclusions

In conclusion, we have demonstrated a scheme for the realization of dynamic plasmonic color displays with scanning functions. Such scanning functions are enabled by lateral hydrogenation/dehydrogenation of the microscopic screen through metal/dielectric transitions. We have shown several examples of scanning plasmonic color displays with different dynamic effects by tailoring the number and geometries of the Pd gates. In addition, we have demonstrated a highly secure encryption approach using a single scanning plasmonic QR code, which contains switchable dual information. Our samples show no significant degradations in switching performance under ambient conditions after three months. For practical applications, gaschromic or electrochromic loading of hydrogen can be utilized for enhanced switching speed and durability.<sup>190,218</sup> Our work advances the established design concepts for plasmonic color printing as well as provides insights into the development of optical information storage and anticounterfeiting features.<sup>219,220</sup>



## 8. Conclusions and outlook

### 8.1. Conclusions

In this thesis, we discuss a relatively new member in nanoplasmonics, magnesium (Mg), and its important role for the development of dynamic plasmonic nanodevices at visible frequencies.

In Chapter 2, we first reviewed the theoretical background of plasmonics, including light-metal interactions, surface plasmon polaritons, and localized surface plasmons. The LSPRs depends on the dielectric function of metals, the geometry of the nanostructures, and the surrounding refractive index of the nanostructures. Then, we introduced a series of active metals, hydrogen-storage metals, which undergo a phase transition upon hydrogenation and dehydrogenation, accompanied with changes of optical and electric properties. The reversible properties can be promising candidates for hydrogen sensing and dynamic plasmonics. Among them, magnesium is the most promising, as it exhibits excellent optical properties at high frequencies and undergoes reversible transitions between metal and dielectric hydride states. This sets the basis of Mg for dynamic nanoplasmonics. In particular, the structural properties and the dielectric functions of the two distinct states are discussed in detail. Subsequently, we highlight the experimental investigations on the physical mechanisms of Mg nanoparticles during hydrogenation and dehydrogenation. We also outline the strategies to enhance the stability, reversibility, and durability of Mg-based nanodevices.

In Chapter 3, we demonstrated a novel hydrogen-regulated chiral plasmonic system. Each chiral structure consisted of four Au and four Mg particles that were arranged in a gammadion-like geometry. The chiroptical responses of the plasmonic structures could be dynamically switched off/on simply by hydrogenation/dehydrogenation. Such a dynamic control concept may lead to plasmonic chiral platforms for a variety of gas detection schemes by exploiting the high sensitivity of CD spectroscopy. In addition, it will enable the realization of tunable circular polarizers and polarization modulators regulated by hydrogen.

In Chapter 4, we demonstrated a dynamic plasmonic display technique, which enabled plasmonic microprint displays with good reversibility, plasmonic animations with subwavelength resolution, and highly secure plasmonic encryption. The plasmonic pixels comprising Mg nanoparticles were arranged in a lattice with various particle sizes and interparticle distances to achieve brilliant colors in a broad spectral range. Through hydrogenation, different color squares underwent a series of vivid color changes until all colors vanished. The hydrogenation process was essentially associated with a gradual decrease of the metallic fraction of the particles, forming  $MgH_2$  as dielectric surrounding. We discovered that the color squares composed of smaller Mg particles vanished faster than those composed of larger Mg particles. This is consistent with previous studies that

smaller Mg nanocrystallites possessed faster kinetics. Such distinct color transformation kinetics of the Mg particles with different sizes allowed for the realization of plasmonic animations with subwavelength resolution. Through smart material processing, information encoded on selected pixels, which were indiscernible to both optical and scanning electron microscopies, could be read out using hydrogen as a decoding key, suggesting a new generation of information encryption and anti-counterfeiting applications.

In Chapter 5, we reported a dynamic color display scheme using pixelated FP cavities. Each pixel consisted of a dielectric HSQ pillar, which was sandwiched between an Al mirror and a metallic capping layer composed of Mg/Ti/Pd. By tuning the pillar heights using grey-scale lithography, a series of FP cavities were formed. Before hydrogenation, the Mg/Ti/Pd capping layer efficiently reflected the visible light, resulting in no color generation. This defined a blank state. Upon hydrogen exposure, Mg was gradually transformed to MgH<sub>2</sub>, the effective thickness of the metallic capping layer decreased and light started to transmit through it. When Mg was fully hydrogenated into MgH<sub>2</sub>, colors were selectively reflected from these FP resonators of different heights. Such asymmetrical FP resonators with ultrathin lossy capping generated vivid and high-contrast colors with a wide gamut, representing a color state. Due to the well-modulated and sharp FP resonances, the generated colors were more saturated and richer than those from Mg nanoparticles. This scheme utilized a Mg layer directly from thin film deposition to achieve dynamic color changes without any post-nanofabrication steps. This avoided exhaustive optimization and special care for catalytic nanoparticle manufacturing, which could significantly influence the catalytic efficiency and performance.

In Chapter 6, we demonstrated fast lateral hydrogen diffusion in quasi-free magnesium films without the blocking effect. We discovered that self-organized finger patterns made of MgH<sub>2</sub> can be generated over tens of micrometres along the diffusion direction. Their front mobility is large at all times and not hampered by the well-known ‘blocking effect’ generally observed in the published work. We demonstrated that the finger patterns are effectively a self-recording of the entire H diffusion history. The fast lateral H diffusion and the possibility to manipulate H streamlines by inclusion of different diffusion objects or local gaps enable entirely new possibilities for applications in hydrogen storage systems and active plasmonics.

In Chapter 7, we demonstrated a scheme for the realization of dynamic plasmonic color displays with scanning functions. The microscopic scanning screen was a Ti/Mg layer on a SiO<sub>2</sub> substrate. To enable the scanning characteristics, the left side of the screen was in contact with a Pd strip, which worked as a gate for hydrogen loading or unloading. Al nanoparticles, *i.e.*, the plasmonic pixels, were arranged on top of the scanning screen spaced by a 20 nm Al<sub>2</sub>O<sub>3</sub> layer. Upon hydrogen loading, hydrogenation of Mg started from the Pd gate such that the plasmonic pixels were laterally scanned, following the hydrogen diffusion direction. During the process, the scanning screen transited from a mirror (Mg) to a transparent spacer (MgH<sub>2</sub>). We showed that the scanning effects can be manipulated by tailoring the number and geometries of the Pd gates. In addition, we have demonstrated

a highly secure encryption approach using a single scanning plasmonic QR code, which contains switchable dual information. Our work advances the established design concepts for plasmonic color printing as well as provides insights into the development of optical information storage and anticounterfeiting features.

## 8.2. Outlook

Mg for dynamic nanoplasmatics is a viable route to realizing plasmonic nanodevices with novel functionalities, given its design flexibility and large modulation of the optical responses. Other than plasmonic color generation, in which only the amplitude of light is tailored, metasurfaces can also manipulate the phase of light at an unprecedented level. This capability has enabled a wealth of ultrathin optical devices for beam focusing and steering<sup>8</sup>, vortex beam generation<sup>221</sup>, and holography<sup>156</sup>. There are remaining issues, which need to be addressed for construction of high-performance dynamic systems for real-world applications.

First, optical approaches, such as s-SNOM provide physical understanding of the *in-situ* hydrogenation and dehydrogenation processes with resolution of several tens of nanometers. Deeper insights on such processes on the atomic level can be achieved using environmental transmission electron microscopy (TEM). The core of environmental TEM is to deliver high-resolution imaging with gas in the TEM chamber.<sup>222,223</sup> For instance, Mg nanoparticles of different sizes, shapes, geometries, *etc.*, can be fabricated by advanced EBL on an ultra-thin TEM grid. Tomography and diffraction patterns of the particles before and after hydrogenation can be obtained and carefully examined. In addition, *in-situ* electron-energy loss spectropy of the Mg nanoparticles can be carried out during hydrogenation/dehydrogenation. Such characterizations will enable visualization of the phase-transition dynamics of the Mg nanoparticles in a controlled gaseous environment and allow for understanding the fundamental atomic mechanisms of gas-solid reactions on the atomic level. In turn, the gained knowledge of the time-resolved dynamic and kinetic mechanisms on the atomic level will provide insightful blueprints to design Mg-based dynamic nanodevices with high performance.

Second, to further improve reversibility and durability, alloying Mg with other metals including nickel, yttrium (Y), vanadium, iron (Fe), *etc.*, should be attempted.<sup>70</sup> Kalisvaart *et al.*, showed that Mg films alloyed with Al, Fe, and Ti could enhance reaction kinetics and no degradation in performance was observed after 100 absorption/desorption cycles.<sup>224</sup> Baldi *et al.*, and Slaman *et al.*, demonstrated that Pd capped Mg-Ti alloy films showed faster kinetics with good reversibility over 150 cycles.<sup>89,90</sup> Remarkably, Tajima *et al.*, reported optical switching of Mg<sub>4</sub>Ni films over 4000 cycles.<sup>91</sup> Therefore, research efforts on patterning Mg alloy particles for dynamic optical nanodevices will be very rewarding.

Third, to enhance switching rates, other hydrogenation/dehydrogenation means can be utilized. Den Broeder *et al.*, demonstrated electromigration of hydrogen in Y films, in

which the diffusing species in the insulating yttrium trihydride was the H-anion.<sup>190</sup> This concept can be applied to Mg-based systems as well so that the hydrogenation/dehydrogenation processes in Mg can be conveniently controlled by external electric fields at fast speeds. This will also eventually solve the portability issue of the gas-phase reactions.<sup>91</sup>

So far, Mg-based dynamic nanodevices have been utilized for applications in plasmonic chirality switching, dynamic colors displays and metasurface elements. This exploits only a glimpse of opportunities that Mg can offer. There are many interesting topics that deserve research endeavors. For instance, the out-of-plane expansion of Mg nanoparticles is as large as 30%.<sup>84,187</sup> This provides a unique model system to realize plasmonic devices with nanoscale mechanical responses. Also, Mg can be utilized in the studies of switchable nonlinear effects, offering a new platform to examine the intriguing enhancement and symmetry questions in nonlinear plasmonics. Furthermore, Mg can be applied for plasmonic sensing, which is not only limited to detection of hydrogen. Rather, it can be extended to offer general dynamic platforms for tunable surface-enhanced Raman scattering, fluorescence, infrared absorption, and others. We believe the unsolved challenges and new scientific inquiries will stimulate exciting studies of Mg-based dynamic nanoplasmonics and their related applications.

# Bibliography

- [1] Barnes, W. L.; Dereux, A.; Ebbesen, T. W. Surface plasmon subwavelength optics. *Nature* **424**, 824–830, **2003**.
- [2] Schuller, J. A.; Barnard, E. S.; Cai, W.; Jun, Y. C.; White, J. S.; Brongersma, M. L. Plasmonics for extreme light concentration and manipulation. *Nat. Mater.*, **9**, 193–204, **2010**.
- [3] Halas, N. J.; Lal, S.; Chang, W.-S.; Link, S.; Nordlander, P. Plasmons in strongly coupled metallic nanostructures. *Chem. Rev.*, **111**, 3913–3961, **2011**.
- [4] Tokel, O.; Inci, F.; Demirci, U. Advances in plasmonic technologies for point of care applications. *Chem. Rev.*, **114**, 5728–5752, **2014**.
- [5] Curto, A. G.; Volpe, G.; Taminiau, T. H.; Kreuzer, M. P.; Quidant, R.; van Hulst, N. F. Unidirectional emission of a quantum dot coupled to a nanoantenna. *Science*, **329**, 930–933, **2010**.
- [6] Liu, N.; Liedl, T. DNA-assembled advanced plasmonic architectures. *Chem. Rev.*, **118**, 3032–3053, **2018**.
- [7] Kristensen, A.; Yang, J. K. W.; Bozhevolnyi, S. I.; Link, S.; Nordlander, P.; Halas, N. J.; Mortensen, N. A. Plasmonic colour generation. *Nat. Rev. Mater.*, **2**, 16088, **2016**.
- [8] Ding, F.; Pors, A.; Bozhevolnyi, S. I. Gradient metasurfaces: a review of fundamentals and applications. *Rep. Prog. Phys.*, **81**, 026401, **2018**.
- [9] Soukoulis, C. M.; Wegener, M. Past achievements and future challenges in the development of three-dimensional photonic metamaterials. *Nat. Photonics*, **5**, 523–530, **2011**.
- [10] Zheludev, N. I.; Kivshar, Y. S. From metamaterials to metadevices. *Nat. Mater.*, **11**, 917–924, **2012**.
- [11] Krasavin, A. V.; Zheludev, N. I. Active plasmonics: controlling signals in Au/Ga waveguide using nanoscale structural transformations. *Appl. Phys. Lett.*, **84**, 1416–1418, **2004**.
- [12] Jiang, N.; Zhuo, X.; Wang, J. Active plasmonics: Principles, structures, and applications. *Chem. Rev.*, **118**, 3054–3099, **2018**.
- [13] Nemati, A.; Wang, Q.; Hong, M.; Teng, J. Tunable and reconfigurable metasurfaces and metadevices. *Opto-Electron. Adv.*, **1**, 180009, **2018**.
- [14] Kuzyk, A.; Jungmann, R.; Acuna, G. P.; Liu, N. DNA origami route for nanophotonics. *ACS Photonics*, **5**, 1151–1163, **2018**.
- [15] Zhou, C.; Duan, X.; Liu, N. DNA-nanotechnology-enabled chiral plasmonics: from static to dynamic. *Acc. Chem. Res.*, **50**, 2906–2914, **2017**.
- [16] Wang, L.; Li, Q. Photochromism into nanosystems: towards lighting up the future nanoworld. *Chem. Soc. Rev.*, **47**, 1044–1097, **2018**.
- [17] Fofang, N. T.; Grady, N. K.; Fan, Z.; Govorov, A. O.; Halas, N. J. Plexciton dynamics: exciton–plasmon coupling in a J-aggregate–Au nanoshell complex provides a mechanism for nonlinearity. *Nano Lett.*, **11**, 1556–1560, **2011**.
- [18] Gao, Y.; Huang, C.; Hao, C.; Sun, S.; Zhang, L.; Zhang, C.; Duan, Z.; Wang, K.; Jin, Z.; Zhang, N.; Kildishev, A. V.; Qiu, C.-W.; Song, Q.; Xiao, S. Lead halide perovskite nanostructures for dynamic color display. *ACS Nano*, **12**, 8847–8854, **2018**.
- [19] Liu, M.; Hwang, H. Y.; Tao, H.; Strikwerda, A. C.; Fan, K.; Keiser, G. R.; Sternbach, A. J.; West, K. G.; Kittiwatanakul, S.; Lu, J.; Wolf, S. A.; Omenetto, F. G.; Zhang, X.; Nelson, K. A.; Averitt, R. D. Terahertz-field-induced insulator-to-metal transition in vanadium dioxide metamaterial. *Nature* **487**, 345–348, **2012**.
- [20] Yin, X.; Steinle, T.; Huang, L.; Taubner, T.; Wuttig, M.; Zentgraf, T.; Giessen, H. Beam switching and bifocal zoom lensing using active plasmonic metasurfaces. *Light Sci. Appl.*, **6**, e17016, **2017**.
- [21] Si, G.; Zhao, Y.; Leong, E. S. P.; Liu, Y. J. Liquid-crystal-enabled active plasmonics: a review. *Materials*, **7**, 1296–1317, **2014**.
- [22] Grigorenko, A. N.; Polini, M.; Novoselov, K. S. Graphene plasmonics. *Nat. Photonics*, **6**, 749–758, **2012**.
- [23] Sanz, J. M.; Ortiz, D.; Alcaraz de la Osa, R.; Saiz, J. M.; González, F.; Brown, A. S.; Losurdo, M.; Everitt, H. O.; Moreno, F. UV plasmonic behavior of various metal nanoparticles in the near- and far-field regimes: geometry and substrate effects. *J. Phys. Chem. C*, **117**, 19606–19615, **2013**.
- [24] Blaber, M. G.; Arnold, M. D.; Ford, M. J. A review of the optical properties of alloys and intermetallics for plasmonics. *J. Phys. Condens. Matter.*, **22**, 143201, **2010**.
- [25] Palm, K. J.; Murray, J. B.; Narayan, T. C.; Munday, J. N. Dynamic optical properties of metal hydrides. *ACS Photonics*, **5**, 4677–4686, **2018**.
- [26] Maier, S. A.: *Plasmonics: Fundamentals and Applications*; Springer (New York), **2007**.

- [27] Vial, A.; Grimault, A.-S.; Macías, D.; Barchiesi, D.; de la Chapelle, M. L. Improved analytical fit of gold dispersion: Application to the modeling of extinction spectra with a finite-difference time-domain method. *Phys. Rev. B*, **71**, 085416, **2005**.
- [28] Ritchie, R. H. Plasma losses by fast electrons in thin films. *Phys. Rev.*, **106**, 874–881, **1957**.
- [29] Lal, S.; Link, S.; Halas, N. J. Nano-optics from sensing to waveguiding. *Nat. Photonics*, **1**, 641–648, **2007**.
- [30] Luk'yanchuk, B.; Zheludev, N. I.; Maier, S. A.; Halas, N. J.; Nordlander, P.; Giessen, H.; Chong, C. T. The Fano resonance in plasmonic nanostructures and metamaterials. *Nat. Mater.*, **9**, 707–715, **2010**.
- [31] Shrestha, V. R.; Lee, S.-S.; Kim, E.-S.; Choi, D.-Y. Aluminum plasmonics based highly transmissive polarization-independent subtractive color filters exploiting a nanopatch array. *Nano Lett.*, **14**, 6672–6678, **2014**.
- [32] Zeng, B.; Gao, Y.; Bartoli, F. J. Ultrathin nanostructured metals for highly transmissive plasmonic subtractive color filters. *Sci. Rep.*, **3**, 2840, **2013**.
- [33] Ellenbogen, T.; Seo, K.; Crozier, K. B. Chromatic plasmonic polarizers for active visible color filtering and polarimetry. *Nano Lett.*, **12**, 1026–1031, **2012**.
- [34] Wen, L.; Chen, Q.; Hu, X.; Wang, H.; Jin, L.; Su, Q. Multifunctional silicon optoelectronics integrated with plasmonic scattering color. *ACS Nano*, **10**, 11076–11086, **2016**.
- [35] Wang, H.; Wang, X.; Yan, C.; Zhao, H.; Zhang, J.; Santschi, C.; Martin, O. J. F. Full color generation using silver tandem nanodisks. *ACS Nano*, **11**, 4419–4427, **2017**.
- [36] Zijlstra, P.; Chon, J. W.; Gu, M. Five-dimensional optical recording mediated by surface plasmons in gold nanorods. *Nature* **459**, 410–413, **2009**.
- [37] Ye, M.; Sun, L.; Hu, X.; Shi, B.; Zeng, B.; Wang, L.; Zhao, J.; Yang, S.; Tai, R.; Fecht, H.-J.; Jiang, J.-Z.; Zhang, D.-X. Angle-insensitive plasmonic color filters with randomly distributed silver nanodisks. *Opt. Lett.*, **40**, 4979–4982, **2015**.
- [38] Franklin, D.; Frank, R.; Wu, S.-T.; Chanda, D. Actively addressed single pixel full-colour plasmonic display. *Nat. Commun.*, **8**, 15209, **2017**.
- [39] Li, Z.; Clark, A. W.; Cooper, J. M. Dual color plasmonic pixels create a polarization controlled nano color palette. *ACS Nano*, **10**, 492–498, **2016**.
- [40] Ebbesen, T. W.; Lezec, H. J.; Ghaemi, H. F.; Thio, T.; Wolff, P. A. Extraordinary optical transmission through sub-wavelength hole arrays. *Nature* **391**, 667–669, **1998**.
- [41] Yokogawa, S.; Burgos, S. P.; Atwater, H. A. Plasmonic color filters for CMOS image sensor applications. *Nano Lett.*, **12**, 4349–4354, **2012**.
- [42] Inoue, D.; Miura, A.; Nomura, T.; Fujikawa, H.; Sato, K.; Ikeda, N.; Tsuya, D.; Sugimoto, Y.; Koide, Y. Polarization independent visible color filter comprising an aluminum film with surface-plasmon enhanced transmission through a subwavelength array of holes. *Appl. Phys. Lett.*, **98**, 093113, **2011**.
- [43] Stewart, J. W.; Akselrod, G. M.; Smith, D. R.; Mikkelsen, M. H. Toward multispectral imaging with colloidal metasurface pixels. *Adv. Mater.*, **29**, 1602971, **2017**.
- [44] Rezaei, S. D.; Hong Ng, R. J.; Dong, Z.; Ho, J.; Koay, E. H. H.; Ramakrishna, S.; Yang, J. K. W. Wide-gamut plasmonic color palettes with constant subwavelength resolution. *ACS Nano*, **13**, 3580–3588, **2019**.
- [45] Clausen, J. S.; Hojlund-Nielsen, E.; Christiansen, A. B.; Yazdi, S.; Grajower, M.; Taha, H.; Levy, U.; Kristensen, A.; Mortensen, N. A. Plasmonic metasurfaces for coloration of plastic consumer products. *Nano Lett.*, **14**, 4499–4504, **2014**.
- [46] Zhu, X.; Vannahme, C.; Højlund-Nielsen, E.; Mortensen, N. A.; Kristensen, A. Plasmonic colour laser printing. *Nat. Nanotechnol.*, **11**, 325–329, **2016**.
- [47] Tan, S. J.; Zhang, L.; Zhu, D.; Goh, X. M.; Wang, Y. M.; Kumar, K.; Qiu, C.-W.; Yang, J. K. W. Plasmonic color palettes for photorealistic printing with aluminum nanostructures. *Nano Lett.*, **14**, 4023–4029, **2014**.
- [48] Kumar, K.; Duan, H.; Hegde, R. S.; Koh, S. C. W.; Wei, J. N.; Yang, J. K. W. Printing colour at the optical diffraction limit. *Nat. Nanotechnol.*, **7**, 557–561, **2012**.
- [49] Xue, J.; Zhou, Z.-K.; Wei, Z.; Su, R.; Lai, J.; Li, J.; Li, C.; Zhang, T.; Wang, X.-H. Scalable, full-colour and controllable chromotropic plasmonic printing. *Nat. Commun.*, **6**, 8906, **2015**.
- [50] Xiong, K.; Tordera, D.; Emilsson, G.; Olsson, O.; Linderhed, U.; Jonsson, M. P.; Dahlén, A. B. Switchable plasmonic metasurfaces with high chromaticity containing only abundant metals. *Nano Lett.*, **17**, 7033–7039, **2017**.
- [51] Cheng, F.; Gao, J.; Luk, T. S.; Yang, X. Structural color printing based on plasmonic metasurfaces of perfect light absorption. *Sci. Rep.*, **5**, 11045, **2015**.
- [52] Chen, Y.; Duan, X.; Matuschek, M.; Zhou, Y.; Neubrech, F.; Duan, H.; Liu, N. Dynamic color displays using stepwise cavity resonators. *Nano Lett.*, **17**, 5555–5560, **2017**.

- [53] Yang, Z.; Chen, Y.; Zhou, Y.; Wang, Y.; Dai, P.; Zhu, X.; Duan, H. Microscopic interference full-color printing using grayscale-patterned Fabry-Perot resonance cavities. *Adv. Opt. Mater.*, **5**, 1700029, **2017**.
- [54] Yang, Z.; Zhou, Y.; Chen, Y.; Wang, Y.; Dai, P.; Zhang, Z.; Duan, H. Reflective color filters and monolithic color printing based on asymmetric Fabry-Perot cavities using nickel as a broadband absorber. *Adv. Opt. Mater.*, **4**, 1196–1202, **2016**.
- [55] Wu, Y. K.; Hollowell, A. E.; Zhang, C.; Guo, L. J. Angle-insensitive structural colours based on metallic nanocavities and coloured pixels beyond the diffraction limit. *Sci. Rep.*, **3**, 1194, **2013**.
- [56] Raj Shrestha, V.; Lee, S.-S.; Kim, E.-S.; Choi, D.-Y. Polarization-tuned dynamic color filters incorporating a dielectric-loaded aluminum nanowire array. *Sci. Rep.*, **5**, 12450, **2015**.
- [57] Cui, Y.; Hegde, R. S.; Phang, I. Y.; Lee, H. K.; Ling, X. Y. Encoding molecular information in plasmonic nanostructures for anti-counterfeiting applications. *Nanoscale*, **6**, 282–288, **2014**.
- [58] Xu, T.; Wu, Y.-K.; Luo, X.; Guo, L. J. Plasmonic nanoresonators for high-resolution colour filtering and spectral imaging. *Nat. Commun.*, **1**, 59, **2010**.
- [59] Tseng, M. L.; Yang, J.; Semmlinger, M.; Zhang, C.; Nordlander, P.; Halas, N. J. Two-dimensional active tuning of an aluminum plasmonic array for full-spectrum response. *Nano Lett.*, **17**, 6034–6039, **2017**.
- [60] Schlapbach, L.; Züttel, A. Hydrogen-storage materials for mobile applications. *Nature* **414**, 353–358, **2001**.
- [61] Züttel, A.; Remhof, A.; Borgschulte, A.; Friedrichs, O. Hydrogen: the future energy carrier. *Phil. Trans. R. Soc. A*, **368**, 3329–3342, **2010**.
- [62] Schiermeier, Q.; Tollefson, J.; Scully, T.; Witze, A.; Morton, O. Energy alternatives: Electricity without carbon. *Nature* **454**, 816–823, **2008**.
- [63] Schuth, F.; Bogdanovic, B.; Felderhoff, M. Light metal hydrides and complex hydrides for hydrogen storage. *Chem. Commun.*, 2249–2258, **2004**.
- [64] Züttel, A. Materials for hydrogen storage. *Mater. Today*, **6**, 24–33, **2003**.
- [65] Klebanoff, L.: *Hydrogen Storage Technology: Materials and Applications*; Taylor and Francis, Hoboken, **2012**.
- [66] Huheey, J. E.: *Inorganic chemistry : principles of structure and reactivity*; Harper & Row: New York, **1983**.
- [67] Manchester, F. D.; San-Martin, A.; Pitre, J. M. The H-Pd (hydrogen-palladium) System. *J. Phase Equilibria*, **15**, 62–83, **1994**.
- [68] Griessen, R.; Strohfeldt, N.; Giessen, H. Thermodynamics of the hybrid interaction of hydrogen with palladium nanoparticles. *Nat. Mater.*, **15**, 311–317, **2016**.
- [69] von Rottkay, K.; Rubin, M.; Duine, P. A. Refractive index changes of Pd-coated magnesium lanthanide switchable mirrors upon hydrogen insertion. *J. Appl. Phys.*, **85**, 408–413, **1999**.
- [70] Sun, Y.; Shen, C.; Lai, Q.; Liu, W.; Wang, D.-W.; Aguey-Zinsou, K.-F. Tailoring magnesium based materials for hydrogen storage through synthesis: Current state of the art. *Energy Storage Mater.*, **10**, 168–198, **2018**.
- [71] Drude, P. Zur Elektronentheorie der Metalle. *Ann. Phys. (Berl.)*, **306**, 566–613, **1900**.
- [72] Palik, E. D.: *Handbook of optical constants of solids*; Academic Press: New York, **1998**.
- [73] Krozer, A.; Kasemo, B. Hydrogen uptake by Pd-coated Mg: absorption-decomposition isotherms and uptake kinetics. *J. Less-Common Met.*, **160**, 323–342, **1990**.
- [74] Noritake, T.; Towata, S.; Aoki, M.; Seno, Y.; Hirose, Y.; Nishibori, E.; Takata, M.; Sakata, M. Charge density measurement in MgH<sub>2</sub> by synchrotron X-ray diffraction. *J. Alloys Compd.*, **356–357**, 84–86, **2003**.
- [75] Huot, J.; Ravnsbæk, D. B.; Zhang, J.; Cuevas, F.; Latroche, M.; Jensen, T. R. Mechanochemical synthesis of hydrogen storage materials. *Prog. Mater. Sci.*, **58**, 30–75, **2013**.
- [76] Isidorsson, J.; Giebels, I. A. M. E.; Arwin, H.; Griessen, R. Optical properties of MgH<sub>2</sub> measured in situ by ellipsometry and spectrophotometry. *Phys. Rev. B*, **68**, 115112, **2003**.
- [77] Gremaud, R.; Broedersz, C. P.; Borsa, D. M.; Borgschulte, A.; Mauron, P.; Schreuders, H.; Rector, J. H.; Dam, B.; Griessen, R. Hydrogenography: an optical combinatorial method to find new light-weight hydrogen-storage materials. *Adv. Mater.*, **19**, 2813–2817, **2007**.
- [78] Zhu, C.; Sakaguchi, N.; Hosokai, S.; Watanabe, S.; Akiyama, T. In situ transmission electron microscopy observation of the decomposition of MgH<sub>2</sub> nanofiber. *Int. J. Hydrg. Energy*, **36**, 3600–3605, **2011**.
- [79] Kelekar, R.; Giffard, H.; Kelly, S. T.; Clemens, B. M. Formation and dissociation of MgH<sub>2</sub> in epitaxial Mg thin films. *J. Appl. Phys.*, **101**, 114311, **2007**.
- [80] Kooi, B. J.; Palasantzas, G.; De Hosson, J. T. M. Gas-phase synthesis of magnesium nanoparticles: a high-resolution transmission electron microscopy study. *Appl. Phys. Lett.*, **89**, 161914, **2006**.

- [81] Appusamy, K.; Blair, S.; Nahata, A.; Guruswamy, S. Low-loss magnesium films for plasmonics. *Mater. Sci. Eng. B*, **181**, 77–85, **2014**.
- [82] Ares, J. R.; Leardini, F.; Díaz-Chao, P.; Ferrer, I. J.; Fernández, J. F.; Sánchez, C. Non-isothermal desorption process of hydrogenated nanocrystalline Pd-capped Mg films investigated by Ion Beam Techniques. *Int. J. Hydrot. Energy*, **39**, 2587–2596, **2014**.
- [83] Uchida, H. T.; Wagner, S.; Hamm, M.; Kürschner, J.; Kirchheim, R.; Hjörvarsson, B.; Pundt, A. Absorption kinetics and hydride formation in magnesium films: effect of driving force revisited. *Acta Mater.*, **85**, 279–289, **2015**.
- [84] Mooij, L.; Dam, B. Hysteresis and the role of nucleation and growth in the hydrogenation of Mg nanolayers. *Phys. Chem. Chem. Phys.*, **15**, 2782–2792, **2013**.
- [85] Baldi, A.; Gonzalez-Silveira, M.; Palmisano, V.; Dam, B.; Griessen, R. Destabilization of the Mg-H system through elastic constraints. *Phys. Rev. Lett.*, **102**, 226102, **2009**.
- [86] Ostenfeld, C. W.; Johansson, M.; Chorkendorff, I. Hydrogenation properties of catalyzed and non-catalyzed magnesium films. *Surf. Sci.*, **601**, 1862–1869, **2007**.
- [87] Uchida, H. T.; Kirchheim, R.; Pundt, A. Influence of hydrogen loading conditions on the blocking effect of nanocrystalline Mg films. *Scr. Mater.*, **64**, 935–937, **2011**.
- [88] van der Sluis, P.; Ouwerkerk, M.; Duine, P. A. Optical switches based on magnesium lanthanide alloy hydrides. *Appl. Phys. Lett.*, **70**, 3356–3358, **1997**.
- [89] Slaman, M.; Dam, B.; Pasturel, M.; Borsa, D. M.; Schreuders, H.; Rector, J. H.; Griessen, R. Fiber optic hydrogen detectors containing Mg-based metal hydrides. *Sens. Actuators, B: Chem.*, **123**, 538–545, **2007**.
- [90] Baldi, A.; Borsa, D. M.; Schreuders, H.; Rector, J. H.; Atmakidis, T.; Bakker, M.; Zondag, H. A.; van Helden, W. G. J.; Dam, B.; Griessen, R. Mg–Ti–H thin films as switchable solar absorbers. *Int. J. Hydrot. Energy*, **33**, 3188–3192, **2008**.
- [91] Tajima, K.; Yamada, Y.; Bao, S.; Okada, M.; Yoshimura, K. Flexible all-solid-state switchable mirror on plastic sheet. *Appl. Phys. Lett.*, **92**, 041912, **2008**.
- [92] Bérubé, V.; Radtke, G.; Dresselhaus, M.; Chen, G. Size effects on the hydrogen storage properties of nanostructured metal hydrides: a review. *Int. J. Energy Res.*, **31**, 637–663, **2007**.
- [93] Wagemans, R. W. P.; van Lenthe, J. H.; de Jongh, P. E.; van Dillen, A. J.; de Jong, K. P. Hydrogen storage in magnesium clusters: quantum chemical study. *J. Am. Chem. Soc.*, **127**, 16675–16680, **2005**.
- [94] Sterl, F.; Strohfeldt, N.; Walter, R.; Griessen, R.; Tittl, A.; Giessen, H. Magnesium as novel material for active plasmonics in the visible wavelength range. *Nano Lett.*, **15**, 7949–7955, **2015**.
- [95] Nordlien, J. H.; Ono, S.; Masuko, N.; Nişancioğlu, K. Morphology and structure of oxide films formed on magnesium by exposure to air and water. *J. Electrochem. Soc.*, **142**, 3320–3322, **1995**.
- [96] Ngene, P.; Westerwaal, R. J.; Sachdeva, S.; Haije, W.; de Smet, L. C. P. M.; Dam, B. Polymer-induced surface modifications of Pd-based thin films leading to improved kinetics in hydrogen sensing and energy storage applications. *Angew. Chem. Int. Ed.*, **53**, 12081–12085, **2014**.
- [97] Delmelle, R.; Ngene, P.; Dam, B.; Bleiner, D.; Borgschulte, A. Promotion of hydrogen desorption from palladium surfaces by fluoropolymer coating. *ChemCatChem*, **8**, 1646–1650, **2016**.
- [98] Wu, P. C.; Losurdo, M.; Kim, T.-H.; Garcia-Cueto, B.; Moreno, F.; Bruno, G.; Brown, A. S. Ga–Mg core–shell nanosystem for a novel full color plasmonics. *J. Phys. Chem. C*, **115**, 13571–13576, **2011**.
- [99] COMSOL Multiphysics User's Guide, version 4.3; Comsol AB, Brulington, MA, **2012**.
- [100] Reddy, J. N.: *An introduction to the finite element method*; New York: McGraw-Hill, **1993**.
- [101] Bonner, W. A. The origin and amplification of biomolecular chirality. *Origins Life Evol. B.*, **21**, 59–111, **1991**.
- [102] Luisi, P. L.: *The Emergence of Life - From Chemical Origins to Synthetic Biology*; Cambridge University Press, **2006**.
- [103] Meierhenrich, U. J. Amino acids and the asymmetry of life. *Eur. Rev.*, **21**, 190–199, **2013**.
- [104] Fasman, G. D.: *Circular dichroism and the conformational analysis of biomolecules*; Springer, Boston, MA, **1996**.
- [105] Huck, N. P. M.; Jager, W. F.; de Lange, B.; Feringa, B. L. Dynamic control and amplification of molecular chirality by circular polarized light. *Science*, **273**, 1686–1688, **1996**.
- [106] Koumura, N.; Zijlstra, R. W.; van Delden, R. A.; Harada, N.; Feringa, B. L. Light-driven monodirectional molecular rotor. *Nature*, **401**, 152–155, **1999**.
- [107] de Jong, J. J.; Lucas, L. N.; Kellogg, R. M.; van Esch, J. H.; Feringa, B. L. Reversible optical transcription of supramolecular chirality into molecular chirality. *Science*, **304**, 278–281, **2004**.
- [108] Ikeda, K.; Liu, W.; Shen, Y. R.; Uekusa, H.; Ohashi, Y.; Koshihara, S.-y. Photo-induced chirality switching in a cobaloxime complex crystal. *J. Chem. Phys.*, **122**, 141103, **2005**.

- [109] Reddy, R. A.; Schroder, M. W.; Bodyagin, M.; Kresse, H.; Diele, S.; Pelzl, G.; Weissflog, W. Field-induced switching of chirality in undulated ferroelectric and antiferroelectric SmCP phases formed by bent-core mesogens. *Angew. Chem. Int. Ed.*, **44**, 774–778, **2005**.
- [110] Hasegawa, T.; Morino, K.; Tanaka, Y.; Katagiri, H.; Furusho, Y.; Yashima, E. Temperature-driven switching of helical chirality of Poly[(4-carboxyphenyl)acetylene] induced by a single amidine enantiomer and memory of the diastereomeric macromolecular helicity. *Macromolecules*, **39**, 482–488, **2006**.
- [111] Murata, K.; Aoki, M.; Suzuki, T.; Harada, T.; Kawabata, H.; Komori, T.; Ohseto, F.; Ueda, K.; Shinkai, S. Thermal and light control of the sol-gel phase transition in cholesterol-based organic gels. Novel helical aggregation modes as detected by circular dichroism dichroism and electron microscopic observation. *J. Am. Chem. Soc.*, **116**, 6664–6676, **1994**.
- [112] Hentschel, M.; Schäferling, M.; Duan, X.; Giessen, H.; Liu, N. Chiral plasmonics. *Sci. Adv.*, **3**, e1602735, **2017**.
- [113] Matuschek, M.; Singh, D. P.; Jeong, H.-H.; Nesterov, M.; Weiss, T.; Fischer, P.; Neubrech, F.; Liu, N. Chiral plasmonic hydrogen sensors. *Small*, **14**, 1702990, **2018**.
- [114] Zhou, C.; Xin, L.; Duan, X.; Urban, M. J.; Liu, N. Dynamic plasmonic system that responds to thermal and aptamer-target regulations. *Nano Lett.*, **18**, 7395–7399, **2018**.
- [115] Urban, M. J.; Zhou, C.; Duan, X.; Liu, N. Optically resolving the dynamic walking of a plasmonic walker couple. *Nano Lett.*, **15**, 8392–8396, **2015**.
- [116] Jeong, H.-H.; Mark, A. G.; Fischer, P. Magnesium plasmonics for UV applications and chiral sensing. *Chem. Commun.*, **52**, 12179–12182, **2016**.
- [117] Rogacheva, A. V.; Fedotov, V. A.; Schwanecke, A. S.; Zheludev, N. I. Giant gyrotropy due to electromagnetic-field coupling in a bilayered chiral structure. *Phys. Rev. Lett.*, **97**, 177401, **2006**.
- [118] Gansel, J. K.; Thiel, M.; Rill, M. S.; Decker, M.; Bade, K.; Saile, V.; von Freymann, G.; Linden, S.; Wegener, M. Gold helix photonic metamaterial as broadband circular polarizer. *Science*, **325**, 1513–1515, **2009**.
- [119] Hendry, E.; Carpy, T.; Johnston, J.; Popland, M.; Mikhaylovskiy, R. V.; Lapthorn, A. J.; Kelly, S. M.; Barron, L. D.; Gadegaard, N.; Kadodwala, M. Ultrasensitive detection and characterization of biomolecules using superchiral fields. *Nat. Nanotechnol.*, **5**, 783–787, **2010**.
- [120] Kuzyk, A.; Schreiber, R.; Fan, Z.; Pardatscher, G.; Roller, E.-M.; Högele, A.; Simmel, F. C.; Govorov, A. O.; Liedl, T. DNA-based self-assembly of chiral plasmonic nanostructures with tailored optical response. *Nature* **483**, 311–314, **2012**.
- [121] Shen, X.; Song, C.; Wang, J.; Shi, D.; Wang, Z.; Liu, N.; Ding, B. Rolling up gold nanoparticle-dressed DNA origami into three-dimensional plasmonic chiral nanostructures. *J. Am. Chem. Soc.*, **134**, 146–149, **2012**.
- [122] Shen, X.; Asenjo-Garcia, A.; Liu, Q.; Jiang, Q.; García de Abajo, F. J.; Liu, N.; Ding, B. Three-dimensional plasmonic chiral tetramers assembled by DNA origami. *Nano Lett.*, **13**, 2128–2133, **2013**.
- [123] Kuzyk, A.; Schreiber, R.; Zhang, H.; Govorov, A. O.; Liedl, T.; Liu, N. Reconfigurable 3D plasmonic metamolecules. *Nat. Mater.*, **13**, 862–866, **2014**.
- [124] Zhou, C.; Duan, X.; Liu, N. A plasmonic nanorod that walks on DNA origami. *Nat. Commun.*, **6**, 8102, **2015**.
- [125] Hentschel, M.; Schäferling, M.; Weiss, T.; Liu, N.; Giessen, H. Three-dimensional chiral plasmonic oligomers. *Nano Lett.*, **12**, 2542–2547, **2012**.
- [126] Yin, X.; Schäferling, M.; Metzger, B.; Giessen, H. Interpreting chiral nanophotonic spectra: the plasmonic Born-Kuhn model. *Nano Lett.*, **13**, 6238–6243, **2013**.
- [127] Cui, Y.; Kang, L.; Lan, S.; Rodrigues, S.; Cai, W. Giant chiral optical response from a twisted-arc metamaterial. *Nano Lett.*, **14**, 1021–1025, **2014**.
- [128] Duan, X.; Yue, S.; Liu, N. Understanding complex chiral plasmonics. *Nanoscale*, **7**, 17237–17243, **2015**.
- [129] Zhang, S.; Zhou, J.; Park, Y.-S.; Rho, J.; Singh, R.; Nam, S.; Azad, A. K.; Chen, H.-T.; Yin, X.; Taylor, A. J.; Zhang, X. Photoinduced handedness switching in terahertz chiral metamolecules. *Nat. Commun.*, **3**, 942, **2012**.
- [130] Zhang, S.; Park, Y.-S.; Li, J.; Lu, X.; Zhang, W.; Zhang, X. Negative refractive index in chiral metamaterials. *Phys. Rev. Lett.*, **102**, 023901, **2009**.
- [131] Cao, T.; Zhang, L.; Simpson, R. E.; Wei, C.; Cryan, M. J. Strongly tunable circular dichroism in gammadiion chiral phase-change metamaterials. *Opt. Express*, **21**, 27841–27851, **2013**.
- [132] Yin, X.; Schäferling, M.; Michel, A.-K. U.; Tittl, A.; Wuttig, M.; Taubner, T.; Giessen, H. Active chiral plasmonics. *Nano Lett.*, **15**, 4255–4260, **2015**.
- [133] Duan, X.; Chen, S.; Cheng, H.; Li, Z.; Tian, J. Dynamically tunable plasmonically induced transparency by planar hybrid metamaterial. *Opt. Lett.*, **38**, 483–485, **2013**.

- [134] Borsa, D. M.; Baldi, A.; Pasturel, M.; Schreuders, H.; Dam, B.; Griessen, R.; Vermeulen, P.; Notten, P. H. L. Mg–Ti–H thin films for smart solar collectors. *Appl. Phys. Lett.*, **88**, 241910, **2006**.
- [135] Baldi, A.; Palmisano, V.; Gonzalez-Silveira, M.; Pivak, Y.; Slaman, M.; Schreuders, H.; Dam, B.; Griessen, R. Quasifree Mg–H thin films. *Appl. Phys. Lett.*, **95**, 071903, **2009**.
- [136] Baldi, A.; Pálsson, G. K.; Gonzalez-Silveira, M.; Schreuders, H.; Slaman, M.; Rector, J. H.; Krishnan, G.; Kooi, B. J.; Walker, G. S.; Fay, M. W.; Hjörvarsson, B.; Wijngaarden, R. J.; Dam, B.; Griessen, R. Mg/Ti multilayers: Structural and hydrogen absorption properties. *Phys. Rev. B*, **81**, 224203, **2010**.
- [137] Ngene, P.; Radeva, T.; Slaman, M.; Westerwaal, R. J.; Schreuders, H.; Dam, B. Seeing hydrogen in colors: low - cost and highly sensitive eye readable hydrogen detectors. *Adv. Funct. Mater.*, **24**, 2374–2382, **2014**.
- [138] Strohfeldt, N.; Tittl, A.; Schaferling, M.; Neubrech, F.; Kreibig, U.; Griessen, R.; Giessen, H. Yttrium hydride nanoantennas for active plasmonics. *Nano Lett.*, **14**, 1140–1147, **2014**.
- [139] Liu, N.; Tang, M. L.; Hentschel, M.; Giessen, H.; Alivisatos, A. P. Nanoantenna-enhanced gas sensing in a single tailored nanofocus. *Nat. Mater.*, **10**, 631–636, **2011**.
- [140] Tittl, A.; Mai, P.; Taubert, R.; Dregely, D.; Liu, N.; Giessen, H. Palladium-based plasmonic perfect absorber in the visible wavelength range and its application to hydrogen sensing. *Nano Lett.*, **11**, 4366–4369, **2011**.
- [141] Tittl, A.; Yin, X.; Giessen, H.; Tian, X.-D.; Tian, Z.-Q.; Kremers, C.; Chigrin, D. N.; Liu, N. Plasmonic smart dust for probing local chemical reactions. *Nano Lett.*, **13**, 1816–1821, **2013**.
- [142] Wadell, C.; Syrenova, S.; Langhammer, C. Plasmonic hydrogen sensing with nanostructured metal hydrides. *ACS Nano*, **8**, 11925–11940, **2014**.
- [143] Johnson, P. B.; Christy, R. W. Optical constants of the noble metals. *Phys. Rev. B*, **6**, 4370–4379, **1972**.
- [144] Lindström, R.; Johansson, L.-G.; Thompson, G. E.; Skeldon, P.; Svensson, J.-E. Corrosion of magnesium in humid air. *Corros. Sci.*, **46**, 1141–1158, **2004**.
- [145] Miyata, M.; Hataida, H.; Takahara, J. Full-color subwavelength printing with gap-plasmonic optical antennas. *Nano Lett.*, **16**, 3166–3172, **2016**.
- [146] Olson, J.; Manjavacas, A.; Liu, L.; Chang, W.-S.; Foerster, B.; King, N. S.; Knight, M. W.; Nordlander, P.; Halas, N. J.; Link, S. Vivid, full-color aluminum plasmonic pixels. *Proceedings of the National Academy of Sciences*, **111**, 14348, **2014**.
- [147] Duempelmann, L.; Luu-Dinh, A.; Gallinet, B.; Novotny, L. Four-fold color filter based on plasmonic phase retarder. *ACS Photonics*, **3**, 190–196, **2016**.
- [148] Franklin, D.; Chen, Y.; Vazquez-Guardado, A.; Modak, S.; Boroumand, J.; Xu, D.; Wu, S.-T.; Chanda, D. Polarization-independent actively tunable colour generation on imprinted plasmonic surfaces. *Nat. Commun.*, **6**, 7337, **2015**.
- [149] Xu, T.; Walter, E. C.; Agrawal, A.; Bohn, C.; Velmurugan, J.; Zhu, W.; Lezec, H. J.; Talin, A. A. High-contrast and fast electrochromic switching enabled by plasmonics. *Nat. Commun.*, **7**, 10479, **2016**.
- [150] Goh, X. M.; Zheng, Y.; Tan, S. J.; Zhang, L.; Kumar, K.; Qiu, C.-W.; Yang, J. K. W. Three-dimensional plasmonic stereoscopic prints in full colour. *Nat. Commun.*, **5**, 5361, **2014**.
- [151] Gu, Y.; Zhang, L.; Yang, J. K. W.; Yeo, S. P.; Qiu, C.-W. Color generation via subwavelength plasmonic nanostructures. *Nanoscale*, **7**, 6409–6419, **2015**.
- [152] Duan, X.; Kamin, S.; Sterl, F.; Giessen, H.; Liu, N. Hydrogen-regulated chiral nanoplasmonics. *Nano Lett.*, **16**, 1462–1466, **2016**.
- [153] Isidorsson, J.; Giebels, I. A. M. E.; Griessen, R.; Di Vece, M. Tunable reflectance Mg–Ni–H films. *Appl. Phys. Lett.*, **80**, 2305–2307, **2002**.
- [154] Slaman, M.; Dam, B.; Schreuders, H.; Griessen, R. Optimization of Mg-based fiber optic hydrogen detectors by alloying the catalyst. *Int. J. Hydrog. Energy*, **33**, 1084–1089, **2008**.
- [155] Montelongo, Y.; Tenorio-Pearl, J. O.; Williams, C.; Zhang, S.; Milne, W. I.; Wilkinson, T. D. Plasmonic nanoparticle scattering for color holograms. *Proc. Natl. Acad. Sci. U.S.A.*, **111**, 12679–12683, **2014**.
- [156] Zheng, G.; Muhlenbernd, H.; Kenney, M.; Li, G.; Zentgraf, T.; Zhang, S. Metasurface holograms reaching 80% efficiency. *Nat. Nanotechnol.*, **10**, 308–312, **2015**.
- [157] King, N. S.; Liu, L.; Yang, X.; Cerjan, B.; Everitt, H. O.; Nordlander, P.; Halas, N. J. Fano resonant aluminum nanoclusters for plasmonic colorimetric sensing. *ACS Nano*, **9**, 10628–10636, **2015**.
- [158] Richner, P.; Galliker, P.; Lendenmann, T.; Kress, S. J. P.; Kim, D. K.; Norris, D. J.; Poulikakos, D. Full-spectrum flexible color printing at the diffraction limit. *ACS Photonics*, **3**, 754–757, **2016**.
- [159] Roberts, A. S.; Pors, A.; Albrektsen, O.; Bozhevolnyi, S. I. Subwavelength plasmonic color printing protected for ambient use. *Nano Lett.*, **14**, 783–787, **2014**.

- [160] James, T. D.; Mulvaney, P.; Roberts, A. The plasmonic pixel: large area, wide gamut color reproduction using aluminum nanostructures. *Nano Lett.*, **16**, 3817–3823, **2016**.
- [161] Zhu, X.; Yan, W.; Levy, U.; Mortensen, N. A.; Kristensen, A. Resonant laser printing of structural colors on high-index dielectric metasurfaces. *Sci. Adv.*, **3**, e1602487, **2017**.
- [162] Chen, Q.; Cumming, D. R. S. High transmission and low color cross-talk plasmonic color filters using triangular-lattice hole arrays in aluminum films. *Opt. Express*, **18**, 14056–14062, **2010**.
- [163] Cao, L.; Fan, P.; Barnard, E. S.; Brown, A. M.; Brongersma, M. L. Tuning the color of silicon nanostructures. *Nano Lett.*, **10**, 2649–2654, **2010**.
- [164] Burgos, S. P.; Yokogawa, S.; Atwater, H. A. Color imaging via nearest neighbor hole coupling in plasmonic color filters integrated onto a complementary metal-oxide semiconductor image sensor. *ACS Nano*, **7**, 10038–10047, **2013**.
- [165] Bao, J.; Bawendi, M. G. A colloidal quantum dot spectrometer. *Nature* **523**, 67–70, **2015**.
- [166] Stipe, B. C.; Strand, T. C.; Poon, C. C.; Balamane, H.; Boone, T. D.; Katine, J. A.; Li, J.-L.; Rawat, V.; Nemoto, H.; Hirotsune, A.; Hellwig, O.; Ruiz, R.; Dobisz, E.; Kercher, D. S.; Robertson, N.; Albrecht, T. R.; Terris, B. D. Magnetic recording at  $1.5 \text{ Pb m}^{-2}$  using an integrated plasmonic antenna. *Nat. Photonics*, **4**, 484–488, **2010**.
- [167] Olson, J.; Manjavacas, A.; Basu, T.; Huang, D.; Schlather, A. E.; Zheng, B.; Halas, N. J.; Nordlander, P.; Link, S. High chromaticity aluminum plasmonic pixels for active liquid crystal displays. *ACS Nano*, **10**, 1108–1117, **2016**.
- [168] Stec, G. J.; Lauchner, A.; Cui, Y.; Nordlander, P.; Halas, N. J. Multicolor electrochromic devices based on molecular plasmonics. *ACS Nano*, **11**, 3254–3261, **2017**.
- [169] Duan, X.; Kamin, S.; Liu, N. Dynamic plasmonic colour display. *Nat. Commun.*, **8**, 14606, **2017**.
- [170] Crivello, J.-C.; Dam, B.; Denys, R. V.; Dornheim, M.; Grant, D. M.; Huot, J.; Jensen, T. R.; de Jongh, P.; Latroche, M.; Milanese, C.; Milčius, D.; Walker, G. S.; Webb, C. J.; Zlotea, C.; Yartys, V. A. Review of magnesium hydride-based materials: development and optimisation. *Appl. Phys. A*, **122**, 97, **2016**.
- [171] Spatz, P.; Aebsicher, H. A.; Krozer, A.; Schlapbach, L. The diffusion of H in Mg and the nucleation and growth of  $\text{MgH}_2$  in thin films. *Z. Phys. Chem.*, **181**, 393–397, **1993**.
- [172] Rydén, J.; Hjörvarsson, B.; Ericsson, T.; Karlsson, E.; Krozer, A.; Kasemo, B. Unusual kinetics of hydride formation in Mg–Pd sandwiches, studied by hydrogen profiling and quartz crystal microbalance measurements. *J. Less-Common Met.*, **152**, 295–309, **1989**.
- [173] Westerwaal, R. J.; Broedersz, C. P.; Gremaud, R.; Slaman, M.; Borgschulte, A.; Lohstroh, W.; Tschersich, K. G.; Fleischhauer, H. P.; Dam, B.; Griessen, R. Study of the hydride forming process of in-situ grown  $\text{MgH}_2$  thin films by activated reactive evaporation. *Thin Solid Films*, **516**, 4351–4359, **2008**.
- [174] Mooij, L. P. A.; Baldi, A.; Boelsma, C.; Shen, K.; Wagemaker, M.; Pivak, Y.; Schreuders, H.; Griessen, R.; Dam, B. Interface energy controlled thermodynamics of nanoscale metal hydrides. *Adv. Energy Mater.*, **1**, 754–758, **2011**.
- [175] Bannenberg, L. J.; Schreuders, H.; van Eijck, L.; Heringa, J. R.; Steinke, N.-J.; Dalgliesh, R.; Dam, B.; Mulder, F. M.; van Well, A. A. Impact of nanostructuring on the phase behavior of insertion materials: the hydrogenation kinetics of a magnesium thin film. *J. Phys. Chem. C*, **120**, 10185–10191, **2016**.
- [176] Jung, H.; Cho, S.; Lee, W. Enhanced hydrogen storage properties of Pd/Ti/Mg/Ti multilayer films using the catalytic effects of Pd. *Appl. Phys. Lett.*, **106**, 193902, **2015**.
- [177] Vajeeston, P.; Ravindran, P.; Kjekshus, A.; Fjellvåg, H. Pressure-induced structural transitions in  $\text{MgH}_2$ . *Phys. Rev. Lett.*, **89**, 175506, **2002**.
- [178] Manchester, F. D.: *Phase diagrams of binary hydrogen alloys*; ASM International: Materials Park, OH, **2000**.
- [179] Efimenko, K.; Rackaitis, M.; Manias, E.; Vaziri, A.; Mahadevan, L.; Genzer, J. Nested self-similar wrinkling patterns in skins. *Nat. Mater.*, **4**, 293–297, **2005**.
- [180] O’Leary, M. A.; Boas, D. A.; Chance, B.; Yodh, A. G. Refraction of diffuse photon density waves. *Phys. Rev. Lett.*, **69**, 2658–2661, **1992**.
- [181] Remhof, A.; Wijngaarden, R. J.; Griessen, R. Refraction and reflection of diffusion fronts. *Phys. Rev. Lett.*, **90**, 145502, **2003**.
- [182] Crank, J.: *The mathematics of diffusion*; Clarendon Press: Oxford, Eng, **1975**.
- [183] Chung, J. Y.; Nolte, A. J.; Stafford, C. M. Diffusion-controlled, self-organized growth of symmetric wrinkling patterns. *Adv. Mater.*, **21**, 1358–1362, **2009**.
- [184] Qu, J.; Sun, B.; Yang, R.; Zhao, W.; Wang, Y.; Li, X. Hydrogen absorption kinetics of Mg thin films under mild conditions. *Scr. Mater.*, **62**, 317–320, **2010**.
- [185] Li, W.; Li, C.; Ma, H.; Chen, J. Magnesium nanowires: enhanced kinetics for hydrogen absorption and desorption. *J. Am. Chem. Soc.*, **129**, 6710–6711, **2007**.

- [186] Jeon, K.-J.; Moon, H. R.; Ruminski, A. M.; Jiang, B.; Kisielowski, C.; Bardhan, R.; Urban, J. J. Air-stable magnesium nanocomposites provide rapid and high-capacity hydrogen storage without using heavy-metal catalysts. *Nat. Mater.*, **10**, 286–290, **2011**.
- [187] Sterl, F.; Linnenbank, H.; Steinle, T.; Morz, F.; Strohfeldt, N.; Giessen, H. Nanoscale hydrogenography on single magnesium nanoparticles. *Nano Lett.*, **18**, 4293–4302, **2018**.
- [188] Renner, J.; Grabke, H. J. Bestimmung von Diffusionskoeffizienten bei der Hydrierung von Legierungen. *Z. Metallkd.*, **69**, 639–642, **1978**.
- [189] Fukai, Y.: *The Metal-Hydrogen System: Basic Bulk Properties*; Springer: Berlin ; New York, **2005**.
- [190] den Broeder, F. J. A.; van der Molen, S. J.; Kremers, M.; Huiberts, J. N.; Nagengast, D. G.; van Gogh, A. T. M.; Huisman, W. H.; Koeman, N. J.; Dam, B.; Rector, J. H.; Plota, S.; Haaksma, M.; Hanzen, R. M. N.; Jungblut, R. M.; Duine, P. A.; Griessen, R. Visualization of hydrogen migration in solids using switchable mirrors. *Nature* **394**, 656–658, **1998**.
- [191] Remhof, A.; Borgschulte, A. Thin-film metal hydrides. *ChemPhysChem*, **9**, 2440–2455, **2008**.
- [192] Oono, Y.; Puri, S. Study of phase-separation dynamics by use of cell dynamical systems. I. Modeling. *Phys. Rev. A*, **38**, 434–453, **1988**.
- [193] Kerssemakers, J. W. J.; van der Molen, S. J.; Koeman, N. J.; Günther, R.; Griessen, R. Pixel switching of epitaxial Pd/YH<sub>x</sub>/CaF<sub>2</sub> switchable mirrors. *Nature* **406**, 489–491, **2000**.
- [194] Kerssemakers, J. W. J.; van der Molen, S. J.; Günther, R.; Dam, B.; Griessen, R. Local switching in epitaxial YH<sub>x</sub> switchable mirrors. *Phys. Rev. B*, **65**, 075417, **2002**.
- [195] Kerssemakers, J. W. J.; van der Molen, S. J.; Günther, R.; Dam, B.; Griessen, R. In situ monitoring of optical and structural switching in epitaxial YH<sub>x</sub> switchable mirrors. *J. Alloys Compd.*, **330–332**, 342–347, **2002**.
- [196] Völkl, J.; Alefeld, G.: *Hydrogen in Metals I*; Springer-Verlag, Berlin, **1978**; Vol. 28.
- [197] Lai, W.; Ciucci, F. Thermodynamics and kinetics of phase transformation in intercalation battery electrodes – phenomenological modeling. *Electrochim. Acta*, **56**, 531–542, **2010**.
- [198] de Man, S.; Gonzalez-Silveira, M.; Visser, D.; Bakker, R.; Schreuders, H.; Baldi, A.; Dam, B.; Griessen, R. Combinatorial method for direct measurements of the intrinsic hydrogen permeability of separation membrane materials. *J. Membrane Sci.*, **444**, 70–76, **2013**.
- [199] Pivak, Y.; Gremaud, R.; Gross, K.; Gonzalezsilveira, M.; Walton, A.; Book, D.; Schreuders, H.; Dam, B.; Griessen, R. Effect of the substrate on the thermodynamic properties of PdH<sub>x</sub> films studied by hydrogenography. *Scr. Mater.*, **60**, 348–351, **2009**.
- [200] Duan, X.; Liu, N. Scanning plasmonic color display. *ACS Nano*, **12**, 8817–8823, **2018**.
- [201] Schittny, R.; Kadic, M.; Guenneau, S.; Wegener, M. Experiments on transformation thermodynamics: molding the flow of heat. *Phys. Rev. Lett.*, **110**, 195901, **2013**.
- [202] Leonhardt, U. Cloaking of heat. *Nature* **498**, 440–441, **2013**.
- [203] Armand, M.; Tarascon, J.-M. Building better batteries. *Nature* **451**, 652–657, **2008**.
- [204] Chu, S.; Cui, Y.; Liu, N. The path towards sustainable energy. *Nat. Mater.*, **16**, 16–22, **2016**.
- [205] Lin, D.; Liu, Y.; Pei, A.; Cui, Y. Nanoscale perspective: Materials designs and understandings in lithium metal anodes. *Nano Research*, **10**, 4003–4026, **2017**.
- [206] Zhang, X.; Krischok, A.; Linder, C. A variational framework to model diffusion induced large plastic deformation and phase field fracture during initial two-phase lithiation of silicon electrodes. *Comput. Methods Appl. Mech. Eng.*, **312**, 51–77, **2016**.
- [207] Xiao, X.; Zhou, W.; Kim, Y.; Ryu, I.; Gu, M.; Wang, C.; Liu, G.; Liu, Z.; Gao, H. Regulated breathing effect of silicon negative electrode for dramatically enhanced performance of Li-ion battery. *Adv. Funct. Mater.*, **25**, 1426–1433, **2015**.
- [208] Zhang, S. Chemomechanical modeling of lithiation-induced failure in high-volume-change electrode materials for lithium ion batteries. *npj Comput. Mater.*, **3**, 7, **2017**.
- [209] Albrecht, J.; Matveev, A. T.; Strempfer, J.; Habermeier, H.-U.; Shantsev, D. V.; Galperin, Y. M.; Johansen, T. H. Dramatic role of critical current anisotropy on flux avalanches in MgB<sub>2</sub> films. *Phys. Rev. Lett.*, **98**, 117001, **2007**.
- [210] Heydari, E.; Sperling, J. R.; Neale, S. L.; Clark, A. W. Plasmonic color filters as dual-state nanopixels for high-density microimage encoding. *Adv. Funct. Mater.*, **27**, 1701866, **2017**.
- [211] Lee, Y.; Park, M.-K.; Kim, S.; Shin, J. H.; Moon, C.; Hwang, J. Y.; Choi, J.-C.; Park, H.; Kim, H.-R.; Jang, J. E. Electrical broad tuning of plasmonic color filter employing an asymmetric-lattice nanohole array of metasurface controlled by polarization rotator. *ACS Photonics*, **4**, 1954–1966, **2017**.
- [212] Gutruf, P.; Zou, C.; Withayachumnankul, W.; Bhaskaran, M.; Sriram, S.; Fumeaux, C. Mechanically tunable dielectric resonator metasurfaces at visible frequencies. *ACS Nano*, **10**, 133–141, **2016**.
- [213] Gholipour, B.; Adamo, G.; Cortecchia, D.; Krishnamoorthy, H. N. S.; Birowosuto, M. D.; Zheludev, N. I.; Soci, C. Organometallic perovskite metasurfaces. *Adv. Mater.*, **29**, 1604268, **2017**.

- [214] Shu, F.-Z.; Yu, F.-F.; Peng, R.-W.; Zhu, Y.-Y.; Xiong, B.; Fan, R.-H.; Wang, Z.-H.; Liu, Y.; Wang, M. Dynamic plasmonic color generation based on phase transition of vanadium dioxide. *Adv. Opt. Mater.*, **6**, 1700939, **2018**.
- [215] Sun, S.; Yang, W.; Zhang, C.; Jing, J.; Gao, Y.; Yu, X.; Song, Q.; Xiao, S. Real-time tunable colors from microfluidic reconfigurable all-dielectric metasurfaces. *ACS Nano*, **12**, 2151–2159, **2018**.
- [216] Guay, J.-M.; Cala Lesina, A.; Cote, G.; Charron, M.; Poitras, D.; Ramunno, L.; Berini, P.; Weck, A. Laser-induced plasmonic colours on metals. *Nat. Commun.*, **8**, 16095, **2017**.
- [217] Liu, N.; Guo, H.; Fu, L.; Kaiser, S.; Schweizer, H.; Giessen, H. Plasmon hybridization in stacked cut-wire metamaterials. *Adv. Mater.*, **19**, 3628–3632, **2007**.
- [218] Yamada, Y.; Miura, M.; Tajima, K.; Okada, M.; Yoshimura, K. Influence on optical properties and switching durability by introducing Ta intermediate layer in Mg–Y switchable mirrors. *Solar Energy Materials and Solar Cells*, **125**, 133–137, **2014**.
- [219] Li, J.; Kamin, S.; Zheng, G.; Neubrech, F.; Zhang, S.; Liu, N. Addressable metasurfaces for dynamic holography and optical information encryption. *Sci. Adv.*, **4**, eaar6768, **2018**.
- [220] Yu, P.; Li, J.; Zhang, S.; Jin, Z.; Schutz, G.; Qiu, C.-W.; Hirscher, M.; Liu, N. Dynamic Janus metasurfaces in the visible spectral region. *Nano Lett.*, **18**, 4584–4589, **2018**.
- [221] Yu, N.; Genevet, P.; Kats, M. A.; Aieta, F.; Tetienne, J.-P.; Capasso, F.; Gaburro, Z. Light propagation with phase discontinuities: generalized laws of reflection and refraction. *Science*, **334**, 333–337, **2011**.
- [222] Narayan, T. C.; Baldi, A.; Koh, A. L.; Sinclair, R.; Dionne, J. A. Reconstructing solute-induced phase transformations within individual nanocrystals. *Nat. Mater.*, **15**, 768–774, **2016**.
- [223] Biggins, J. S.; Yazdi, S.; Ringe, E. Magnesium nanoparticle plasmonics. *Nano Lett.*, **18**, 3752–3758, **2018**.
- [224] Kalisvaart, W. P.; Harrower, C. T.; Haagsma, J.; Zahiri, B.; Luber, E. J.; Ophus, C.; Poirier, E.; Fritzsche, H.; Mitlin, D. Hydrogen storage in binary and ternary Mg-based alloys: A comprehensive experimental study. *Int. J. Hydrol. Energy*, **35**, 2091–2103, **2010**.



# Curriculum Vitae

## Personal Data

Xiaoyang Duan  
 Gender: Male.  
 Date of birth: May 15<sup>th</sup> 1990.  
 Place of Birth: Linfen, Shanxi, P. R. China.  
 Nationality: Chinese.  
 ResearcherID: M-5453-2015  
 ORCID: [0000-0002-8720-3788](https://orcid.org/0000-0002-8720-3788)  
 Email: [xiaoyang4duan@gmail.com](mailto:xiaoyang4duan@gmail.com)



## Scientific career and education

2015.10 ~ 2019.07	Max-Planck-Institute for Intelligent Systems, Germany Heidelberg University, Germany Kirchhoff-Institute for Physics, PhD candidate advisor: Prof. Dr. Laura Na Liu
2013.10 ~ 2015.10	University of Stuttgart, Germany Physics Department, M. Sc. in Physics advisor: Prof. Dr. Laura Na Liu
2009.09 ~ 2013.06	Nankai University, P. R. China School of Physics, B. Sc. in Applied Physics

## Awards

- ◆ 2019, “2018 Chinese Government Award for Outstanding Self-financed Students Abroad” from the China Scholarship Council.
- ◆ 2017, The best poster award at the “Nanophotonics and Micro/Nano Optics International Conference 2017” in Barcelona, Spain.
- ◆ 2013, The Second Prize of “Challenge Cup” National College Student Curricular Academic Science and Technology Works Competition.
- ◆ 2013, The Grand Prize of “Challenge Cup” Tianjin College Student Curricular Academic Science and Technology Works Competition.
- ◆ 2013, The Grand Prize of Nankai Excellent Technological Innovation.
- ◆ 2011~2012, The First Prize of Nankai Individual Special Scholarship (for Excellent Technological Innovation).
- ◆ 2011~2012, National Encouragement Scholarship.
- ◆ 2010, Champion of the China Undergraduate Physicists’ Tournament.
- ◆ 2009~2012, Model of Excellent Students of Nankai University.
- ◆ 2009~2012, The First Prize of Excellent Undergraduate Scholarship, Nankai University.

## Publications

(\* implies equal contribution)

- [1] **Xiaoyang Duan**, Na Liu  
*Magnesium for dynamic nanoplasmonics*  
*Accounts of Chemical Research*, invited (2019).
- [2] **Xiaoyang Duan**, Ronald Griessen, Rinke J. Wijngaarden, Simon Kamin, Na Liu  
*Self-recording and manipulation of fast long-range hydrogen diffusion in quasifree magnesium*  
*Physical Review Materials*, 2, 085802 (2018).
- [3] **Xiaoyang Duan**, Na Liu  
*Scanning Plasmonic Color Display*  
*ACS Nano*, 12, 8817 (2018).
- [4] Chao Zhou, Ling Xin, **Xiaoyang Duan**, Maximilian J. Urban, Na Liu  
*A dynamic plasmonic system that responds to thermal and aptamer-target regulations*  
*Nano Letters*, 18, 7395 (2018).

- [5] Chao Zhou, **Xiaoyang Duan**, Na Liu  
*DNA-nanotechnology-enabled chiral plasmonics: from static to dynamic*  
*Accounts of Chemical Research*, 50, 2906 (2017).
- [6] Yiqin Chen\*, **Xiaoyang Duan\***, Marcus Matuschek\*, Yanming Zhou, Frank Neubrech, Huigao Duan, Na Liu  
*Dynamic color displays using stepwise cavity resonators*  
*Nano Letters*, 17, 5555 (2017).
- [7] Mario Hentschel, Martin Schäferling, **Xiaoyang Duan**, Harald Giessen, Na Liu  
*Chiral plasmonics*  
*Science Advances.*, 3, e1602735 (2017).
- [8] **Xiaoyang Duan**, Simon Kamin, Na Liu  
*Dynamic plasmonic colour display*  
*Nature Communications*, 8, 14606 (2017).
- [9] Maximilian J. Urban, Palash K. Dutta, Pengfei Wang, **Xiaoyang Duan**, Xibo Shen, Baoquan Ding, Yonggang Ke, Na Liu  
*Plasmonic Toroidal Metamolecules Assembled by DNA Origami*  
*Journal of the American Chemical Society*, 138, 5495 (2016).
- [10] Anton Kuzyk, Yangyang Yang, **Xiaoyang Duan**, Simon Stoll, Alexander O. Govorov, Hiroshi Sugiyama, Masayuki Endo, Na Liu  
*A light-driven three-dimensional plasmonic nanosystem that translates molecular motion into reversible chiroptical function*  
*Nature Communications*, 7, 10591 (2016).
- [11] **Xiaoyang Duan**, Simon Kamin, Florian Sterl, Harald Giessen, Na Liu  
*Hydrogen-Regulated Chiral Nanoplasmonics*  
*Nano Letters*, 16, 1462 (2016).
- [12] Maximilian J. Urban, Chao Zhou, **Xiaoyang Duan**, Na Liu  
*Optically Resolving the Dynamic Walking of a Plasmonic Walker Couple*  
*Nano Letters* 15, 8392–8396 (2015).
- [13] **Xiaoyang Duan**, Song Yue, Na Liu  
*Understanding complex chiral plasmonics*  
*Nanoscale*, 7, 17237 (2015).
- [14] Chao Zhou, **Xiaoyang Duan**, Na Liu  
*A plasmonic nanorod that walks on DNA origami*  
*Nature Communications*, 6, 8102 (2015).
- [15] **Xiaoyang Duan**, Shuqi Chen, Wenwei Liu, Hua Cheng, Zhancheng Li, Jianguo Tian  
*Polarization-insensitive and wide-angle broadband nearly perfect absorber by tunable planar metamaterials in the visible regime*  
*Journal of Optics*, 16, 125107 (2014).
- [16] **Xiaoyang Duan**, Shuqi Chen, Hua Cheng, Zhancheng Li, Jianguo Tian  
*Dynamically tunable plasmonically induced transparency by planar hybrid metamaterial*  
*Optics Letters*, 38, 483 (2013).
- [17] Hua Cheng, Shuqi Chen, Ping Yu, **Xiaoyang Duan**, Boyang Xie, Jianguo Tian  
*Dynamically tunable plasmonically induced transparency in periodically patterned graphene nanostrips*  
*Applied Physics Letters*, 103, 203112 (2013).
- [18] Jianxiong Li, Shuqi Chen, Ping Yu, Hua Cheng, **Xiaoyang Duan**, Jianguo Tian  
*Realization of near-field linear nano-polarizer by asymmetric nanoaperture and bowtie nanoantenna*  
*Optical Express*, 21, 10342 (2013).
- [19] **Xiaoyang Duan**, Shuqi Chen, Haifang Yang, Hua Cheng, Junjie Li, Wenwei Liu, Changzhi Gu, Jianguo Tian  
*Polarization-insensitive and wide-angle plasmonically induced transparency by planar metamaterials*  
*Applied Physics Letters*, 101, 143105 (2012).
- [20] Shuqi Chen, Hua Cheng, Haifang Yang, Junjie Li, **Xiaoyang Duan**, Changzhi Gu, Jianguo Tian  
*Polarization insensitive and omnidirectional broadband near perfect planar metamaterial absorber in the near infrared regime*  
*Applied Physics Letters*, 99, 253104 (2011).

## Acknowledgment

Looking back over the past four years of my PhD at Max Planck Institute Intelligent for Systems and Heidelberg University, I want to acknowledge all the people who helped me and who contributed to this thesis.

First, I sincerely thank Prof. Laura Na Liu for her excellent supervision and guidance throughout my entire master's studies and PhD studies in Germany. I am very thankful to her for giving me the opportunity to work together, for giving me enough freedom in research projects, for always being encouraging and motivating. I will never forget the countless moments when an interesting idea was inspired from intense discussions with her.

I would like to thank Prof. Yana Vaynzof, Prof. Ulrich Schwarz, and Prof. Annemarie Pucci for being so kind to be the examination committee and for all their support.

Furthermore, I would like to thank:

- Prof. Ronald Griessen, for his creative ideas and deep insights in physics, especially in hydrogen-metal systems, and also for fruitful collaborations.
- Prof Huigao Duan, for his supports, discussions, and fruitful collaborations.
- Prof. Jürgen Weiss for giving me the opportunity to work in the clean room at the Max Planck Institute for Solid State Research, as well as Thomas Reindl for his help and guidance.
- Prof. Harald Giessen for giving me the opportunity to work in the clean room at the 4<sup>th</sup> Institute at the University of Stuttgart. I also thank Dr. Mario Hentschel, Monika Ubl, and Ramon Walter for all their supports and guidance in the clean room.
- Dr. Frank Neubrech for being so kind to help me to optimize this thesis.
- Simon Kamin, Marcus Matuschek, and Maximilian Urban for being great colleagues for a long time and good friends, for all the shared projects, for enthusiastic and selfless help, for always lightening moods.
- Chao Zhou, Anton Kuzyk, Xibo Shen for interesting discussions and technical supports in chemistry.

Last but not the least, I would like to thank all my friends for staying with me through all the good and bad times. Finally, my deepest thanks go to my parents who give me the everlasting love, encouragement and support to catch my dream.